Université de Neuchâtel

INSTITUT DE PHYSIQUE DE L'UNIVERSITÉ DE NEUCHÂTEL

THESE

INTITULÉE

INTERPLAY OF FRUSTRATION AND GEOMETRY IN JOSEPHSON JUNCTION ARRAYS ON A DICE LATTICE

PRÉSENTÉE À LA FACULTÉ DES SCIENCES
DE L'UNIVERSITÉ DE NEUCHÂTEL
POUR L'OBTENTION DU GRADE DE DOCTEUR ÈS SCIENCES

PAR

MAURO TESEI

PHYSICIEN DIPLÔMÉ DE L'UNIVERSITÉ DE NEUCHÂTEL

SOUTENUE LE 11 OCTOBRE 2005

EN PRÉSENCE DU DIRECTEUR DE THÈSE
PROF. PIERO MARTINOLI

ET DES RAPPORTEURS
DR. BERNARD PANNETIER
PROF. HANS BECK ET PROF. FRÉDÉRIC MILA

Neuchâtel, décembre 2005

Résumé

Mots clés : Supraconductivité, jonctions Josephson, modèle XY, dégénérescence accidentelle, frustration, dynamique des vortex.

Key words : Superconductivity, Josephson junctions, XY model, accidental degeneracy, frustration, vortex dynamics.

Cette thèse est dédiée aux effets de compétition entre le champ magnétique appliqué et la géométrie du pavage de réseaux de jonctions Josephson dans le cas particulier d'un pavage T_3 ("dice"). Il s'agit en fait de l'étude d'un système modèle dans des conditions réelles. Le comportement des réseaux de jonctions classiques a été étudié en fonction du champ magnétique appliqué, de la température et de la fréquence avec laquelle le système est excité. Les propriétés de transport des réseaux de jonctions Josephson réalisées par effet de proximité sont mises en évidence par des mesures de l'impédance de surface effectuées au moyen d'une technique inductive qui distingue les travaux de recherche menés au sein du groupe.

Selon la valeur du champ magnétique appliqué, il sera impossible pour le réseau de jonctions de se placer dans un minimum absolu d'énergie. Le système doit alors trouver un compromis entre les différentes contraintes liées à la fois au champ magnétique appliqué et à la géométrie du réseau. C'est dans une telle situation que le système est dit frustré. Le comportement est radicalement différent selon l'état de frustration, i.e. selon le champ magnétique appliqué. La particularité du pavage T_3, composé de losanges orientés selon trois directions différentes, se manifeste lorsque le champ appliqué est tel que chaque losange du réseau est traversé par un demi quantum de flux. Dans ce cas la cohérence de phase, et par conséquent la supraconductivité, dans l'échantillon est presque supprimée et la dissipation est plus importante que pour n'importe quelle autre valeur de champ magnétique. Une comparaison entre cet état dit totalement frustré et un état qui au contraire présente une forte cohérence de phase a permis de révéler une riche variété de phénomènes. Les propriétés liées au modèle de mécanique statistique étudié, le modèle "XY", appliqué à cette géométrie particulière permettent de comprendre une partie seulement des observations. Il a donc été nécessaire d'aller au-delà du système modèle et pour la première fois les effets d'écrantage magnétique provenant du réseau de jonctions ont été pris en compte afin de comprendre le comportement critique. Ces effets magnétiques peuvent même être

dominants dans la région critique du modèle statistique et en changer le comportement, comme dans le cas de l'état totalement frustré.
Par ailleurs les observations expérimentales montrent à basse température une dynamique similaire pour plusieurs états de frustration et pour différentes géométries du pavage. Ces similitudes reflètent la prédominance de paramètres intrinsèques au type de réseaux de jonctions étudié et à leur procédé de fabrication.

Cette thèse répond à plusieurs interrogations surgies à la suite de travaux antérieurs, notamment sur le comportement critique de l'état totalement frustré. A son tour ce travail laisse quelques questions ouvertes concernant les mécanismes qui ont majeure influence sur la dynamique des vortex et plus généralement des défauts topologiques dans les réseaux de jonctions Josephson classiques.

Acknowledgements

I would like to thank my thesis director, Prof. Piero Martinoli, who gave me the opportunity to do my Ph.D. in his group, guided me under his supervision and helped me with useful discussions.

I am indebted to Dr. Ricardo Théron for his encouragements and for the help he gave me throughout the whole period of my Ph.D. I appreciated the time we spent in the laboratories and the useful discussions we had. The large amount of experimental work would not have been possible without his precious advice, and the know-how of the mechanics and electronics workshops of the institute.

I am grateful to Dr. Bernard Pannetier for all I learned working with him during my stay in the Centre de Recherche sur les Très Basses Températures (CRTBT) CNRS in Grenoble (France).

I am thankful to Dr. Bernard Pannetier, Prof. Hans Beck and Prof. Frédéric Mila for having accepted to be examiners for this thesis.

I would like to express my gratitude to all the members of the group, Piero, Ricardo, Alain, Chris, Silvia, Oscar, and Veronica, for their friendship and the good working atmosphere they created.

Last but not least, I wish to thank my parents and all my friends for their support during the last years.

Contents

List of Figures

List of Tables

Abbreviations and Notations

SC : superconducting
SNS : Superconducting-Normal-Superconducting
JJ(s) : Josephson junction(s)
JJA(s) : Josephson junction array(s)
WN(s) : wire network(s)
FFXY : fully frustrated XY (model)
DW(s) : domain wall(s)
ZEDW(s) : zero energy domain wall(s)
BKT : Berezinskii-Kosterlitz-Thouless
GS : ground state(s)

f : frustration parameter, or reduced flux, defined as the magnetic flux threading a unit cell of the array Φ_{cell} in units of the flux quantum ϕ_0
$f \overset{def}{=} \Phi_{cell}/\phi_0 \overset{dice}{\equiv} (\sqrt{3}/2)(Ba^2/\phi_0)$, B is the applied transverse magnetic field
ϕ_0 : flux quantum $\phi_0 = h/2e \cong 2.07 \cdot 10^{-15}$ Tm^2
Z : dynamic sheet impedance $Z(T, f, \omega) = R_Z + i\omega L_Z$
G : dynamic sheet conductance $G(T, f, \omega) = 1/R_G + 1/(i\omega L_G) \equiv 1/Z$
I_S : superconducting current
I_{CJ} : single junction critical current in zero field
J_{CJ} : single junction critical current density
L_J : kinetic inductance, not renormalized by fluctuations, $L_J = (\hbar/2e)/I_{CJ}(0)$
θ_{ij} : gauge invariant phase difference between two neighbouring sites i and j
$\theta_{ij} = \varphi_j - \varphi_i + A_{ij}$
φ_i : superconducting order parameter in site i
A_{ij} : linear integral of the vector potential along the bond $< ij >$
E_J : junction energy $E_J(T, f) = -J\cos(\theta_{ij})$
E_m : magnetic energy stored in each current loop around the array cells
$E_m = (1/2)\mathcal{L}I_S^2$ where $\mathcal{L}$ =26pH is the inductance of the rhombic loop
J : Josephson coupling energy, $J = (\hbar/2e)I_{CJ}$
L_J : single junction inductance in zero field, $L_J(T) = (\phi_0/2\pi)^2 J(T)^{-1}$
τ : reduced temperature, defined as $\tau \overset{def}{=} k_B T/J(T)$
Λ : effective penetration depth, $\Lambda = 2L/\mu_0$
Γ : dynamic helicity modulus, $\Gamma(T, \omega) = L^{-1}/L_J^{-1}$

T_{CS} : transition temperature of the (Pb) superconducting islands

R_N : normal state sheet resistance, $R_N \approx 2\text{m}\Omega$

R_N^J : normal state sheet resistance of the junctions, $R_N^J < R_N$

l : normal electron mean free path

ξ_N : coherence length in the normal metal, clean limit ($l >> \xi_N$) $\xi_{N_C} = \hbar v_F/(2\pi k_B T)$, dirty limit ($l << \xi_N$) $\xi_{N_D} = \sqrt{\hbar v_F l/(6\pi k_B T)}$

ℓ_J : junction length, $\ell_J = 1\mu\text{m}$

δM : variation of the mutual inductance between the drive and receive coils

M_c : inductance of the current distribution in the film, $M_c \cong 1.047\text{nH}$

M_{ss} : total change of the signal, $M_{ss} = \delta M(T << T_{CS}) - \delta M(T > T_{CS})$

q : topological charge of (fractional) vortices

Introduction

Motivations

Two dimensional Josephson junction arrays (JJAs) have been widely studied during the last decades since they provide an excellent physical realization of model systems for fundamental concepts of condensed matter physics and statistical mechanics. Under some conditions, which will be further clarified, JJAs constitute indeed a physical achievement of the 2D XY model for which there exists a large amount of literature [1, 2]. A rich variety of critical phenomena appears in JJAs, those commonly studied are related to disorder, topological defects or incommensurability. An essential concept at the basis of this thesis is frustration [3]. A system is referred to as *frustrated* when it is impossible to put it in an absolute minimum of energy, in such a way that the system must find a compromise in order to be in a state of relative energy minimum. The *frustration parameter* f is defined as the magnetic flux per lattice cell Φ_{cell} in units of the flux quantum ϕ_0, $f \overset{def}{=} \Phi_{cell}/\phi_0$. This parameter, also called *reduced flux*, governs the interplay between the applied magnetic field and the lattice geometry. This thesis is devoted to geometry and frustration effects on the dynamics of JJAs.

Usually the structures appearing in the inverse sheet magnetoinductance $L^{-1}(f)$, which is a measurement of the phase coherence in the JJA, are attributed to a vortex lattice, created by the external applied magnetic field, commensurate to the underlying periodic geometric lattice. Note that the incommensurability between the geometric and the magnetic lattices may be obtained in lattices whose elementary structures have different effective areas [4]. However, in regular lattices as those with square, triangular, or honeycomb geometries, structures in $L^{-1}(f)$ are observable at some rational values of frustration f, and in particular at full frustration ($f = 1/2$). In the case of JJAs on a dice lattice, which is a periodic lattice with rhombic elementary cells, we observe at full frustration a well depressed superfluid response, i.e. a weak but finite phase coherence. In a similar context, the energy spectrum of a single tight binding electron moving in the fully frustrated dice lattice was shown to exhibit no dispersion [5]. This field induced localization effect was described in terms of destructive quantum interferences leading to Aharonov Bohm cages in which the wave function is bounded. Such a dynamic localization phenomenon is reflected, in fully frustrated superconducting wire networks (WNs) with dice lattice, in a depression

of the transition line $T_c(f)$ and of the critical current [6]. Moreover, magnetic decoration experiments [7, 8] supported the idea of a disordered vortex pattern at full frustration. This conjecture was definitively adopted when the ground state of the fully frustrated XY ($FFXY$) model, which applies to both JJAs and wire networks at low temperature, on a dice lattice was shown to be highly degenerate due to the existence of zero energy domain walls (DWs) [9]. At sufficiently high temperature, such DWs can cross each other and form kinks. These mobile point defects in the entangled network of DWs weaken the superconducting phase coherence. The nature of the depression of the superfluid response in fully frustrated JJAs on a dice lattice is then quite different from the one in WNs [6]. In the framework of the $FFXY$ model, the mechanism of degeneracy removal is too weak to select a ground state vortex pattern [10]. In addition, because of anharmonic fluctuations the finite size effect is enhanced [11], leading to an almost impossible observation of a true phase transition in samples with accessible size. Indeed no peak in $L^{-1}(f)$ at $f = 1/2$, which would be the signature of a coherent state, is observed at low temperature even well below the estimated critical temperature [10]. The very long relaxation times related to the disentanglement of the DWs lead to a dynamics with glass-like features. This scenario is completely different from the one observed in numerical simulations [12] where the hysteretic behaviour of the helicity modulus, while cooling down and heating the system, was described as a manifestation of a glassy dynamics.
When the temperature is sufficiently low the system enters in a regime where the energy is dominated by the magnetic interaction of screening currents circulating in neighbouring cells. Thanks to the measurement technique it is possible to probe the superconducting phase coherence of JJAs and for the first time, to observe such magnetic effects which take place at a higher temperature than the critical one [10]. At low temperature the finite phase coherence of the fully frustrated state is achieved by bound fractional vortices. When the temperature is increased the fractional vortex pairs unbinding is hidden by magnetic effects. Therefore the observed superfluid response shows no genuine phase transition but rather a crossover from a low temperature phase with a frozen vortex lattice to a high temperature phase characterized by a liquid vortex state.

The role of the magnetic energy is shown to be dominant not only at full frustration but also for other frustrated states, as for example the $f = 1/3$ state. This frustrated state is very interesting because the vortex pattern is predicted to be disordered down to zero temperature [13]. But at the same time the phase coherence is stabilized by pairs of half-vortices. The unbinding of such pairs (BKT type transition) and hence the loss of phase coherence is not hidden by magnetic effects, as is the case at full frustration since the magnetic energy is dominant only at lower temperatures. Indeed the inverse sheet inductance $L^{-1}(T)$ exhibits a drop in the temperature range where the half vortices BKT type transition is predicted to happen. Moreover, the temperature dependence of the frustration structures in $L^{-1}(f)$ and $R(f)$ around $f = 1/3$ confirm the previous observation.

The dynamics features at low temperature are shared by all frustrated states, pointing to a behaviour dominated by some intrinsic characteristics of SNS JJAs. Assuming a residual frustration and small variations in the JJ coupling constants, the observed frequency dependencies of the real component of the sheet impedance $R_Z(\omega)$ as well as the sheet conductance real component $R_G(\omega)$, are well described by a simple hopping model. This behaviour is ascribed to thermally activated hopping of single (non interacting) vortices between neighbouring cells in a random potential created by disorder in the coupling constant.

Outline

This thesis is separated in six chapters. The subject of the thesis is introduced and motivated in the present chapter.
Chapter 1 is devoted to the fundamental concepts related to Josephson junction arrays (JJAs) (damping regimes, magnetic screening, frustration, topological defects and their ground states, phase transitions, etc.), as well as an introduction to the dice lattice, and a summary attempt of vortex dynamics in JJAs.
The samples are characterized in chapter 2. The fabrication process is explained and a few intrinsic quantities as the electron mean free path and the single junction critical current I_{CJ} are discussed on the basis of standard four probe measurements. The values of $I_{CJ}(T)$ are compared to those obtained from inductive measurements. The magnetic screening effects are discussed in terms of the effective 2D penetration depth and the competing energies. A section is dedicated to the linear response regime, and another one is especially devoted to the classification of the probed samples which are distinguished by the relation between the reduced and the thermodynamic temperatures. Finally, a curious observation is shown in the last section.
Chapter 3 is dedicated to the experimental setup. The two coil mutual inductance technique is described in details. The linearity of the electronic setup is discussed on the basis of measurements performed on a lead film. The thermometry parameters are given in a separated section. The refrigerator system is characterized by the cooling power. Special care is put on the magnetic screening which is characterized by raw measurements and preliminary results near zero field.
The core of the thesis is made by chapter 4. The first section describes the frustration structures observed at many temperatures and frequencies. The second section focuses on the fully frustrated state with its family of degenerate ground states and the degeneracy removal. The low temperature dynamics is discussed on the basis of the impedance Z (or conductance G) measurements performed at several vortex densities f. The second frustrated state which is investigated with details is the $f = 1/3$ frustrated state. Again the discussion starts with its ground states followed by the observations of the phase transition. A ground state for $f = 1/6$ is proposed and its possible phase transition is discussed. Finally these selected frustrated states are compared on the basis of magnetoinductance

$L(f)$ measurements and a mean field calculation of $L(f)$ which takes into account the anisotropic properties of the system. The barrier energies at these selected frustrated states are measured by two methods which give different results. Surprisingly, in the case of the unfrustrated state ($f = 0$), both results are one order of magnitude (or more) larger than the calculated value. The last chapter contains the conclusions.

At the end of this document are the appendix with the detailed calculation of the mutual inductance function $\delta M(Z)$, some pictures of the cryostat, a diagram of the electronic setup and a detailed explanation of the data treatment.

Chapter 1

Basic physics

In this chapter we introduce the fundamental aspects of the physics that will be discussed in this thesis, as well as the notation of the main physical quantities that will be used.

1.1 Single Josephson junction

A Josephson junction (JJ) consists of two superconducting (SC) electrodes separated by a short link. Depending on the nature of the link, the JJs are classified in two families. Tunnel junctions have an insulating link, and weak link junctions include topological junctions (for example constrictions or point contact junctions) and proximity effect junctions (see section 2.1) which are used in this thesis. For a general review about the tunnel and weak link junctions see [14, 15].

A supercurrent I_S can flow through a junction (between electrodes i and j) without inducing any dissipation. This is the dc Josephson effect [16] which reads as

$$I_S = I_{CJ} \sin(\theta_{ij}) \tag{1.1}$$

where $\theta_{ij} = \varphi_j - \varphi_i + A_{ij}$ is the gauge invariant phase difference between the electrodes i and j. Since at sufficiently low temperature the amplitude ρ of the complex superconducting order parameter $\Psi = \rho \exp[i\varphi]$ is not a relevant degree of freedom, only the phase (φ) fluctuations are of importance (London's limit). Thus each electrode i is characterized by a phase φ_i and A_{ij} is the linear integral of the vector potential between the electrodes i and j; $A_{ij} = (2\pi/\phi_0) \int_i^j \vec{A}\vec{ds}$, ϕ_0 being the flux quantum. The expression of the maximum supercurrent, or critical current I_{CJ}, depends on the kind of junction. In particular, the proximity effect JJs are discussed in section 2.2.3. When we apply a bias current higher than I_{CJ}, we get a finite voltage V and the Josephson current oscillates with a frequency $\omega/2\pi$ given by the ac Josephson effect [16]

$$\omega = \frac{d\theta}{dt} = \frac{2e}{\hbar} V \tag{1.2}$$

Equation (1.1) is not sufficient to describe real junctions where dissipative and capacitive effects take place. This is provided by the well known *Resistively and Capacitively Shunted*

Junction (*RCSJ*) model [17, 18] in which the ideal junction is shunted by a resistance R, which accounts for the dissipation in the finite voltage regime (1.2), and a capacitance C which geometrically shunts both electrodes. Notice that the capacitance does not shunt the electrodes to ground.
The junction description (in terms of its gauge invariant phase difference) arising from the *RCSJ* model is analogous to the description of a pendulum with a mass $(\hbar/2e)^2 C$ moving in a tilted periodic potential (the *tilted washboard* model) [17, 18]. The relevant parameter of this model is the McCumber parameter (or damping parameter) $\beta_C = (2e/\hbar) I_{CJ} C R^2$ which defines the damping regime of the pendulum motion. When $\beta_C < 1$ the junction is said to be *overdamped*, implying that the analogous pendulum mass is negligible. If $\beta_C > 1$, *underdamped regime*, the dynamics develops inertial features.

The behaviour of the junction is mainly determined by the McCumber parameter and by the dominating energy. Three kinds of energy are in competition :

1. The energy E_J of a junction connecting electrodes i and j is the work done by a Cooper pair to go through the junction; $E_J = \int_i^j V I_S dt \overset{(1.1),(1.2)}{=} -J\cos(\theta_{ij})$ with $J = (\hbar/2e) I_{CJ}$ the Josephson coupling energy.
2. The charge energy $E_C = (e^*)^2/2C$ is related to the JJ capacity and e^* is the effective JJ charge. In the literature, e^* is sometimes defined as the single electron charge e, but it is usually assumed to be twice the charge of the single electron, i.e. the free Cooper pair charge. Then $E_C = 2e^2/C$.
3. The thermal energy $k_B T$.

Actually there is a fourth kind of energy which is the magnetic energy associated with screening currents. Its effects on the behaviour of the JJAs are discussed in section 1.2.1 and in the framework of our experimental observations (see chapter 4).
Depending on the dominating energy, the Josephson coupling energy J or the charge energy E_C, the JJ physics is described as respectively in a classical or quantum regime. In the case of a *SNS* (SC-Normal metal-SC) junction the capacity and charge effects can easily be ignored leading to the *RSJ* model.
The magnitude of the dissipative channel resistance R is of the order of the normal state resistance R_N. It is not supposed to have large variations while decreasing the temperature. Thus at zero temperature ($T = 0$), and at low bias current ($I << I_{CJ}$), the SNS JJ is described by a kinetic inductance $L_J(0) = (\hbar/2e)/I_{CJ}(0)$. When the temperature is increased, one has to take into account the dissipative channel and calculate the voltage across the junction. By assuming a small bias current, the junction conductance G_{ij} is [19]

$$G_{ij} = R_{ij}^{-1} + [i\omega L_{ij}]^{-1} \qquad\qquad L_{ij} = \frac{\hbar}{2e}\frac{1}{I_{CJ}(T) cos\theta_{ij}} \tag{1.3}$$

where $R_{ij} \approx R_{ij}^n$, the normal state junction resistance.

To conclude this first section, the single Josephson junction parameters of our samples are summarized in the same way as was done by van der Zant in his thesis [20]. The "R-C" phase diagram (Fig.1.1) shows the phase boundary between the classical and quantum regimes and also the overdamped and underdamped regimes. Our junctions are far inside the classical overdamped regime.

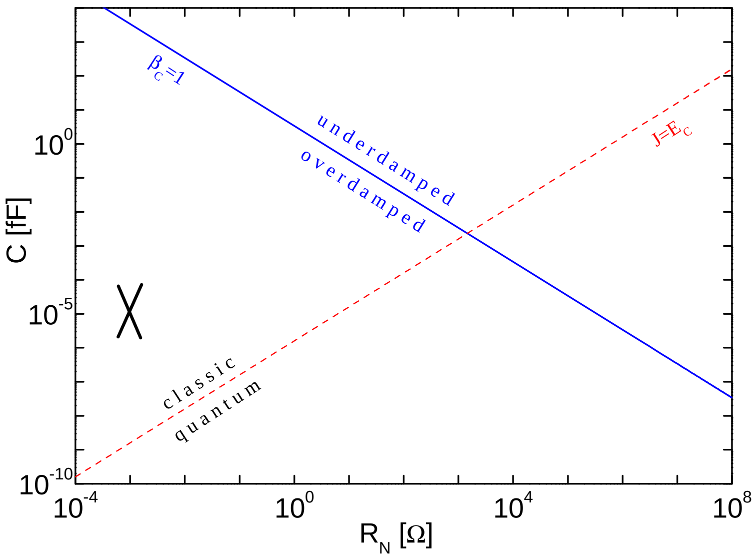

Figure 1.1: Single junction R-C phase diagram. The capacitance of our proximity effect JJs is calculated assuming parallelepiped junctions and the McCamber parameter is calculated at zero temperature. The black cross represents our JJs location with $C \approx 10^{-5} fF$ and $R_N \approx m\Omega$.

1.2 Josephson junction arrays

A Josephson junction array (JJA) is an ensemble of superconducting (SC) grains which form a lattice and are connected to each other by JJs. The lattice can be regular with a periodic distribution of the SC grains (triangular, square, honeycomb, dice lattices) or irregular with a percolative distribution of the SC grains [1].

The single JJ properties (see Fig. 1.1) are valid for the whole array leading to a classical overdamped JJA.

1.2.1 Magnetic screening effects

The Ochsenfeld-Meissner effect applies on two size scales of the JJA : locally on each JJ, and at larger scales on each elementary cell of the array. Inside the JJ the geometry of the Josephson currents is modified by the Meissner screening fields. Quantitatively this phenomenon arises when the JJ width (w_J) is of the order of the Josephson penetration depth $\lambda_J = \sqrt{\hbar/(2e\mu_0 d J_{CJ})}$ [17], where J_{CJ} is the critical current density $[A/m^2]$ and d is the junction length. For small JJs ($w_J \ll \lambda_J(T)$), this screening effect can easily be neglected. The elementary cells of the array form loops around which screening currents can circulate. The magnetic energy stored in these current loops has important consequences on the JJA behaviour when it is of the same order of the Josephson energy, which is the main energy scale of the system.

In the following sections we consider the weak screening regime where the effects of the screening currents induced in the array are negligible. *The local field is given only by the external applied field.* In addition, we assume arrays with all identical JJs, i.e. same coupling constant for all junctions ($J_{ij} \equiv J$).

1.2.2 Classical 2D XY model

When the properties listed in the last section are fulfilled (classical overdamped array with a real and continuous phase parameter and the weak screening limit), the JJAs can be described by the XY model. By assuming only nearest neighbours $< ij >$ Josephson interaction, the JJA Hamiltonian is

$$H_{JJA} = J(T) \sum_{<ij>} (1 - \cos\theta_{ij}) \tag{1.4}$$

The field modulation of the temperature dependent coupling constant, $J(T) = (\hbar/2e) I_{CJ}(T)$, is neglected (see 2.3). The single junction inductance (1.3) can then be written, in zero field and at zero current, as :

$$L_J(T) = \left[\frac{\hbar}{2e}\right] \frac{1}{I_{CJ}(T)} = \left[\frac{\hbar}{2e}\right]^2 \frac{1}{J(T)} \tag{1.5}$$

The JJA Hamiltonian (H_{JJA}) is isomorphic to the XY Hamiltonian [21]

$$H_{XY} = -J_{XY} \sum_{<ij>} \cos\theta_{ij}$$

with the gauge invariant phase difference θ_{ij} introduced in section 1.1. The phases (φ_i) of the order parameter on each SC island are the fluctuating variables, which in terms of the XY model represent the orientation of the spins situated on each site. It becomes clear that a JJA can be considered as a physical realization of the 2D XY model. Nevertheless, in order to compare samples with different coupling constants $J(T)$ and with theoretical models where the coupling constant J_{XY} is temperature-independent, one usually defines a dimensionless parameter [22] called *reduced temperature* τ

$$\tau = k_B T / J(T) \tag{1.6}$$

The non fluctuating variables $A_{ij} = -A_{ji}$ defined in section 1.1 are related to the reduced flux f which is defined as

$$f \overset{def}{=} \sum_{\square} A_{ij}/(2\pi) = \Phi_{cell}/\phi_0 \tag{1.7}$$

(the sum is calculated around an elementary cell $\square$ of the array). The reduced flux f is the ratio between the magnetic flux per cell Φ_{cell} and the flux quantum ϕ_0. Then, the fluxoid quantization leads to

$$\sum_{\square} \theta_{ij} = 2\pi(m - f) \tag{1.8}$$

where m is the *vorticity* (or *topological charge*).

Using the notion of vorticity (1.8), a vortex (or anti-vortex) is a configuration of phases φ_i such that the sum of the phase differences θ_{ij} along a path around the core of the vortex is equal to an integer multiple of 2π (or -2π). More generally a vortex is a stable topological excitation of an ordered phase (or low temperature phase) characterized by a continuous symmetry U(1). With these definitions in mind, one realizes that the reduced flux f gives the vortex density.
The expression "frustration" is referred to as the impossibility to find a set of phases which simultaneously minimize the energies of all bonds in a lattice. Thus, the reduced flux f is also called *frustration parameter*, since it allows modification of the phase distribution (1.8) by changing the applied magnetic field (1.7) in order to frustrate the system.

The XY Hamiltonian is an even function of f and it is periodic in f with period 1. The values of f can be reduced to the interval [0,1/2] [21] and thus the maximum irreducible value, $f = 1/2$, is referred to as *fully frustrated* [3, 23].
If the applied field is uniform on the sample scale and with all equal cell areas, the system is called uniformly frustrated, i.e. uniformly frustrated XY model, which can be studied by a family of four basic periodic lattices (square, triangular, honeycomb and dice). When the geometry of the lattice induces a deformation of the field distribution, the periodicity and the symmetry of the Hamiltonian are broken, leading to the phenomenon of hidden incommensurability [4].

Ground states

Given a known lattice geometry, the usual way to determine the ground state(s) (GS) is to apply the current conservation law at all sites i (this results from the variation of the Hamiltonian with respect to φ_i) and the fluxoid quantization (1.8) in all loops. When a transverse magnetic field is applied, a fixed density of vortices f is induced into the array as in the mixed state of a type II superconductor. However the ground state is not a periodic triangular (Abrikosov) lattice of equally spaced vortices as in an uniform superconductor. Indeed, due to the array structure, the vortices have to sit at the centers of the unit cells.

The underlying lattice geometry acts as an effective periodic pinning potential, which combined with the repulsive interaction between vortices, determines the vortex lattice at low temperature. The problem in finding the frustrated ground state vortex configuration(s) for an arbitrary vortex density f and a given periodic lattice remains unsolved.

The unfrustrated case, $f = 0$, is trivial because the Hamiltonian is minimized with $\theta_{ij} = 0$ for all $< ij >$. The GS is infinitely degenerate because of the possibility of rotating the parallel phases by a constant phase (U(1) symmetry group).

The situation is more complicated in frustrated cases, $f \neq 0$, since the possibility of a global rotation of the spins is accompanied by a discrete degeneracy. The fully frustrated ($f = 1/2$) square lattice is probably the most famous example of such a degeneracy with a checkerboard state of alternating cells with vorticity 0 and 1, or equivalently alternating positive and negative half vortices (1.8). More generally a GS can be described in a charge representation (of vortices) as positive or negative (fractional) vortices with a topological $(m - f)$ charge on the dual lattice [23]. There are other examples besides the square lattice ; the checkerboard pattern of the fully frustrated triangular lattice or the fully frustrated honeycomb lattice with positive and negative half vortices [21, 23, 24, 25]. These states are thus doubly degenerate because of the possibility to obtain two GS with opposite chirality (symmetry group U(1)xZ_2) [3].

It is then possible to have both GS simultaneously, but separated by a *domain wall* (DW). More generally a DW is a topological excitation separating two GS which cannot be related to each other by symmetry [24, 26]. (Notice that this definition does not imply that both GS have opposite chirality.)

In order to obtain a new GS, the domain wall should not increase the system energy. The possibility to construct *zero energy domain walls* (ZEDWs) is referred to as *accidental degeneracy* [27], i.e. not related to symmetry. To remove accidental degeneracies, it is necessary to take into account the spin waves' contribution to the free energy F of the system. Spin waves are long wavelength spin thermal excitations, which in the theory of XY models are excitations of small amplitude in the vicinity of GS. This degeneracy removal mechanism is called *order-from-disorder* [28].

It is usually sufficient to consider only harmonic fluctuations of F [27]. They allow selection of the GS at finite low temperature and the selected state has the highest degree of symmetry. Nevertheless, anharmonic contributions are sometimes unavoidable. For example the fully frustrated honeycomb lattice shows within the XY model a hidden gauge symmetry between the GS which is lifted by anharmonic terms of the free energy F [11].

When the harmonic contributions are sufficient to remove the accidental degeneracy, the spin waves induced free energy difference δF (per unit length) of DWs between different GS is proportional to the temperature; $\delta F \propto T/J$ [27], whereas when anharmonicities have to be taken into account, $\delta F \propto T^2/J$ [11]. This power law enhances the *finite size effect*, because of the probability to create a DW across the whole sample (of characteristic linear size L) given by $\rho \sim \exp(-\delta F \mathrm{Ł}/k_B T)$ (spontaneous formation of DWs crossing the sample). The probability to observe a vortex ordering, i.e. a unique vortex configuration, is achieved when $\rho \ll 1$ or equivalently $\mathrm{Ł} \gg L_c \sim J/T$, whose proportionality factor depends on the frustration value of the considered lattice. In the case of the fully frustrated honeycomb lattice of Reference [11], $Ł_c \geq 10^5$ (in units of the lattice parameter).

1.2.3 Phase transitions

As mentioned in the last section, in an unfrustrated ground state the spins are all parallel to each other. When increasing temperature, spin waves appear in the system destroying this perfect ordered state. More generally, and following the argument developed by Peierls [29] for crystalline structures, there is no long range order in 2D solids. The argument of Peierls has been rigourously verified by Mermin and Wagner [30]: they proved that there is no spontaneous magnetization in an isotropic 2D (or 1D) Heisenberg model at finite temperature. Despite such general theorems forbidding conventional long range order, Kosterlitz and Thouless proposed a new definition for ordering in 2D systems which is not based on the behaviour of a two point correlation function vanishing at non zero temperature. They called it a *topological long range order* [31] which is not the true long range order of the conventional type [29]. This new type of order, characterized by an algebraic decay of correlations, is associated with superfluidity in two dimensions, and applied also to the XY model of magnetism.

At low temperatures it is energetically favorable for the system to form bound vortex-antivortex pairs (dipole-like pairs), because the single vortex energy increases logarithmically with the system size. On the other hand, bound pairs with opposite but equal vorticity have a finite energy. The phase transition associated with the loss of topological order takes place when the largest vortex pair unbinds, and has been predicted for unfrustrated infinite 2D homogeneous systems by Berezinskii [32] and Kosterlitz and Thouless [31, 33] leading to the so called universal *BKT transition.* Experimental evidence for the BKT transition has been shown in arrays of proximity coupled JJs [34]. Due to the possibility to map the topological excitations of various physical systems onto a 2D Coulomb gas model, the same critical features are found in many different systems, as for example superfluid helium films [35, 36] or superconductor thin films [37]. At the transition, the Coulomb gas crosses over from a dielectric phase (vortex-antivortex pairs) to a metallic phase (free vortices and antivortices).

In numerical simulations, the presence of a phase transition is usually signaled by a vanishing helicity modulus Γ which measures the system phase correlations, i.e. the response of the system to a phase twist. The helicity modulus Γ is defined by the free energy increase due to an infinitesimal phase twist δ in the border of the sample, $\Gamma = \lim \partial^2 F/\partial\delta^2\big|_{\delta\to 0}$. At the universal BKT transition temperature T_{BKT}, there is a universal jump in the superfluid density [38], which in terms of the helicity modulus experiences a universal jump $\Gamma(T_{BKT}) = (2/\pi)k_B T_{BKT}$. The universal relation [38] may be generalized to fractional topological charges q,

$$\Gamma(T_C) = (1/q^2)(2/\pi)k_B T_C \qquad [10] \tag{1.9}$$

Above T_C the system is characterized by an exponential decay of correlations.

In JJAs the helicity modulus, as well as the zero frequency inverse kinetic inductance, drop discontinuously to zero when T_{BKT} is approached from below [39]. This results obtained within a Josephson lattice model (Josephson Hamiltonian) are in agreement with zero field Monte Carlo simulations [23], and in the continuum limit they recover the analogue of the superfluid density drop [38].

Since the XY Hamiltonian is periodic in f with period 1 (see section 1.2), the phase transition behaviour is indistinguishable for integer values of f [40]. For rational values of f the transition looks like the one at the unfrustrated state, taking place at a lower temperature [23]. If the GS is characterized by a U(1)xZ_2 symmetry, the melting of the DWs, with the increase of the temperature, leads to another symmetry breaking, i.e. the discrete Z_2 symmetry breaking of the Ising model, driven by the DWs proliferation at T_I. This second type of phase transition is associated with the vortex pattern disordering.
Both types of transition (BKT-type and *Ising*-type) can be distinct [41] or can merge into a single one. For the fully frustrated XY model on the square lattice, two scenarios have been proposed : $T_{BKT} < T_I$ or $T_{BKT} = T_I$ [23]. On one hand, the single transition predicted for the triangular and square lattices implies a new class of universality [42]. On the other hand, distinct transitions have been predicted for the square lattice [43]. Only recently, it has been proved for triangular and square lattices that the only possible scenario is the second one with $T_I > T_{BKT}$ [26]. The fractional vortices carried by the DWs corners screen the interaction of the integer vortices at $T > T_I$. Thus there cannot be vortex pairs, and T_{BKT} must be lower than T_I.
Out of equilibrium, fully frustrated JJAs show a symmetry breaking that changes the order of the transitions ($T_I < T_{BKT}$), i.e. when the drive current is well above the zero temperature critical current [44]. Another way to break the symmetry is to modulate the coupling energy in one of the lattice directions. This allows experimental distinction of both transitions. Such a modulation has been applied to the square lattice and both transitions have been studied analytically and numerically [45, 46, 47]. One of the four bonds of each elementary square cell is weaker than the three others (weak bond WB). The periodic repetition of such a WB along one direction of the lattice leads to a displacement of the minimum in the charge potential energy. In the fully frustrated state ($f = 1/2$), this displacement creates a link across the WBs, between half integer charges located in neighbouring cells, leading to dipole charges. Because of these dipoles, the domain walls will mainly run along strong bonds rather than along weak bonds. When the temperature is increased above T_I, the fractional charges (dipoles) remain bound until the temperature $T_{BKT} > T_I$ is reached. This scenario ($T_{BKT} > T_I$) has been experimentally observed on modulated square arrays [48].

Some critical reduced temperatures for different frustrated states have been calculated for triangular, square and honeycomb lattices by mean field approach (MF) and numerical Monte Carlo simulations (MC) [21, 23, 24, 25, 41]. These critical temperatures are summarized in Table 1.1. Notice that these values are obtained neglecting the charging effect (RSJ model), in the weak screening limit. The mean field approach does not properly take into account phase fluctuation effects near T_c. The critical temperatures for the dice lattice at various values of f are discussed in chapter 4.

Square array f =	**0**	**1/5**	**1/4**	**1/3**	**1/2**
τ_c^{MF}	2	1.5	1.4	1.4	1.4
τ_c^{MC}	0.93				0.45

Triangular array f =	**0**	**1/5**	**1/4**	**1/3**	**1/2**
τ_c^{MF}	3		1.73	1.5	1.5
τ_c^{MC}	1.45		∼0.13-0.3	0.16	0.53

Honeycomb array f =	**0**	**1/5**	**1/4**	**1/3**	**1/2**
τ_c^{MF}	1.5		1.3	1.27	1.21
τ_c^{MC}	0.65		0.17	0.23	0.12

Table 1.1: Critical reduced temperatures for frustrated square, triangular and honeycomb arrays.

Depinning and melting transitions

In the previous section we described the Ising type transition as a vortex pattern disordering due to the DWs melting. More generally, the nature of the phase transition of frustrated JJAs is related to the melting of the vortex lattice which interacts with the periodic pinning potential induced by the underlying array structure.

The phenomenon of 2D melting was first introduced by Kosterlitz and Thouless [31] for a 2D crystal. In such a 2D solid no long range order can exist [30], but the low temperature phase is nevertheless characterized by a slow power-law decay of spatial correlations. This quasi long range order phase [31], or "2D solid" phase, was thought to melt because of the unbinding of topological lattice defects (dislocation pairs), into a hexatic phase characterized by a quasi long range (sixfold) orientational order (but short range translational order) [49]. When the temperature is increased, this "quasi liquid" melts into a normal (or isotropic) liquid.

By introducing an underlying periodic array structure, the above summarized 2D melting scenario is altered by the appearance of a new low temperature phase in which the "2D solid" is pinned to the array structure, leading to a "pinned solid". At a depinning temperature T_p the pinned solid achieves a transition to a "floating solid" phase where the solid decouples from the underlying structure, and it behaves as a 2D solid on a uniform substrate. The floating 2D solid is not necessarily commensurate with the periodic underlying lattice, but it is not completely free as shown in driven periodic JJAs [50]. Finally at a higher temperature T_m the floating solid will melt into the liquid phase.

Such phase transitions have been observed in 2D superconducting networks with numerical simulations of the 2D lattice Coulomb gas for square and honeycomb underlying lattice geometries with a dilute vortex density $f \ll 1$ and with dense systems near full frustration (vortex density $f = 1/2 - \varepsilon$) [51].

For the dilute case the system exhibits a frustration dependent transition temperature $T_p(f) \sim f$, as was earlier predicted [21]. Only for sufficiently dilute systems this first order depinning transition leads to a floating triangular (Abrikosov) vortex lattice whose depinning gives rise to a drift of the vortex lattice, i.e. a flux flow resistance which marks the

loss of dc superconductivity. It is then reasonable to interpret the depinning temperature T_p to be the superconducting transition temperature [21]. The higher melting temperature T_m is observed to become $f-$independent as $f \to 0$, while $T_p(f \to 0) \to 0$. Very similar melting and depinning phase diagrams were obtained with numerical simulations of the frustrated 2D XY model in the dilute system limit [52] where both pinned and floating vortex solid phases exist. For more dense systems (f not sufficiently small), the depinning and melting transitions coincide, i.e. the floating phase with algebraic order is absent [53]. These simulations are in apparent discrepancy with analytical theories [54] predicting a critical frustration, below which $T_p < T_m$, about twice the value obtained by the above numerical simulations. When the finite values of the pinning potential amplitude and of the dislocation fugacity exp[−dislocation core energy/$k_B T$] are taken into account [55], the phase diagram agrees with the simulations.
For dense systems in equilibrium (frustrations close to $f = 1/2$) [51], the transitions are associated with missing or excess vortices (defects) lying on the checkerboard ground state. In that case, the depinning transition to the floating vortex phase is followed by the succession of two melting transitions [51]. The first leads the system to the isotropic defect liquid, and the second one represents the disordering of the $f - 1/2$ vortex background.

The reason why depinning and melting transitions have not been observed experimentally may be attributed to energy barriers (E_b) that a vortex has to overcome in order to hop between neighbouring cells of the superconducting network (JJAs or wire networks). This barrier [22] may be sufficiently high that it is most likely to observe only a vortex liquid (as the temperature is decreased) characterized by an Arrhenius-like behaviour of the vortex mobility ($\exp[-Eb/k_B T]$) [56, 57].

1.2.4 Equivalent electric network

In section 1.1 we saw that a single SNS Josephson junction is well described by the *RSJ* model. If we assume all identical junctions (same geometrical parameters), the single junction conductance (1.3) is the same for all JJs, G_{JJ}. The quantity which is actually measured is not the single junction conductance G_{JJ}, but the sheet conductance G (or equivalently the sheet impedance $Z = 1/G$). For a regular array, G is proportional to G_{JJ} [19] and the G over G_{JJ} ratio, which depends on the lattice geometry, is called *geometrical factor*. For the square array $G_{square} = G_{JJ}$, for the triangular array $G_{triangular} = \sqrt{3}G_{JJ}$, and for the honeycomb one $G_{honeycomb} = (1/3)\sqrt{3}G_{JJ}$. The dice lattice geometrical factor can be obtained applying the inverse *star-triangle transformation* [4] to the triangular array. More generally, it can be calculated for any type of regular lattice [58]. In the case of the dice lattice (see section 1.3)

$$G^{dice} = \frac{2}{3}\sqrt{3}\, G_{JJ} \longleftrightarrow Z^{dice} = \frac{\sqrt{3}}{2}\, Z_{JJ} \tag{1.10}$$

The array can be described by a unique macroscopic conductance G which is then obtained in the framework of the *RSJ* model. This model comes from the two-fluid model which refers to an early one [59] where one considers two parallel elements of current. The two-fluid model assumes that the total electron density n is the sum of the condensed or superconducting electron density n_s and that of normal electrons, or quasi-particles, n_n [18]. The total current $\vec{j}$ is the sum of the quantum superconducting current $\vec{j}_s$ (first London equation) and the normal current $\vec{j}_n$ given by Ohm's law ($\vec{j}_s$ and $\vec{j}_n$ are out of phase in $\pi/2$.)

$$\frac{\partial}{\partial t}\vec{j}_s = \frac{1}{d}\frac{\partial}{\partial t}\vec{K}_S = \frac{1}{\lambda_L^2 \mu_0}\vec{E} \qquad\qquad \vec{j}_n = \sigma_n \vec{E}$$

where K_S is the sheet current density and d the film thickness.
In an electric analogy the first London equation is related to the voltage across a kinetic inductance L_J ($V = Ed = -L_J\, dI/dt$). Then in a two-fluid approach $L_J = \mu_0 \lambda_L^2/d$ or by introducing an effective penetration depth [18] :

$$\Lambda \overset{def}{=} 2\lambda_L^2/d \qquad\qquad L_J = \frac{1}{2}\mu_0 \Lambda \tag{1.11}$$

At this point, the dissipation is only due to the normal currents since the fluctuations (spin waves and vortices) are part of a collective (topological) phenomenon which appears only when an array of JJs is considered (see section 1.2.2). The vortex induced dissipation is introduced as an impedance $Z_v = R_v + i\omega_0 L_v$ in series [37] with the unrenormalized superfluid density L_J, and both are in parallel with the sheet resistance $R = geometrical\ factor \times R_{JJ}$ due to the quasi-particles (normal electrons). The JJA equivalent electric network is shown in Fig.1.2a). The contributions to the total electric field $\vec{E}$ are associated with the non-dissipative motion of the superfluid background and the vortex motion.

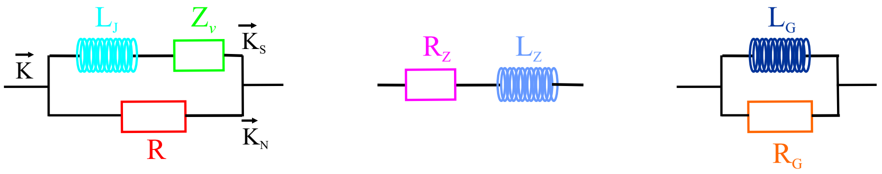

a) b) c)

Figure 1.2: a) Diagram of the two fluid model for a JJA. The total sheet current $\vec{K} = \vec{K}_N + \vec{K}_S$ is shared in parallel between a normal dissipative channel (resistance R of the order of the normal state sheet resistance R_N) and a superfluid channel (unrenormalized kinetic inductance L_J and vortex impedance Z_v). b) Sheet impedance components. c) Sheet conductance components.

$$\vec{E} = L_J \frac{d\vec{K}_S}{dt} + Z_v \vec{K}_S$$

Fig.1.2b) illustrates the components of the measured sheet impedance Z which can be written as a sheet inductance L_Z in series with a sheet resistance R_Z; $Z = R_Z + i\omega L_Z$.

Equivalently the sheet conductance $G = 1/Z$ illustrated in Fig.1.2c) can be written as $G = R_G^{-1} + (i\omega L_G)^{-1}$ where

$$R_G = \frac{R_Z^2 + (\omega L_Z)^2}{R_Z} \qquad\qquad L_G = \frac{R_Z^2 + (\omega L_Z)^2}{\omega^2 L_Z}$$

We clearly see that it is possible to equate the two fluid model diagram with the conductance diagram. The vortex impedance components can be written as

$$R_v = \frac{R_G^{-1} - R^{-1}}{(R_G^{-1} - R^{-1})^2 + (\omega L_G)^{-2}} \qquad\qquad L_v = \frac{L_G}{1 + (R_G^{-1} - R^{-1})^2 (\omega L_G)^2} - L_J$$

- At low temperature ($T < T_C$), when $R >> \omega L_J + Z_v$, the two fluid diagram is naturally equivalent to the diagram c) with $R_v = R_Z$ and $L_v + L_J = L_Z$.
  Since L_G is a function of R_Z, $L_G = L_Z$ only at low frequency ($\omega/2\pi < 100Hz$) when $R_Z \ll \omega L_Z$.

- At high temperature (slightly below and above T_C) $R_G = R_Z$.

Since the sheet inductance L is related to the dynamic helicity modulus $\Gamma(\omega, \tau)$ [60] : $\Gamma(\omega, \tau) = [\phi_0/(2\pi)]^2 L^{-1} = L^{-1}/L_J^{-1}$, then using (1.9) the sheet inductance at T_c can be written

$$L^{-1}(T_c) = \frac{1}{q^2} \frac{8\pi k_B T_c}{\phi_0^2} \tag{1.12}$$

where q is the topological charge of the vortices. The helicity modulus Γ takes into account the *collective* stiffness of the JJA discarding JJ individual properties.

1.3 Introduction to the dice lattice

The physics of systems with independent electrons confined on 2D structures can be strongly influenced by the underlying lattice geometry. Such systems with many regular lattices (as for example square, triangular or honeycomb) share the same spectral properties which depend on the value of f. When f is a rational number, $f = p/q$, the spectrum is continuous and it is formed by q bands. The common feature of these regular lattices is that their sites have the same coordination number z for each lattice (z=3,4 and 6 for the honeycomb, square and triangular lattice respectively).

The dice lattice is a modified triangular lattice where one third of the bonds are removed. Fig.1.3 shows the periodic structure of this geometry which is an in-plan projection of a cube (dice) along the (111) direction. There are three types of sites (A, B and C) per elementary tile with two different coordination numbers; $z = 3$ for B and C, $z = 6$ for A. Each bond connects two sites with different z. The lattice is composed by three triangular sub-lattices, each one including one of the three sites (A, B or C) only.

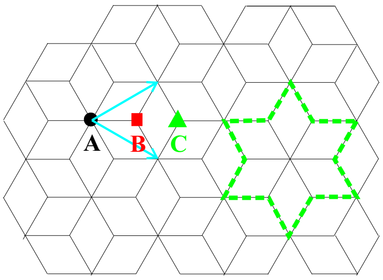

Figure 1.3: Dice lattice structure with a rhombic elementary cell (blue base vectors) and three types of different cites (A, B and C) indicated with different colored symbols. The smallest Aharonov-Bohm cage is indicated (green dashed line).

1.3.1 Localization phenomenon

It has been demonstrated, based on this lattice geometry (but the results hold for a much more general class of systems), that the localization of the electronic wave function may depend only on the local topology [61]. The special features due to the interplay between this peculiar lattice geometry and the magnetic field have been investigated, from a theoretical point of view, in the framework of the tight binding model [5]. When each rhombic cell is exposed to half a quantum of flux ($f = 1/2$), the energy spectrum of a single tight binding electron is surprisingly quantized to three infinitely degenerate levels.

The evolution of a wave packet through any lattice depends on the lattice geometry and the frustration f. In the case of the dice lattice the quantum dynamics is strongly influenced by the magnetic field when the system is fully frustrated ($f = 1/2$). In reference [5] the authors consider the propagation of the wave packet initially located on a single site. If the applied field is such that $f = 1/2$, the electron motion is bounded to a finite number of sites. This phenomenon can be understood in terms of Aharonov-Bohm (AB) destructive quantum interferences leading to the localization of the electronic wave function within AB cages, whose size depends on the coordination number of the site where the wave packet is initially located. The smallest cage, illustrated in Fig.1.3, is obtained with A-type initial sites. If the initial site is of type B or C, the electron motion is bound to a larger Aharonov-Bohm cage (see Figs.2.3 in section 2.1).

This phenomenon occurs in absence of disorder. If one introduces enough disorder (for example topological defects) in the lattice, the cages may be destroyed and the wave packet may spread over the full lattice leading to the disappearance of this effect. The localization phenomenon was established in the case of non interacting electrons. If the interaction between electrons is taken into account, the wave function is no more vanishing on the sites of the Aharonov-Bohm cages.

The dice geometry is not the only one to have (closed) cages: the same phenomenon appears in more complicated structures with many types of cells (not only rhombic cells). In the case of the regular square or triangular lattices all the cages are infinite no matter what the vortex density.

1.3.2 Experimental observations on wire networks

From an experimental point of view, this interference phenomenon between charged particles has consequences on transport measurements. The first experiments were performed on superconducting wire networks [6] which are sensitive to the phase coherence of the order parameter. The superconducting wire networks are described, near T_C, by the linearized Ginzburg-Landau equations [62, 63] which can be mapped onto the eigenvalue equations of a tight binding Hamiltonian. This analogy allows comparisons between the measurements and the theoretical model used in Reference [5].

In the framework of superconducting networks, such a localization phenomenon implies that the wave function cannot carry phase information through the network. Transport anomalies are then expected. The relevant quantities are the transition line $T_C(H)$ and the critical current density (per wire) $J_C(H)$, which can be compared to the spectrum calculated in [5]. The authors of Reference [6] observed a pronounced minimum in the transition line $T_C(H)$ at $f = 1/2$ associated with a large resistive transition indicating strong phase fluctuations. The network linear Ginzburg-Landau equations associated with the tight binding spectrum well describe the data. At full frustration the theoretical model predicts a vanishing critical current which is instead observed to exhibit a non vanishing minimum. Two kinds of explanations were proposed for this incomplete suppression of $J_c(f = 1/2)$: *i*) a finite size effect, and *ii*) the influence of the non linear term in the Ginzburg-Landau equations which was not taken into account to establish the theoretical model. The well pronounced peak observed at $f = 1/3$ was attributed to a strongly pinned vortex configuration. Another peak appears at $f = 1/6$ almost as large as at $f = 1/3$. As mentioned above, the dice lattice includes a triangular lattice formed by the six fold sites A. The dice lattice spectrum is related to the triangular one at frustration $f_{triangular} = 3f_{dice}/2$ [64]. However it is not possible to explain the singularity at $f = 1/2$ of the dice lattice with such a correspondence. The $f = 1/6$ state of the dice lattice corresponds to the $f = 1/4$ state of the triangular lattice which, in the framework of the uniformly frustrated XY model, exhibits an accidental degeneracy [27] which could attenuate the phase coherence: this is in contradiction with the experimental observation. The fully frustrated state of the dice lattice corresponds to the $f = 3/4$ state of the triangular lattice which, in the XY model, is equivalent to the $f = 1/4$ state. This analogy would imply having the same behaviour at $f = 1/6$ as at $f = 1/2$ in the dice lattice: such is not the case [6].

The localization effect [5] was also observed in normal (non superconducting) metallic wire networks [65], where strong magnetoresistance oscillations with period ϕ_0 were observed. Similar experiments performed on square lattices [65] did not show such a behaviour attributed to the cage effect which is expected to be robust against disorder effects [66].

1.3.3 From wire networks to Josephson junction arrays

As mentioned in section 1.1, at sufficiently low temperature only the phase of the superconducting order parameter is relevant. Then the energy of an array of weakly connected superconducting islands can be described by a Hamiltonian of the form

$$H = \sum_{<ij>} V(\theta_{ij}) \tag{1.13}$$

where the interaction function V depends on the type of the coupling, i.e. on the form of the current-phase relation in the link $< ij >$. The argument θ_{ij} is the gauge invariant phase difference introduced in the first section. Since the superconducting grain phases φ_i are defined modulo 2π, the function $V(\theta)$ is periodic in θ.
The minimization of the energy on each phase variable leads to a set of equations which represent the current conservation on each site $I_{ij} = -I_{ji}$. In the harmonic approximation of (1.13), the array of superconducting islands behaves as a network of inductances (with energy $\sum_{ij} L_{ij} I_{ij}^2$) given by [67, 68]

$$L_{ij} = \left[\frac{\hbar}{2e}\right]^2 \frac{1}{V''(\theta_{ij})} \tag{1.14}$$

Even with identical junctions (identical coupling constant) the inductances may change from link to link depending on the θ_{ij} distribution, i.e. the frustration state.
In the case of networks of long and thin wires (lattice parameter$\gg$coherence length$\gg$wire diameter) as those explored by [6], the coupling between neighbouring sites is harmonic $V(\theta_{ij}) \propto \theta_{ij}^2$. The inductance is then independent of the frustration, whereas in JJAs, due to the periodic potential (1.4), the frustration can induce a pronounced modulation of the single junction inductance (1.3).

Another important difference between wire networks and JJAs is the resistive transition width. In the case of wire networks the resistive transition takes place typically in a few mK [6], whereas in the case of JJAs the transition width can extend over 1K. From an experimental point of view this could appear as an advantage, the JJAs being more suitable to study the transition region.
On the other hand, the wire networks have the advantage to be described by the linearized Ginzburg-Landau equations which are related to the single electron hopping problem [5]. This is the case only for temperatures close to T_C, whereas below T_C a discrete superconducting system (wires or junctions) in external magnetic field is described by the frustrated XY model (see 1.2.2) for which exists a vast literature.
If the interplay between the lattice geometry and the applied magnetic field described in [5, 6] still exists within the framework of the fully frustrated XY model, its nature would be completely different and it is certainly impossible to talk about "dynamic localization".

1.4 Vortex Dynamics

The static critical behaviour of the unfrustrated XY model, which describes the static phase transition (at zero frequency) in unfrustrated JJAs, is well known in terms of the vortex unbinding mechanism (BKT theory). But the dynamic aspects of the transition are not yet well established because of controversial features between many theoretical (analytical and numerical) approaches and experimental observations [69]. From a theoretical point of view, there are mainly two phenomenological descriptions for dynamic properties of vortex fluctuations at zero field; the Ambegaokar, Halperin, Nelson and Siggia (AHNS) [36] description and the Minnhagen phenomenology (MP) [70]. Both dynamic extensions of the BKT theory are based on a neutrally charged 2D (two components) Coulomb gas model, but they differ in the frequency dependence prediction of the linear response. On the one hand, the AHNS theory predicts a power-law behaviour with a temperature dependent exponent. On the other hand, an anomalous dynamic response emerges from the MP treatment with an anomalously slow low-frequency vortex mobility.

1.4.1 AHNS description

In the AHNS analysis the dissipation is due to diffusive motion of vortices described by a phenomenological equation. For sufficiently high temperatures, the dynamic response function should be well described by the Drude response because of the negligible interaction between the particles in comparison with the strong thermal fluctuations. Notice that the AHNS theory is an extension to high frequencies, but obtained independently of the zero-frequency limit results derived by Huberman *et al.* [71].

The earliest experimental evidence for the BKT transition was provided by the torsional oscillator experiment of Bishop and Reppy [35]. They measured the superfluid transition in thin oscillating 2D helium films. The period shift and the quality factor Q of the torsional oscillator measured as a function of temperature showed a peak in dissipation Q^{-1} and a fall off of the period shift at a temperature above the static BKT transition. These results were well explained by the AHNS theory. The AHNS model based on a phenomenological equation for the vortex motion in a helium film can be considered as the continuum limit of the lattice model used by Shenoy [72] who evaluated the response of JJAs subject to an oscillatory field. The dynamic conductivity of classic overdamped JJAs calculated in a microscopic way [72] was shown to exhibit a similar behaviour to the phenomenological response function of helium films (AHNS).

As was pointed out by Bishop and Reppy, if the measurements are performed at finite frequency, one doest not expect to see the discontinuous jump predicted by the static BKT theory, but one expects to find a continuous variation with temperature at the transition. Actually, it turns out from the AHNS theory and Shenoy calculations that the vortex pairs which equilibrate to an external oscillating field are those selected by a characteristic length $r_\omega = \sqrt{14D/\omega}$ where D is the vortex diffusion constant and depends on the lattice geometry. The vortex-pairs size scale which is probed is then set by r_ω. The second relevant length scale is the maximum bound-pair size, i.e. the minimum free vortex separation ξ_+ [33] for $T > T_{BKT}$. At finite frequency, it is impossible to observe any structure in the response function at T_{BKT} because only finite scales r_ω are probed, whereas at T_{BKT} infinite-sized pairs unbind. A crossover can be observed at a temperature $T_C(\omega)$ such that $r_\omega = \xi_+(T_C(\omega))$ (the external perturbation probes free vortices). When $T \gg T_C(\omega) > T_{BKT}$, the response comes from unbound pairs whose size is larger than ξ^+, i.e. from free vortices. Increasing the frequency, we decrease the observation window (r_ω) and thus also $\xi^+(T_C(\omega))$. That means that $T_C(\omega))$ increases. At the zero frequency limit $T_C(\omega \to 0) \to T_{BKT}$.

1.4.2 Minnhagen phenomenology

From one side, AHNS and Shenoy yield the same results, in particular the low frequency behaviour of the real and imaginary parts of the dielectric function $\epsilon(\omega)$ have a Drude's form. On the other side, measurements of the dynamic impedance of JJAs [73] revealed a frequency dependence compatible with MP treatment and cannot be described by a simple Drude form of $\epsilon(\omega)$. The measurements [73] revealed an anomalously slow low-frequency vortex mobility $\mu_v \sim 1/|\ln\omega|$ which vanishes logarithmically in the limit of small frequencies. The Minnhagen phenomenology is supported by numerical simulations with time dependent Ginzburg-Landau (TDGL) dynamics [74] whose application corresponds to local dissipation (on each superconducting grain). It has been suggested [75] that the mechanism responsible for the anomalous dynamics is the coupling between the perpendicular currents, described by the vortices, and the longitudinal currents (spin wave part). The dynamic properties of the spin waves are different depending on the type of dynamics, i.e. TDGL dynamics or resistively shunted junction (RSJ) dynamics. In the framework of non local dissipation (RSJ dynamics), the vortex conductivity exhibits a finite zero-frequency limit, whereas with local dissipation (TDGL dynamics) it shows the same MP behaviour. Other theoretical treatments show that with a local dissipation the anomalous dynamics appears already as a property of a single vortex motion [76]. Later, numerical simulations [77] showed that the vortex response is well described by MP for both types of dynamics (TDGL and RSJ). Further theoretical investigations of the dynamic conductivity as well as the vortex mobility, based on the screened Coulomb gas [78], showed that the MP anomalous behaviour emerges in a new intermediate scale (or frequency) regime $r_\omega \leq \xi$, where ξ is a vortex screening length provided by a nonzero free vortex density whose origin can be thermal or flux-induced. In this new scale regime larger vortex pairs probed at low frequency move more slowly because of a logarithmically interacting medium of smaller pairs. Additional analytical calculations [79] attribute the anomalous phenomenology to the motion of pairs in a Coulomb potential screened by interacting free vortices. Another possibility arises from pinning effects due to the underlying discrete lattice or induced by disorder. Using numerical simulations this possibility has been demonstrated to occur for the one-component (charges of only one sign) 2D Coulomb gas model on a triangular lattice [53]. In absence of disorder, a crossover from a (normal) Drude-like response to an anomalous response was observed and associated with the depinning transition temperature. A similar crossover is obtained at a temperature well above T_d only if disorder (pinning sites) is introduced into the model. This is in contradiction with the vortex correlation effects found in analytical results [78] which suggest an anomalous response in certain parameter region. The thermodynamic crossover [53] was also observed at a fixed temperature as the magnetic field is increased [80] and it is linked to a suppression of the resistance.

1.4.3 Experimental observations

On the experimental side, the dynamic response of classical overdamped JJAs has been studied by measuring their ac impedance (Z) [1]. To our knowledge, a temperature dependent exponent, as predicted by the AHNS theory, was never observed in Z. Nonconventional behaviour was found in early experiments [73], thereby providing some evidence for the MP model. We find that the impedance frequency dependence can be ascribed, below T_{BKT}, to vortex hopping between neighbouring pinning sites [81], provided a finite concentration of single vortices is present. The disagreement between theories and experiments may result from the combination of a nonuniform Josephson coupling constant distribution and the presence of unbound vortices.

Chapter 2

Sample characterization

This chapter focuses on some properties characterizing the investigated samples. The fabrication process is explained in the first section. In the second section, the electronic mean free path extracted from four probe measurements is compared to the coherence length of the normal metal in order to examine the clean and dirty limits. The values of the single junction critical current obtained from dynamic resistance measurements (dV/dI vs I) are shown to be in very good agreement with those extracted from inductive measurements. The reduced temperatures versus real temperature obtained from inductive measurements are illustrated, for the three probed samples, in the last section.

2.1 Sample fabrication

The arrays we investigate are made with proximity effect Josephson junctions. Lead (Pb) superconducting electrodes are located on the top of a normal metal (copper) thin film and they are separated from each other by a fixed distance, which is the junction gap. The junctions are then achieved by the normal metal bridges in between the electrodes (see Fig.2.1). The choice of the materials for the electrodes and the normal metal layer is suitable for studying proximity phenomena because copper and lead do not form any alloy. Moreover, the transition temperature of the lead (bulk) is rather high ($T_C^{Bulk} \sim 7.2K$). Then the temperature range accessible with our standard liquid helium cryostat is rather

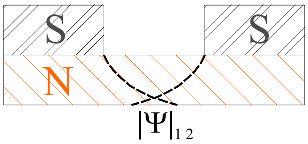

Figure 2.1: Proximity-effect Josephson junction. In the normal (N) metal, in between the superconducting (S) electrodes, the proximity effect [82] takes place leading to an overlap of the order parameters $\Psi_{1,2} \neq 0$ (dashed lines).

large, below and above T_C^{Bulk}.
The sample fabrication process is achieved in a clean room. The sample is composed of three layers. The first one is a one inch diameter silicium (Si) wafer on which is evaporated a $5200\mathring{A}$ thick copper layer (purity 99.999%). The third one is a $2500\mathring{A}$ thick lead (Pb) layer (purity 99.9995%) which is evaporated immediately after the copper in order to avoid any contamination at the interface. The molybdenum crucibles are heated by Joule effect. Before the evaporation process takes place the wafer is cleaned up with an argon rf-discharge (pressure $2 \cdot 10^{-2}$mbar). The typical pressure during the metal evaporations is of the order of 10^{-5} mbar. Once the evaporation is complete the room pressure inside the evaporator is established by introducing dry nitrogen instead of air. The nitrogen molecules absorbed by the metallic layers avoid oxidizing of the lead at the copper-lead interface, which would lead to variations in the coupling constants [83].
The pattern in the lead layer is obtained by a standard optic lithography. A $7500\mathring{A}$ thick Shipley S3008 positive photoresist layer is spread out on the top of the lead layer. The pattern is drawn in the resist with a short exposition (a few seconds) to an i-line (360nm) mask aliner followed by a developer bath of one minute. The lattice constant is $8\mu m$, and the junctions are $1\mu m$ long and $2\mu m$ wide. The sample is then exposed to an argon ion gun until the full lead thickness in between the resist bridges has been etched. (The gun is stopped when the under copper layer becomes visible.)
The Fig.2.2 illustrates the process steps and Figs.2.3 are SEM pictures of a JJA on the dice lattice.

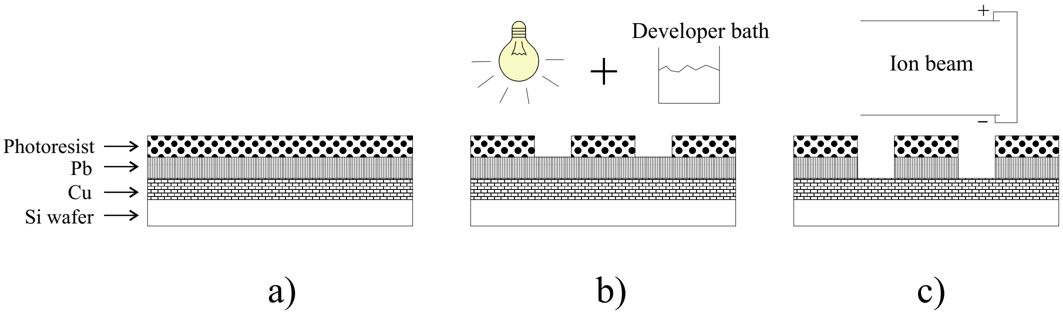

Figure 2.2: Sample fabrication process. a) Preparation of the three layers (copper, lead and photoresist) on a silicium wafer. b) Exposition and development of the photoresist. c) Etching of the lead layer.

2.2 Resistive measurements

The electron mean free path l extracted from resistive measurements gives us an information about the relative purity of the samples in terms of the coherence length in the normal metal ξ_N (dirty limit ξ_{N_D} or clean limit ξ_{N_C}). Then the single junction critical

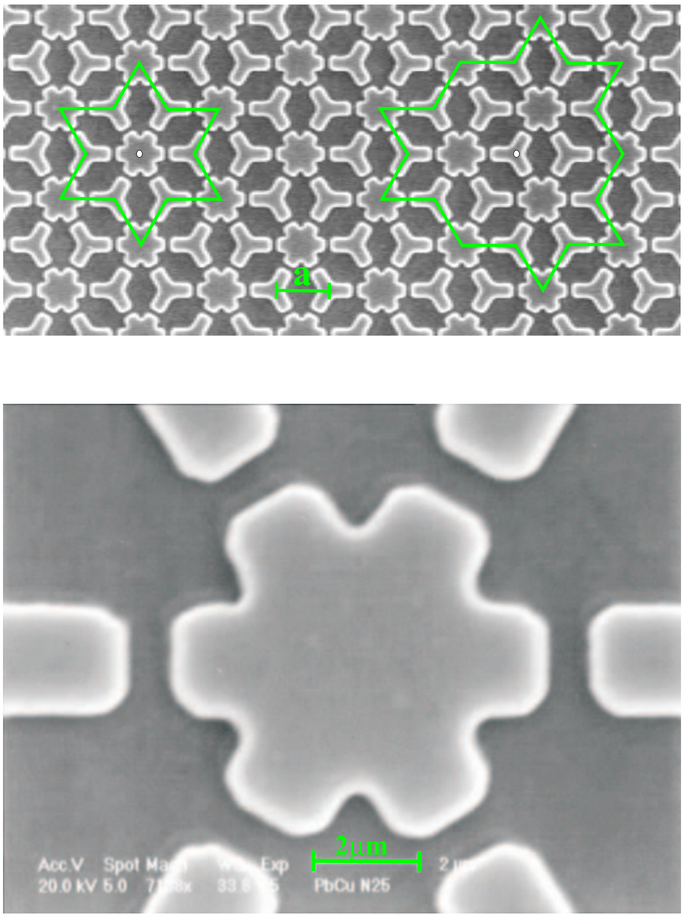

Figure 2.3: SEM pictures of a JJA. Top: portion of the array. The smallest type of AB cage (centered in A type site) and a cage centered in a B type site (see section 1.3) are indicated. Bottom: six fold lead island on the top of the underlying copper layer (dark background). The round V-shapes are due to the photolithography. The lattice constant $a = 8\mu m$ and the junction gap is about $1\mu m$ long and $2\mu m$ wide.

current obtained with four point measurements is compared to the one extracted from inductive measurements.

2.2.1 van der Pauw measurements

The first kind of four probe measurements was performed with a van der Pauw configuration [84] at remanent field (not compensated ambient field, see section 3.7). The contact points form a square located at the border line of the substrate, i.e. on the copper layer around the junction array, see Fig.2.4. A dc current (up to $100mA$) circulates between two neighbouring points and the voltage is measured between the two others. With such a

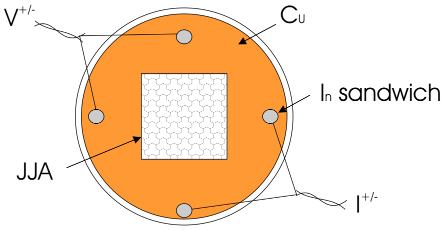

Figure 2.4: van der Pauw configuration. The twisted wire pairs ($V^{\pm}$ and $I^{\pm}$) are welded on the copper film with indium pressed on them (In sandwich) in order to have a good electric contact and avoid to heat the sample with a soldering iron which could damage the Josephson junction array.

symmetric configuration it is possible to use a simplified expression for the resistance [84]

$$\rho/d = \overline{R} \cdot \pi/\ln 2 \tag{2.1}$$

where ρ is the resistivity of the metallic film, d its thickness and $\overline{R}$ the mean of the resistances measured with two different contact point pairs. This simplified expression is valid since both values of the measured resistances are almost the same.

At room temperature, the lead islands are shunted by the copper layer ($\rho_{Pb}/\rho_{Cu}(290K) \cong 20$). We measured $\overline{R}(290K) \cong 6.49m\Omega$. Using $\rho \equiv \rho(290K)_{Cu(bulk)}$ as a known value $\rho = 1.68 \cdot 10^{-8}\Omega m$ [85], and applying (2.1), we obtain a copper layer thickness $d = 5700\mathring{A}$. This value is in good agreement with the copper thickness measured after its deposition (see section 2.1). The van der Pauw sheet resistance (ρ/d) measurement at low temperature was performed with copper around the Josephson array. This implies a non vanishing resistance at low temperature. Fig.2.5 shows a four probe measurement of the sheet resistance performed with an ac current of $0.88mA_{RMS}$ at 235Hz. At $T_{CS} \cong 6.61K$, the lead islands undergo their resistive transition leading to a first rapid decrease of the sheet resistance. For $T < T_{CS}$, ρ/d values are higher than what could be expected if the copper around the array were absent. Nevertheless, this does not affect the temperature dependence. The level of the plateau above T_{CS} gives the normal state sheet resistance ($\rho/d \equiv R_N \cong 1.75m\Omega$) of the bilayer (Cu/Pb) which is supposed to be given essentially by the underlying copper film. While the temperature is decreased below T_{CS}, the sheet resistance is decreased to the normal state sheet resistance of the junctions (R_N^J). For $T < T_N$, the proximity effect takes place [82], i.e. the phase coherence settles between the superconducting Pb islands [86]. The lower the temperature the more the superconductivity extends over the array across the copper bridges.

From these high and low temperature resistive measurements, it is possible to extract some characteristic values of the sample. The first one is the residual resistivity ratio given by $\rho(\text{room temperature})/\rho(T \geq T_{CS})$

$$\text{(residual resistivity ratio) } RRR \equiv \frac{\rho_e(290K)}{\rho_e(10K)} = \frac{\overline{R}(290K)}{\overline{R}(10K)} \cong 17 \tag{2.2}$$

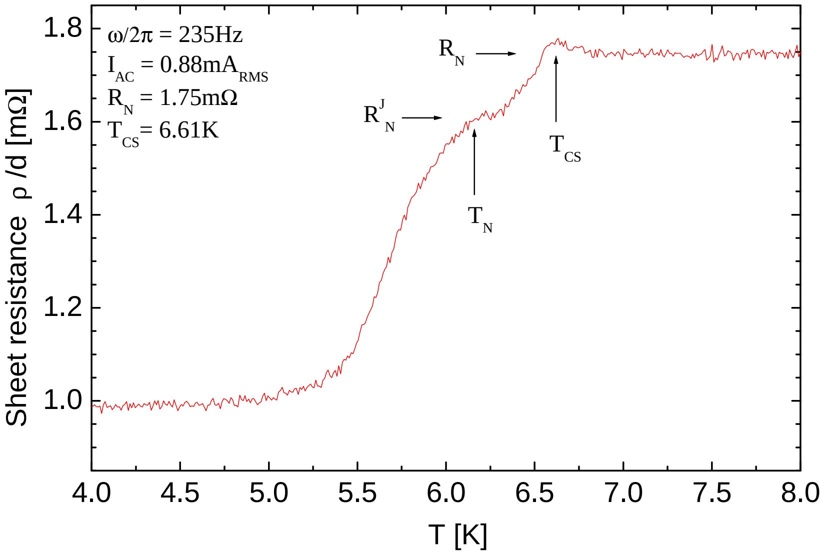

Figure 2.5: Sheet resistance vs temperature measured with an ac current of $0.88mA_{RMS}$ at 235Hz. The values are normalized according to the normal state resistance measured with a dc current; $\overline{R}(10K) = 0.387m\Omega$. See text for remarks related to the non vanishing resistivity at the lowest temperatures.

(The subscript e indicates the effective value and b the bulk one).

Such a low ratio indicates a rather high density of impurities within the sample, which is an indication of a rather dirty sample.
The effective resistivity (ρ_e) of thin films was calculated considering the finite size effect [87] :

$$\frac{\rho_e}{\rho_b} = \frac{4}{3}\frac{(1-p)}{(1+p)(d/l_b)\ln(l_b/d)} \tag{2.3}$$

where $\rho_e = \rho_b + \rho_s$, ρ_b is the bulk resistivity (temperature-dependent phonon contribution and temperature-independent impurity and defect contribution) and ρ_s is the resistivity due to the surface scattering (size effect). Here p, the fraction of electrons that are specularly reflected, is supposed to be vanishingly small since the de Broglie wave length (λ_B) of the electrons contributing to the current transport in the copper is of the order of the interatomic distance ($\lambda_B = \sqrt{h^2/2m\varepsilon_{F_{Cu}}} \cong 4.6 \cdot 10^{-10}m$) and is assumed to be small compared to the roughness scale of the surface. The above expression is valid in the limit when the electron mean free path of the bulk material $l_b \gg d$ and hence is not valid at room temperature since $l_b(290K) \cong 0.04\mu m \ll d \cong 5700\mathring{A}$. This value is obtained using the temperature independence of the product $\rho_b l_b$ [87] :

$$\rho_b l_b(10K) = \rho_b l_b(290K) = 7.7 \cdot 10^{-16}\Omega m^2 \tag{2.4}$$

Using (2.2),(2.3) with $p = 0$, and (2.4), we get the bulk normal electron mean free path

$$l_b(10K) \cong 3.4\mu m$$

which is much larger than the thickness $d \cong 0.57\mu m$ as requested for (2.3).
In view of the previous results (2.2) and (2.4), the high value of the ratio $l_b(10K)/l_b(290K) \cong 100$ is a clear indication of the importance of the scattering resistivity (ρ_s) in thin films such as those we fabricate.
It is now possible to discuss the purity of the sample. According to a theoretical point of view, the normal N underlying metal coherence length ξ_N is compared to the bulk value of the mean free path l_b. One has to distinguish between two limits [14, 17] ;

$$\text{In the clean limit } (l_b \gg \xi_N): \quad \xi_N \equiv \xi_{N_C}(T) = \hbar v_F / 2\pi k_B T$$

$$\text{In the dirty limit } (l_b \ll \xi_N): \quad \xi_N \equiv \xi_{N_D}(T) = \sqrt{\hbar v_F l / 6\pi k_B T}$$

where $v_F = 1.57 \cdot 10^6 \; ms^{-1}$ is the Fermi velocity and $l \equiv l_e$ is the effective mean free path (both quantities being related to the copper). We do not know what the value of l_e is, but it should be smaller than l_b, and $\xi_{N_D}(T)$ should be smaller than $\xi_{N_C}(T)$. Since l has not a strong effect on ξ_{N_D}, we assume $l \approx d$, then $\xi_{N_C}(T_{CS}) \cong 0.29\mu m$ and $\xi_{N_D}(T_{CS})|_{l \equiv d} \cong 0.24\mu m$. Both quantities are smaller than the value of l_b, even at the lowest measurable temperature, around 2K. This result would indicate that we do not have to deal with the dirty limit, in contradiction with the first result (2.2). Nevertheless, we have to be careful since we do not know the exact value of l_e. Moreover, we considered a diffusive scattering ($p = 0$ in (2.3)), but there may be partial specular scattering as was observed in evaporated films [87]. Thus, we cannot clearly conclude about the purity of our samples.

2.2.2 I-V characteristics

In order to get the single junction critical current $I_{CJ}(T)$ and to compare it to the value obtained by inductive measurements, once all the measurements were performed on the sample, we measured both the dynamic resistance dV/dI and the resistance V_{dc}/I_{dc} as a function of a dc current I_{dc}. An ac current of small fixed amplitude ($I_{ac}^{RMS} = 120\mu A$) at $\omega/2\pi = 230$Hz was superposed on the dc bias current I_{dc}. This has been done in a non compensated remanent field (see section 3.7). Because of the small value of the sheet resistance ($\approx m\Omega$, see Fig.2.5), and in order to be able to measure a signal with a low excitation amplitude, the sample geometry was modified. This is the reason why we performed this measurement at the end of the experiments. With a thousand parallel junctions, the current one would need is simply a thousand times the critical current of a junction, which would lead to an important increase of the sample temperature. In addition, the induced voltage between both sides of the square would be too small to be measured. As a consequence, we cut the square sample in order to form a thin strip as long as possible (see Figs.2.6 and 2.7). The lead is $300\mu m$ wide (48 parallel junctions). The space between each branch is $100\mu m$ and the strip is about 12cm long.

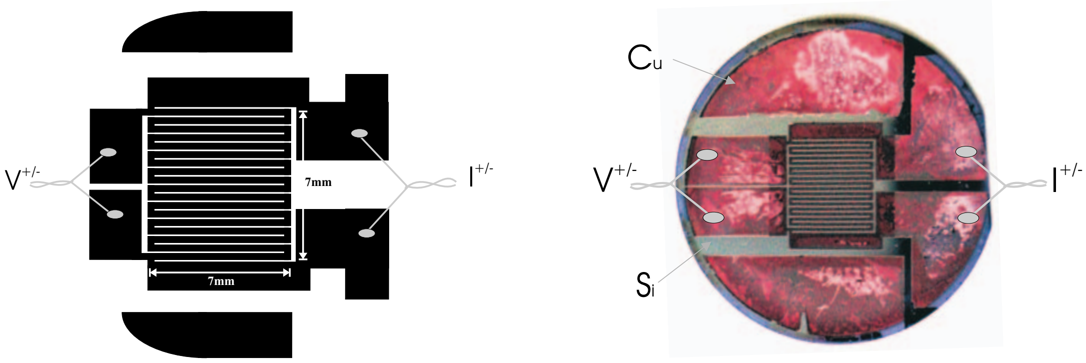

Figure 2.6: Modified sample for dynamic resistance measurements. Left side : scheme of the mask. The branches of the strip are $300\mu m$ wide and they are equally spaced by $100\mu m$. The strip is about 12cm long. Right side : picture of the modified sample. The copper on both sides is let on the substrate to dissipate the heat due to the measurement current. See Figs.2.7 for more details.

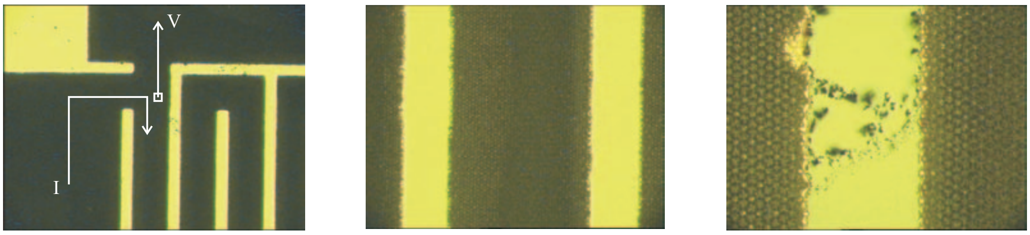

Figure 2.7: Pictures (zooms) of the modified sample. Left side : picture of one corner of the mask. The contact points to measure the voltage are located at the beginning of the strip. Center : picture of three branches of the strip. There is no shortcut between them. Right side : an example to avoid on a test sample showing a non complete photolithographic process leaving an archipelago of SC islands in between the branches.

The ac current I_{ac} is obtained from the voltage generator of the lock-in (wire resistance $\cong 83\Omega$ at T=4.2K). The dc bias current I_{dc} measured with a resistance of $1K\Omega$ is obtained by a dc current source. Both I_{ac} and I_{dc} are superposed on the same wire using a simple T-connector. The first harmonic of the ac component of the response signal is measured with the lock-in, and a nanovoltmeter measures the dc response. To avoid any shift effect on the dc voltage measurement, the polarity of the dc current is changed for each value following the sequence $+I_{dc}, -I_{dc}, -I_{dc}, +I_{dc}$ and the corresponding V_{dc} is given by the arithmetic mean of each absolute voltage. In order to have the strongest thermal contact with the cold source, the sample is directly immersed in the helium bath, i.e. no vacuum pot (see section 3.2, Fig.3.2). The sample is then cooled down by pumping on the helium bath. Fig. 2.8 shows the I-V characteristics at temperatures from $4.145K$ down to $1.68K$. As the current is increased, three different regions can be distinguished. At $24mA$ the curvatures of each

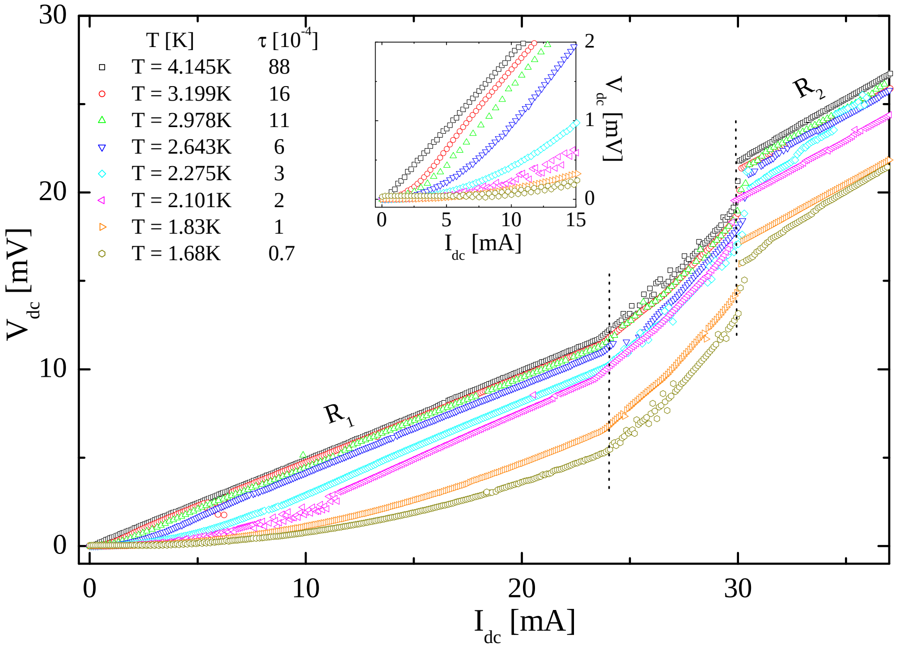

Figure 2.8: I-V characteristics of the modified sample. The dc current is applied to the 48 parallel junctions. The measurements have been performed at temperatures between $4.145K$ and $1.68K$ from which these few selected isotherms show the general trend. The resistances R_1 and R_2 given by the slopes of the highest temperature curves are respectively $490m\Omega$ and $680m\Omega$. The inset shows the zero-current limit region.

isotherm sharply increases and then at $30mA$ there is a jump in the voltage of 2 to 3 mV for each curve. For the highest temperatures, we observe a linear response in the first and third regions (below $24mA$ and above $30mA$). When decreasing the temperature, the first linear region, below $24mA$, disappears. This behaviour will be clearly observable in the dynamic resistance (dV/dI) measurements (see Fig.2.9). The measured resistances in the ohmic regions are $R_1 \cong 490m\Omega$ and $R_2 \cong 680m\Omega$ (the step in between is not linear). The sheet resistance ρ/d is given by $R = \rho L/S = (\rho/d)(L/w)$ where d is the sample thickness, $L = 12cm$ is the strip length and $w = 300\mu m$ is the width of the strip. In the first region $\rho/d \cong 1.23m\Omega$. It increases to $1.70m\Omega$ after the jump. In the intermediate region, the magnetic field induced by the bias current penetrates into the SC islands destroying the phase coherence in the JJA. Above the jump, the superconductivity disappears and the sample is in the normal state (ohmic behaviour), i.e. the sample behaves as a copper thin film and the sheet resistance $(w/L)R_2$ is the same as the one measured with the van der Pauw configuration (see Fig.2.5).

2.2.3 Critical current

Following the procedure used in [56] and [88], which is based on the previous works of [89], we assume that the measured current I_{dc} which corresponds to the maximum of differential resistance (dV/dI) gives a good estimate of the intrinsic (unrenormalized) critical current. This is assumed despite the fact that we are not dealing with single junctions but with a 2D array. Fig.2.9 shows differential resistance curves from which is obtained the temperature dependence of the single junction critical current $I_{CJ}(T)$. The plateau following the maximum of dV/dI curves corresponds to the ohmic region where the constant slope gives the resistance R_1 of the I-V characteristics. The single junction critical current I_{CJ} is obtained from the critical current I_C measured on the strip with 48 parallel junctions; $I_{CJ} = I_C/48$. There are two expressions for $I_{CJ}(T)$ in proximity effect junctions. The first one is referred to as the de Gennes critical current and the second as the Zaikin-Schon expression.

de Gennes critical current

The expression of de Gennes for the single junction critical current [82]

$$I_{CJ}(T) = I_{CJ}(0)\ \left(1 - \frac{T}{T_{CS}}\right)^2\ \exp[-\frac{\ell_J}{\xi_N(T)}] \tag{2.5}$$

has two parameters: the critical current at zero temperature, $I_{CJ}(0)$, and the ratio $\ell_J/\xi_N(T)$ where ℓ_J is the normal metal bridge length and $\xi_N(T)$ the normal metal coherence length already defined in section 2.2.1. The de Gennes expression is valid for non frustrated metal junctions (SNS), for temperatures slightly below T_{CS}, in the dirty limit ($l_b \ll \xi_{N_D}$), and for thick junctions ($\ell_J \gg \xi_{N_D}$) such as those we fabricate (see section 2.2.1). The last requirement reads

$$\frac{\ell_J}{\xi_N(T_{CS})}\sqrt{\frac{T}{T_{CS}}} \gg 1 \longleftrightarrow T \gg T_{CS}\frac{\xi^2}{\ell_J^2} = \frac{\hbar v_F l}{6\pi k_B \ell_J^2} \equiv T_0 \tag{2.6}$$

where T_0 is the Thouless temperature. An estimate of T_0 with $l \equiv d = 0.57\mu m$ and $\ell_J = 1\mu m$ gives $T_0 \cong 360mK$.

Zaikin-Schon critical current

The expression for the single junction critical current that we will use [90] is also valid for non frustrated metal junctions (SNS), in the dirty limit and for thick junctions but at low temperatures only, i.e. $T \ll T_{CS}$.

Actually the expression given in [90] is essentially a sum of all the Matsubara frequencies ω defined as $\hbar\omega = (2n+1)\pi k_B T$. Nevertheless, it is possible to take the first term of the sum only (n=0), as long as $T \gg T_0$. We write the expression given in Ref.[90] for $I_{CJ}(T)$ in another form. First, we define the function $X(T) = \pi k_B T/\Delta(T)$ where the superconducting order parameter Δ is given by the BCS theory, since according to the

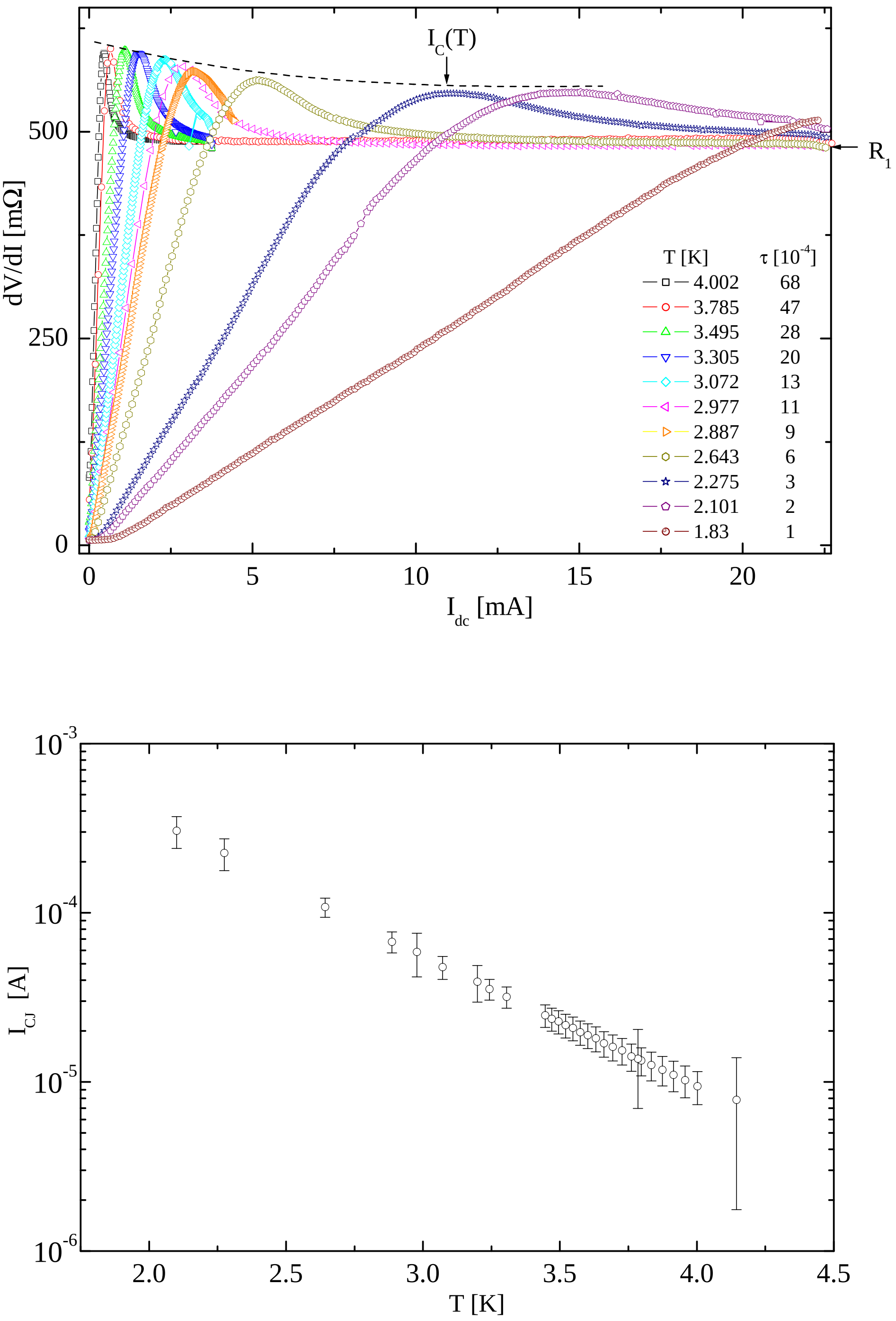

Figure 2.9: Dynamic resistance measurements (top) and single junction critical current (bottom) obtained from the position of the maximum of the dV/dI curves.

assumption in Ref.[90] the gap remains unchanged near the NS boundaries, i.e. good electric contact at the interface NS. Using the two-fluid temperature dependence [91] :

$$\Delta(T) = \Delta(0)\ \left[1 - \left(\frac{T}{T_{CS}}\right)^4\right]^{1/2} \qquad\qquad \Delta(0) = 1.76 k_B T_{CS}$$

We define the function

$$F[X(T)] = \frac{3+2\sqrt{2}}{(1+X^2)\left[1 + \frac{X}{(1+X^2)^{1/2}} + \sqrt{2}\left(1 + \frac{X}{(1+X^2)^{1/2}}\right)^{1/2}\right]^2}$$

Thus the single junction critical current, above T_0;

$$I_{CJ}(T) = \frac{64\pi k_B T_{CS}}{(3+2\sqrt{2})eR_N}\ \frac{\ell_J}{\xi_N(T_{CS})}\left(\frac{T}{T_{CS}}\right)^{3/2} F[X(T)]\exp[-C\ \sqrt{T}]$$

with $C = \ell_J/[\xi_N(T_{CS})\sqrt{T_{CS}}]$

The function $F[X(T)]$ allows distinction of the following limit cases;

- ⋆ high temperature limit, i.e. $T \leq T_{CS} \Leftrightarrow k_B T \gg \Delta$
  That means $X(T) \gg 1$, then $F[X(T)] \cong \frac{3+2\sqrt{2}}{(4X)^2} = (3+2\sqrt{2})\frac{\Delta(T)^2}{(4\pi k_B T)^2}$
  This leads to the result obtained by Likharev [14] for $T \leq T_{CS}$ and in the very dirty limit, i.e. when $\ell_J/\xi_N \to \infty$

$$I_{CJ}(T \leq T_{CS}) = \frac{4}{\pi}\frac{\Delta(T)^2}{eR_N k_B T}\frac{\ell_J}{\xi_N(T)}\exp[-\ell_J/\xi_N(T)]$$

- ⋆ low temperature limit, which is the case that will be of major interest to us, i.e. $T \ll T_{CS} \Leftrightarrow k_B T \ll \Delta$
  This implies that $X(T) \ll 1$, then $F[X(T)] \cong 1 - \frac{2+\sqrt{2}}{1+\sqrt{2}}X$.
  When $X \to 0 \Rightarrow F \to 1$ and we find the same expression as in [90] valid for low temperatures:

$$I_{CJ}(T \ll T_{CS}) = \frac{64\pi}{(3+2\sqrt{2})}\frac{k_B T}{eR_N}\ \frac{\ell_J}{\xi_N(T)}\exp[-\ell_J/\xi_N(T)] \tag{2.7}$$

An estimate of $I_{CJ}(T)$ for $T = 0$ [90] reads as :

$$I_{CJ}(T=0) = k_B T_0\ \frac{\pi}{eR_N} \tag{2.8}$$

Notice that by substituting $k_B T_0$ by $\Delta(0)/2$ we recover the critical current expression for a tunnel junction at zero temperature [92].

Comparison with inductive measurements

The way we extract the single junction critical current I_{CJ} as well as the reduced temperature τ from inductive measurements is explained in details in Appendix D. Fig.2.10 shows the data obtained from four probes and inductive measurements. Clearly the dc measurements confirm quantitatively very well the inductive ones. Notice that both types of measurements were performed in an absolutely independent way. The critical current at zero temperature estimated using (2.8) with (2.6) and a normal state resistance $R_N = 1m\Omega$ is $I_{CJ}^{ZaikinSchon}(0) = 97mA$. The inductive measurements are treated using the expression (2.7), as long as $T > T_0$. We cannot use this expression to extrapolate the data to zero temperature. On the other hand, if we use the de Gennes expression (2.5) to fit the data (dc or inductive), we get $I_{CJ}^{deGennes}(0) = 70mA$. But the de Gennes expression is not valid well below T_{CS}. Thus the single junction critical current at zero temperature is slightly below $100mA$.

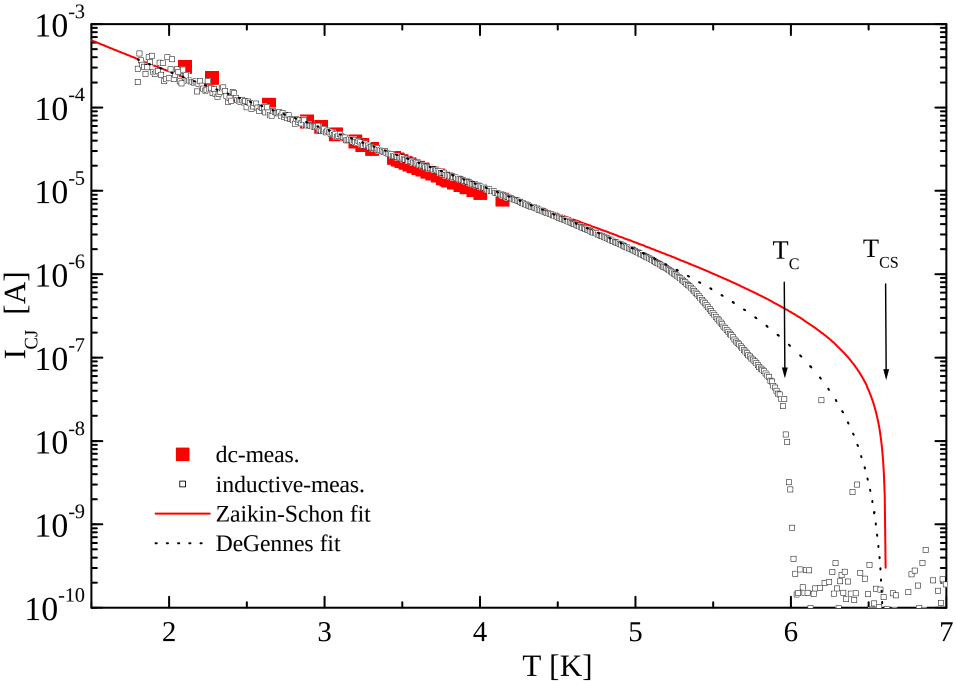

Figure 2.10: Temperature dependence of the single junction critical current. Red squares: values obtained with the four probes measurements (Fig.2.9). Black empty squares: values obtained from inductive measurements at $f = 0$ and $\omega/2\pi = 12$Hz. Red line: Zaikin-Schon based fit of the inductive data (fitting parameters *slope* = 5.73, *intercept* = 38.29 and $\ell_J/\xi_N(T_{CS}) \cong 14$). Black dotted line: de Gennes based fit (fitting parameters $I_C(0) = 70mA$ and $\ell_J/\xi_N(T_{CS}) \cong 8.8$).

The ratio $\ell_J/\xi_N(T_{CS}) \cong 14$ is obtained from the low temperature region with a Zaikin-

Schon fit. Using the results of the last section ($\xi_N(T_{CS}) \approx 0.3\mu m$), one gets an effective junction length $\ell_J \cong 4\mu m$, i.e. four times longer than the nominal value. The de Gennes fit gives a ratio $\ell_J/\xi_N(T_{CS}) \cong 8.8$ which leads to an effective junction length $\ell_J \cong 2.6\mu m$, also larger than the nominal value $\ell_J = 1\mu m$.

This is the first time that inductive measurements performed with the two coil technique are confirmed by four probe measurements. The very good agreement between the single junction critical current obtained using both measurement methods confirms the inductive measurement technique and the data treatment we apply.

2.3 Magnetic screening effects

When a Josephson junction array is exposed to an external magnetic field, screening currents are induced in the array and a magnetic energy is associated to these circulating currents. We have to consider the effect of the transverse field on the Josephson junctions and the screening currents circulating around each cell.

It is possible to neglect the induced Meissner screening fields inside the junctions, which lead to an inhomogeneous distribution of the Josephson currents, as long as the junction width $w_J << \lambda_J$ the Josephson penetration depth (see section 1.2.1). This is the case, for all our samples, for temperatures higher than 3.2K ($\tau \approx 4 \cdot 10^{-3}$) (see Fig.2.11). At lower temperatures the flux threading a plaquette is no longer determined only by the external field. The magnetic energy stored in each current loop around the plaquettes, E_m, has to

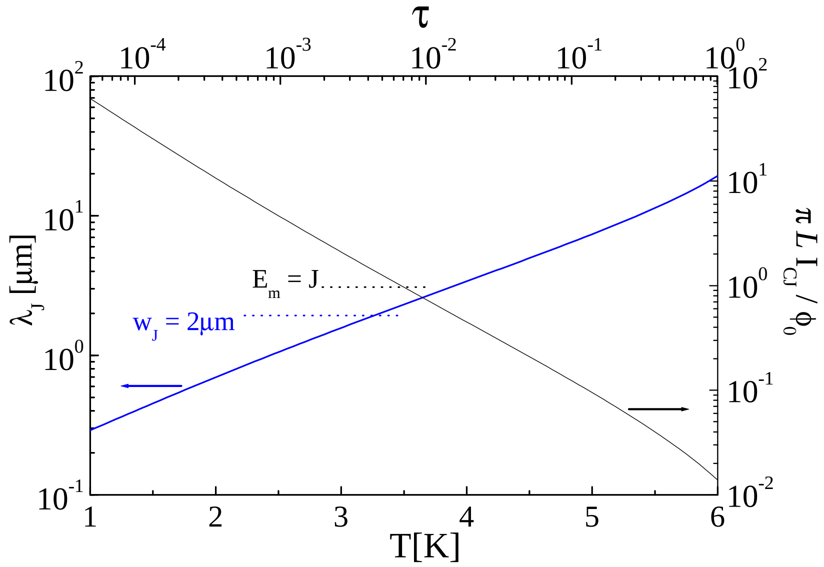

Figure 2.11: Josephson penetration depth λ_J and magnetic energy over Josephson energy ratio as a function of real (bottom axis) and reduced (upper axis) temperatures.

be compared to the Josephson coupling energy J (see section 1.1).

$$E_m = \frac{1}{2}\mathcal{L}I_S^2 \leq \frac{1}{2}\mathcal{L}I_{CJ}^2 \qquad\qquad J = \frac{\phi_0}{2\pi}I_{CJ}$$

Then the ratio $E_m/J \leq \pi\mathcal{L}I_{CJ}/\phi_0$. The inductance $\mathcal{L} = 26pH$ of the rhombic loop has been calculated using the numerical results of [93] for a wire with rectangular cross section. Fig.2.11 shows that the magnetic energy is dominant compared to the Josephson energy for temperatures below $\tau \sim 7 \cdot 10^{-3}$, almost the same temperature at which $w_J \approx \lambda_J$.
Another way to quantify the capacity of the array to screen external magnetic fields is to compare the effective penetration depth $\tilde{\Lambda}$ (see section 3.2.2) with the lattice constant a, see Fig.2.12. The dotted line in Fig.2.12 indicates the temperature below which the sheet inductance becomes frustration-independent.

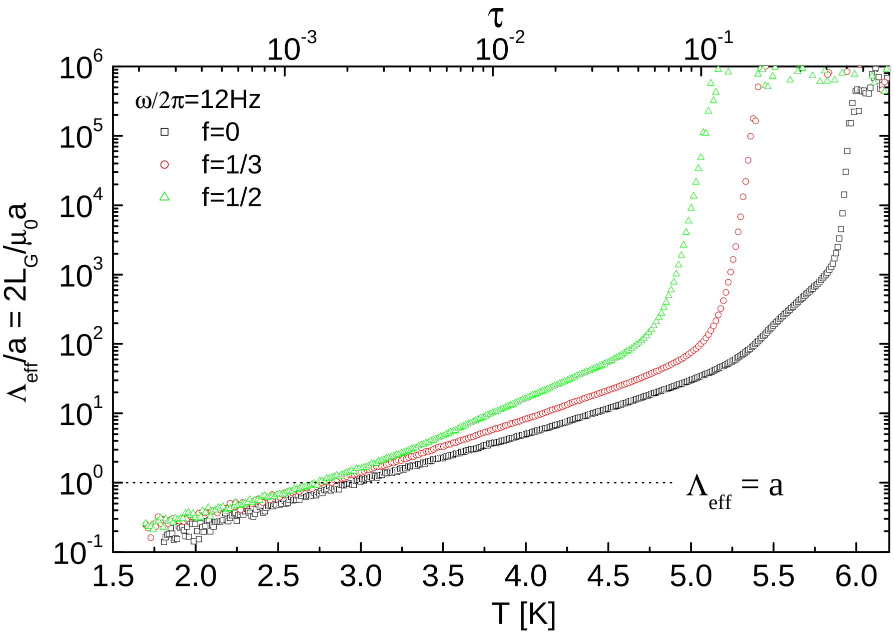

Figure 2.12: Temperature dependence of the effective penetration depth ($\Lambda_{eff} \equiv \tilde{\Lambda}$) over lattice constant ratio.

In the week screening limit ($E_m << J(T)$) the local field is equal to the applied field. The vortices are not magnetic objects carrying an integer number of flux quanta, but phase configurations which satisfy the fluxoid quantization (1.8).
In the strong screening limit ($E_m >> J(T)$), because of current loops, the junction array behaves as a multiply connected superconductor, and the XY model is no longer valid. In this regime the vortices are real magnetic objects interacting with currents trough Lorentz forces.

2.4 Sample linear response

This short section is devoted to the linear response regime. Preliminary results are shown without going into details since the inductive measurement technique and the measured physical quantities are explained in chapter 3.
Fig.2.13 shows the temperature dependence of both components of the row signal (X and Y) normalized with respect to the saturation signal (see chapter 3.1) for three values of the excitation current. Looking at the Y components, which reflect the dissipative response, one can see that they are independent of the excitation current except in the transition region, for $5K < T < 6K$ (see inset). This is also the case for the X components, which reflect the superfluid response. When measured with the highest current (green curve), the superfluid response (X) is slightly depressed in the transition region. This means that with this excitation current, the phase coherence in the sample is lost quicker with increasing temperature. The associated dissipation (green dissipative Y curve) is enhanced in the same temperature region. The excitation current tends to destroy the superconductivity in the sample. With smaller drive currents (red and black curves), such effects are not observed, and with the smallest drive current (ten times smaller than the usual value $I_d = 0.5\mu A^{RMS}$) the signal over noise ratio is too small to perform good measurements. We can conclude assuming that with an applied drive current $I_d = 0.5\mu A^{RMS}$ there are no effects of nonlinearity.

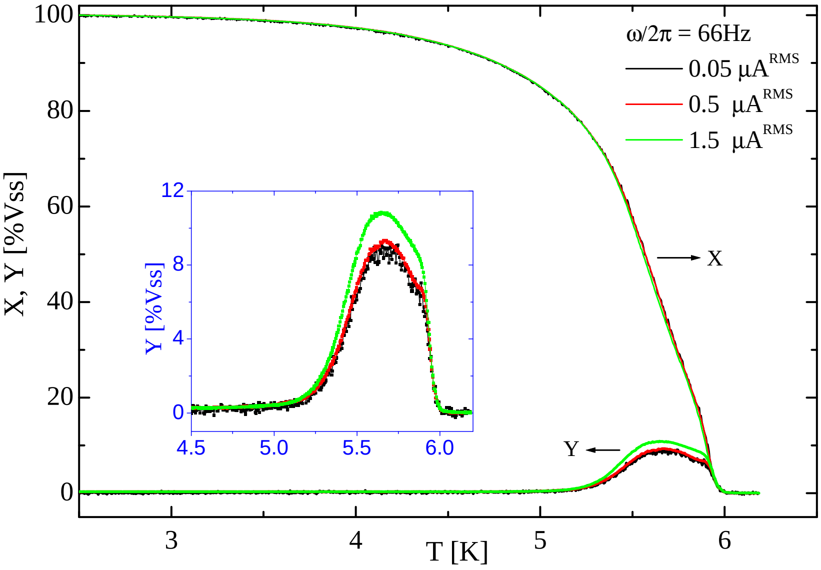

Figure 2.13: Normalized dissipative (Y) and inductive (X) components vs temperature for three values of drive current I_d (measurements performed with $I_d = 0.5\mu A^{RMS}$). The blue inset is a zoom of the Y component in the transition region.

2.5 Reduced temperature

During the period of this work many samples were probed, but the main results presented in this thesis are obtained with three different samples. In order to distinguish them and to be able to compare the results, the number of the respective sample is attributed to each figure (see the figure caption: [sample1],[sample2] or [sample3]). The related function $\tau(T)$ is shown in Fig.2.14 with experimental parameters R_N and T_{CS}.

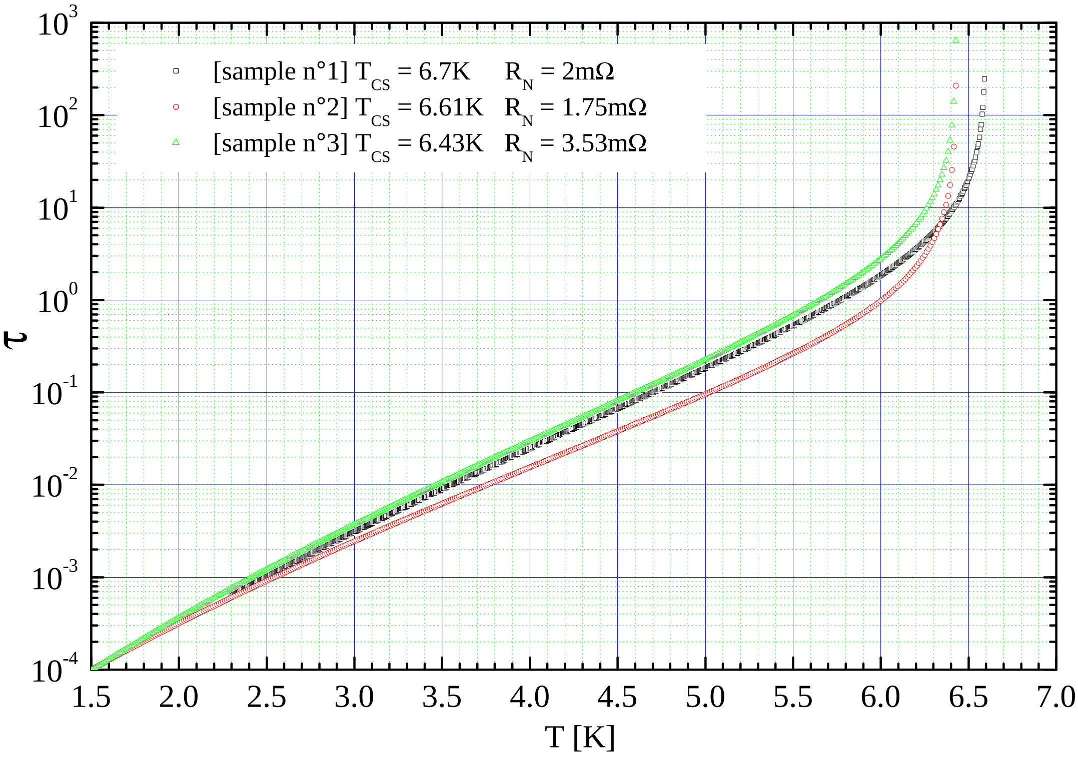

Figure 2.14: Reduced temperature τ as a function of absolute temperature T for each probed sample.

2.6 Low temperature phase discontinuity

When the samples are probed at very low temperature, a small but clear discontinuity in the signal phase is observed at a measured temperature $T \cong 2.18K$, as illustrated in the left inset of Fig.2.15. While the position and the amplitude of this jump depend neither on frequency nor on magnetic field, it is possible to observe this only at frequencies above a few KHz since at lower frequencies the signal over noise ratio is too small. The measured temperature where the discontinuity appears is so close to the lambda point ($T_\lambda \cong 2.17K$ at ambient pressure), below which He-4 becomes superfluid, that it seems obvious to associate both phenomena. Nevertheless, this effect is not yet understood.

The superconducting transition of the Pb islands is observed as a saturation of the signal phase (right inset) at T_{CS}. For this peculiar sample, $T_{CS} \cong 6.43$K.

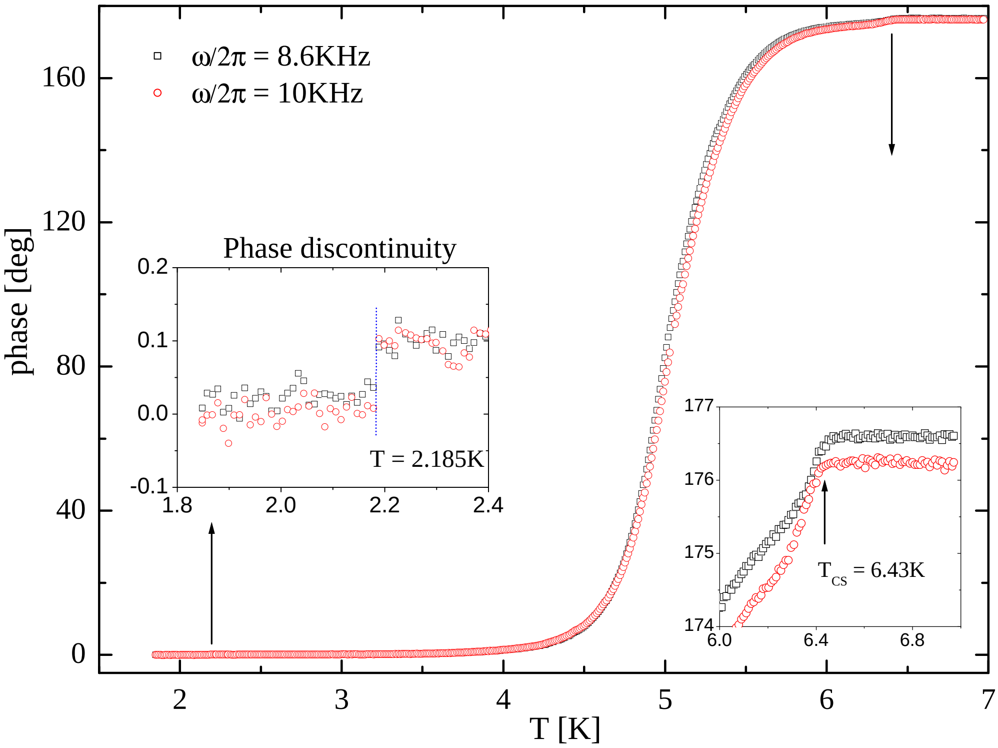

Figure 2.15: [sample3] Signal phase vs temperature measured at high frequency. Left inset: low temperature phase discontinuity at $T \cong 2.18K$. Right inset: SC island phase transition at T_{CS}.

Chapter 3

Experimental setup

The aim of this chapter is to describe the experimental setup used to measure the sheet impedance (Z), or conductance ($G = 1/Z$), of 2D superconducting samples. The four probe measurements discussed in the previous chapter were performed in order to characterize the samples. All the results illustrated in the following chapters are obtained using the two-coil mutual inductance technique described in this chapter.

Starting with the sample, we discuss the measurement technique, the electronic setup, the thermometry, the cryostat main elements, and the magnetic screening where a few preliminary results are shown.

3.1 Measurement technique

The measurement technique [94] described here has been used for many years in the study of the superconducting properties of wire networks [57], Josephson arrays [1] as well as high temperature superconducting thin films [95, 96]. The sample is exposed to an ac magnetic field ($\sim nT$, see also Fig.3.22) provided by a *drive* coil in which flows an ac current I_d ($\sim \mu A$) of frequency $\omega_0 \sim 0.1Hz - 100KHz$. When the sample is in the normal (non superconducting) state, eddy currents produce an ac magnetic field which in turn induces an ac flux through the loops of a *receive* coil. The same phenomenon is true in the superconducting state where Meissner screening currents flow. Fig.3.1 and Table 3.1 illustrate the geometry of the system. The receive coil is a gradiometer, i.e. two coils (the upper one and the lower one, see Fig.3.1) astatically wound in order to compensate any signal due to ac magnetic fields whose origin is far compared to the distance between both coils. It will turn out to be very useful that the receive coil configuration is asymmetric versus the drive coil. Then, even in the absence of any sample, a purely inductive signal called *pick-up* can be measured.

The net flux produced by the screening currents in the receive coil is non zero. This leads to a mutual inductance (M) between the drive and receive coils whose variation δM depends on the intensity of the screening currents ($\overrightarrow{K}$), i.e. on the sheet impedance (Z) of the sample.

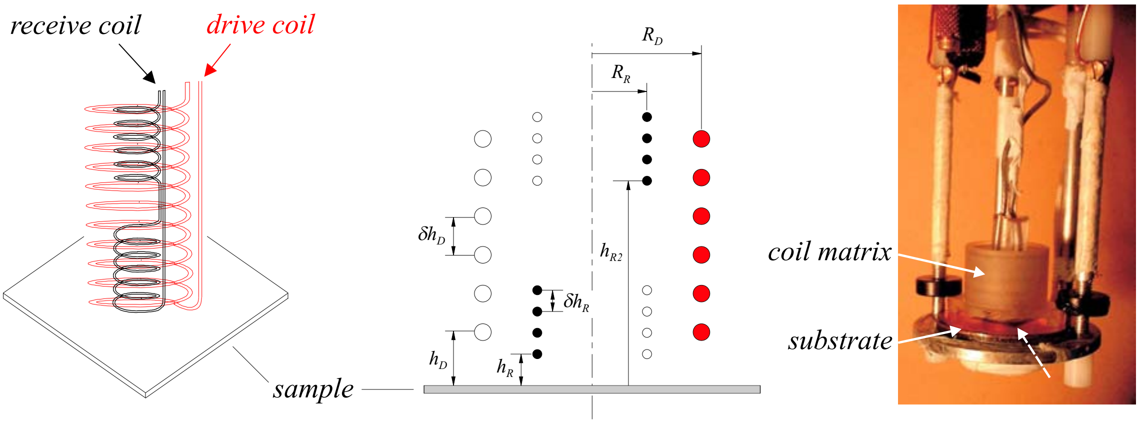

(a) (b) (c)

Figure 3.1: (a) Schematic view of the drive coil with the astatic receive coil inside and the sample below. (b) Schematic view with the fabrication parameters in Table 3.1. (c) Picture of the coils in an epoxy resin (Stycast 1266) matrix on the top of the sample. The dashed arrow indicates the JJA (dark square) patterned in the center of the sample.

Coil	Drive	Receive
Radius	$R_D = 2.05\,\mathrm{mm}$	$R_R = 1.47\,\mathrm{mm}$
Number of turns	$N_D = 25$	$N_R = 2 \times 18$
Distance between turns	$\delta h_D = 0.2\,\mathrm{mm}$	$\delta h_R = 0.055\,\mathrm{mm}$
Distance 1st turn-sample	$h_D = 0.7\,\mathrm{mm}$	$h_R = 0.2\,\mathrm{mm}\ ,\quad h_{R2} = 4.7\,\mathrm{mm}$
Inductance	$L_E \approx 1.5\,\mu\mathrm{H}$	$L_R \approx 1.2\,\mu\mathrm{H} \times 2$
Material	Cu ($\oslash$100 μm)	NbTi ($\varnothing$50 μm)

Table 3.1: Parameters of the drive and of the receive coils; see text for details.

3.2 The measurement system

The diagram of the measurement system is illustrated in Fig.3.2. The drive current I_d with frequency ω_0 is supplied by the internal voltage generator of a lock-in through a resistance R_D in order to have a current source. This excitation signal is decoupled from the lock-in by a transformer to avoid ground loops. On the one side, the superconducting (SC) loop (see Fig.3.2) is coupled to the drive coil through the mutual inductance ($M(Z)$) and on the other side to the rf squid through the input coil. The SHE 330X rf squid from BTi (Biomagnetic Technologies, Inc.) is operated in the flux-locked loop mode and measures the flux variation induced in the receive coil by the screening currents. The compensation signal is measured by phase sensitive detection using the lock-in. Both in phase and quadrature components are numerically manipulated to extract the physical information contained in Z from the mutual inductance change $\delta M(Z)$.

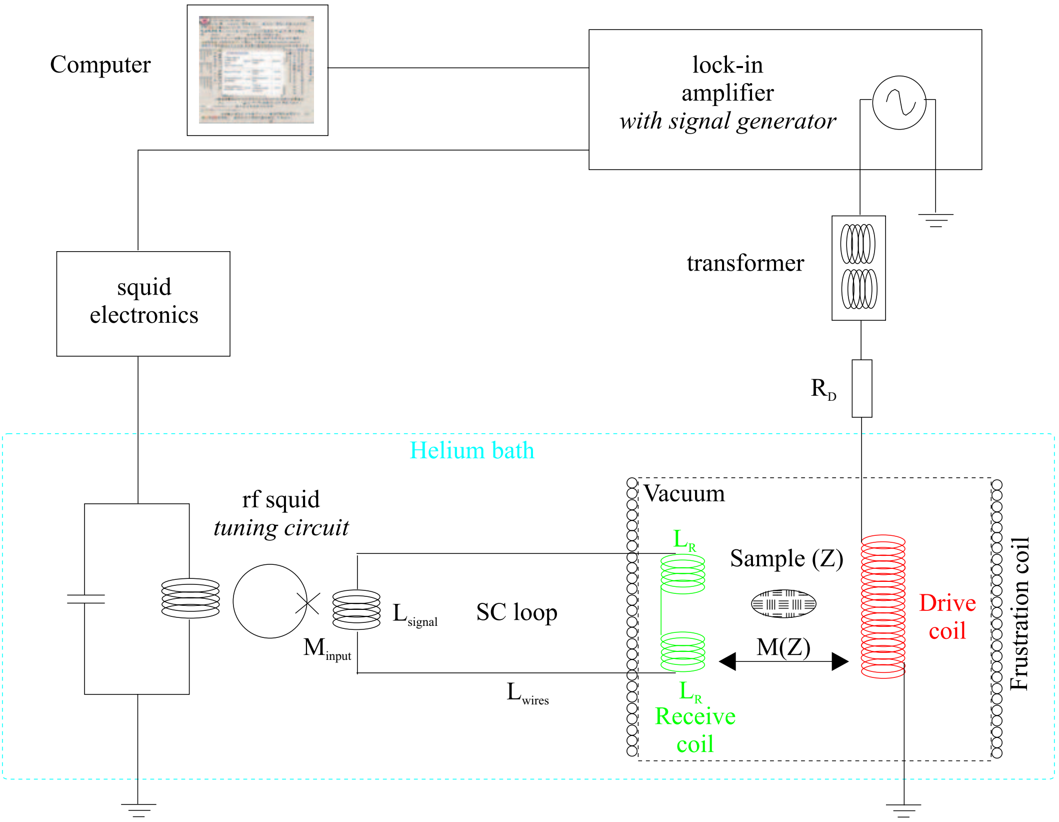

Figure 3.2: Schematic view of the measurement system. The excitation of the system is achieved by the EG&G7260 lock-in amplifier and the drive coil (Fig.3.1 and Table 3.1). The sample, the drive coil and the receive coil are in a vacuum cylindrical chamber surrounded by the superconducting frustration coil which is surrounded by the helium bath. The superconducting (SC) loop couples the receive coil ($2 \times L_R \cong 2 \times 1.2\mu H$) to the squid coil through $M_{input} \cong 20nH$ with $L_{signal} = 2\mu H$. The wound wires of the SC loop are about one meter long. Their estimated [97] inductance is $L_{wires} = 0.3\mu H$. The setup is monitored by a personal computer using GPIB connections.

The diagram of the complete electronic setup is described in appendix (C).

3.2.1 The transfer function

The transfer function is the ratio between the flux change in the receive coil and the one induced in the squid. This is a pure geometrical function depending on the self inductance of each element (see Fig.3.2). Since the detection circuit is superconducting, the total flux change through it should be zero, i.e. the flux through the receive coil is balanced by the sum of the fluxes through every other element of the SC loop. The flux through the squid,

ϕ_{squid}, is then given by

$$\phi_{squid} = \frac{M_{input}}{2L_R + L_{wires} + L_{signal}} \cdot \phi_{receive} \cong 4.26 \cdot 10^{-3} \cdot \phi_{receive} \tag{3.1}$$

The squid has its own voltage/flux gain that is selected by the sensitivity range ×1, ×10, ×100 respectively $20mV/\phi_0$, $200mV/\phi_0$, $2V/\phi_0$. The usual range is ×1, $20mV/\phi_0$. The voltage measured by the lock-in is then related to the drive current (I_d) through the transfer function

$$V_{lock-in} \equiv V_{squid} = \frac{\phi_{squid}}{\phi_0} \cdot 20mV \cong 0.085mV \cdot \frac{\delta M(Z)\ I_d}{\phi_0} \tag{3.2}$$

The mutual inductance variation ($\delta M(Z)$) is calculated in section 3.2.2. Notice that since the detection circuit is a superconducting closed loop, the signal is frequency-independent. The technique sensitivity is discussed in section (3.2.4).

3.2.2 Electrodynamics of the measurement system

The quantity $\delta M(Z)$ introduced above is defined through the expression relating the flux induced in the receive coil, $\phi_{receive}$, to the drive current I_d circulating in the drive coil.

$$\phi_{receive} = \delta M(Z) \times I_d$$

The details of the calculation can be found in Appendix A where we first considered the sample as a finite 2D round film. Since it has not yet been possible to numerically evaluate the expression of $\delta M(Z)$ for such a finite sample, we assumed the 2D film to be infinite. This leads to a much simpler expression for $\delta M(Z)$. We then show (in Appendix A) that the effects of the displacement currents ($\propto \dot{\vec{E}}$ in Maxwell equations) bring only 1% change in $\delta M(Z)$ at one GHz. This section illustrates a few steps of the calculation without taking into account the finite size effect and the effects of the displacement currents.

The definition of the sheet impedance Z (see section 1.2.4) is based on the relation

$$\overrightarrow{E}(\vec{x}, t) = Z\ [\overrightarrow{K}_S(\vec{x}, t) + \overrightarrow{K}_N(\vec{x}, t)]$$

where the superconducting and the normal sheet current distributions (respectively $\vec{K}_S$ given by the London equation and $\vec{K}_N$ given by Ohm's law) are continuous (homogeneous and isotropic sample over the characteristic length scales selected by the coils).
We solved the Maxwell equations choosing the Coulomb gauge ($\vec{\nabla}\vec{A}$) for the total vector potential $\vec{A}(\vec{x}, t)$ and assuming a frequency dependence of the form $\vec{A}_0(\vec{x}) \exp[i\omega_0 t]$ (linear frequency response)

$$\left(\frac{1}{c^2}\partial_t^2 - \Delta\right) \overrightarrow{A}(\vec{x}, t) = \mu_0 \vec{j}(\vec{x}, t)$$

where $\vec{j}(\vec{x}, t)$ is the sum of the current density in the drive coil $\vec{j}_d$ and the current density in the sample.

We introduce an effective penetration depth for a 2D system of thickness d (see section 1.2.4)

$$\Lambda \overset{def}{=} \frac{2\,\lambda^2}{d}$$

and the kinetic inductance is $L_J = \frac{1}{2}\,\mu_0\Lambda$ [18]. Then the sheet currents are

$$\overrightarrow{K}_S \overset{def}{=} \vec{j}_s d = \frac{-2}{\mu_0\Lambda}\,\left(\frac{\phi_0}{2\pi}\overrightarrow{\nabla}\varphi + \overrightarrow{A}\right) = \frac{-1}{L_J}\,\left(\frac{\phi_0}{2\pi}\overrightarrow{\nabla}\varphi + \overrightarrow{A}\right)$$

$$\overrightarrow{K}_N \overset{def}{=} \vec{j}_n d = \sigma_n\ d\ \vec{E}\ = -i\omega_0\ \sigma_n\ d\ \overrightarrow{A}(\vec{x},t)$$

This leads to the sheet impedance

$$Z = \left(\frac{1}{i\omega_0 L_J\varepsilon(\omega,T)} + \sigma_n d\right)^{-1} \overset{def}{=} \left[\frac{1}{Z_S} + \frac{1}{Z_N}\right]^{-1}$$

where Z_S and Z_N are respectively the low and high temperature limits of Z. The complex dielectric function $\varepsilon(\omega,T)$ is associated with the vortex induced dissipation (bound and unbound vortices) [37].

The Maxwell equation for $\vec{A}(\vec{x},t)$ is solved in the Fourier space (q_t is the in-plane component of $\vec{q}$).

In the film plane ($z=0$)

$$\hat{A}(q_x,q_y,z=0,\omega) = \frac{\mu_0}{2}\,\frac{\hat{j}_d(q_x,q_y,-iq_t,\omega)}{q_t+\tilde{\Lambda}^{-1}}$$

$$\tilde{\Lambda} = \frac{2}{i\omega_0\mu_0}Z = \left((\varepsilon\Lambda)^{-1} + \frac{i\omega_0\mu_0\sigma_n d}{2}\right)^{-1}$$

$\tilde{\Lambda}$ is an effective penetration depth renormalized by the normal currents (Fig.3.3).

Back in real space, the film current distributions are

$$\vec{K}_S(\rho) = I_d\int_0^\infty dq_t\ q_t\frac{F(\rho)}{Z_S\left[\frac{1}{Z_S}+\frac{1}{Z_N}\right]+\frac{2Z_S}{i\omega_0\mu_0}q_t}\ \hat{\varphi}$$

$$\vec{K}_N(\rho) = I_d\int_0^\infty dq_t\ q_t\frac{F(\rho)}{Z_N\left[\frac{1}{Z_S}+\frac{1}{Z_N}\right]+\frac{2Z_N}{i\omega_0\mu_0}q_t}\ \hat{\varphi}$$

with

$$F(\rho) = \exp[-q_t h_d]J_1(q_t\rho)R_d\ J_1(q_t R_d)\ \frac{1-\exp[-q_t N_d\ \delta h_d]}{1-\exp[-q_t\delta h_d]}$$

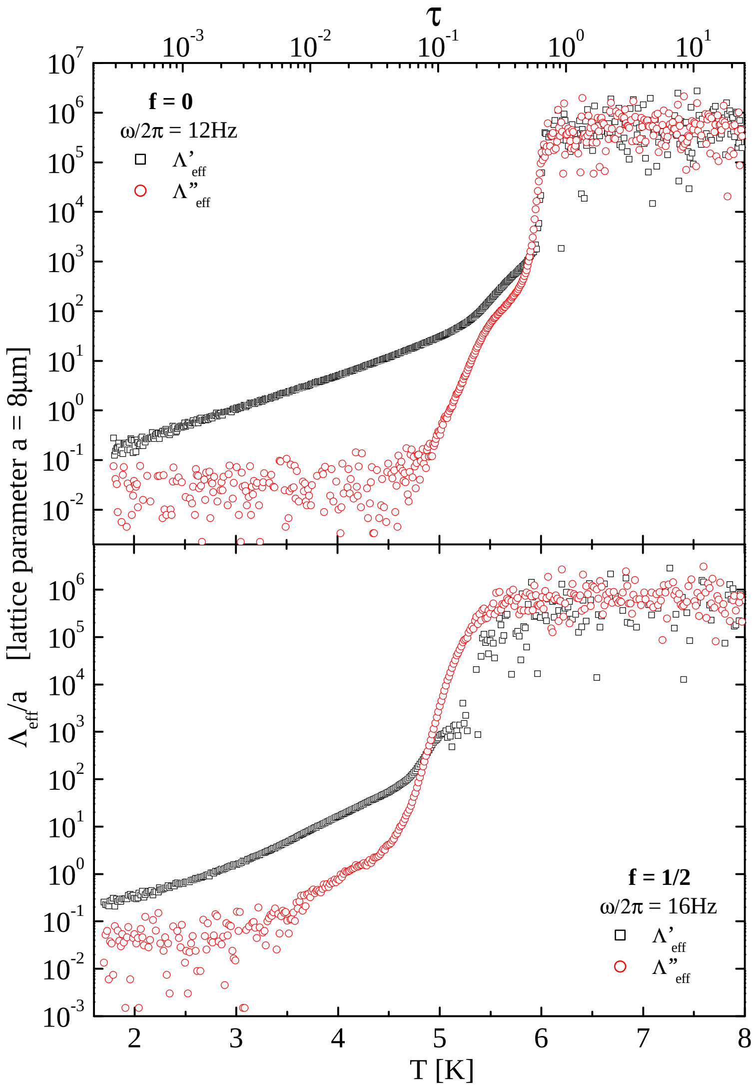

Figure 3.3: [sample2] Temperature dependence of the effective penetration depth $\Lambda_{eff} \equiv \tilde{\Lambda}$ (real $\tilde{\Lambda}'$ and imaginary $\tilde{\Lambda}''$ components) measured at low frequency. The quantitative difference between the unfrustrated state $f = 0$ (top) and the fully frustrated state $f = 1/2$ (bottom) lies in the intermediate temperature range; $3.5K < T < 6K \leftrightarrow 10^{-2} < \tau < 1$.

At low temperature the sample behaves as a pure inductor, $Z_S = i\omega_0 L_J$ and

$$\vec{K}_S(\rho)\,|_{T<<T_c} \approx I_d \int_0^\infty dq_t \; q_t \frac{F(\rho)}{1+\dfrac{2L_J}{\mu_0}q_t}\;\hat{\varphi}$$

is much bigger than K_N since $Z_N/Z_S \geq 1$.

At high temperature $(T > T_c)$

$$\vec{K}_N(\rho)\,|_{T>T_c} \approx I_d \int_0^\infty dq_t\; q_t \frac{F(\rho)}{1+\dfrac{2R_N}{i\omega_0\mu_0}q_t}\;\hat{\varphi}$$

which is much bigger than K_S. Fig.3.4 shows the radial distribution of K_S and K_N at low temperature and high temperature respectively. The high temperature regime is dominated by $Z_N \equiv R_N$. In that case, K_N is complex with a major imaginary component, i.e. essentially dissipative. The radial distributions of K_S at low temperature and of $Im\{K_N\}$ at high temperature share the same appearance and maximum at $\rho \cong R_d \cong 2mm$, while $Re\{K_N\}$ does not behave in the same way close to the sample border $(\rho = 5mm)$.

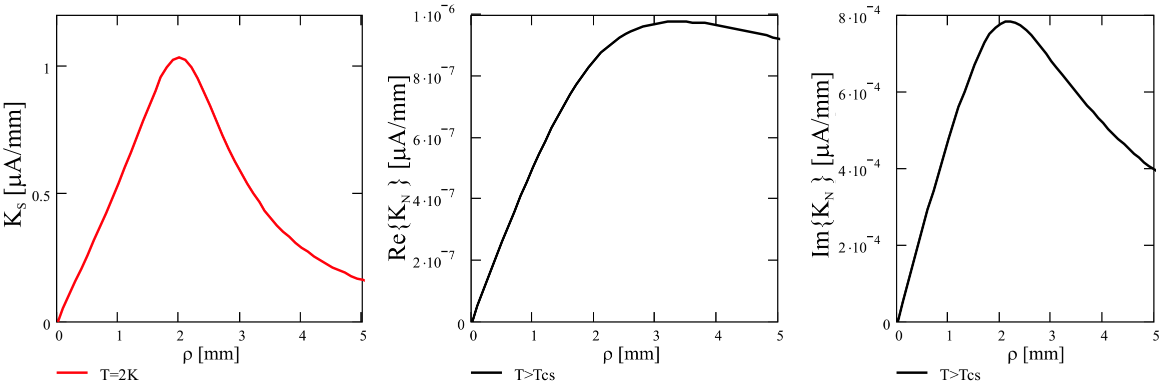

Figure 3.4: Radial sheet current density distributions ($I_d = 0.5\mu A_{rms}$). Left side (red curve): superconducting current distribution at fixed low temperature (T=2K) where $Z \equiv Z_S = i\omega_0 L_J$. Right side (black curves): normal current distribution (real and imaginary components) in the normal state $(T > T_c)$ where $Z \equiv Z_N = R_N$.

Once we find $\hat{A}(q_x, q_y, z = 0, \omega)$, we put it back into the equation for $\hat{A}(\vec{q}, \omega)$ without taking the drive current $\vec{j}_d$ into account, since the corresponding $\vec{A}_d$ is compensated by both the lower and the upper receive coils (gradiometer). The flux induced in the receive coil and hence the mutual inductance change are obtained by the linear integral of $\hat{A}(q_t, z = h_r + l\delta h_r, \omega)$ over $N_R/2$ turns of the lower detection coil. Because of the astatic configuration of the receive coils, the upper receive coil reduces the signal by a factor $(1 - \exp[-q_t\delta])$ $(\delta = h_{r2} - h_r$ is the distance between the bottom of the lower receive coil and the bottom of the upper receive coil).

$$\delta M(Z) = \int_0^\infty dq_t \, \frac{\tilde{M}(q_t)}{1 + \dfrac{2q_t}{i\omega_0\mu_0} Z} \tag{3.3}$$

where the function $\tilde{M}(q_t)$ contains all the geometrical parameters

$$\tilde{M}(q_t) = \pi\mu_0 \; F_d(q_t) F_r(q_t) \; \exp[-q_t(h_r + h_d)] \cdot (1 - \exp[-q_t\delta])$$

$$F_\alpha(q_t) = R_\alpha \; J_1(q_t R_\alpha) \; \frac{1 - \exp[-q_t N_\alpha \; \delta h_\alpha]}{1 - \exp[-q_t \delta h_\alpha]} \qquad \alpha \equiv drive, receive$$

As one can see from the expression above, unlike the usual experimental methods using four probe contacts where the voltage is proportional to Z, the signal is here a function of Z^{-1} (see also 3.2.4). That means that the smaller the impedance the larger the signal. Nevertheless, it is necessary to invert the integral relation to extract the information contained in M.

As introduced in section 1.2.4, the sheet impedance can be written $Z = R_Z + i\omega L_Z$. The imaginary (or inductive) component is related to the kinetic inductance renormalized by the vortices, whereas the real component involves all the dissipative process (vortex and quasi-particle induced dissipations).

$$\delta M' = \int_0^\infty dq_t \, \frac{\tilde{M}(q_t)}{\left(1 + \dfrac{2q_t L_Z}{\mu_0}\right)^2 + \left(\dfrac{2q_t R_Z}{\omega_0\mu_0}\right)^2} \left(1 + \frac{2q_t L_Z}{\mu_0}\right) \tag{3.4}$$

$$\delta M'' = \int_0^\infty dq_t \, \frac{\tilde{M}(q_t)}{\left(1 + \dfrac{2q_t L_Z}{\mu_0}\right)^2 + \left(\dfrac{2q_t R_Z}{\omega_0\mu_0}\right)^2} \left(\frac{2q_t R_Z}{\omega_0\mu_0}\right) \tag{3.5}$$

Since the relative positions of the drive and receive coils ($h_d - h_r$) are known within the fabrication resolution, there is only one free parameter in $\tilde{M}(q_t)$: h_r (or h_d) the distance from the sample to the first loop of the receive (or drive) coil, which must be determined experimentally with a calibration procedure. Fig.3.5 shows how this parameter acts on the mutual inductance distribution $\tilde{M}$.

3.2.3 Calibration procedure

In order to determine the height h_r we consider the total change of the signal M_{ss} between the normal state (no screening) and the diamagnetic state (full screening)

$$M_{ss} \overset{def}{=} \delta M(T << T_{cs}) - \delta M(T > T_{cs})$$

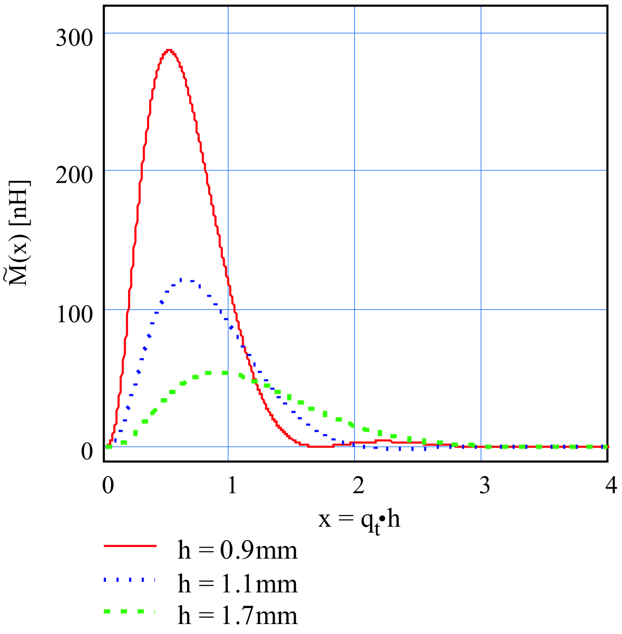

Figure 3.5: Geometrical function $\tilde{M}$ (spectral response function) versus the transverse Fourier component $q_t\times\, h$. $(h = h_r + h_d)$. The coils must be as close as possible to the sample to maximize the response. For the calibrated value $h = 0.9mm$, the signal is peaked at $x_p \cong 0.54$ which means that the coil system is most sensitive to a distribution current peaked at $r = 1/x_p \cong R_D$.

On one hand, M_{ss} is extracted from a measurement of a lead (Pb) thin film (see Fig.3.6) at sufficiently low frequency for which the contribution of the normal currents to the inductive component of the signal can be neglected. On the other hand, in the normal state, the impedance is purely ohmic, $Z \equiv R_N \sim m\Omega$, and at sufficiently low frequency (below $100Hz$) $\delta M' < 10^{-7}M_{ss}$ and $\delta M'' < 10^{-3}M_{ss}$ for an ideal compensation of the receive coil (no pick-up signal). Notice that since in the normal state L_Z is not defined, $\delta M'$ is due to the geometrical inductance associated with the normal current distribution. One can then set $\delta M(T > T_{cs})$ to zero. Below the transition temperature the screening effect is perfect since the applied magnetic field is many orders of magnitude smaller than the critical field. Indeed, in a first approach the sample can be considered as a thin disk of radius r and thickness d. If we suppose the applied field to be homogeneous on the sample scale, the demagnetizing factor $\eta = 1 - \pi d/4r \approx 1 - 10^{-5}$ (sample thickness $d = 1000\AA$ and radius $r = 0.5cm$) [98]. The lead (Pb) bulk critical field, $B_c^{Pb}(T = 0) \approx 80mT$, is then reduced by 5 orders of magnitude, whereas the applied magnetic field $B_{appl.}(I_d = 0.5\mu A_{rms}) \sim nT$. In that case, the effective penetration depth $\tilde{\Lambda}$ is zero, hence $Z \equiv Z_S = 0$ and $\delta M(T << T_{cs}) = \int_0^\infty dq_t\tilde{M}(q_t)$.

$$M_{ss} = \delta M(Z = 0) - \delta M(Z = \infty) = \int_0^\infty dq_t\tilde{M}(q_t)$$

As one can guess from Fig.3.5, the integration converges rapidly. One can now determine the parameter h_r in such a way that the integration of $\tilde{M}(h_r)$ leads to the measured value. Coming back to the transfer function (section 3.2.1), the total change of the signal (M_{ss}) corresponds to the voltage (3.2) (see Fig.3.6)

$$V_{ss} = 0.085mV \cdot \frac{M_{ss}\, I_d}{\phi_0} \approx 2.76mV_{rms} \qquad (I_d = 0.5\mu A_{rms})$$

By equating both expressions for M_{ss} one gets the required value h_r and

$$M_{ss} \equiv M(Z=0) = \int_0^{\infty} dq_t \tilde{M}(q_t) \cong 130nH$$

Nevertheless, after this calibration procedure the lead film is changed with a patterned sample and hence the distance h_r will change a little. We will correct the effect of this unavoidable δh_r in the data preparation before the numerical inversion (see appendix D). Fig.3.6 shows an example of a calibration measurement on a lead film and a measurement on a sample (JJA). Both real Re$\{\delta M\}$ and imaginary Im$\{\delta M\}$ components of the mutual

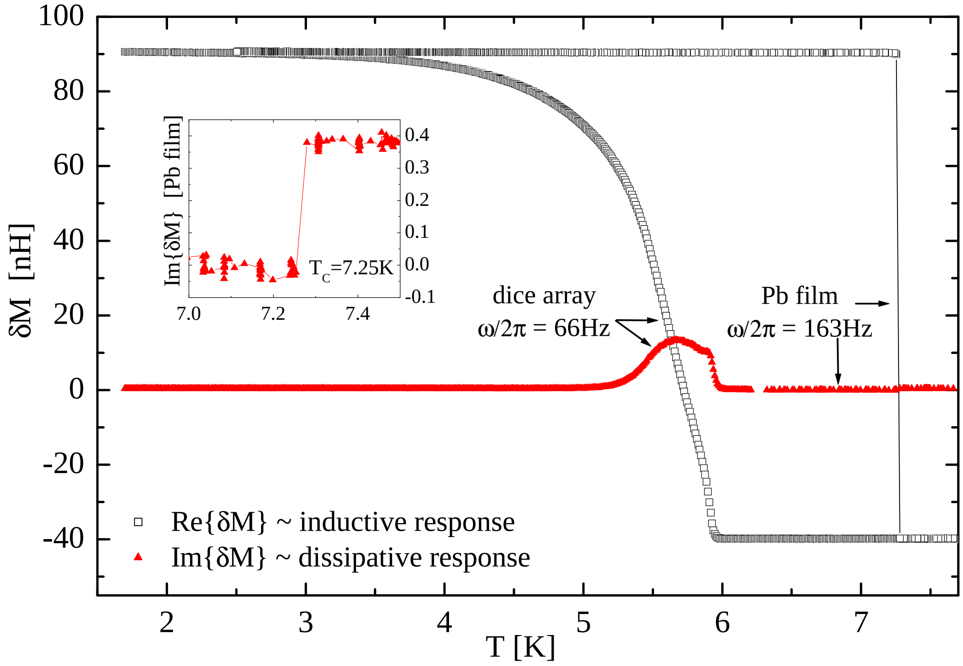

Figure 3.6: [sample2] Temperature dependence of the mutual inductance change in zero magnetic field (raw data). The real component of δM, Re$\{\delta M\}$, mostly reflects the inductive response whereas the imaginary component, Im$\{\delta M\}$, reflects the dissipative response (see section 3.2.4). The inset is a zoom of the Pb film dissipative response in the transition range.

inductance change δM are reported as a function of temperature in zero magnetic field. The phase transition of the lead film takes place at around $7.25K$, whereas the array experiences its transition at a lower temperature. In the case of a Pb film, the superconducting transition is very sharp with a dissipative component going to zero in the low temperature state (see red inset) where the response is purely inductive. In the normal phase eddy currents are measurable at sufficiently high frequency. In the case of an array of JJs, the transition is very smooth with dissipation close to the phase transition. This process also exists in a superconducting film but in a very narrow region which is difficult to observe in a pure material. Notice the non vanishing inductive signal in the normal state, i.e. the *pick-up* signal. The dissipative component gives the derivative of the inductive component [99].

Pick-up signal Since the drive and the receive coils are not perfectly balanced, there is an inductive signal called *pick-up*, even in absence of any sample. This is clearly illustrated in Fig.3.6 where a non zero inductive signal ($Re\{\delta M\}$) is observed in the high temperature phase (the normal state). In that case the *pick-up* is negative, but it could be positive depending on the relative position of the receive and drive coils along their main axis. The large pick-up signal of the coil system ($\sim M_{ss}/3$) is useful to set the phase reference for the measurements (see also Fig.3.7).

3.2.4 Rapid inversion procedure and technique sensitivity

Since the spectral response function $\tilde{M}(q_t)$ is peaked at x_p (see Fig.3.5) one could try to replace it with a delta function $\tilde{M}(x) \cong M_{ss}\delta(x - \langle x\rangle)$ which implies $M_{ss} = \int_0^\infty dx\tilde{M}(x)$.

$$\delta M(Z) \approx \int\limits_0^\infty dx \; \frac{M_{ss}}{1 + \dfrac{2xZ}{i\omega_0\mu_0 h}} \; \delta(x - \langle x\rangle) = \frac{M_{ss}}{1 + \dfrac{2\langle x\rangle Z}{i\omega_0\mu_0 h}} \tag{3.6}$$

where we replaced $x = q_t h$ as is in Fig.3.5 (with such coordinate change $\tilde{M}(x) = \tilde{M}(q_t)/h$). $\langle x\rangle$ is expected to be close to x_p. If $\tilde{M}$ was symmetric versus x_p, then $\langle x\rangle = x_p$. But $\langle x\rangle \cong 0.8$ such that $\tilde{M}(\langle x\rangle) = M_{ss} = 130nH$. This approximation will be the starting point of the numerical inversion procedure used to treat the data. Surprisingly, as far as δM is not too close to M_{ss} (or too small), the correction brought by the numerical inversion is negligible.

The normalized mutual inductance

$$m = m' + m'' = \frac{\delta M(Z)}{M_{ss}} = \frac{V(Z) - V_{pick-up}}{V_{ss}} \approx [1 + Z/i\omega_0 M_c]^{-1} \tag{3.7}$$

where $M_c = \mu_0 h/2\langle x\rangle \cong 1.047\text{nH}$ is the inductance of the current distribution in the film and $V(Z)$ is the two-component signal (X, Y) given by the squid (see Fig.3.6).

This expression leads to a discussion about the intrinsic limits of the measurement technique. The resolution on Z is a function of the characteristic inductance M_c (3.7) which is a function of $\langle x\rangle$. That means that if we decrease the drive coil radius R_d, we shift the Z measurement range. The most favorable situation as far as the resolution in Z is concerned is when $Z/i\omega_0 M_c$ is of the order of one. At low temperature, i.e. in the diamagnetic limit where Z is purely inductive $Z = i\omega_0 L_J$, $\delta M(Z)$ approaches its maximum value M_{ss}. The experimental resolution (signal over noise ratio) allows measurements of a difference between $\delta M(Z)$ and M_{ss} better than one percent (of M_{ss}). That means that L_J/M_c is of the order of $1/100$, and the estimated sensitivity threshold is of the order of $1pH$. In the normal state the sheet impedance is fixed by the normal state sheet resistance $R_N \approx m\Omega$, leading to a signal m of the order of $10^{-6}\omega_0$.

Coming back to the equation (3.6) and using the notation introduced above $Z = i\omega_0 L_Z + R_Z$, the approximate solutions for both components are

$$R_Z = \omega_0\ M_c \frac{m''}{m'^2 + m''^2} = \omega_0 M_c \frac{Y_n}{X_n^2 + Y_n^2} \tag{3.8}$$

$$L_Z = M_c \left(\frac{m'}{m'^2 + m''^2} - 1 \right) = M_c \left(\frac{X_n}{X_n^2 + Y_n^2} - 1 \right) \tag{3.9}$$

where $X_n = (X - pickup)/V_{ss}$ and $Y_n = Y/V_{ss}$ are the normalized voltage components. The inductive component is frequency-independent, but the resolution of the dissipative component is given by R_Z/ω_0.

Normal state

For $T \geq T_{cs}$, $Z = R_N$. Using (3.7), the components of the measured voltage ($V = X + iY$) are

$$X/V_{ss} = \left[1 + \left(\frac{R_N}{\omega_0 M_c} \right)^2 \right]^{-1} + \alpha \qquad Y/V_{ss} = \frac{R_N}{\omega_0 M_c} \cdot \left[1 + \left(\frac{R_N}{\omega_0 M_c} \right)^2 \right]^{-1} \tag{3.10}$$

where the pickup $\alpha = V_{pick-up}/V_{ss}$ is $\alpha \cong -1/3$.

Diamagnetic state

For $T << T_c$, $\omega_0 L_Z << R_Z$, $Z = i\omega_0 L_Z$

$$X/V_{ss} = \left[1 + \frac{L_Z}{M_c} \right]^{-1} + \alpha \qquad Y = 0 \tag{3.11}$$

The imaginary (dissipative) component should be vanishingly small for $T \to 0$ as long as the above expression for Z is valid.

Intermediate temperature range

We call X the inductive component and Y the dissipative component because they measure essentially the superfluid and the dissipative response respectively. But for intermediate temperatures we see from the expressions (3.8) and (3.9) that both components X and Y are included in the expressions of R_Z and L_Z.

$$X/V_{ss} = \frac{\omega_0^2 M_c(M_c + L_Z)}{R_Z^2 + \omega_0^2(M_c + L_Z)^2} + \alpha \qquad Y/V_{ss} = \frac{\omega_0 M_c R_Z}{R_Z^2 + \omega_0^2(M_c + L_Z)^2} \tag{3.12}$$

3.3 Electronic setup linearity

An important and useful feature of a measurement system is its ability to work in a "linear" way. That means that the output signal amplitude is proportional to the input signal amplitude. In our case the lock-in provides the output voltage signal and the input comes from the sample response which is itself, as described in the previous sections, proportional to the excitation current. In order to check for the system behaviour it is important to use a sample for which the response is well known. This is the reason why we used a lead film (see Fig.3.6). Moreover, we are sure to be far from the critical field (see 3.2.3, [98]).

3.3.1 Amplitude dependence

Fig.3.7a) shows that for a given temperature and a fixed frequency the amplitude of the signal is indeed proportional to the drive force (i.e. the drive current) for values well above the excitation current used in this work, i.e. $0.5\mu A_{RMS}$. The same behaviour is observed in the normal and superconducting phases. Fig.3.7b) shows that the phase does not change with the excitation current. Therefore the electronic of the measurement system is linear in amplitude.

3.3.2 Frequency dependence

The signal has a frequency dependence (Figs.3.7a) which is due to the SQUID electronics according to Fig.3.8a). In the intermediate frequency range (range II), the signal is almost frequency-independent. Its increase above 10^3Hz (range III) is due to the resonant circuit of the rf-SQUID. For the highest (range IV) and the lowest (range I) frequencies, the signal over noise ratio may be too small to perform good measurements. These frequency dependencies have no consequence as long as the normalization process (see Appendix D) takes them into account.

On one hand, in the highest frequency range, the pick-up over full signal ratio (Fig.3.8b) exhibits a variation of 3%. According to (3.10) this variation cannot be explained by eddy currents, since the ratio should then be increased and eddy currents cannot induce such an important variation which induces strong effects for measurements near M_{ss}. Indeed, we observed inexplicable behaviours of the resistance and the inverse inductance measured

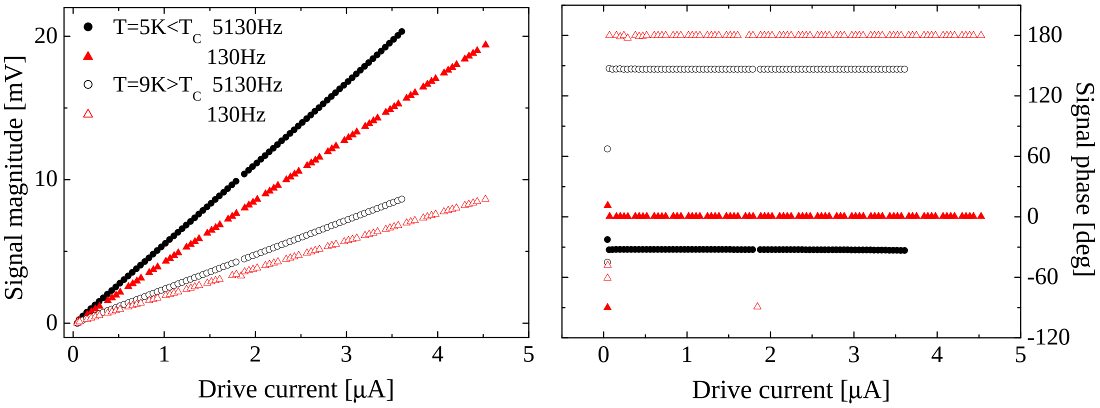

a) b)

Figure 3.7: a) Signal magnitude vs drive current in the superconducting phase ($T < T_C$) and in the normal phase ($T > T_C$) for two different frequencies. b) Related signal phase dependence.

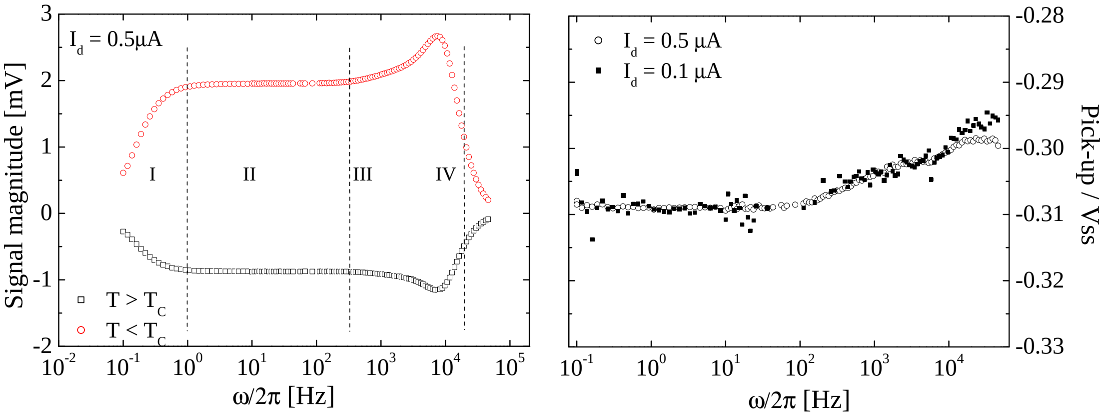

a) b)

Figure 3.8: a) Signal magnitude vs excitation frequency in the SC and normal states. We distinguish 4 frequency ranges (I, II, III and IV) discussed in the text. b) Pick-up over full signal ratio measured for two values of the drive current.

at low temperature and at high frequencies ($\omega/2\pi > 10$KHz). On the other hand, at low frequencies (below one herz), the signal magnitude decrease is due to the amplifier which allows galvanic decoupling between the excitation source (lock-in internal oscillator) and the drive coil. Such a decoupling is necessary to avoid ground loops. We used two kinds of transformers characterized by Figs.3.9.

- a pre-amplifier (model 113 of Princeton Applied Research) used below 4KHz for a typical signal magnitude of 2mV
- a simple transformer 10:1 used above 4KHz

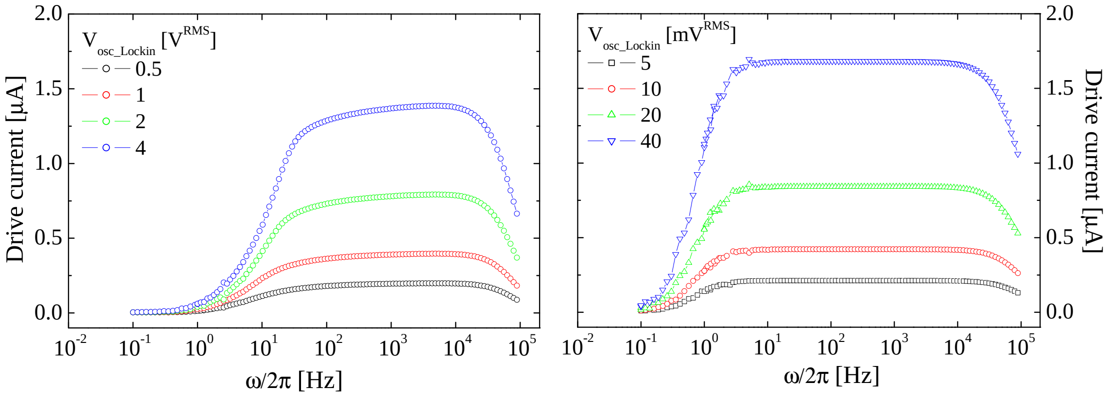

a) b)

Figure 3.9: Frequency dependence of the drive current for various fixed oscillator voltages. a) passive transformer at the output of the lock-in oscillator. b) pre-amplifier model 113.

The drive current has been chosen as low as possible in such a way that the system to be studied is perturbed as less as possible (see section 2.4). But at the same time the resulting output signal should emerge from noise.

3.4 Thermometry

The main elements of the thermometry are the thermometer, which is a GERMISTOR GR-200A-5000 SER.15899 (GRT probe), and the heater made with a resistive wire rolled round a copper braid fixed on the sample holder. The GRT probe is located under the sample holder, inside the sapphire cap, and the heater is fixed around the sample holder, i.e. between the 1K-pot and the sample (see Appendix B and Fig.3.1).
The first measurements were performed with a home made temperature control illustrated in Fig.3.10. The temperature set point is given by the computer to the voltage comparator as a voltage $U(T) = R(T) \cdot I_{GRT} \cdot A$ using the Digital-Analog Converter (DAC) of the lock-in. The resistance $R(T)$ is calculated using Chebichev polynomials (see Tab.3.2), and a constant excitation current I_{GRT} circulates in the GRT probe. The amplification factor A is defined below. In order to use the full scale of the voltage comparator [0-10V], the GRT probe voltage is first amplified (factor B). The voltage difference between the sensor signal and the set point is applied to the current source input through the Gain-Integrator-Differentiator (PID) controller to stabilize the temperature to the set point.

The parameters A, B and I_{GRT} cannot be chosen in an independent way. The current I_{GRT} has to be as low as possible to avoid heating the probe. The dissipated power in the thermometer, at the lowest temperature ($T = 1.5K$), is of the order of $100nW$. The I_{GRT} current value sets the temperature T_R at which the range change of the voltmeter happens, i.e. when the GRT probe resistance becomes higher than the ratio (range/I_{GRT}). But T_R is modified by factor A which is used to eliminate the offset between the set point and the stabilized temperature. The PID parameters are then fixed with the Ziegler-Nichols algorithm [100]. Tab.3.2 shows the set of parameters.
This setup control achieves a temperature stabilization better than $2mK$ below $4K$ and less than $4mK$ below $8K$.

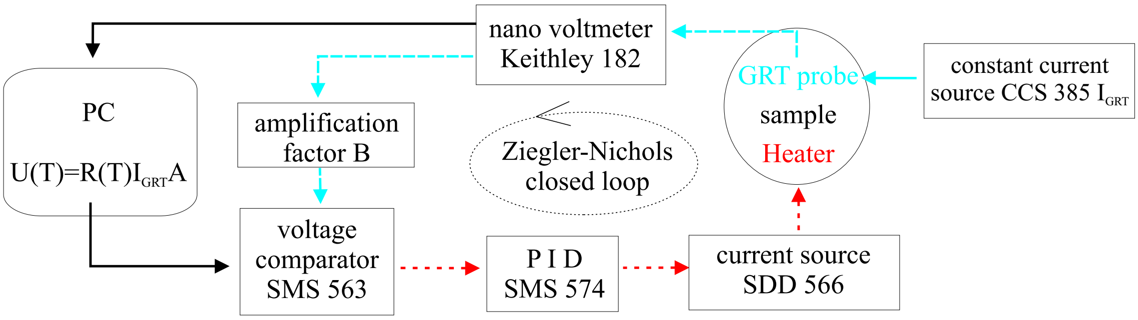

Figure 3.10: Temperature monitoring scheme including an external GPIB link to the computer (PC). See Tab.3.2 for numerical values.

Chebichev coefficients	I_{GRT}	T_R	A and B	PID
$a_0 = 4.3897$ $a_3 = 0.7973$ $a_6 = 0.0467$ $a_1 = 4.4219$ $a_4 = 0.3187$ $a_7 = 0.0152$ $a_2 = 1.9426$ $a_5 = 0.1150$ $a_8 = 0.0101$	$2\mu A$	$4.4K$	$A(T < T_R) = 300$ $A(T \geq T_R) = 2990$ $B = 30$	$P = 2.5$ $5s \leq I \leq 10s$ $D = OFF$

Table 3.2: Thermometry parameters. See explications for each parameter in text and scheme in Fig.3.10.

Afterwards we used a temperature controller (*Lakeshore DRC 91CA*) which achieves a stabilization at least twice better than the preceding one (less than $1mK$ below $5K$ and less than $2mK$ below $8K$) (see Appendix C).

3.5 Refrigerator system

The system is operating as a standard continuous He-4 evaporation refrigerator. The sample holder is thermally decoupled from the 1K-pot with white delrin cylinders and it is cooled through two copper wire bridges (see Appendix B and Fig.3.1). It should be emphasized that the cryostat used for these measurements was fabricated during the Ph.D.

thesis of Dr. R. Théron [58].
The 1K-pot (evaporator) has a cylindrical volume of about $20cm^3$ filled with He-4 from the liquid helium bath trough a $30cm$ long impedance. The equilibrium temperature is a few mK above the helium bath temperature ($4.2K$) indicating a negligible heat load. When the evaporator is pumped at a constant flow rate, i.e. at constant pressure, it maintains a constant temperature as a function of the power dissipated in the evaporator, up to some critical value [101]. The main characteristics of the refrigerator are the minimum stable equilibrium temperature, $1.6K$ in our case, and the maximum thermal overload in continuous operation. Fig.3.11 shows the temperature at equilibrium and during an overload for a few flow rates as a function of the heat power. For such a measurement, the heat power should be applied directly to the 1K-pot and the thermometer should be located inside it. Since we do not have such a configuration, we applied the heat power to three different heaters. The first one is rolled round the 1K-pot, the second one is on the sample holder and finally the third one is under the sapphire capsule in which the thermometer is located. Notice that the heater used for the measurements was the one located on the sample holder. If the heat power is increased, then the temperature remains unchanged until the *cooling power* is reached. The right inset of Fig.3.11 shows the effect of the relative position of the heater and the cold plate on the cooling power.

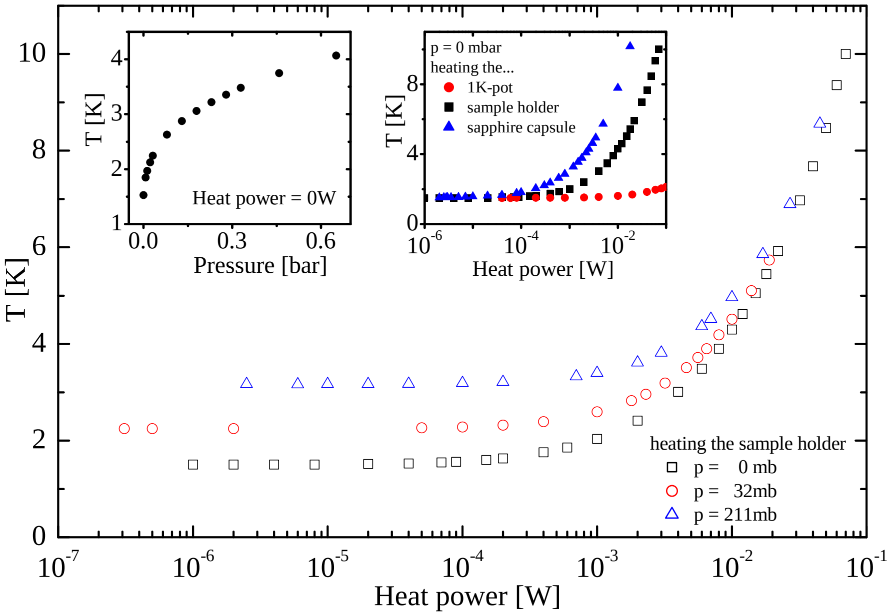

Figure 3.11: Temperature measured near the sample as a function of the heat power for three different pumping pressures. Left inset : temperature versus pressure without heating. Right inset : temperature versus heat power at the lowest pressure using three different heaters located farer and farer from the thermometer.

The 1K-pot and the measurement system are enclosed in a cylindrical pot (Inner Vacuum Chamber - IVC, see Appendix B) which is pumped to decouple the sample from the external helium bath. In order to decrease the time necessary to cool down the sample from 290K to 4.2K, we made a carbon sorb (with its own heater) which was fixed under the 1K-pot. With only $\sim 1-3mb$ pure He exchange gas inside the IVC the cooling down delay is reduced by a factor of 4 (3 hours instead of a whole night).

Dewar The dewar has a capacity of about 40 liters which allows continuous refrigeration for more than 5 days before refilling it with liquid He-4. The rate of evaporation is about 0.25L per hour when the magnetic field switch is closed (not heated) and 0.35L per hour if it is heated (see section 3.6).

3.6 Magnetic field

The frustration coil (FC) is made with a superconducting wire (NbTi, $diam. = 200\mu m$) rolled round the inner vacuum chamber (see Fig.3.2). The six layer coil of 426 loops has an inner diameter of $4.2cm$ and a length of $10cm$. The induced magnetic field is $285mG/mA$, which means that in the case of our JJAs, whose basic cell area is $S_{BC} \cong 55\mu m^2$, a vortex density $f = 1$ is reached with a magnetic field of $\sim 370mG$. The sample is located at the center of the frustration coil whose field homogeneity over its radius is B(center)/B(radius)$\cong$ 1.015 [102] and frustration coil inductance $L_{FC} \cong 0.1H$. The estimated homogeneity of the field over the sample length is better than 1 part in 10^4.
Since we expect sharp frustration structures, we need to fix the frustration without further deviations. This is the reason why we use a SC switch. It was necessary to replace the initial mechanical switch with a thermic one, in order that the applied frustration does not change once the switch is closed. The thermic switch allows interruption of the superconducting circuit by heating a segment of it, as illustrated in Fig.3.12. The welding resistance R must be zero in order to maintain the magnetic energy stored in the frustration coil. Figs.3.13 illustrate a bad point welding. In less than 10 minutes, the frustration

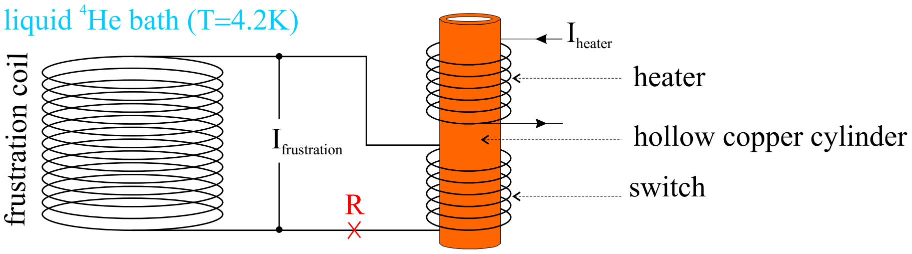

Figure 3.12: Superconducting frustration circuit (frustration coil-switch). Heater (manganin): $R(290K) \cong 270\Omega$. Switch on with $I_{heater} \geq 22mA (P \cong 120mW)$. The red cross (R) illustrates the point welding closing the SC circuit.

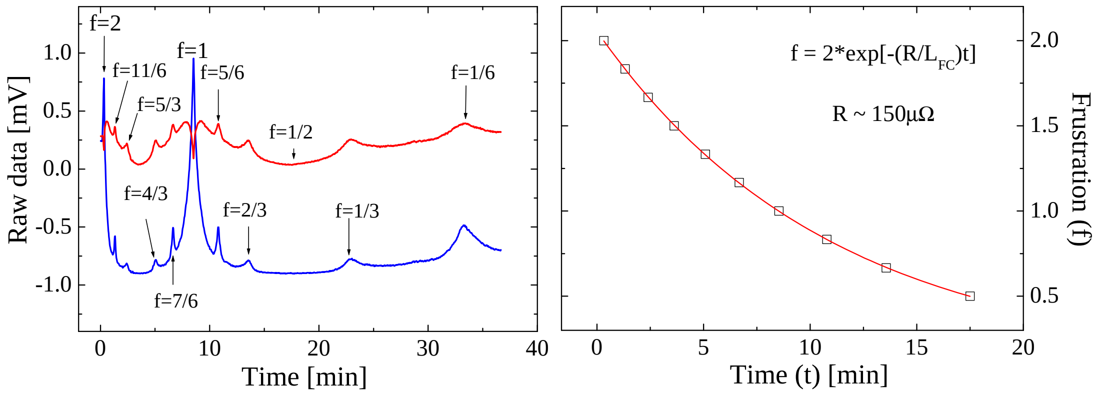

a) b)

Figure 3.13: Energy loss in the frustration circuit. a) raw inductive and dissipative components versus time once the switch has been closed at $f = 2$. b) frustration versus time. The characteristic time of the exponential energy loss is $L_{FC}/R \cong 656 sec$. With the frustration coil inductance $L_{FC} = 0.1 H$, the resistance $R \cong 150 \mu\Omega$ which is enough to lose quickly the magnetic energy stored in the frustration coil.

decreases from $f = 2$ to $f = 1$. In this example, the resistance of the welding point was only $R \cong 150\mu\Omega$ but it was sufficient to forbid any measurements at fixed f.

Finally we succeed with a switch that provides a stabilization of the signal for more than 18 hours.

3.7 Magnetic Screening

Looking for the best way to screen the samples from external magnetic fields, we observed how the residual field can more or less modify the dynamics of the JJAs at low frustration ($f \leq 1\%$). The first magnetic screen is a double μ-metal cylinder inside which the dewar stays. At the sample level, the ambient magnetic field is reduced by a factor $B(outside)/B(inside) \approx 50$.

The quality of the magnetic screening can be well characterized using a JJA as a probe. The response has been measured as a function of the applied magnetic field, i.e. versus the frustration. In such a measurement, rational f values give rise to a peak in the inductive response which corresponds to a local minimum in the dissipative component, in peculiar at zero frustration ($f = 0$).

The first information is given by the value of the applied magnetic field B_a which corresponds to the unfrustrated ($f = 0$) peak in the inductive component, or to the minimum of the corresponding dip in the dissipative response, (see Fig.3.14). This peculiar value of B_a is called *offset* and is due to the residual field around the sample. Nevertheless, if this residual field is homogeneous over the sample area, we can compensate it using the frustration coil (at least as long as the perpendicular direction to the sample plane is concerned).

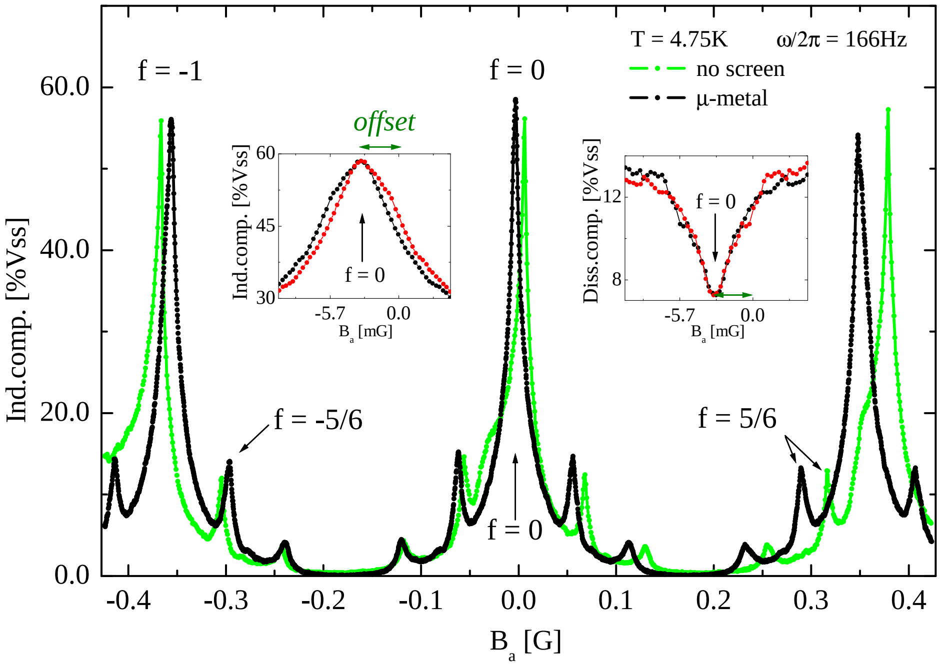

Figure 3.14: Inductive component normalized with respect to the maximum signal V_{ss} versus the applied field B_a at 4.75K and a frequency of 166Hz. The green curve has been measured without any screening around the frustration coil (FC) except the external μ-metal cylinder. Notice that the peaks at integer values of f ($f = \pm 1$ and $f = 0$) show an asymmetric structure while this effect is not observed at $f = \pm 5/6$, for example. The black curve has been measured with a thin μ-metal sheet rolled round the FC. Insets: inductive and dissipative components close to $f = 0$. The red curves are reversed versus the position of the peak/dip. The green asymmetric structure is reduced to the small one shown in the insets. The asymmetry is still present, showing how JJAs are sensitive to frustration effects.

A second information about the magnetic screening is given by the symmetry of the structures. Fig.3.14 shows how the asymmetry of the structures at $f = 0$ or $f = \pm 1$ may be cancelled by a μ-metal sheet rolled over the frustration coil. These asymmetric structures are the signature of an inhomogeneous residual field. The insets of Fig.3.14 show how symmetric the structure is at $f = 0$ when we use the μ-metal screen. The asymmetry of the peaks at $f = 0$ and at $f = 1$ is more pronounced than the one at $f = -1$, no matter how we cooled down the system (fast field cooling, slow field cooling or zero field cooling at $f = -1$ or $f = 0$). We used a Hall probe to detect the presence of any magnetic material

around the sample. The only variation of the probe up to 10mGauss was measured close to the stainless steel disc above the 1-K pot in the vicinity of the soldered joints.
First observation (step 1) : *the μ-metal screen allows much more symmetric frustration structures, i.e. more homogeneous field.*

There is another kind of measurement which gives a lot of information about the magnetic screening, i.e. the temperature measurement. Fig.3.15 shows the temperature dependence of the dissipative component for a few frustrations close to $f = 0$. We clearly observe the appearance of an additional dissipative response which manifests as a broad peak that we will call a *bump* to distinguish it from the thinner peak at higher temperature.

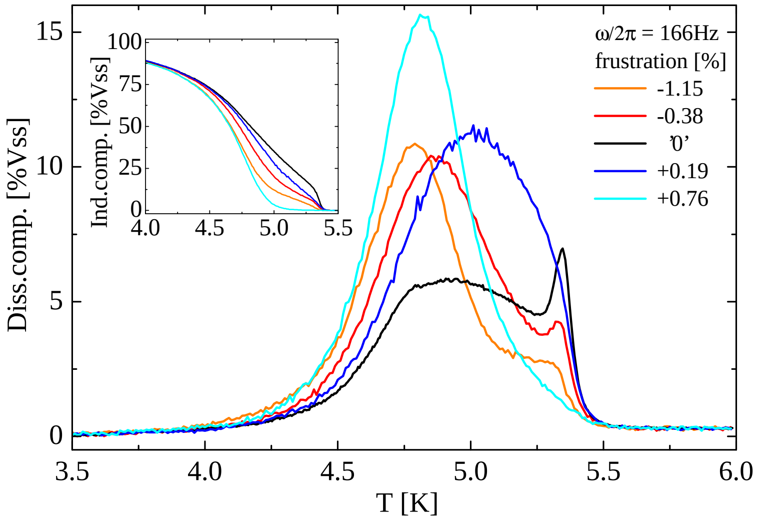

Figure 3.15: Temperature dependence of the dissipative component (raw data) at a fixed frequency of 166Hz and at a few frustrations around the best $f = 0$ (black curve). No magnetic screening except the external μ-metal cylinder. Notice how the bump varies with changing f, whereas the peak does not move. Inset: Inductive component.

It seems that these temperature measurements are in agreement with the previous frustration curves (Fig.3.14), in the case of no magnetic screens. In Fig.3.15, the black curve was measured around $f = 0$. Starting with $f = -1.15\%$, and going to the "$f = 0$" black curve, the bump becomes flatter and the peak appears. Then, increasing f from "zero" to $+0.76\%$, the peak is absorbed by the bump which becomes higher and thinner with increasing frustration. We observe that the evolution of these peaked and bumped structures is not symmetric with respect to the "$f = 0$" curve: this is related to the asymmetric structure of the $f = 0$ peak in the frustration measurements (Fig.3.14).
The same observation is valid for the inductive component shown in the inset of Fig.3.15. In the case of the positive frustration $f = +0.76\%$, the inductive component is still zero whereas it is finite for the largest negative $f = -1.15\%$. This means that for positive

f values close to zero the inductive component decreases more rapidly than for negative f values. In other words, disorder is established more rapidly with positive f than with negative f (of same absolute value). This is in good agreement with Fig.3.14 (without μ-metal).
At this point the question is "Is one of these dissipative structures representative of the BKT transition and if so, which one ? "
Second observation (step 2) : *Since the peak emerged from the bump, we tried to go further in reducing the bump as much as possible in such a way that the thinner peak becomes prominent.*

Fig.3.16 shows that step 2 is not realized with a μ-metal screen rolled round the frustration coil. On the one hand, we observed that the μ-metal screen enhances the symmetry of the frustration structure at $f = 0$ (Fig.3.14) but on the other hand, the temperature measurements show how the peak disappears inside the bump.

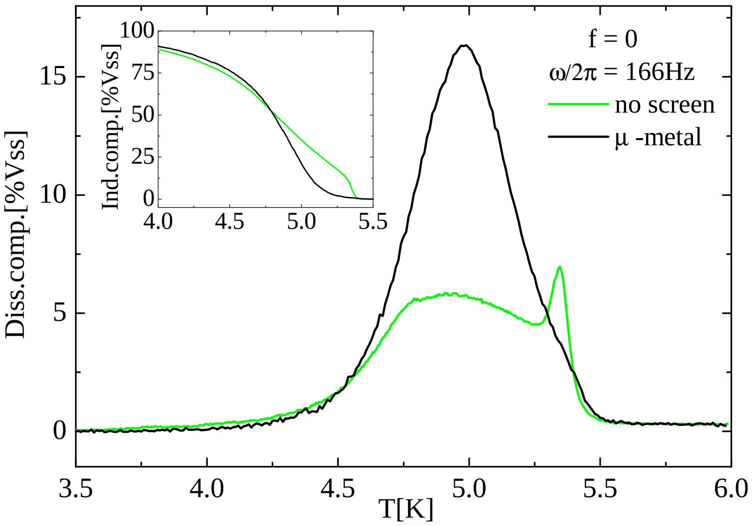

Figure 3.16: Effect of the μ-metal screen on the temperature dependence of the dissipative and inductive (inset) components.

We then fixed the frustration to the best '$f = 0$' and we measured the temperature dependence of the signal for a few frequencies in four decades between 1Hz and 10KHz (see Figs.3.17). We clearly observe a dissociation of both peaks in the dissipative component when decreasing the excitation frequency. It even seems possible to separate both dissipative processes if the frequency were below one hertz. The measurements were performed with open thermic switch, explaining the noisy curve at the lowest frequency (black line at 6Hz). As was mentioned in the calibration section (Fig.3.6), the dissipative component is roughly given by the derivative of the inductive component. This is clearly shown for

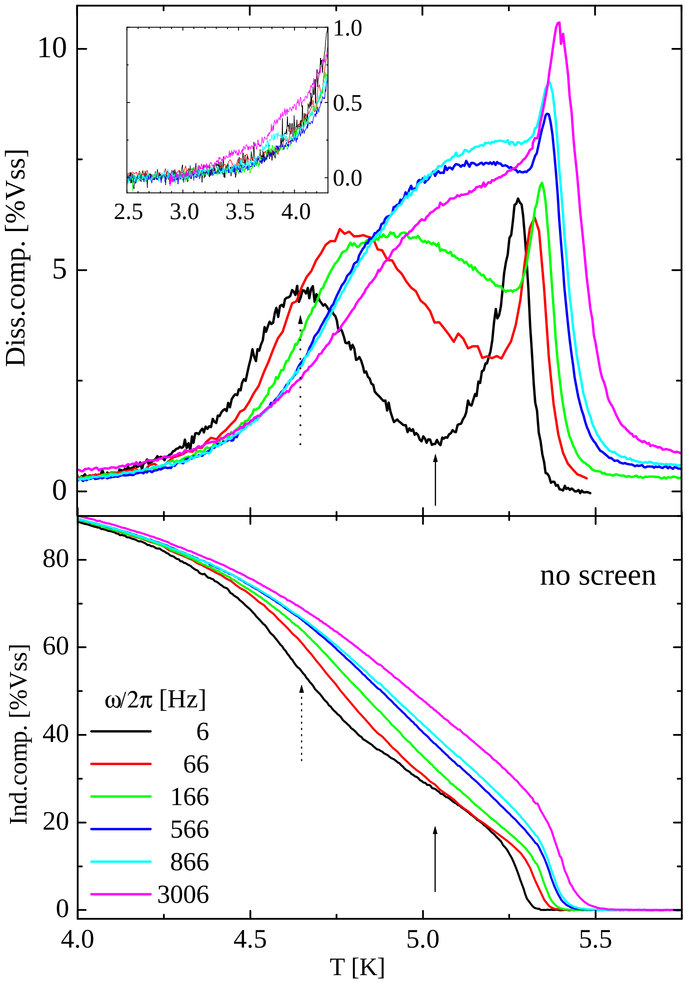

Figure 3.17: Effect of frequency on the temperature dependence of the dissipative (top) and inductive (bottom) components. The inset of the top figure is a zoom of the lowest temperature region.

the lowest frequency, for which the two inflexion points of the inductive component correspond to the position of respectively the maximum of the bump and the minimum in between the bump and the peak of the dissipative component (dotted and solid arrows in Figs.3.17). The dissipative component provides a much more sensitive probe than the inductive one. Indeed other dissipative processes appear at the highest frequencies in the lower temperature range (inset of the top figure), whereas it is almost impossible to observe the associated curvature variations in the inductive components (not illustrated).

We then tried to gain magnetic screening quality by adding a double layer rolled over the μ-metal sheet. This second layer is composed of a thin lead sheet rolled with a thin copper sheet and forms a double spiral in order to avoid the lead sheet forming a closed superconducting surface around the frustration coil. At the same time, the copper sheet provides a Faraday cage against rapid variations of the external magnetic field. This "spiral" magnetic screen results in an important increase of the offset (10 times the usual value) explained by the flux line trapping by the Cu/Pb sheet. The offset has been reduced with a Pb sheet shorter than the μ-metal one.

Finally the configuration that gave the most symmetric and pronounced frustration structures as well as the most prominent peak in the temperature measurement was the one with the Cu/Pb double sheet rolled over the frustration coil and the μ-metal sheet rolled around the Cu/Pb sheet. Fig.3.18 shows a measurement performed with such a configuration. The temperature measurement with the μ-metal sheet on the outside (red curve)

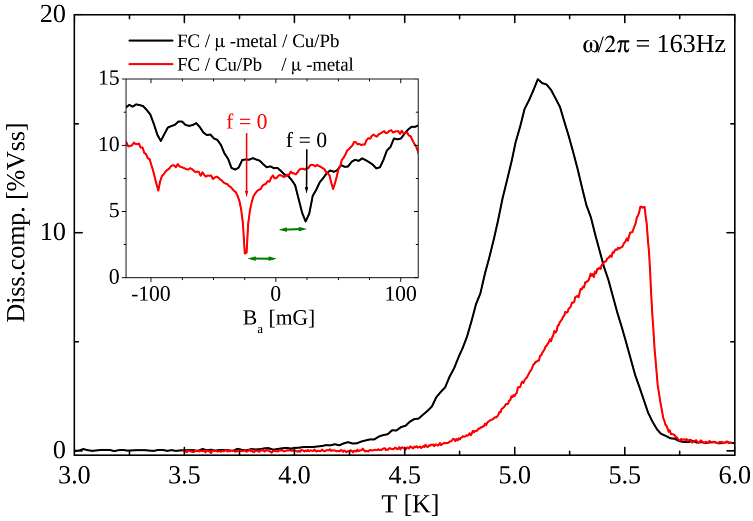

Figure 3.18: Effect of the relative positions of the screens on the temperature and frustration (inset) dependencies of the dissipative raw component. Black curves configuration: frustration coil (FC) then μ-metal sheet and on the outside the Cu/Pb sheet. Red curves configuration: frustration coil (FC) then Cu/Pb sheet and on the outside the μ-metal sheet.

shows that there is still a small amount of inhomogeneous field inside the frustration coil. The transition at $T \cong 5.7K$ is very sharp, but the dissipative signal then decreases slowly with a shoulder below the peak which is a signature of the unsuppressed bump. The inset shows the frustration structures for both relative positions of the magnetic screens. The offsets (green arrows) are almost the same but the structures are much more well defined in the case of the last used configuration (red curve), especially at $f = 0$.

Third observation (step 3) : *the best screening is achieved with a Cu/Pb double sheet rolled over the frustration coil and the μ-metal sheet rolled around the Cu/Pb sheet.*

Additional observation : *a lead (or μ-metal) cylinder closed at the bottom, outside the frustration coil (in the helium bath, in addition to the μ-metal and Cu/Pb sheets rolled round the FC), does not provide better magnetic screening. On the contrary, it traps much more flux, resulting in a large offset, and induces a lot of noise. This is the reason why we suppose that the source of the residual field is close to the sample, i.e. somewhere in between the sample and the previously mentioned lead cylinder. But the source is still unknown.*

Experimentally based conclusions

Even with the best magnetic screening, the sample is still exposed to an inhomogeneous residual field. The effect of this residual field is clearly observable when the applied field (B_a) is very small. Two distinct dissipative processes are observed: one of them, the bump, strongly varies with B_a, whereas the second, the peak, seems to be intrinsic to the sample.

3.7.1 Resistive transition and superfluid density near zero field

The phenomena observed with the previous raw data are reflected in the behaviour of the sheet resistance and the inverse inductance extracted from the same measurements and illustrated in Figs.3.19. The bump observed in the dissipative raw data is reflected as a shoulder in the sheet resistance and a depression of the superfluid density. With decreasing frequency the dissipative shoulder becomes more prominent because the low temperature resistance plateau is also decreased. The inset is a plot of the intersections between the (zero frequency) BKT predicted critical temperature and the frequency dependent inverse inductances [22]. We first note that the static BKT prediction intercepts the inductance curves before they drop down, which is something unusual. For $\omega \rightarrow 0$, $\tau_c(\omega)$ is expected to tend to the BKT transition temperature which, for the unfrustrated dice lattice, can be estimated using Table 1.1 (see section 1.2.3). From one side, applying the linearity relation between τ_c and L^{-1} [22], the ratio between the critical temperature for two different geometries is equal to the ratio of the relative inverse sheet inductances. For example $\tau_c^{triangular}/\tau_c^{square} = L^{-1}_{triangular}/L^{-1}_{square} = \sqrt{3}$. On the other side, the critical temperatures for such regular lattices have been numerically calculated (see Table 1.1) and give approximately the same ratios. Thus it is possible to use the inductive ratios and for the dice lattice $\tau_c^{dice}(f=0) \approx 1$. The measured $\tau_c(\omega)$ in the zero frequency limit is about half the expected value. This discrepancy may be due to some uncertainty in the determination of the reduced temperature τ, but is certainly due, at least partially, to the additional screening effect of the residual field induced vortices which, increasing the dielectric constant, releases the unbinding of the vortex pairs with largest size r_ω (see section 1.4). The measured $\tau_c(\omega)$ is therefore shifted to lower values. Indeed, measurements performed on other samples, where the raw data dissipative bump is closer to the peak (even at lower frequencies then those of Figs.3.17), show a zero frequency limit of $\tau_c(\omega \rightarrow 0) \approx 0.25$, as illustrated in Fig.3.20. The screening conditions of the first mentioned sample were certainly better.

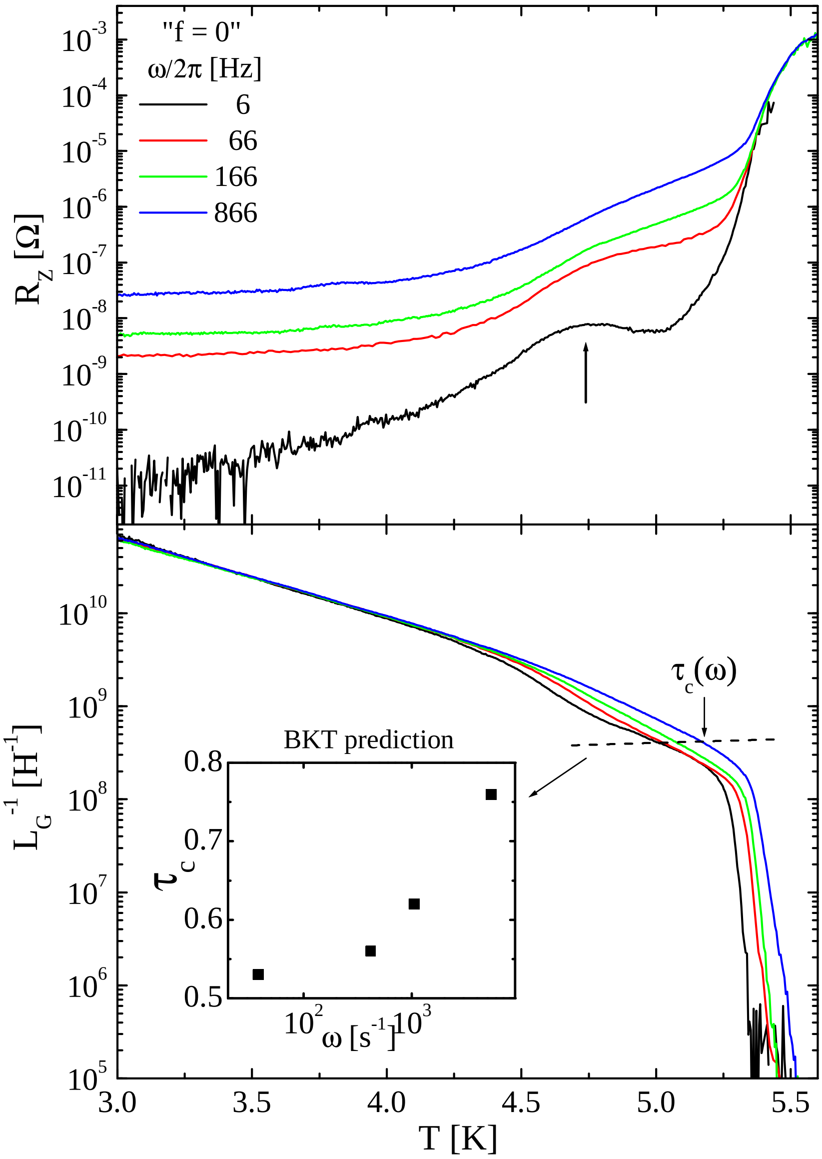

Figure 3.19: Top: resistive transition. The arrow indicates the dissipative process corresponding to the bump in raw data. Bottom: phase coherence disappearance. The inset shows the BKT measured critical temperature versus the excitation frequency ω.

Increasing the frustration results, as was the case in the raw data behaviour, in a unique broader dissipative response. The shoulder in the sheet resistance visible around $f = 0$ (Figs.3.21) disappears, leading to a monotonic resistive transition. The depression around $f = 0$ preceding the jump of the inverse inductance also disappears.

The first dissipative process, the shoulder (or bump), which strongly varies with f, is

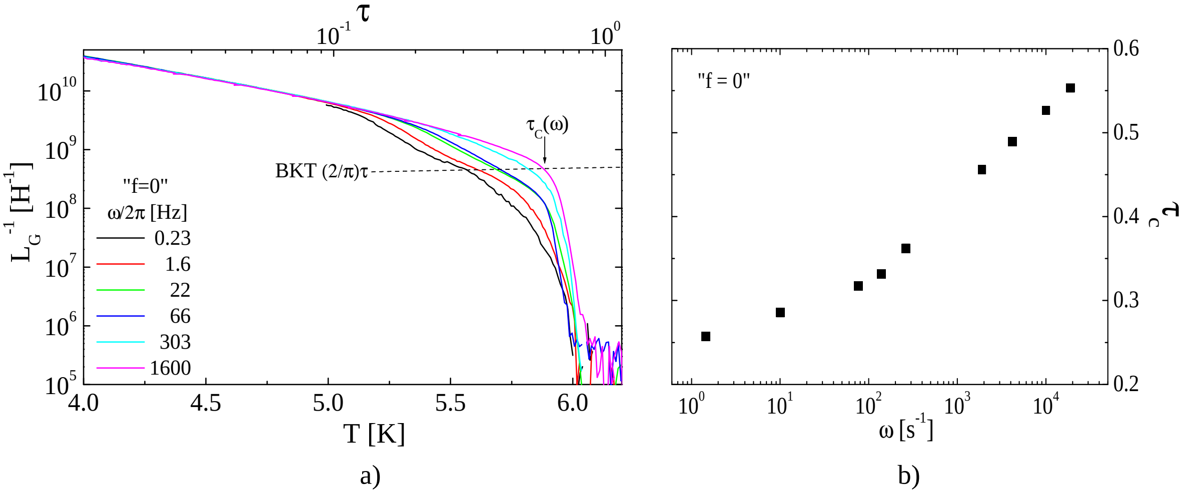

Figure 3.20: [sample2] Unfrustrated state (”$f = 0$”) superfluid density. a) Sheet inverse inductance versus real (bottom axis) and reduced (top axis) temperature. b) BKT critical temperature versus the excitation frequency ω.

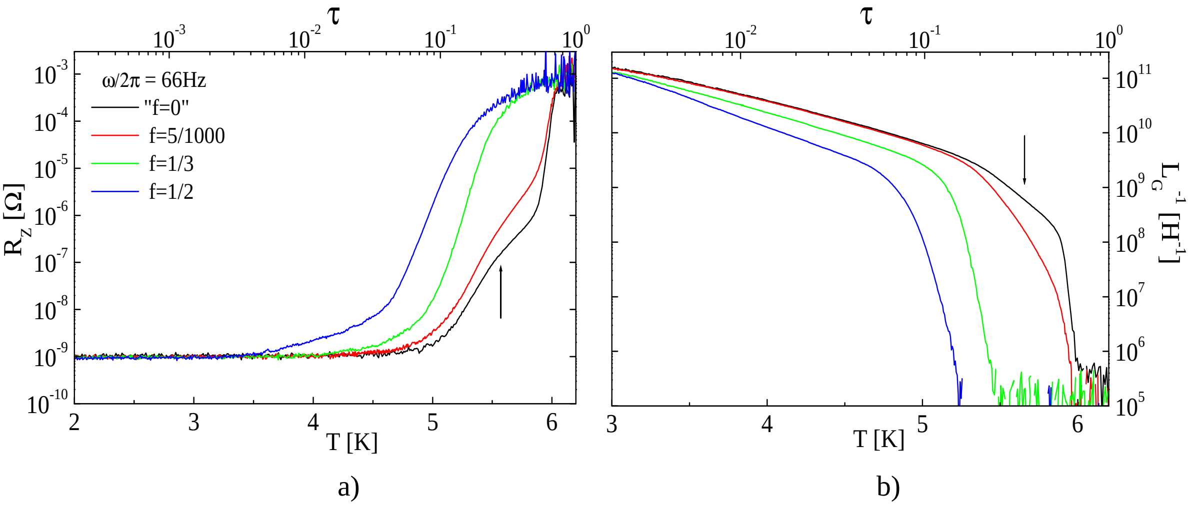

Figure 3.21: [sample2] Frustration dependence of the resistive transition a) and the phase coherence b). The arrows indicate the shoulder discussed in text.

thought to be due to field induced single (non interacting) vortices hopping between neighbouring cells. Since the residual field is inhomogeneous on the sample scale, as illustrated in Fig.3.22, the distribution of these field induced vortices should also be inhomogeneous. At low temperature they are pinned by the lattice potential, but with increasing thermal fluctuations, they are free to be redistributed in the JJA. If such a dynamics is correct, the dissipative shoulder may be due to the motion of this excess of vortices. Nonetheless, this conjecture does not explain the reentrance of the sheet resistance at very low frequency. According to this, the second dissipative process (the peak), which is intrinsic to the sample, should be associated with the BKT transition which results in a very fast variation of the superfluid density (Figs.3.19 and Figs.3.21).

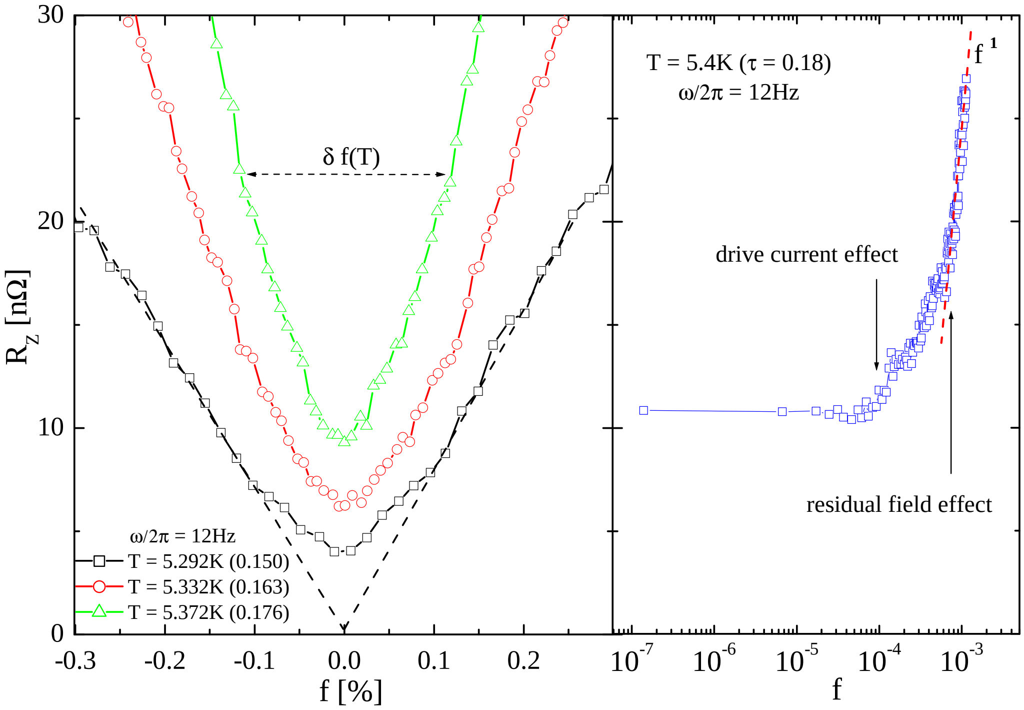

Figure 3.22: [sample2] Magnetoresistance near zero field. Left: deviations from linearity $R_Z(f) \propto f$ and asymmetry $R_Z(-f) \neq R_Z(+f)$ for $f < 10^{-3}$ indicating an inhomogeneous residual field. Right: the drive current ($I_d = 0.5\mu A^{RMS}$) induces a frustration value $f \approx 10^{-4}$.

Chapter 4

Frustrated states

4.1 Frustration structures

The JJA was exposed to an external DC magnetic field in order to observe the various structures in $Z(f)$. Fig.4.1 shows the behaviour of the sheet resistance $R_Z(f)$ and the superfluid density $L_G^{-1}(f)$ when the vortex density f is continuously changed from $f = -1$ to $f = +1$. The symmetry of both components versus $f = 0$, but also versus $f = \pm 1/2$ in the intervals $[0 - \pm 1]$, is related to the symmetry and periodicity properties of the XY Hamiltonian (see section 1.2.2). At the same rational values of f at which the dissipation is depressed, the phase coherence exhibits a peak. These structures are usually attributed to the commensurability between the vortex lattice induced by the applied magnetic field and the underlying array geometry, i.e. the vortex lattice matches the dice lattice. In addition to the unfrustrated state $f = 0$, the vortex densities f for which the structures are the most prominent are $f = 1/3$ and $f = 1/6$. We observe, for these peculiar values of f, a pronounced phase coherence even at the highest temperatures. Surprisingly, at the rational value $f = 1/2$, an absolute maximum of the dissipation is observed and at the same time the phase coherence shows an absolute minimum.

With a lower excitation frequency ($\omega/2\pi = 7.03 Hz$), the measurements of Fig.4.2 show a weak temperature dependence of the sheet resistance and of the inverse sheet inductance at $f = 1/3, 1/6, 1/9$, but a strong temperature dependence at the fully frustrated state $f = 1/2$ whose phase coherence disappears at the highest temperature (even around $f = 1/2$).

Unsurprisingly, an increase in temperature induces an increase in sheet resistance, and at the same time, the disappearance of phase coherence. A frequency variation gives rise to the same effect on the dissipation, but an increase of the frequency, at a fixed temperature, causes the inverse sheet inductance to increase. Fig.4.3 shows very different dynamic aspects between the fully frustrated state and other rational values of the reduced flux (for example $f = 1/3$, $f = 1/6$ or $f = 2/9$).

The sheet resistance $R_Z(f)$ at $f = 1/3, 2/9, 1/6$ strongly increases when the frequency is increased, whereas the fully frustrated state ($f = 1/2$) is less affected by the frequency vari-

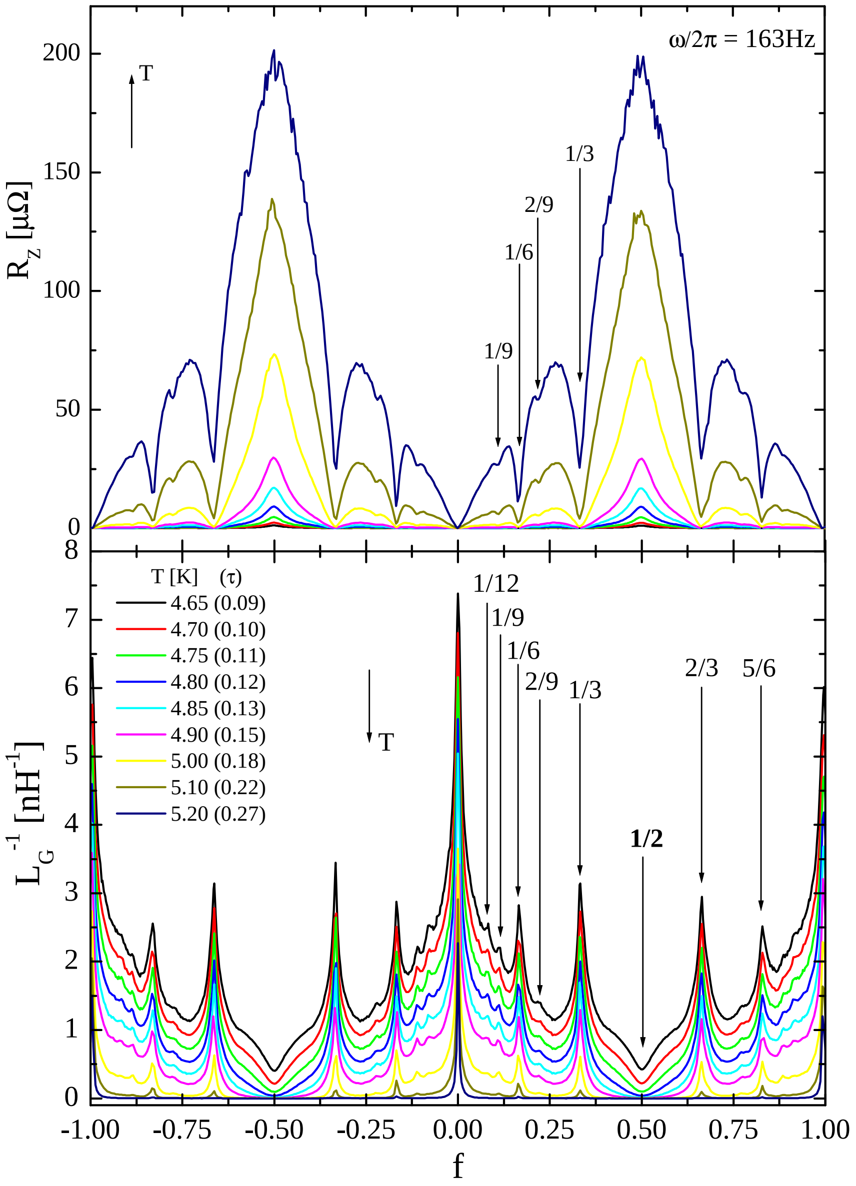

Figure 4.1: [sample1] Top: Magnetoresistance, and Bottom: Inverse magnetoinductance, measured at $\omega/2\pi = 163$Hz in the temperature range $0.09 \leq \tau < 0.3$. The linear scales emphasize the broad dissipation around $f = 1/2$ in $R_Z(f)$ and the commensurate structures in $L_G^{-1}(f)$.

ation. Simultaneously, the phase coherence remains unchanged at $f = 1/3$, but strongly increases at $f = 1/2$. When, at a fixed temperature, the excitation frequency is lowered, the vortex bath is less excited, giving rise to a smaller sheet resistance (due to the vortex motion). At the same time, the vortices (or more generally the topological defects) have

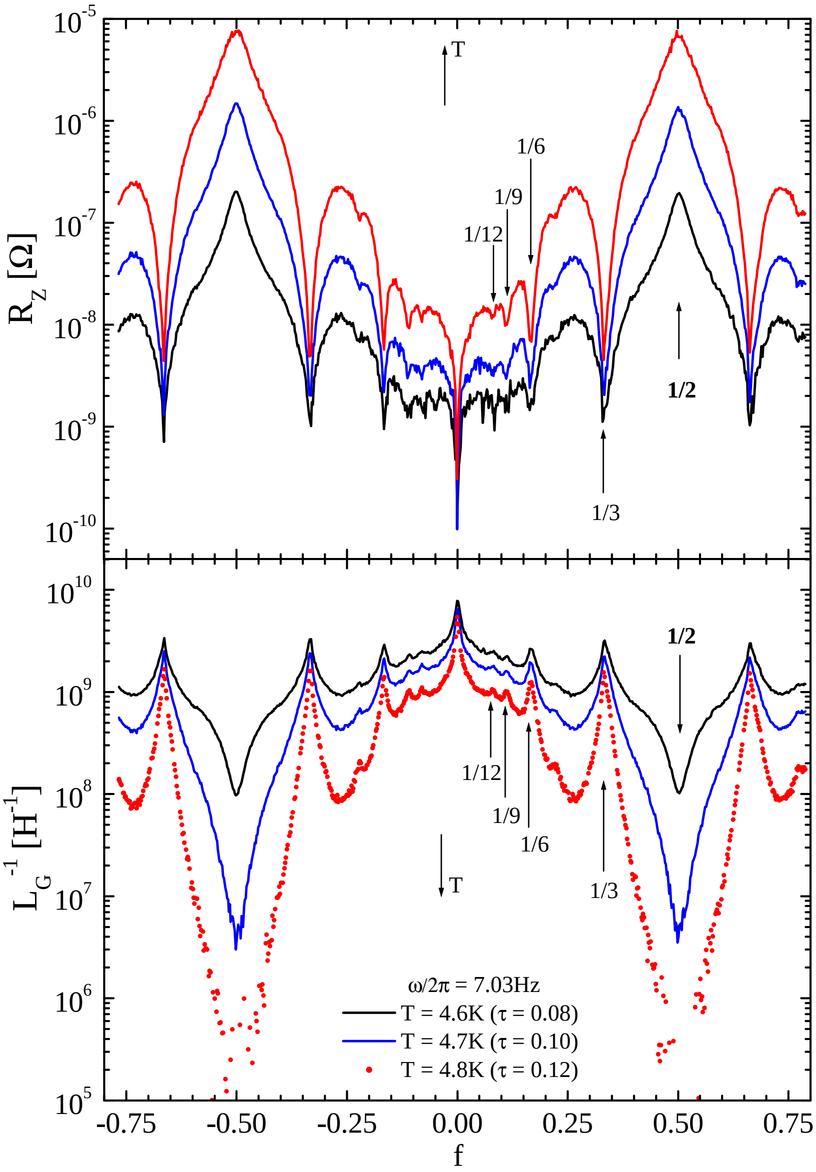

Figure 4.2: [sample1] Top: Magnetoresistance, and Bottom: Inverse magnetoinductance, measured at $\omega/2\pi = 7.03\text{Hz}$. The logarithmic scales emphasize the large amount of dissipation at $f = 1/2$ and the disappearance of the phase coherence around $f = 1/2$.

more time to relax, leading to a decrease of phase coherence. This phenomenon is much more obvious at $f = 1/2$ than at $f = 1/3$.

A more careful observation of the inverse sheet inductance at lower temperatures (Fig.4.4) reveals a large number of structures, for $0 < f < 1/2$, which do not appear in the isotherms of Fig.4.1 and Fig.4.2. At low temperature the smallest structures are more easily iden-

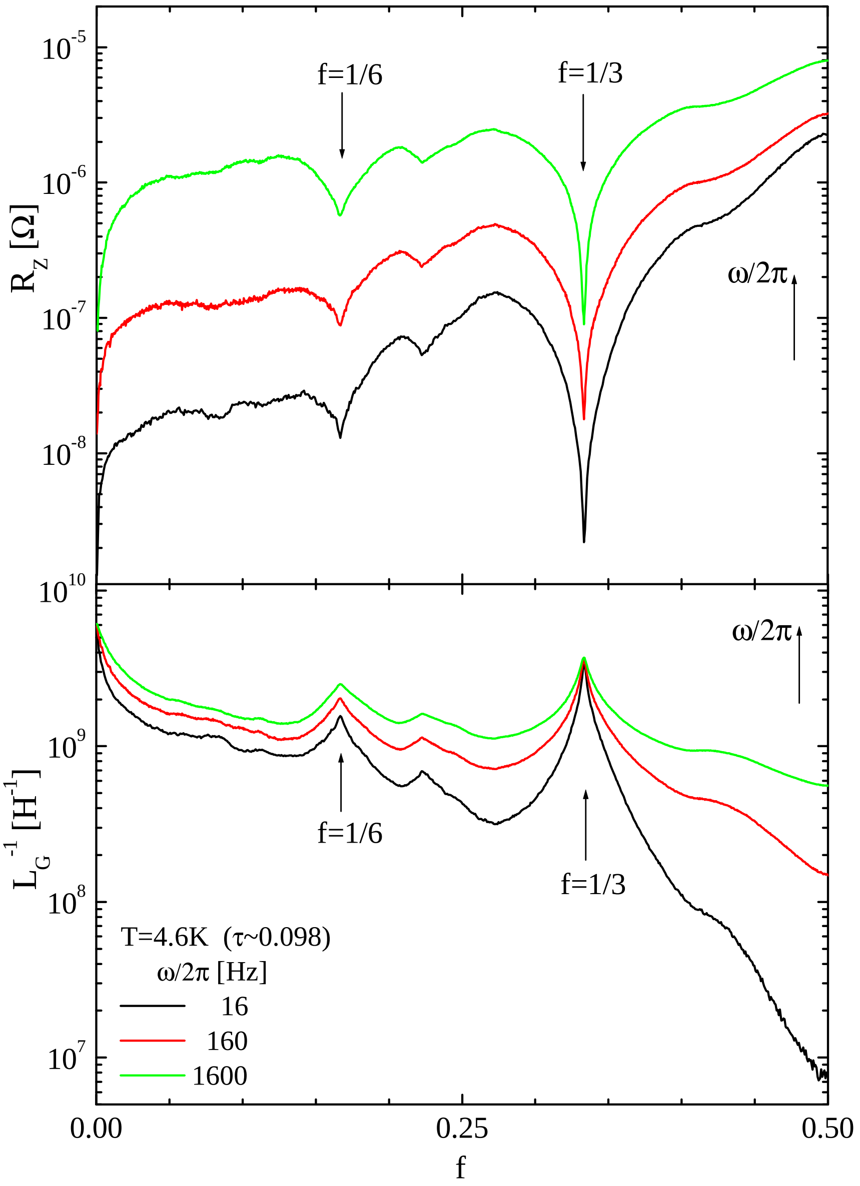

Figure 4.3: [sample3] Excitation frequency effects at different vortex densities. Top: Magnetoresistance, and Bottom: Inverse magnetoinductance, measured at a temperature $\tau \cong 0.098$.

tified in the inverse magnetoinductance than in the magnetoresistance, as illustrated in Fig.4.2. The positions of the observed commensurate structures are listed in the caption of Fig.4.4. The structures appearing for the smallest f values (below $f = 1/12$) are very difficult to observe, even at low temperature and low frequency. Nevertheless it is possible to attribute the presence of a structure to an accumulation of points, since the measure-

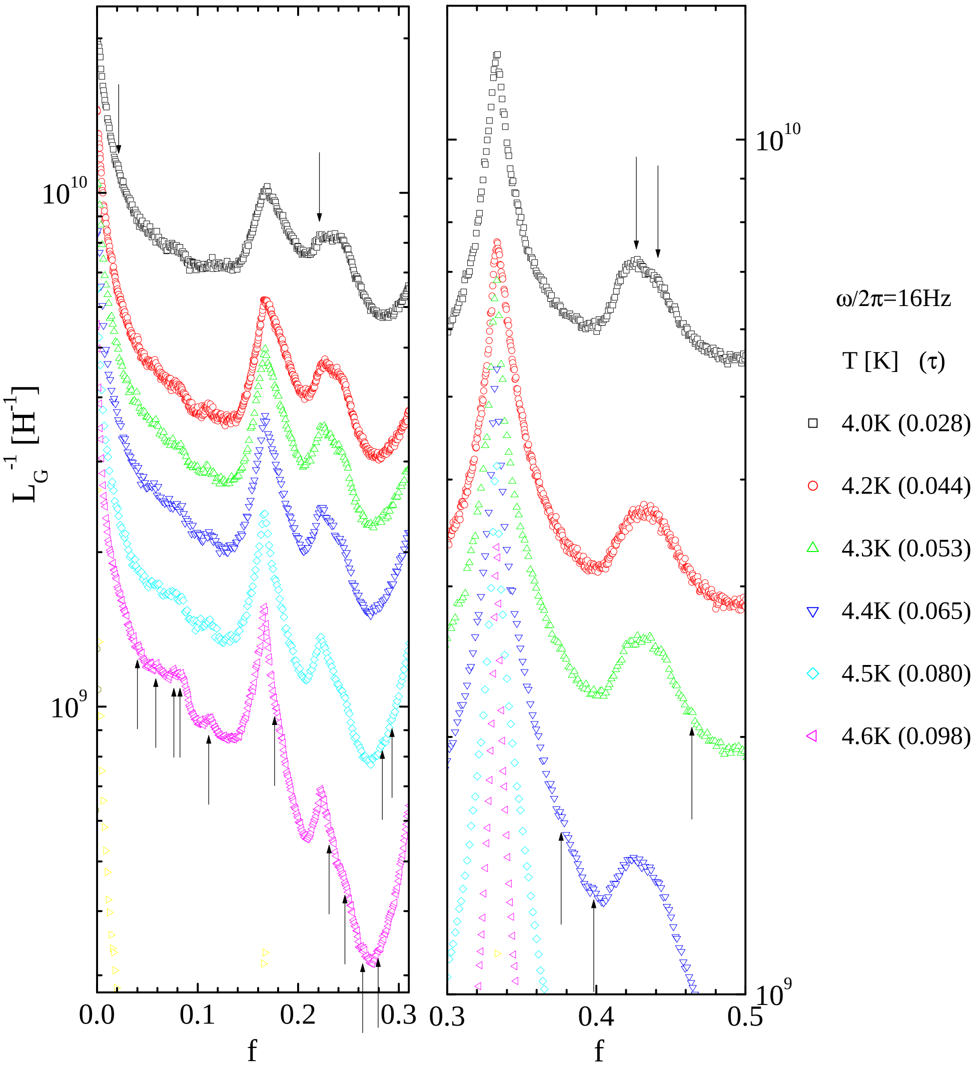

Figure 4.4: [sample3] Inverse magnetoinductance curves measured at low temperature and low frequency. The positions of the observed structures are

$$f = 1/100, 1/60, 1/50, 1/37, 1/24, 1/18, 1/17, 1/13$$
$$f = 1/12, 1/9, 1/6, 3/17, 2/9, 4/17, 1/4, 4/15, 5/18, 2/7, 7/24, 1/3$$
$$f = 3/8, 6/15, 3/7, 4/9, 7/15$$

ment step between two successive points is constant.
As discussed in section 1.3, the dice lattice spectrum is related to the triangular one by the transformation $f_{dice} = (2/3)f_{triangular}$. Notice that the factor (2/3) already appeared when the dice lattice was compared to the triangular one. This factor is the value of the ratio between the bond densities of both lattices (see section 1.3) and the ratio between their sheet conductances (see section 1.2.4).

It is then possible to compare the positions of the commensurate structures of the dice lattice with those of the triangular lattice, for which the structure positions in the interval $1/4 < f < 1/2$ are given by the relation $f_{triangular} = 1/2 - 1/(2N)$ with N an integer ≥ 2 [103].
Applying the transformation described above, the relation valid for the triangular lattice becomes, for a dice lattice with $1/6 < f < 1/3$:

$$f = 1/3 - 1/(3N) \text{ with } N \text{ an integer} \geq 2$$

The sequence of structures observed in the triangular lattice [103]

$$f = 1/4, 1/3, 3/8, 2/5, 5/12, 3/7, 7/16, 1/2$$

is transformed, for the dice lattice, into the sequence

$$f = 1/6, 2/9, 1/4, 4/15, 5/18, 2/7, 7/24, 1/3$$

Indeed, such a sequence is observed (see caption of Fig.4.4) with two additional structures at $f = 3/17, 4/17$. We found another sequence, starting with $f = 1/18$,

$$f = (1/18)\ (1 + n) \text{ with } n = 0, 1, 2, 3, 4, 5$$

For $n > 5$, it is difficult to distinguish the structures because they are too close to each other, but we cannot exclude that the sequence continues with $f \to 1/2$.

In the following sections, we focalize our attention on three peculiar frustrated states. We first look at the fully frustrated state ($f = 1/2$), which exhibits a week phase coherence, even at low temperature. Then we pay attention to two most prominent structures, i.e. at $f = 1/3$ and at $f = 1/6$. The $f = 1/3$ state was the object of recent theoretical work [13]: this gives us the opportunity to compare our observations with theoretical results. The $f = 1/6$ state was never studied before, at least theoretically, and shares many common features with the $f = 1/3$ state. Finally, we summarize our observations by comparing these three states.

4.2 Fully frustrated state

This section focuses on the fully frustrated state ($f = 1/2$). We first discuss the ground state(s) in terms of the vortex configuration(s). Then, increasing the temperature, we discuss the disordering of the vortex pattern and the possibility to observe a phase transition.

4.2.1 Degenerate ground state

In the framework of the fully frustrated XY ($FFXY$) model, a family of vortex patterns has been proposed as a ground state (GS) [9]. This GS is given by the distribution of charged half-vortices in the lattice plaquettes (vorticity $m - f = \pm 1/2$, see section in 1.2.2). Since vortices of the same sign repel each other, they are thought to be located as far from each other as possible. Analogous situations are found in the GS of the fully frustrated XY model with square and triangular lattices where the nearest neighbours of each charged vortex are of opposite sign and occupy the sites of the dual lattice. The dice lattice is dual to the Kagomé lattice, where neighbouring sites cannot be occupied by opposite charged vortices as illustrated in Fig.4.5a). Then half-vortices of the same sign have to form clusters whose minimal size is equal to three. Fig.4.5b) shows the most symmetric distribution in terms of integer vortices ($m = 0, 1$) on a Kagomé lattice [9]. Because of its simplicity and symmetry, this periodic structure was thought [9] to be a ground state of the $FFXY$ model; indeed, this state was proved to have an absolute minimum of energy [10]. In Fig.4.5c) the GS is depicted in a phase representation with the elementary phase pattern shown in Fig.4.5d) whose phase variables ($\theta_1, \theta_2, \theta_3$) are obtained by minimizing the Hamiltonian under the fluxoid quantization (1.8) constraints (see section 1.2.2).

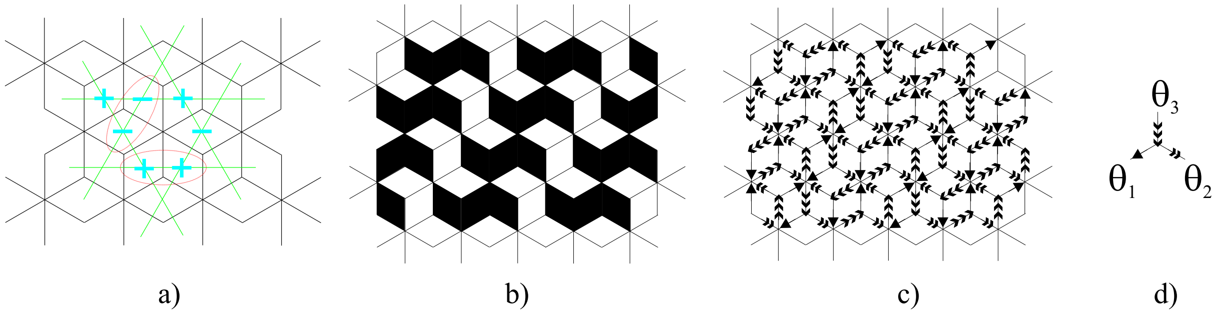

Figure 4.5: Ground state vortex pattern. a) half vortices with alternating (±) sign on a Kagomé (green) lattice. b) triads of integer vortices (black cells) occupying the sites of a Kagomé lattice. c) GS in terms of the phase variable distribution. d) elementary pattern whose reflections and rotations allow construction of the GS.

$$\theta_1 = \arctan\left[(\sqrt{2}-1)/(\sqrt{2}+1)\right] \cong 10^\circ \qquad \theta_2 = \pi/4 + \theta_1 \cong 55^\circ \qquad \theta_3 = \pi/2 - \theta_1 \cong 80^\circ$$

The energy (per triple site) ε can then be calculated (H_{JJA})

$$\varepsilon = 3J[1 - 1/\sqrt{3}] \cong 1.27J \tag{4.1}$$

The periodic state (Fig.4.5b)) has an intrinsic 12-fold degeneracy. Indeed, it is possible to shift the vortex triads one cell along the horizontal direction, leading to three other configurations, and to rotate them by 60° and 120°.
Looking more carefully at this state, it was shown [9] that the phase variables in the lower half of Fig.4.5b) can be rearranged without violating the conditions for a GS expressed in section 1.2.2. This rearrangement is equivalent to the construction of a horizontal zero energy domain wall (ZEDW) (introduced in section 1.2.2) illustrated in Fig.4.6a). Constructing a ZEDW on each line such as the one illustrated in Fig.4.6a), we get a dense 1D network of horizontal ZEDWs, as illustrated in Fig.4.6b), which is still periodic and is 24-fold degenerate. Notice the three different orientations of the vortex triads.

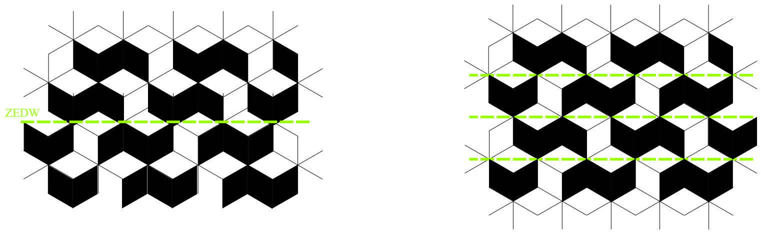

a) b)

Figure 4.6: Ground state vortex pattern. a) Construction of a horizontal ZEDW (dashed green line). Below the ZEDW, the vortices are horizontally shifted one cell to the left. b) 1D network of horizontal ZEDWs.

We obtain a second GS with ZEDWs constructed in the horizontal lines of the state Fig.4.5b) which are not occupied by vortices. Such lines exist also along the 60° direction and allow construction of ZEDWs by rotating the vortex triads of -60° below the DW, as illustrated in Fig.4.7a). Again, repetition of such a DW leads to a dense network of 60° ZEDWs depicted in Fig.4.7b).

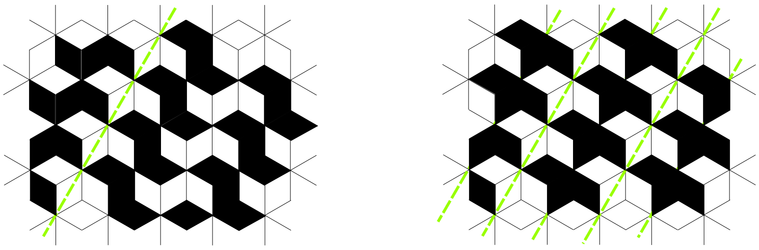

a) b)

Figure 4.7: Ground state vortex pattern. a) Construction of a 60° ZEDW (dashed green line): below the ZEDW the vortex triads are rotated by -60°. b) 1D network of 60° ZEDWs.

Since different types of ZEDWs can cross each other with no increase of the system energy, it is possible to construct a fourth periodic state, with a 24-fold degeneracy, which is a 2D network of crossing horizontal and 60° ZEDWs (see Fig.4.8).

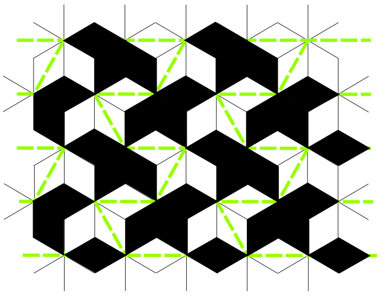

Figure 4.8: Ground state vortex pattern. Periodic 2D network of crossing horizontal and ±60° ZEDWs

The family of the fully frustrated ground states is composed of four periodic states (Figs.4.5b), 4.6b), 4.7b) and 4.8) and configurations including ZEDWs, as for example Figs.4.6a) and 4.7a), whose degeneracy lifting results in one of the previous periodic states. The ground state energy is given in (4.1).

4.2.2 Degeneracy removal within the *FFXY* model

The expectation of a removal of the accidental degeneracy [9], at finite temperature, by linear phase fluctuations (spin waves, see 1.2.2) was confirmed by analytical calculations [10]. Since the harmonic Hamiltonian spectrum is the same for all the periodic GS, only the free energy of anharmonic fluctuations can select a vortex pattern. The vortex configuration with the lowest anharmonic fluctuations' free energy has been determined on the basis of numerical calculations [10]. The selected vortex pattern is the most symmetric one, i.e. Fig.4.5b). Nevertheless, as in the case of the *FFXY* model on the honeycomb lattice [11], discussed in section 1.2.2, the mechanism of degeneracy removal by anharmonic fluctuations is extremely weak and it leads to an enhancement of the finite size effect. The selection of a low temperature vortex pattern, i.e. a vortex pattern ordering, can then take place as long as the sample size is at least of the order of 10^5 (in units of the lattice parameter a). This restriction for the observation of a vortex pattern ordering applies to real JJAs as well as numerical simulations, since for both kinds of experiments the accessible sample size is much smaller (our JJAs have a linear size of $10^3 a$). This could explain why recent magnetic decoration experiments in fully frustrated wire networks with dice lattice geometry show strongly disordered vortex state configurations [7]. Moreover, a statistical study of the occupancy of the lattice cells by vortices [8] shows a very short correlation length indicative of strong disordering which was partially ascribed by the author of reference [9] to geometrical irregularities. On the contrary, Serret *et al.* [8] attribute the absence of ordering to large thermal fluctuations combined with the presence of many vortex configurations frozen by the underlying SC thin film (flux compression technique) while the temperature is decreased. The vortex lattice could be frozen in a different pattern than the true ground state.

Based on their numerical simulations [12], Cataudella and Fazio ascribed the absence of ordering to a glassy dynamics which takes place in a system free from disorder. Below $\tau_{glass} \approx 0.06$ the system enters in a glassy state, characterized by an anomalous (logarithmic) relaxation of the system energy $E(time) \propto 1/log(time)$, preventing it from entering an ordered state. Indeed, the system energy is shown to exhibit a hysteretic behaviour when the sample is heated and cooled down. Such a hysteresis is also found in the helicity modulus which intercepts the BKT prediction line slightly below τ_{glass}, at $\tau_{\mathbf{c}}^{\mathbf{NS}} = \mathbf{0.05}$ ($NS \equiv$ numerical simulations). This value is slightly above the estimated critical temperature of the phase transition associated with the proliferation of DWs [10] and hence the disordering of the vortex pattern, already expected in [9]. In reference [10] the formation of point defects in the DW network, which can be kinks along domain walls or intersections between them, has been taken into account by including its entropic contribution. A numerical evaluation for this contribution leads to a critical temperature $\tau_{\mathbf{c}}^{\mathbf{DW}} \approx \mathbf{0.01}$ ($DW \equiv$ DWs proliferation, or vortex pattern disordering). As explained in section 1.2.3, the continuous degeneracy of the GS provides the existence of a BKT type phase transition, i.e. a discontinuity of the helicity modulus. The argument proposed in [10] is based on fractional vortices appearing at the intersections of DWs and including an excess of vorticity associated with a vortex cluster. These clusters behave as fractional vortices with a topological charge $\pm 1/8$. Roughly speaking, applying the Nelson-Kosterlitz generalization for fractional vortices (see section 1.2.3, eq.(1.9)), $\tau_{\mathbf{c}}^{\mathbf{BKT}} \approx \mathbf{0.013}$ ($BKT \equiv$ BKT type phase transition).

The glassy behaviour found in [12] is ascribed [10] to short relaxation times. Then, the existence of ZEDWs in addition to the finite size of the system, the weakness of the degeneracy removal mechanism, as well as a low transition temperature ($\tau_c \approx 0.01$), lead to the possibility of observing a glass-like behaviour. In other words, when the system is cooled down from high temperatures, many vortex configurations are frozen in a network of intersecting DWs. This DW network has to disentangle in order to restore an equilibrium concentration of point defects. This slow process can be associated with a glass-like behaviour.

According to these theoretical predictions, the superconducting phase coherence at full frustration should be strongly affected by thermal fluctuations down to very low temperatures, as was already partially observed (for $\tau \geq 0.1$) in the preliminary measurements illustrating the frustration structures (section 4.1). This completely contrasts what has been observed up to now in JJAs with other regular geometries [1]. Inverse magnetoinductance curves measured at low temperature, illustrated in Fig.4.9, show no structure at $f = 1/2$, i.e. no peak which would be the signature of a phase transition, even for temperatures below τ_c^{BKT}. The magnetoresistance exhibits, at high temperature and at full frustration ($f = 1/2$), an absolute maximum which persists down to low temperature, without any sign of a curvature inversion which could be attributed to a stable commensurate ground state. Therefore, the drop observed in the inverse sheet inductance, Fig.4.10, can be attributed to a regime crossover rather than to a genuine phase transition. Indeed, the dynamic helicity modulus shows a very smooth jump from the low temperature phase to the high temperature phase.

Nevertheless it is interesting to observe that the zero frequency limit of the BKT-predicted

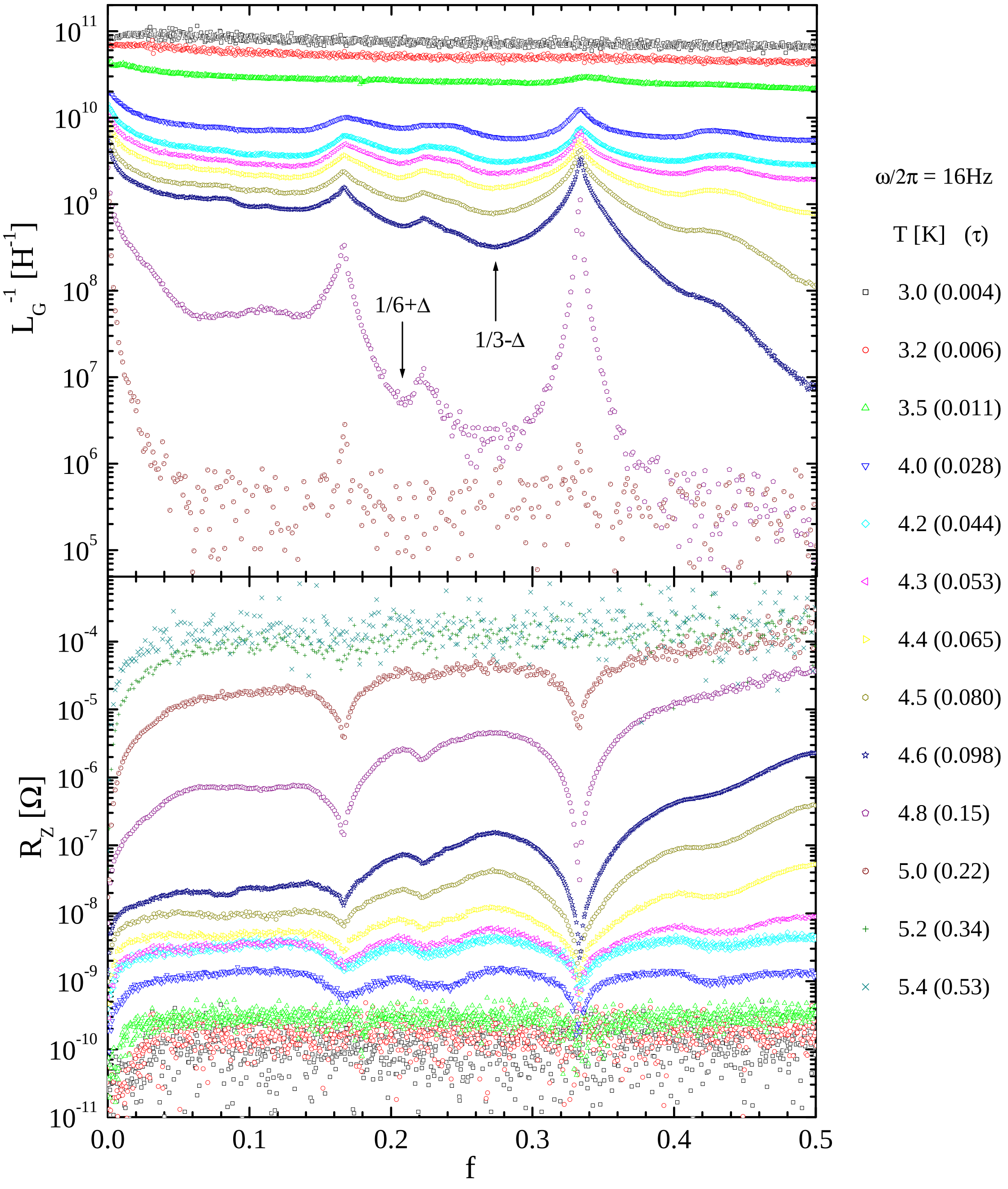

Figure 4.9: [sample3] Inverse magnetoinductance (top) and magnetoresistance (bottom) at frequency $\omega/2\pi = 16Hz$. Evolution of the frustration structures down to low temperatures.

critical temperature (for integer vortices) coincides with τ_c^{NS} of [12] where the phase transition was found to belong to the BKT universality class. Notice that our observation is in good agreement with the numerical result of [12] as far as integer vortices are concerned. If

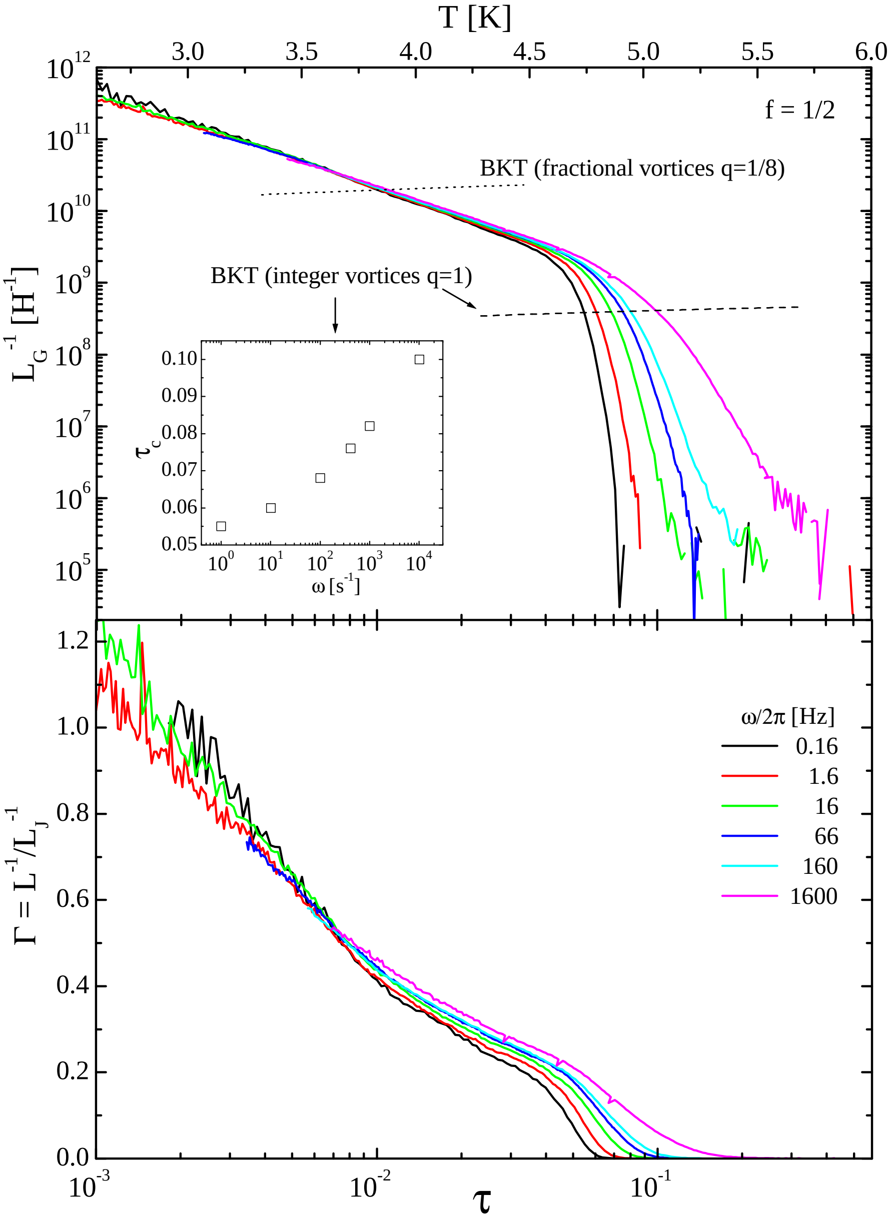

Figure 4.10: [sample2] Inverse sheet inductance (top) and dynamic helicity modulus (bottom) vs real (top axis) and reduced (bottom axis) temperature at $f = 1/2$. The inset shows the low frequency limit of the BKT predicted critical temperature for integer vortices.

the transition is driven by thermally activated fractional vortices with topological charges $q = \pm 1/8$, as predicted in [10], the Nelson-Kosterlitz prediction intercepts the inverse sheet inductance at $\tau \geq 0.01$.

At low temperatures, $L^{-1}(f)$ (Fig.4.9) exhibits an absolute minimum at $f = 1/2$ which becomes more and more pronounced as the temperature is increased to $\tau \approx 0.1$. Above this temperature, the phase coherence is completely lost at full frustration. This crossover temperature (τ^*), between the normal (no phase coherence) and the superconducting (finite SC phase coherence) states is frequency dependent, as illustrated in Fig.4.11. This figure shows a crossover from a frozen vortex liquid ($\tau < \tau^*(\omega)$) to a vortex liquid state ($\tau > \tau^*(\omega)$) [96] (see section 4.2.4). We see in $[Re\{G\}]^{-1}(1/\tau)$ that $\tau^*(\omega = 16Hz) \approx 0.1$,

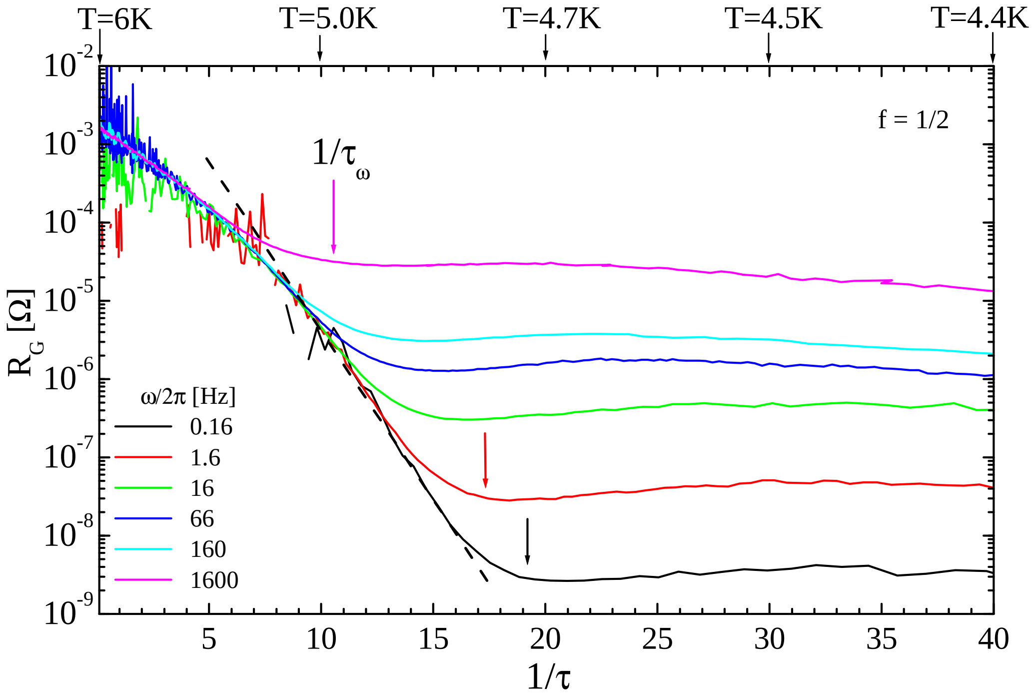

Figure 4.11: [sample2] Sheet resistance versus inverse reduced temperature at full frustration. Regime crossover from a frozen vortex liquid to a vortex liquid state.

the temperature below which the phase coherence appears (Fig.4.9), i.e. the system enters into a frozen vortex liquid or equivalently a disordered vortex solid.

4.2.3 Magnetic effects

As was already shown in section 2.3, when the temperature is lowered, the effective penetration depth decreases until it becomes of the order of the lattice constant a. That means that the sheet inductance becomes frustration-independent (1.14 in section 1.3) for $\tau \leq 0.002$ (see Fig.2.12). But looking at the inverse magnetoinductance and magnetoresistance measurements (Figs.4.9) we observe that the structures disappear for temperatures lower than $\tau \approx 0.03$. The temperature at which the magnetic effects become dominant in the process of selection of a low temperature vortex pattern has been estimated [10] by

comparison between the free energies of anharmonic fluctuations and the magnetic energies in the family of ground states (section 4.2.1). It is shown that the magnetic energy is dominant for temperatures lower than $\tau \approx 0.3$. Thus, the phase transitions associated with the vortex pattern disordering and the helicity modulus vanishing, expected to happen at $\tau_c \approx 0.01$ [10], should be completely hidden by magnetic effects. Moreover, the comparison of the magnetic energy between the various vortex patterns illustrated in section 4.2.1 shows that the magnetic Hamiltonian [10, 104] is minimized in the state Fig.4.6b), instead of Fig.4.5b selected by the *order-from-disorder* mechanism within the $FFXY$ model.
However, our lowest temperature measurements (Figs.4.9) were performed well below (two orders of magnitude) $\tau = 0.3$ without any sign of commensurate structure at the fully frustrated state. This seems to contradict the fact that when the temperature is lowered the magnetic effects are enhanced, leading to the stabilization of a vortex pattern. Nonetheless, the screening effects lead also to the increase of the barriers that the vortices have to overcome in order to move from cell to cell; hence an increase of the relaxation time to equilibrium (see section 4.6). The existence of such high barriers has been argued [10] to be responsible for the difficulty to observe a phase transition with finite frequency measurements. It can also be responsible for the glass-like dynamics observed at low temperature.

4.2.4 Low temperature Glass-like dynamics

The attempts by AHNS and MP, as discussed in 1.4, to describe the vortex dynamics did not take into account the magnetic effects mentioned above. Therefore, their results are not expected to predict the low temperature regime dynamics where the magnetic effects are dominant. According to the dynamic extension of the BKT theory developed for ideal SC networks (for instance ideal JJAs) at strictly zero frustration, the response is dominated by vortex-antivortex (VA) pairs below T_{BKT} and above T_{BKT} for sufficiently high frequencies ($\omega > \omega_\xi$). The characteristic frequency is $\omega_\xi \propto \exp\left[-2b/\sqrt{(T/T_{BKT})-1}\right]$ with $b \approx 1$. Under these conditions the dissipation should be $R_Z(\omega) \propto \omega^{2(T_{BKT}/T)-1}$. The free vortices are expected to dominate the response above T_{BKT} for $\omega < \omega_\xi$, leading to a frequency-independent dissipation.
The frequency dependencies of dissipation and inverse inductance have, at full frustration, qualitatively the same features as those described by the AHNS extension of the BKT theory (valid for the unfrustrated state). Fig.4.12 shows clear plateaus in $R_Z(\omega)$ and $R_G(\omega)$ above T_c since for $\omega L_Z << R_Z$, $R_G \equiv R_Z$ (see section 1.2.4). These plateaus are an indication of a response dominated by free vortices, but the characteristic frequency ω_ξ is not quantitatively well described by the exponential expression of AHNS. The isotherm which exhibits a linear behaviour illustrated with the dashed line ($\propto \omega^1$) should be, following the results of AHNS, the critical temperature. Nevertheless Fig.4.10 shows that at this temperature ($T \cong 4.4K, \tau \cong 0.03$) the phase coherence is still finite. When the temperature is increased, we observe a strong suppression of $L_G^{-1}(\omega)$, which starts with the lowest frequencies. The same behaviour is observed for other vortex densities, as illustrated in Figs.4.13 and 4.14.

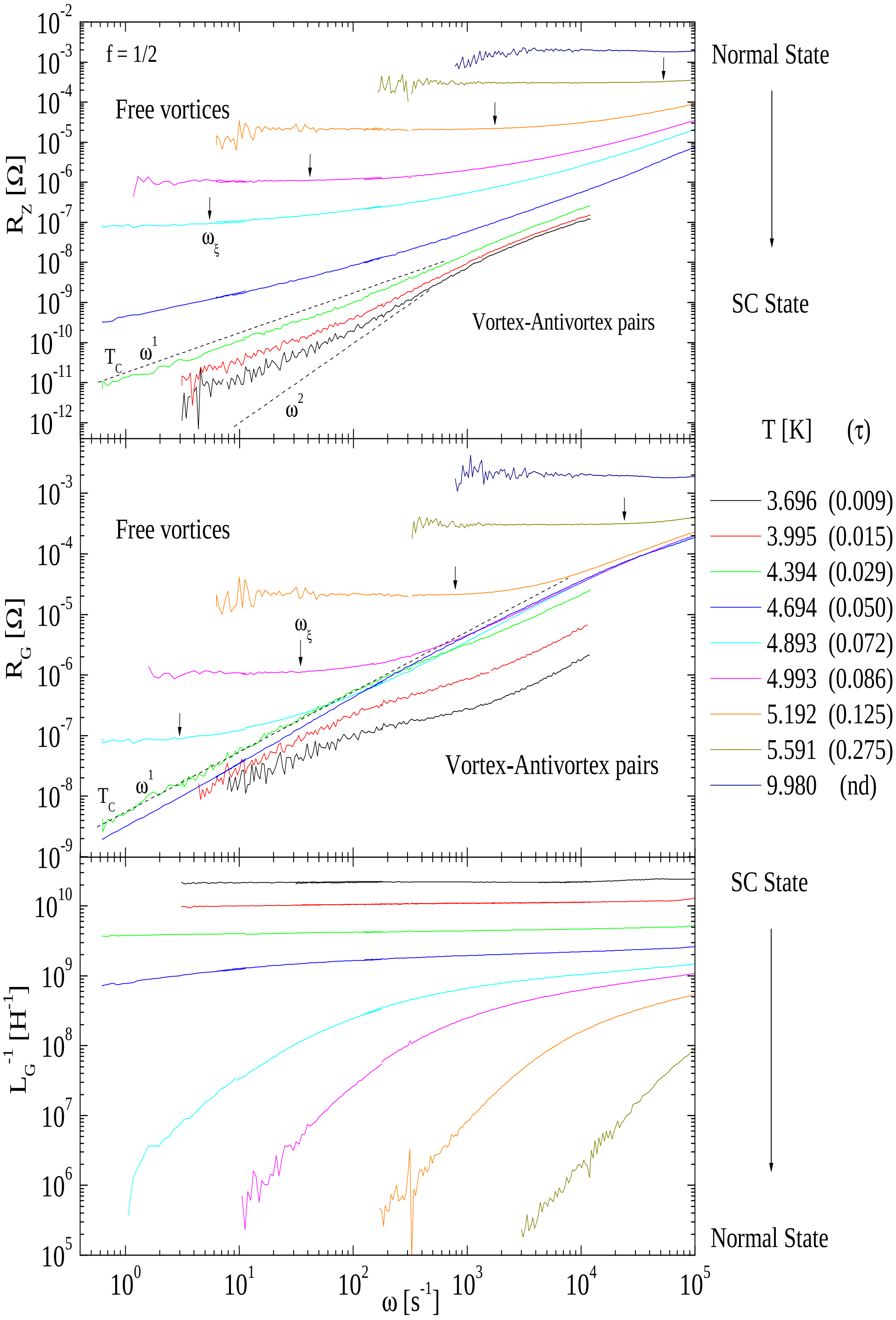

Figure 4.12: [sample2] Frequency dependence of the dissipative responses (R_Z and R_G) and the inverse sheet inductance at $\mathbf{f = 1/2}$. Notice that, for $T > T_c$ and $\omega < \omega_\xi$, $R_G = R_Z$, and below T_c, the saturation of R_Z and the crossing of the isotherms in R_G. The loss of phase coherence is illustrated by the inverse sheet inductance $L_G^{-1}(\omega)$.

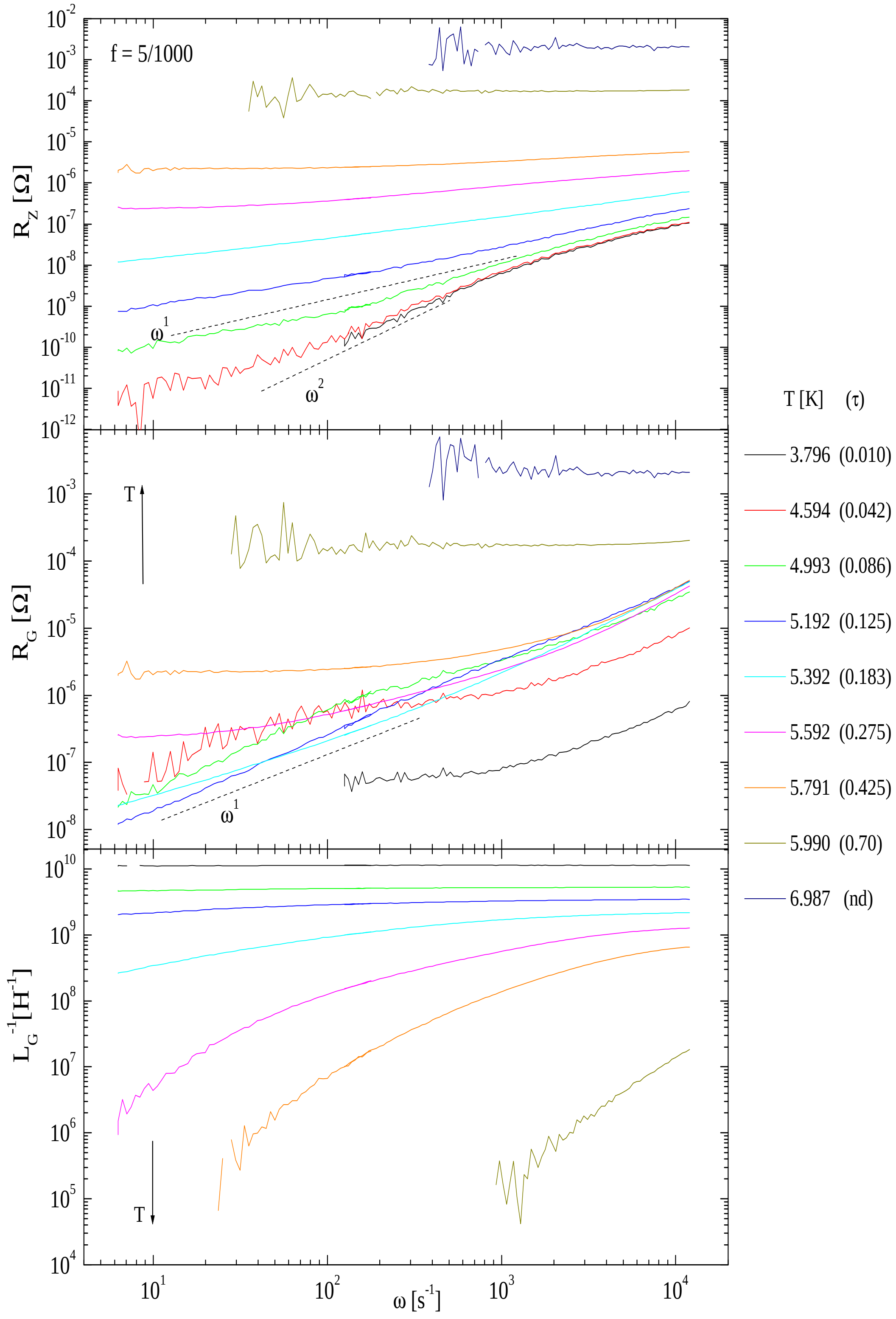

Figure 4.13: [sample2] Frequency dependence of the dissipative responses (R_Z and R_G) and the inverse sheet inductance at **f = 5/1000**.

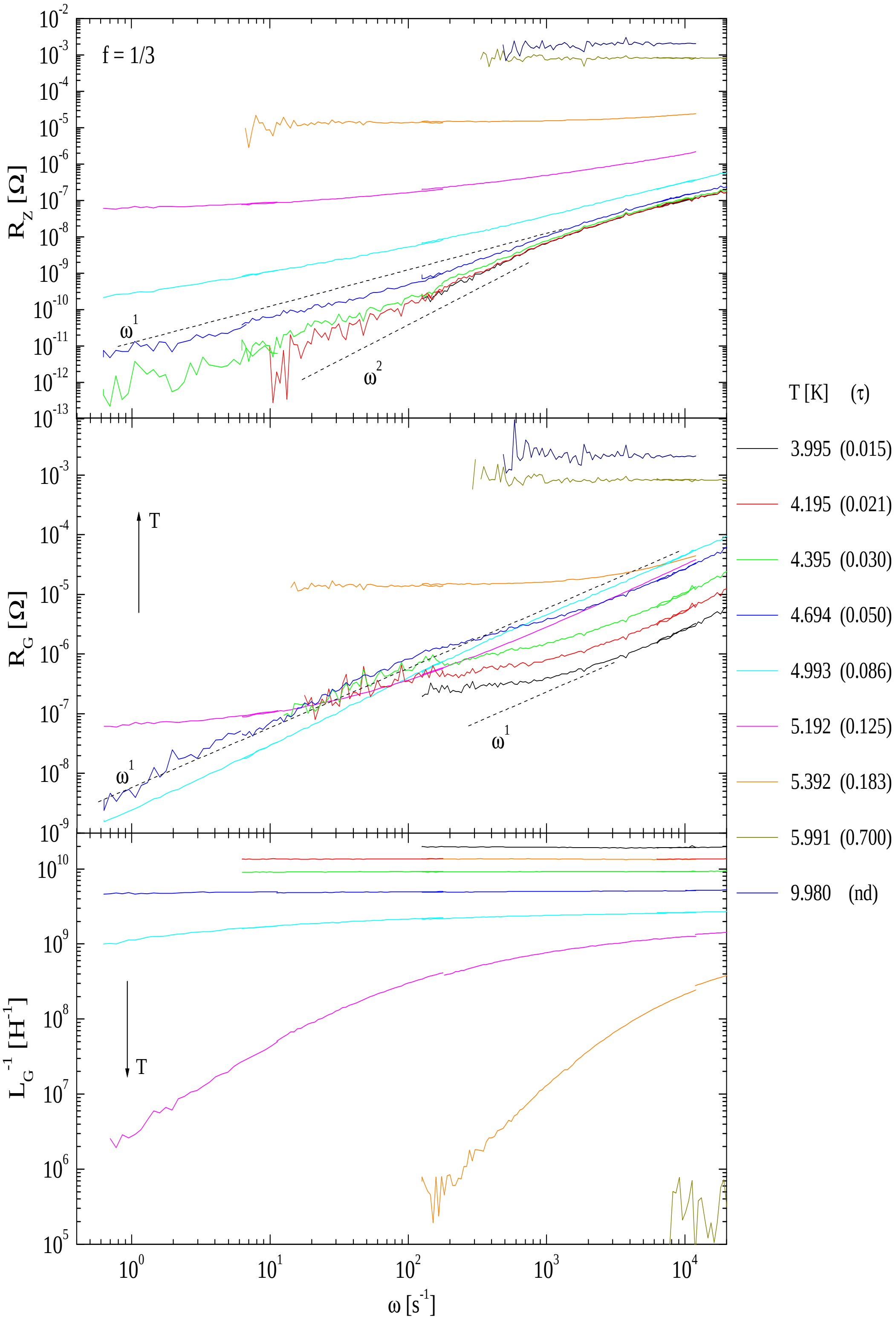

Figure 4.14: [sample2] Frequency dependence of the dissipative responses (R_Z and R_G) and the inverse sheet inductance at $\mathbf{f = 1/3}$.

In section 4.1, it was shown how the temperature and the frequency variables can induce the same effects on the response. Here it is interesting to observe the same phenomenology with the exchange between the temperature and the vortex density f as measurement variable. Fig.4.15 shows the frequency dependence of the dissipative components, as well as the inverse inductance, at a fixed temperature and for various values of f.
All these measurements (at $f = 5/1000, 1/3, 1/2$ and even at a fixed temperature with increasing f) exhibit the same low temperature ($T < T_c$) and low frequency behaviours;

(1.) $Re\{Z\}(\omega, T) \propto w^1$ with a strong temperature dependence

(2.) $[Re\{G\}]^{-1}(\omega, T)$ is also proportional to ω^1 with a crossing of the isotherms while the temperature is increased, i.e. $R_G(T) \sim 1/T^a$

(3.) $L_G^{-1}(\omega, T)$ is weakly increasing with ω but is, as well as $Re\{Z\}$, strongly temperature dependent

These low temperature features can be explained neither by AHNS nor by MP theories, but since they are also observed with other array geometries [105], they can be due to some intrinsic characteristics related to the fabrication of JJAs.

The model is based on the hopping of *vortices* from cell to cell in a random pinning potential created by *hidden disorder*. The basic ingredients are *i)* a residual frustration, and *ii)* a hidden disorder due to the exponential nature of the coupling energy in JJAs. The imperfect suppression of the ambient non-homogeneous magnetic field ($\approx 40nT \leftrightarrow 10^{-3}\phi_0/cell$), discussed in section 3.7, is responsible for the presence of single vortices near "$f = 0$" or vortex lattice defects near rational f (missing vortices on a frozen vortex background). Because of the finite size of the sample, thermally created vortices may also be present, but for the temperature region of interest ($\tau < 10^{-1}$), the thermal energy over the vortex energy ratio $k_BT/E_{vortex} \approx k_BT/J \ln[sample\ size] < 10^{-1}$.
The coupling constant $J(T)$, in arrays of proximity-effect coupled JJs, has an exponential dependence on the junction geometrical parameters :

$$J(T) = J_0(T) \exp[-\ell_J/\xi_N(T)]$$

where ℓ_J is the normal metal bridge length and $\xi_N(T)$ the normal metal coherence length (see section 2.2.3). With an unavoidable random variation of a few percent in the junction geometrical parameters ($\Delta\ell_J/\ell_J \approx 2-4\%$) introduced by the fabrication process, the resulting fluctuations of the coupling energy are very strong $\Delta J(\ell_J)/J = \ell_J/\xi_N \cdot \Delta\ell_J/\ell_J$. With $\ell_J/\xi_N(T_{CS}) = 14$ (section 2.2.3), $\Delta J(\ell_J)/J \approx 30 - 60\%$.

This model explains the results obtained at low temperature, where a *frozen vortex liquid* (or disordered vortex solid) takes place instead of a genuine vortex glass. A vortex glass is usually defined as a thermodynamic phase in which the transport response (resistivity ρ) to a vanishingly small force (current density j) is also vanishingly small, i.e. $\rho(j \to 0) \to 0$. This property has been described as a consequence of infinite barriers which

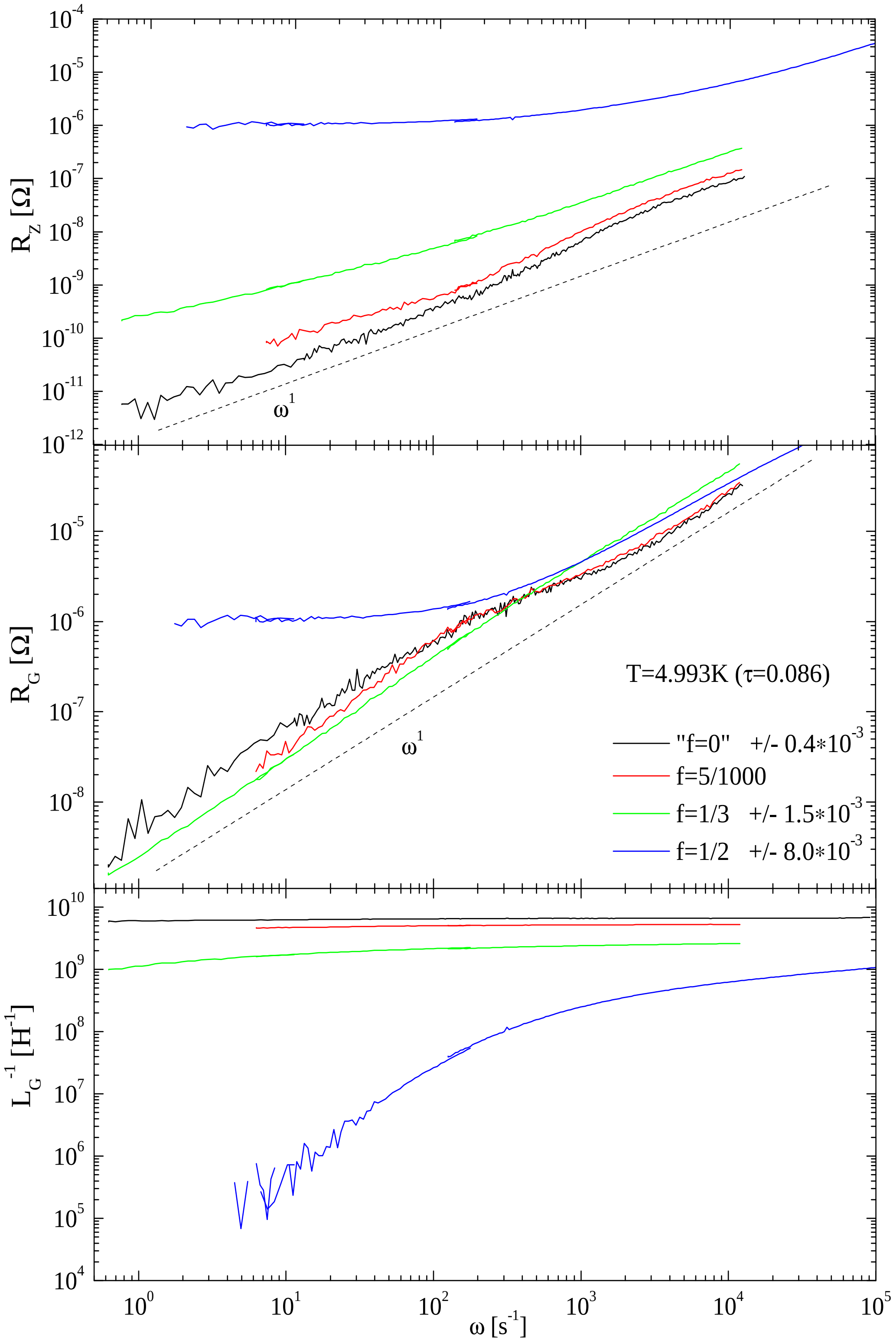

Figure 4.15: [sample2] Frequency dependence of the dissipative responses (R_Z and R_G) and the inverse sheet inductance at $T \approx 5K(\tau = 0.086)$.

pin the vortices in the system [106]. As opposed to the vortex glass, the vortex liquid has finite barriers and non zero resistivity. The glassy nature of a system is characterized by a relaxation time to equilibrium which diverges with the size of the system [107]. Thus at short timescales, it is possible to freeze the high temperature vortex liquid (at $\tau > \tau^*(\omega)$ in Fig.4.11, characterized by a thermally activated vortex motion) in order to enter into a frozen vortex liquid with glass-like dynamics ($\tau < \tau^*(\omega)$) [96].

The approach is based on a two level system [108] of vortices hopping between pairs of metastable states in neighbouring cells [81], as illustrated by Fig.4.16. The pinning potential $U(x, y)$ is not periodic because of disorder in the coupling constants $J(T)$. When a current is applied (sheet current density $\vec{K}$), the resulting Lorentz force ($\vec{F}_L$) tilts the potential, and the difference energy (Δ) between two neighbouring cells is reduced by the work of $\vec{F}_L$ across the barrier; $F_L\, a\cos(\alpha) = a\, K\phi_0\cos(\alpha)$. Therefore the vortex occupation probabilities for neighbouring cells, given by the Boltzmann factor $\exp[-\Delta/k_BT]$, is modified by the factor $\exp[a\; K\phi_0\cos(\alpha)/k_BT]$. The response of the system excited with $\vec{K}$ can be characterized by a deviation from equilibrium ($\vec{K} = 0$) defined by the difference W of the occupation probabilities induced by $\vec{K}$, i.e. $W = (a\phi_0/k_BT)\cos(\alpha)K/(4\cosh^2(\Delta/2k_BT))$ [109]. This allows calculation of the average vortex velocity $\bar{v}$, which is related to the electric field produced by the vortex motion. In a single two level system $\bar{v}(\omega) = i\omega\;\bar{u}(\omega)$ where $\bar{u}(\omega) = a\cos(\alpha)W$ is the average vortex displacement in the $\vec{F}_L$ direction. The static $\bar{u}$ value is generalized for an oscillating $\vec{K}$ using a Debye relaxation model with a relaxation time $\tau(U) = \tau_0\exp[U/K_BT]$ for the vortex thermal activation. The average vortex velocity is then $\bar{v}(\omega) = (a^2\phi_0/8k_BT)K\cosh^{-2}[\Delta/2k_BT]\; i\omega/(1 + i\omega\tau(U))$.

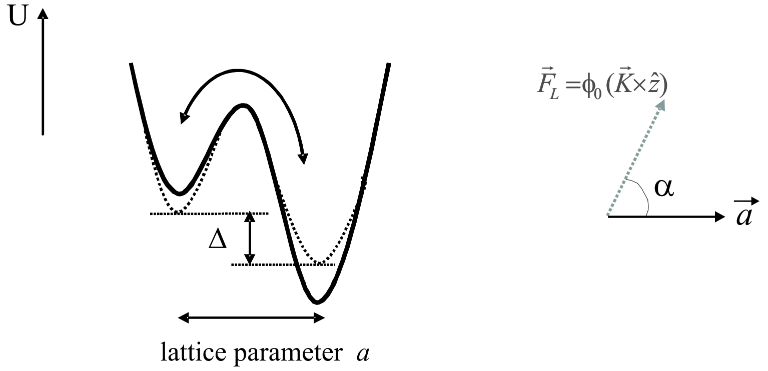

Figure 4.16: Two level system approach. The pinning potential U is represented for one direction $U(x)$. When a force $\vec{F}_L$ acts on the vortices, the effective pinning potential is tilted in such way that Δ is reduced (dotted line).

At this point it is important to distinguish the energy barrier $U(x, y)$ separating two neighbouring sites from the difference between the neighbouring site energies Δ.

The contribution of the vortices to the sheet impedance $Z(\omega) = i\omega L_J + Z_v(\omega)$ is $Z_v(\omega) = \langle E(\omega)\rangle / K$, where the symbol $\langle\ \rangle$ means the average over disorder. In order to be able to calculate the average over all the two level systems of the array, we need to take into account the Δ and U distributions (see diagram in Fig.4.17). The energy difference between two neighbouring metastable states is randomly distributed with a characteristic width $\widehat{\Delta}$ such that $\int_0^\infty D(\Delta) d\Delta = D(0)\widehat{\Delta} = 1$. Since the only energy scale in the system is the coupling constant $J(T)$, $\widehat{\Delta}$ is expected to be of the order of $J(T)$. The energy barrier distribution $P(U)$ is assumed to be uniform up to some characteristic value U_{max}.

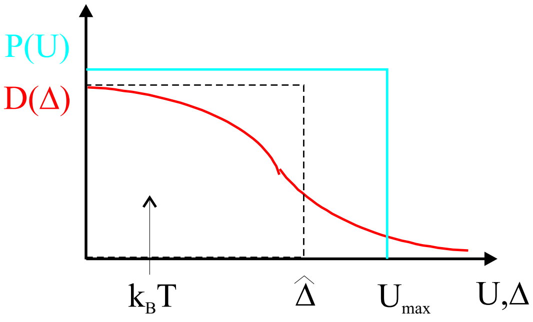

Figure 4.17: Random energy difference distribution $D(\Delta)$ and uniform energy barrier distribution $P(U)$. Thermal energy $k_B T \ll$ characteristic width $\widehat{\Delta}$.

The integration over the Δ distribution leads to the vortex impedance

$$Z_v = i\omega L_J(T) \int_0^\infty dU \frac{P(U)}{1 + i\omega\tau(U)}$$

The uniform distribution of U allows us to cut the integration off at some U_{max} value and to transform the integration into one over τ, since $d\tau/\tau = dU/k_B T$. The τ_0 relaxation time, which corresponds to the $U = 0$ value, is typically of the order $L_J/R_J \approx 10^{-9} - 10^{-8} s$ for $0.001 < \tau < 0.01$.

In order words, the low temperature regime which interests us corresponds to $\omega\tau_0 \ll 1 \ll \omega\tau_{max}$.

$$(1.)\ \ R_Z(\omega,T) = R_v(\omega,T) \approx \frac{\pi}{2}\omega L_J(T)\frac{k_BT}{U_{max}}$$

$$\text{with } U_{max} \propto J(T) \propto L_J^{-1}(T) \qquad R_Z(\omega,T) \propto \omega\frac{\tau^2}{T}$$

$$(2.)\ \ L_Z(\omega,T) = L_G(\omega,T) \approx L_J(T)[1 + \frac{k_BT}{U_{max}}\ln(\frac{1}{\omega\tau_0})]$$

for the lowest frequencies, the logarithmic correction is of the order of one.

$$(3.)\ \ R_G(\omega,T) \approx \frac{2}{\pi}\omega L_J(T)\frac{U_{max}}{k_BT} \propto \frac{\omega}{T}$$

We realize that these expressions are consistent with the observations of the frequency measurements in the low temperature regime, i.e. below τ_c. Because of the τ dependence, the real component of the sheet impedance, R_Z, is strongly temperature dependent whereas the inverse real component of the sheet conductance, R_G, has a weak temperature dependence since it is a function of the real temperature only. In addition, its inverse temperature dependence explains the crossing of the isotherms. The superfluid density ($\omega Im\{G\}$) is practically, at least for the lowest frequencies of our experiments, independent of ω, whereas it exhibits an exponential T-dependence given by the junction inductance $L_J(T) \propto 1/I_{CJ}(T) \approx \exp[\sqrt{T}]$.

Our interpretation of these low temperature features, i.e. thermally activated vortices ($f = 0$) or defects ($f \neq 0$) hopping between metastable states in neighbouring cells, is distinct from the one provided for the glass-like dynamics found in numerical simulations [12] of the pure system (without any kind of disorder) at $f = 1/2$, and related to a hysteretic behaviour.

The high temperature behaviour can be explained by barrier limited diffusion of single (non interacting) vortices at $f = 0$ or vortex lattice defects at $f \neq 0$). This will be the subject of a further section (see section 4.6).

4.3 $f = 1/3$ frustrated state

We have seen, in the case of the fully frustrated state (section 4.2.1), that in spite of the ground state (GS) degeneracy, the vortex pattern can be determined, discarding the magnetic effects, by taking into account the fluctuations' free energies in the vicinity of the GS, i.e. the spin waves free energy. The case of the $f = 1/3$ frustrated state is special in the sense that for the first time, in the framework of the frustrated XY model, the accidental degeneracy of the ground state is so developed that the vortex pattern is disordered at arbitrary low temperature, despite the difference between the free energies of fluctuations [13]. Consequently, the only possible phase transition which can take place is related to the dissociation of fractional vortex pairs. The selection of a vortex pattern, and hence the degeneracy removal, is achieved by magnetic effects, i.e. beyond the XY model.

4.3.1 Zero temperature vortex pattern

The ground state exhibits a well-developed accidental degeneracy, related as was already the case for the fully frustrated state (section 4.2.1), to the creation of zero energy domain walls (ZEDWs). The more simple vortex pattern is the striped state, an Abrikosov-like vortex lattice illustrated in Fig.4.18a). Minimizing the Hamiltonian on the elementary structure, Fig.4.18b), under the fluxoid quantization (1.8) constraints (see section 1.2.2) ($m = 1$ for the cells occupied by a vortex) we get $\theta_{ij} = \pi/3$ on each bond of a cell with a vortex inside (black plaquette), and the current conservation law implies $\theta_{ij} = 0$ on all other bonds, i.e. bonds connecting neighbouring vortex stripes.
The energy (per triple site) $\varepsilon = 2J[1 - \cos(\pi/3)] = J$.

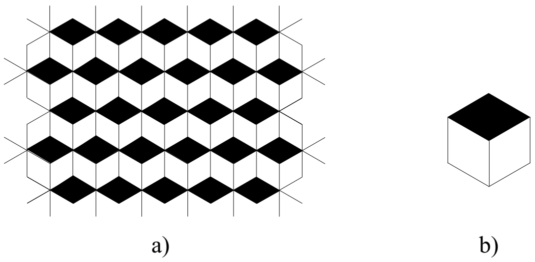

Figure 4.18: Ground state vortex pattern at $f = 1/3$. In each black plaquette is located an integer vortex. a) striped state. b) elementary cluster with no vortices in adjacent cells.

Introducing diagonal ZEDWs in the striped state, we get another GS called *zigzag state* Fig.4.19a) and another one called *honeycomb state* Fig.4.19b) [13]. In all these GS configurations, each hexagon made with three neighbouring cells, as the one in Fig.4.18b), holds only one vortex. This feature allows construction of a mapping between the GS of the XY model and the GS of the antiferromagnetic Ising model on the triangular lattice formed by the sixfold sites (type A sites introduced in section 1.3). A cell with a vortex of the XY

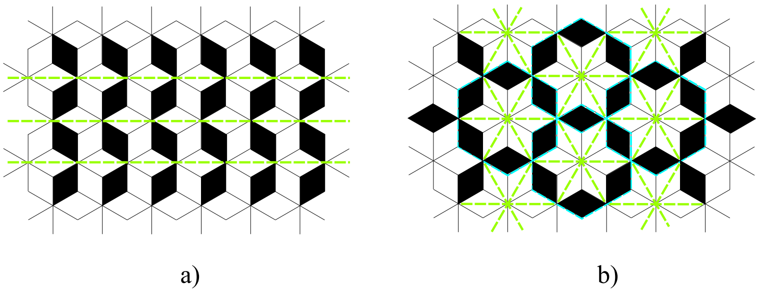

Figure 4.19: *Zero energy domain walls* (green lines). a) zigzag state, and b) honeycomb state.

model corresponds to a bond connecting parallel spins of the Ising model on the A site's triangular lattice. This mapping allows study of the zero temperature vortex pattern [13], since the antiferromagnetic Ising model on a triangular lattice is characterized by a quasi long range order (algebraic decrease of the correlations). This mapping also allows discussion of the dice lattice, at zero temperature, in terms of the solid on solid (SOS) model which describes height fluctuations on the (111) facet of a simple cubic lattice. Thus, the mapping is interesting since the dice lattice is obtained by projection of a cube along the (111) direction (see section 1.3).

In the framework of the SOS model, at zero temperature there is no long range order. Moreover, the value of the rigidity constant, which is equivalent to the coupling constant of the XY model, is far from the value at the transition point. The system is then in the rough phase, i.e. the disordered phase. It results from [13] that, if at $T = 0$ the model was in the smooth phase, then the selected vortex pattern would be the honeycomb one (Fig.4.19b) since it corresponds to a flat state of the SOS model. In terms of the XY model, the formation of the honeycomb state corresponds to quasi long range order. Nevertheless, at T=0 the system is in the rough phase and the driven mechanism for the selection of a ground state is the entropy, since it is the relevant quantity in the probability factor $[\exp[-(U - TS)/k_B T]]$. In terms of the SOS model, the state with the biggest entropy is characterized by a random distribution of steps of opposite sign. Such a typical ground state is disordered with a short range honeycomb modulation, as illustrated by Fig.4.20.

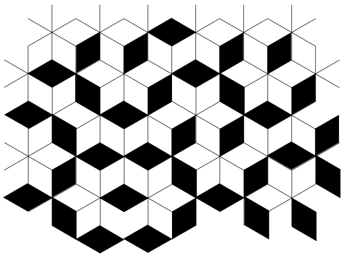

Figure 4.20: Disordered ground state with short range honeycomb modulation.

4.3.2 Degeneracy removal and Phase transition

Thermal fluctuations give rise to spin waves whose free energy favors the honeycomb state, already in the harmonic approximation [13]. In any case, the difference of fluctuation-free energy in the vicinity of the other ground states is very small. In terms of the SOS model, the fluctuations of the SOS variables are weakened, driving the system definitively far from the transition to the ordered phase. The fluctuations are too weak to give rise to an efficient *order-from-disorder* mechanism, and the vortex pattern is disordered down to $T = 0$. The steps of the SOS model correspond to DWs of the XY model through which the phase is rotated by π. This process is valid for each triangular sublattice (see section 1.3). At the intersection of three DWs, the global phase is rotated by π. Thus, a topological excitation appears at the intersection of three DWs: this corresponds to the melting of three steps of the same sign [13], see Fig.4.21. Since this elementary topological excitation induces a phase rotation of π, instead of 2π as should be for integer vortices, such a defect is called *half vortex*.

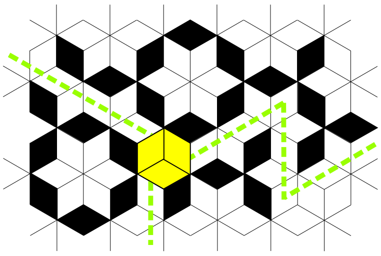

Figure 4.21: Elementary topological excitation of the $f = 1/3$ frustrated state. The defect consists in the intersection of three DWs (dashed green lines), whose core is formed by a hexagonal cluster of three cells (yellow hexagon). Another possible configuration contains cores with two vortices, instead of zero vortices as illustrated here.

For temperatures $\tau \ll 1$, the dislocation nature of such defects is not dominant and they interact as integer vortices which form pairs with zero net vorticity. The helicity modulus is then finite. Thus, the temperature increase leads to the BKT scenario for integer vortices, i.e. a phase transition associated with the unbinding of half vortices occurs and the helicity modulus vanishes. The critical temperature can then be estimated for fractional vortices (see section 1.2.3, eq.(1.9)) to $\tau_c^{HV} \cong 0.28$ ($HV \equiv$ Half Vortices) [13]. This value is not far from the one resulting from numerical simulations: $\Gamma = 0$ for $\tau > \tau_c^{\mathbf{NS}} \cong 0.2$ [12]. At this point of the theoretical investigations [12, 13], which we tried to summarize here, we know that in the frustrated XY model at $f = 1/3$ the vortex pattern is disordered at any finite temperature and becomes quasi ordered only at $T = 0$.

Once more, as was already discussed for the fully frustrated state (section 4.2), we have to consider the magnetic screening effects as a mechanism able to remove the accidental degeneracy. The magnetic interaction energy between neighbouring loop currents is mini-

mized for the striped state [13]. This may explain why this peculiar vortex configuration was observed (without any DWs) in decoration experiments of wire networks [7, 8]. The correlation function [8] shows a wide ordered vortex pattern even with a few percent of excess vortices, indicating a very efficient mechanism of vortex pattern selection.
The critical temperature associated with the vortex pattern selection by the magnetic effects was assumed to take place when, in the framework of the SOS model, the step energy is of the order of the thermal energy [13], i.e. $\tau_c^{MS} \approx 0.01$ ($MS \equiv$ Magnetic Screening), one order of magnitude below the critical temperature associated with the half vortex unbinding.

If we consider from an experimental point of view that magnetic screening effects may have consequences on the JJA's behaviour when the superfluid density ($\sim L^{-1}$) becomes independent of f (at $\tau_\Lambda \approx 10^{-3}$, Fig.2.12 in section 2.3), then the BKT type phase transition should be observable, since it is predicted to occur at a temperature which is two orders of magnitude higher than τ_Λ.
The frequency dependence of the jump in the superfluid response $L_G^{-1}(\tau)$ is reported in the inset of Fig.4.22(top) for half-vortices, according to (1.9) in section 1.2.3. The zero frequency limit $\tau_c(\omega \to 0) \approx 0.07$ is well below the estimated value τ_c^{HV} which is only an estimate from above of the critical temperature. More precisely, this is the temperature at which the helicity modulus is predicted to jump to zero, at zero frequency. Indeed, Fig.4.22(bottom) shows a dynamic helicity modulus Γ (see section 1.2.4) which vanishes at τ of the order of 10^{-1}. But since $\Gamma(\tau)$ does not exhibit a clear jump from zero to a finite value, the only information we get is that the transition temperature is in the range of the smooth drop ($0.05 < \tau < 0.3$). Comparison of the BKT prediction for half vortices ($q = 1/2$) and integer vortices ($q = 1$), Fig.4.22(bottom), clearly shows that the BKT type transition is driven by fractional vortices rather than by integer vortices whose transition temperatures are not in the range of maximum variation of the helicity modulus.

In order to find a criterion to quantify the signature of a coherent state, we studied the evolution of the structure in $Z(f)$ (or $G(f)$) at $f = 1/3$ as function of the temperature, i.e. the temperature dependence of the superfluid peak and the dissipative dip at $f = 1/3$. The measurements were performed at $f = 1/3$ and at the basis of the structure, at $f = 1/3-\Delta$ (see Fig.4.9). In the normal state, there are no frustration structures:

$$\frac{R(f=1/3)}{R(f=1/3-\Delta)} = 1 \qquad\qquad \frac{\Delta L^{-1}}{L^{-1}}(f=1/3) \equiv 1 - \frac{L^{-1}(f=1/3-\Delta)}{L^{-1}(f=1/3)} = 0 \qquad (4.2)$$

While the temperature is decreased, coherent states appear giving rise to structures in $Z(f)$ (and $G(f)$) (see section 4.1), hence a variation of the resistive and inductive ratios (4.2). The dissipation is expected to decrease with temperature for all values of f, but according to Fig.4.23(top), the sheet resistance is more affected at $f = 1/3$ than at $f = 1/3 - \Delta$ for $0.15 < \tau < 0.4$. This means that the dip observable in Figs.4.1, 4.2 and 4.9 appears and expands in this temperature range. At the same time, the superfluid response is expected to increase for all vortex densities. But, as for the resistive

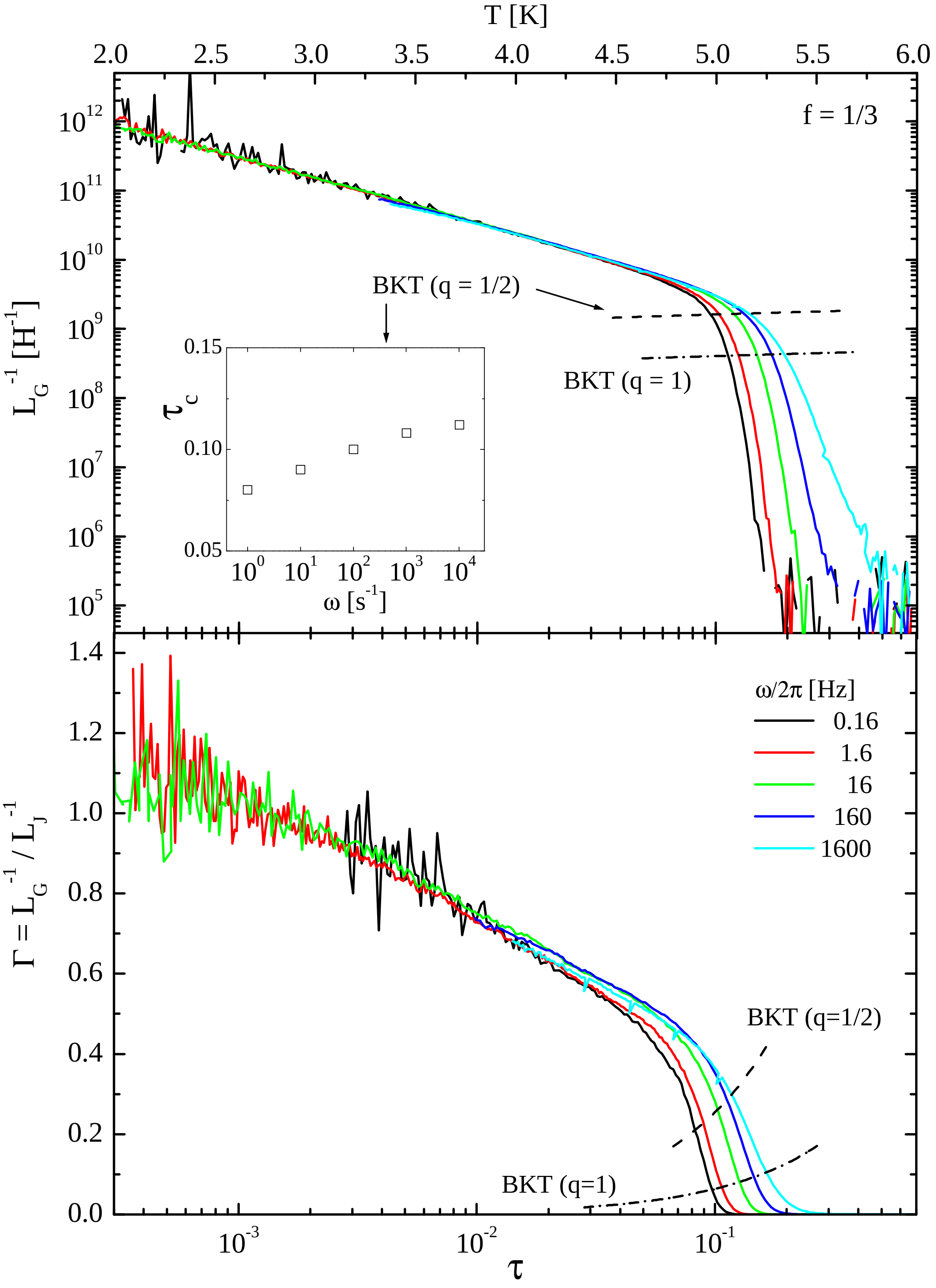

Figure 4.22: [sample2] Inverse sheet inductance (top) and dynamic helicity modulus vs real (bottom axis) and reduced (top axis) temperature at $f = 1/3$. The inset shows the measured half-vortices BKT critical temperatures.

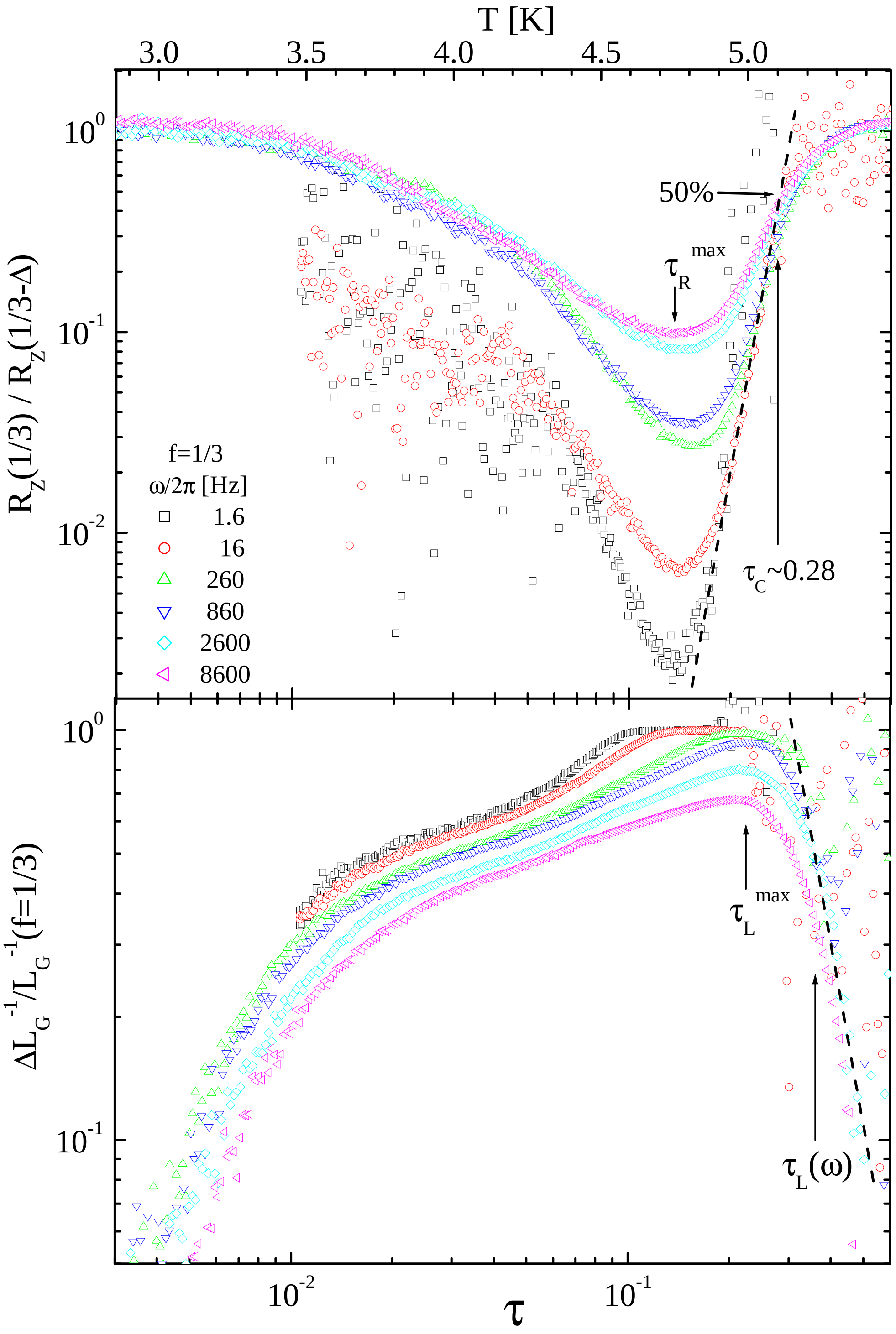

Figure 4.23: [sample3] Evolution of the $f = 1/3$ structure in $Z(f)$.
Top: dissipative dip and Bottom: superfluid peak.

case, the variation is more pronounced at $f = 1/3$ than at $f = 1/3 - \Delta$, and the ratio $L^{-1}(f = 1/3 - \Delta)/L^{-1}(f = 1/3)$ decreases. Thus, $\Delta L^{-1}/L^{-1}(f = 1/3)$ tends to one from below, as shown in Fig.4.23(bottom).

If one defines the transition temperature as the temperature at which the coherent state appears, this temperature would correspond to the one at which the ratio $R(f = 1/3)/R(f = 1/3 - \Delta) < 1$, at $\tau \leq 0.5$. People who perform resistive measurements usually define the transition temperature as the temperature where $R(T)$ drops by some factor which is not rigorously defined. Looking more carefully at Fig.4.23(top) we observe that the curves with different frequencies meet and form an envelope illustrated with a black dashed line. This envelope allows definition of an *ad hoc* critical temperature where the resistance ratio is 50%, i.e. $\tau_c \cong 0.28$.

While the temperature is lowered, the dissipative structure grows up until it reaches some maximum at $\tau_R^{max} \cong 0.15$, i.e. the dissipative dip in Fig.4.9 at $f = 1/3$ is the most pronounced at this temperature. A further temperature decrease, below τ_R^{max}, leads to the disappearance of the structure and the resistive ratio $R(1/3)/R(1/3-\Delta)$ recovers the same value as in the normal state (4.2). The disappearance of the structures at low temperature is attributed to magnetic effects (see sections 4.2.3 and 4.5). Surprisingly, the disappearance of the dissipative dip starts at a temperature τ_R^{max} which is at least one order of magnitude higher than the expected temperature for relevant magnetic effects (see section 2.3). Nonetheless the interpretation of these curves, which describe the evolution of the dissipative dip as defined by (4.2), is difficult and in particular the reentrance below τ_R^{max} since the behaviour of the frustrated state $f = 1/3 - \Delta$ is unknown.

The dynamics of the dissipative dip described above is related to that of the superfluid peak. We see from Fig.4.23(bottom) that for the lowest frequencies (below a few hundred Hertz) the relative inductive ratio saturates in a temperature range which grows up while the frequency is lowered. Actually, increasing the frequency results in a wider peak (see Fig.4.3), hence a bigger value of $L^{-1}(f = 1/3-\Delta)$. The ratio $L^{-1}(f = 1/3-\Delta)/L^{-1}(f = 1/3)$ is then increased and for $\omega/2\pi > 260$Hz, the relative inductive ratio is so decreased that it never reaches one. This behaviour depends on the choice of the Δ value. When the temperature is lowered below some frequency-dependent temperature $\tau_L(\omega)$, which defines an envelope indicated with the dashed line in Fig.4.23(bottom), the increase of $L^{-1}(f = 1/3)$ is slowed down until the superfluid peak reaches its most pronounced structure at $\tau_L^{max} \cong 0.22$. Then, as is the case for the dissipative structure, the superfluid peak disappears and at very low temperatures the relative ratio becomes vanishingly small. Notice that both structures (dissipative dip and superfluid peak) do not start to disappear at the same temperature: $\tau_L^{max} > \tau_R^{max}$.

Notice how the disappearance of the superfluid peak is emphasized for $\tau < 10^{-2}$, but in order to be able to interpret this curvature variation it would be necessary to know the processes governing the low temperature vortex pattern at $f = 1/3 - \Delta$.

Summary

The observed superfluid jump favours a phase transition driven by the unbinding of fractional vortices, instead of integer vortices. Moreover the temperature dependence of the dissipative dip in $Z(f)$ at $f = 1/3$ provides a criterion to define the transition temperature at $\tau_c \cong 0.28$, which is a value in good agreement with those predicted by numerical simulations [12] and by analytical calculations [13]. The interpretation of the disappearance of both structures, dissipative and superfluid, is still an open question since magnetic screening effects are expected to be relevant for lower temperatures.

4.4 $f = 1/6$ frustrated state

In the introductive section 4.1 and in particular in Figs.4.1 and 4.2, we saw that the most prominent structures in R_Z(f) and $L_G^{-1}(f)$ are those at $f = 1/6$ and at $f = 1/3$. In this section we pay more attention to the $f = 1/6$ state. We first discuss the ground state vortex pattern for which we propose some vortex configurations and then the possible phase transition (or crossover) observed for this vortex density.

4.4.1 Ground state vortex patterns

Being inspired by the ground state vortex patterns of the $f = 1/3$ state, we construct a striped state with half the vortex density. Cancelling one in two vortex lines of the $f = 1/3$ striped state we get the $f = 1/6$ striped state illustrated in Fig.4.24a). In the same way, starting with the zigzag state at $f = 1/3$, it is possible to construct a zigzag state at $f = 1/6$, as illustrated in Fig.4.24b). We did not find any way to construct a honeycomb state at $f = 1/6$.

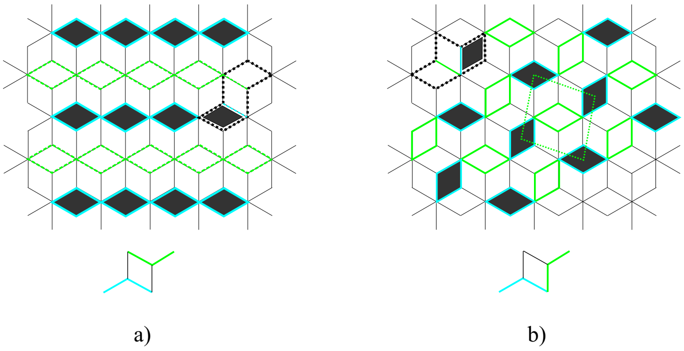

Figure 4.24: Ground state vortex pattern at $f = 1/6$. The elementary blocks are shown in dotted bold black lines and the related elementary pattern, whose repetitions allow construction of the phase configurations, are shown below. a) striped state. b) zigzag state with a rhombic vortex lattice (dotted green line).

Once the vortex configuration is found (black cells in Fig.4.24), the phase variables are obtained as usual by applying the fluxoid quantization which gives : $\theta_{ij} = 5\pi/12$ on blue bonds; $\theta_{ij} = -\pi/12$ on green bonds. The current conservation law implies $\theta_{ij} = 0$ on black bonds.

The energy per triple site is $\varepsilon = J[2 - \cos(\pi/12) - \cos(5\pi/12)] \cong 0.775J$.

The compactness of the elementary structures shown in Fig.4.24 could indicate that these states are robust against thermal fluctuations. This could explain why we observe such prominent peaks in the magnetoinductance at $f = 1/6$ even at high temperature; this points to an ordered state. Nevertheless, structure compactness alone is not an argument, as was demonstrated for the $f = 1/3$ state whose ground state elementary structures are even more compact. Indeed decoration experiments with wire networks on a dice lattice [8] did not exhibit any ordered domains. Notice that these measurements were performed with a small deviation from $f = 1/6$ which was estimated to be sufficient to induce an efficient change in the vortex configuration.

4.4.2 Possible phase transition

The frequency dependence of the superfluid density drop, from the phase coherent state to the normal state, is shown in Fig.4.25. We do not know if there is a phase transition driven by the vortex pairs unbinding mechanism, and if such is the case, what would be the topological charge of these vortices, i.e. integer or fractional vortices ? But, if there is a phase transition of the BKT type with pairs of integer vortices, then the zero frequency limit of the measured critical temperature, as shown in the inset of Fig.4.25, is $\tau_c(\omega \to 0) \cong 0.15$. If we look at the inverse sheet inductance normalized with respect to the single junction value, in other words the helicity modulus illustrated in Fig.4.25(bottom), we realize that the BKT prediction for integer vortices crosses the curves rather far away from the drop at $\tau < 0.1$. This casts doubt on the mechanism that involves integer vortices, favoring fractional vortices which would decrease the critical temperature, so long as the transition is of the BKT type !

The temperature dependence of the frustration structure at $f = 1/6$ has been investigated measuring the dissipative ratio $R_Z(f = 1/6)/R_Z(f = 1/6 + \Delta)$ and the relative inductive ratio $\Delta L_G^{-1}/L_G^{-1}(f = 1/6) = 1 - L_G^{-1}(f = 1/6 + \Delta)/L_G^{-1}(f = 1/6)$ (see Fig.4.9) . The values of the ratios in the normal state and at very low temperature are the same as those for $f = 1/3$ (4.2). In the normal state, the resistive ratio value is one and the inductive ratio value is zero: the same applies at low temperature due to magnetic effects. The dissipative dip at $f = 1/6$ (Fig.4.26) appears at $\tau \approx 1$. This seems in contradiction with Fig.4.9 where we observe no structures for $\tau \approx 0.34$ and above. Actually, the signal over noise ratio is much higher in temperature measurements (Fig.4.26) than in frustration measurements (Fig.4.9), since the thermal switch is closed in the earlier case. This explains why we can distinguish $R_Z(f = 1/6)$ from $R_Z(f = 1/6 + \Delta)$. The general trends of both dissipative and inductive ratios as in Fig.4.26 reflect the same kind of behaviour as in the $f = 1/3$ state (Fig.4.23), i.e. the dissipative dip becomes more and more pronounced while the temperature is lowered, until some characteristic temperature τ_{max} is reached. Simultaneously the superfluid peak increases until it reaches some maximum relative ratio.
In the $f = 1/3$ state, the phase transition is observable since the magnetic energy is the dominating one for temperatures lower than the critical one. If some identical scenario applies for $f = 1/6$, we could define the critical temperature in the same way as for $f = 1/3$: the dissipative ratio $R_Z(1/6)/R_Z(1/6 + \Delta) = 50\%$ at $\tau_c \cong 0.44$.

As is the case in the $f = 1/3$ frustrated state, a curvature change is observed in the inductive ratio in the same temperature range, $\tau \approx 10^{-2}$, indicating an enhancement of the disappearance of the structure.

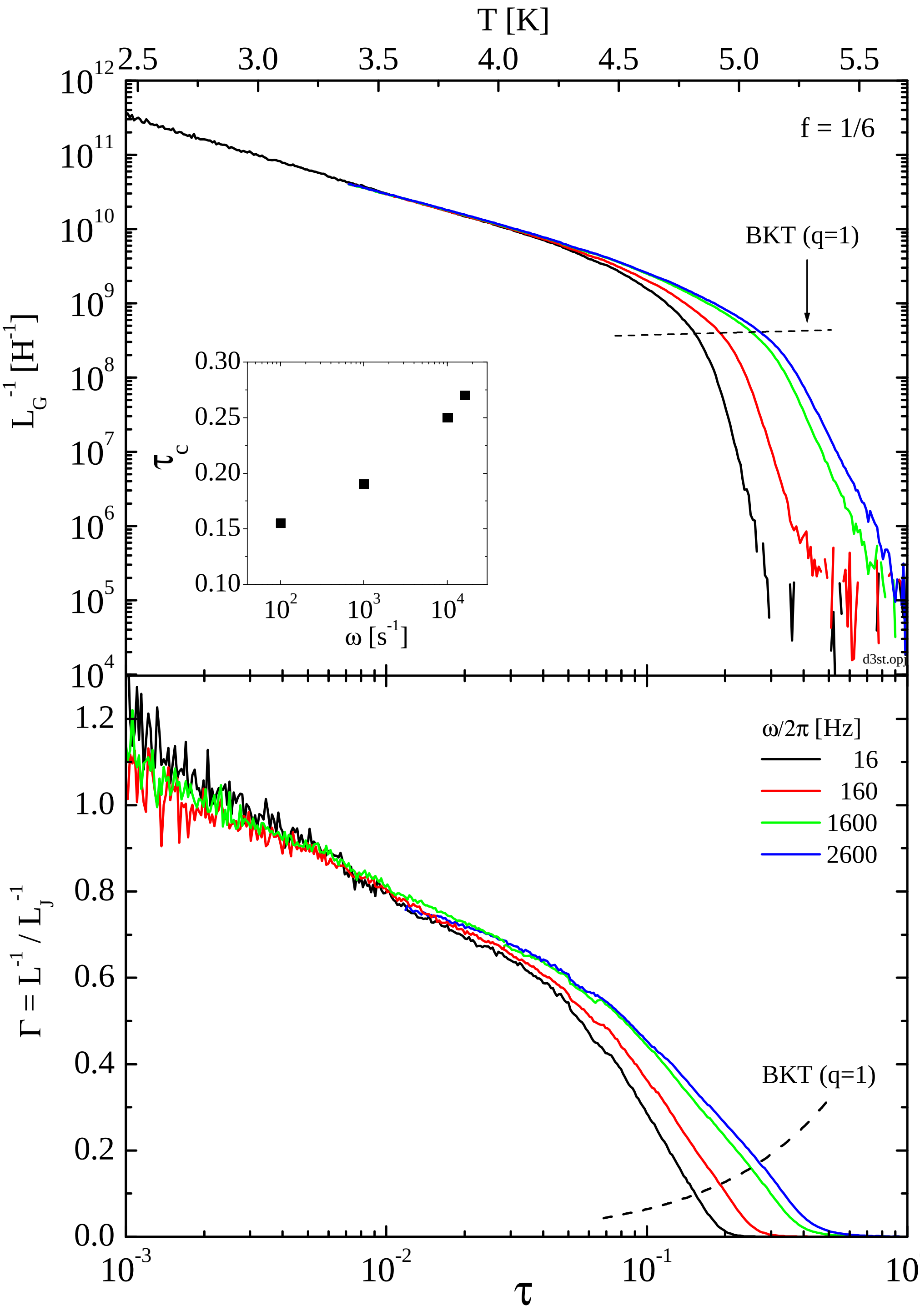

Figure 4.25: [sample3] Inverse sheet inductance (top) and dynamic helicity modulus (bottom) vs real and reduced temperature at $f = 1/6$. The inset shows the measured BKT critical temperatures for integer vortices.

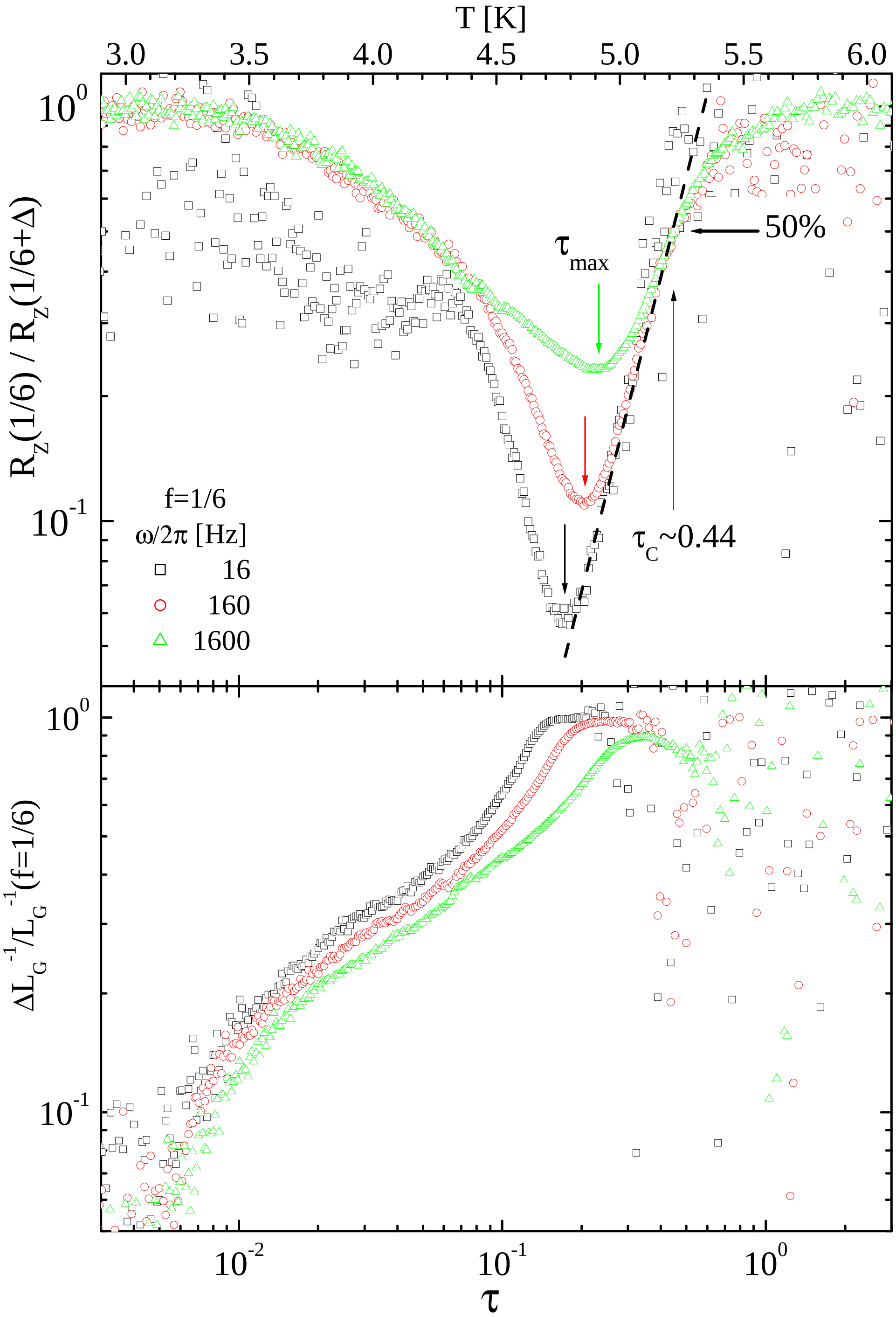

Figure 4.26: [sample3] Evolution of the $f = 1/6$ structure in $Z(f)$.
Top: dissipative dip and Bottom: superfluid peak.

4.5 Comparisons between selected frustrated states

In the previous sections we saw that the structures in R_Z(f) and $L_G^{-1}(f)$ at $f = 1/6$ are nearly as prominent as those at $f = 1/3$. Looking more carefully at measurements with a higher frustration resolution like those in Fig.4.9(bottom), we see that in the narrow temperature range where the structures appear ($\tau \approx 0.22$), the dissipative dip at $f = 1/6$ is almost as pronounced as the one at $f = 1/3$. But then when the temperature is lowered, the phase coherent state at $f = 1/6$ is less pronounced than at $f = 1/3$, where the dissipative structure is deeper and the superfluid peak is higher. The $f = 1/3$ state is also more robust against frequency-induced fluctuations, as illustrated in Fig.4.3. The temperature behaviours of the superfluid responses and the evolutions of the frustration structures are very similar for both $f = 1/3$ and $f = 1/6$ states. Moreover, the ground state family is almost identical. These features could lead to the conclusion that in spite of the well pronounced structures observed in section 4.1, there is no true long range order in the $f = 1/6$ state down to low temperature as is the case for the $f = 1/3$ state. In any case this conjecture should be confirmed by analytical investigations of the $f = 1/6$ state, or even by numerical simulations if the time and size requirements can be fulfilled.

The fully frustrated state shares some of these characteristics, i.e. the low temperature vortex-pattern selection is predicted to be driven by magnetic effects. At $f = 1/2$ these effects do not allow us to observe a genuine phase transition, but a regime crossover from a vortex liquid state to a frozen vortex liquid state. This is confirmed by the glass-like dynamics observed at low temperature. Moreover, the fact that this dynamics is common to many frustrated states enhances the role of the sample nature, i.e. junction arrays with strong variations in the coupling constants.

In the case of fully frustrated JJAs it is not possible to talk of *dynamic localization* of the wave function or formation of *Aharonohv-Bohm cages*, as is the case with wire networks. The phase coherence loss is due to the nature of the ground state which is highly degenerate. We did not observe any vortex pattern ordering which would appear as a coherent state and as a peak in the superfluid response: such a structure could be hidden by magnetic effects.

Comparing the three studied frustrated states, the $f = 1/2$ ground state has the higher energy ($\varepsilon = 1.27J$) followed by the $f = 1/3$ ground state ($\varepsilon = 1J$) and finally the one at $f = 1/6$ ($\varepsilon = 0.775J$). A more interesting quantity to compare between these states is their superconducting phase coherence, i.e. the sheet inductance, or equivalently the helicity modulus.

4.5.1 Sheet magnetoinductance in frozen vortex liquid

We extracted the ratio of the inverse sheet inductances for a few frustrated states from the frustration measurements, i.e. $L^{-1}(f_1)/L^{-1}(f_2)$ for $f_1, f_2 = 0, 1/6, 1/3, 1/2$. We then compared these measured ratios with the values calculated in the ground states (mean field calculation).

Fig.4.27 shows the measurements for three decades of frequency ($\omega/2\pi = 12$Hz,1.6KHz and 16KHz). The figure exhibits, in addition to the $L^{-1}(f)$ curves, tables with the inductance values at selected frustrations and their relative ratios. The temperature dependencies of the ratios $L^{-1}(f_1)/L^{-1}(f_2)$ are illustrated for each frequency in Fig.4.28.

While the temperature is decreased, the frustration dependence of $L(f)$ is suppressed, i.e. the ratios tend to one, for the three decades of frequency. This is a clear manifestation of the screening current effects. According to Fig.2.12, the ratios should merge into one for temperatures below $\tau \approx 0.002$ ($\Lambda_{eff} = a$). Indeed, the same tendency is observed for the highest frequency. This does not forbid the JJA to be sensitive to magnetic effects for higher temperatures. Fig.4.29 shows the frequency dependence for the lowest temperature ($\tau = 0.01$). As we already saw in previous sections, the excitation frequency and the temperature are, in some sense, conjugate variables. If the frequency is increased, the related relaxation time to equilibrium (with external excitation) is decreased, i.e. the phase fluctuations are decreased. Thus the observed frequency behaviour (Fig.4.29) is similar to the one for a fixed frequency with decreasing thermal fluctuations.

The same ratios were calculated in the low temperature vortex pattern, i.e. a mean field calculation based on the ground states illustrated in the previous sections.

Mean field calculation of $L(f)$

At very low temperature where thermal fluctuations can be neglected, the JJA is equivalent to a network of inductances $L_{ij}(\theta_{ij})$ (see section 1.3, equation 1.14). The phase variables θ_{ij} are known in the frustrated ground states (see sections 4.2, 4.3 and 4.4). In order to obtain the sheet inductance $L(f)$, it is necessary to first transform the frustrated inductance network (L_{ij}) into an anisotropic triangular lattice (L'_{ij}) using the star-triangle transformation [67]. Then, the sheet inductance is calculated applying Kirchhoff's laws to the elementary cell of the transformed L'_{ij}. (The values of the sheet magnetoinductances $L(f)$ are summarized in Table 4.1)

Unfrustrated state $f = 0$. This is the most simple case since all bonds of the (transformed) triangular lattice have the same inductance value $L(0) = (\sqrt{3}/2)L_J$.

Fully frustrated state $f = 1/2$. Applying the star-triangle transformation to the four periodic ground states, we obtain two different configurations each with two inductance components, i.e. two main directions (Fig.4.30).

The JJA behaves as a two component inductance network $L(L_x, L_y)$. In the framework of our measurement technique, we would say that we measure a mutual inductance change which is a function of a two component impedance $\delta M(Z_1, Z_2)$.

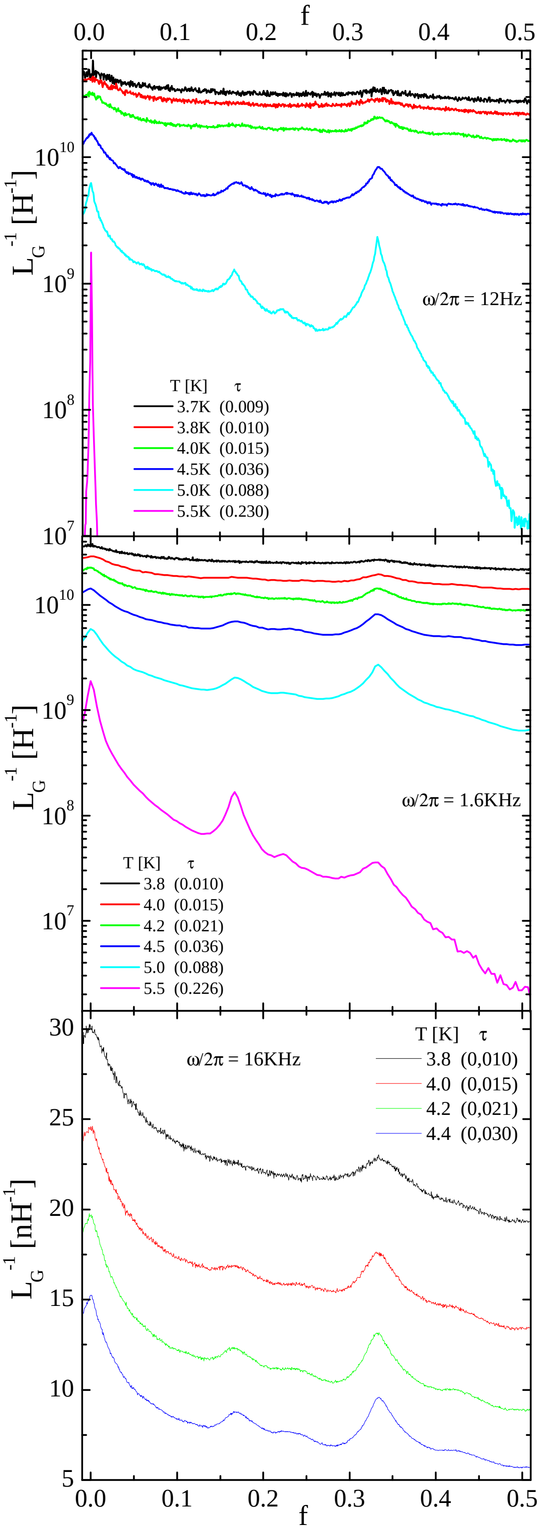

ω/2π = 12Hz

L^{-1} [H^{-1}]

	f=0	f=1/6	f=1/3	f=1/2
T=3.7K	4.6E10	3.3E10	3.5E10	2.8E10
T=3.8K	4.2E10	2.7E10	2.85E10	2.2E10
T=4.0K	3.25E10	1.8E10	2.05E10	1.35E10
T=4.5K	1.55E10	6.3E9	8.35E9	3.5E9
T=5.0K	6.25E9	1.25E9	2.3E9	1.3E8
T=5.5K	1.75E9	---	---	---

$L^{-1}(f_1)/L^{-1}(f_2)$

f_1/f_2	(0)/(1/6)	(0)/(1/3)	(0)/(1/2)	(1/6)/(1/3)	(1/6)/(1/2)	(1/3)/(1/2)
GS	**1.57**	**1.67**	**2.12**	**1.06**	**1.35**	**1.27**
T=3.7K	1.40	1.31	1.64	0.94	1.18	1.25
T=3.8K	1.56	1.47	1.91	0.95	1.23	1.30
T=4.0K	1.81	1.59	2.41	0.88	1.33	1.52
T=4.5K	2.46	1.86	4.43	0.75	1.8	2.39
T=5.0K	5	2.72	48	0.54	9.62	17

ω/2π = 1.6KHz

L^{-1} [H^{-1}]

	f=0	f=1/6	f=1/3	f=1/2
T=3.8K	3.65E10	2.55E10	2.7E10	2.15E10
T=4.0K	2.9E10	1.85E10	1.95E10	1.4E10
T=4.2K	2.25E10	1.28E10	1.42E10	0.88E10
T=4.5K	1.45E10	0.72E10	0.85E10	0.42E10
T=5.0K	0.61E10	0.21E10	0.29E10	0.64E9
T=5.5K	2E9	0.17E9	0.37E8	2E6

$L^{-1}(f_1)/L^{-1}(f_2)$

f_1/f_2	(0)/(1/6)	(0)/(1/3)	(0)/(1/2)	(1/6)/(1/3)	(1/6)/(1/2)	(1/3)/(1/2)
GS	**1.57**	**1.67**	**2.12**	**1.06**	**1.35**	**1.27**
T=3.8K	1.43	1.35	1.7	0.94	1.19	1.26
T=4.0K	1.57	1.48	2.05	0.94	1.3	1.38
T=4.2K	1.76	1.58	2.56	0.9	1.45	1.61
T=4.5K	2.04	1.72	3.4	0.84	1.67	1.97
T=5.0K	2.87	2.14	9	0.75	3.15	4.23
T=5.5K	11.25	52	950	4.7	85	18

ω/2π = 16KHz

L^{-1} [H^{-1}]

	f=0	f=1/6	f=1/3	f=1/2
T=3.8K	3E10	2.25E10	2.3E10	1.93E10
T=4.0K	2.45E10	1.69E10	1.76E10	1.34E10
T=4.2K	1.97E10	1.23E10	1.31E10	0.89E10
T=4.4K	1.53E10	0.88E10	0.96E10	0.57E10

$L^{-1}(f_1)/L^{-1}(f_2)$

f_1/f_2	(0)/(1/6)	(0)/(1/3)	(0)/(1/2)	(1/6)/(1/3)	(1/6)/(1/2)	(1/3)/(1/2)
GS	**1.57**	**1.67**	**2.12**	**1.06**	**1.35**	**1.27**
T=3.8K	1.33	1.3	1.55	0.98	1.17	1.19
T=4.0K	1.45	1.39	1.83	0.96	1.26	1.31
T=4.2K	1.6	1.5	2.2	0.94	1.38	1.47
T=4.4K	1.75	1.6	2.68	0.92	1.54	1.68

Figure 4.27: [sample2] Inverse sheet inductance ratios for $\omega/2\pi$ = 12Hz, 1.6KHz and 16KHz, measured at low temperature. The values are reported in the right panels. The bold numbers are the mean field calculated sheet inductance ratios, i.e. in the ground states (GS).

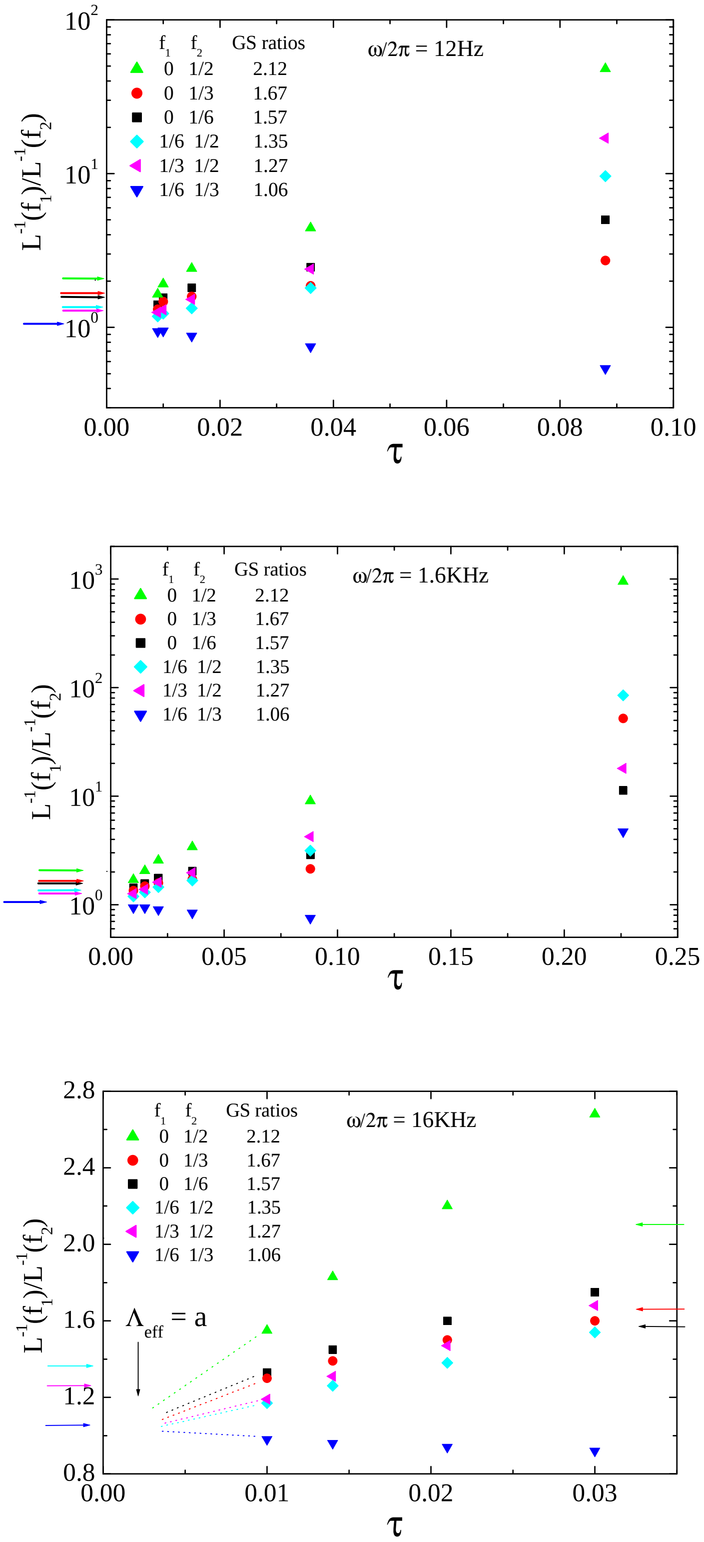

Figure 4.28: [sample2] Inverse sheet inductance ratios versus reduced temperature. The colored arrows indicate the ground state (GS) ratios. The dotted lines are not fits but only indicate the low temperature trend.

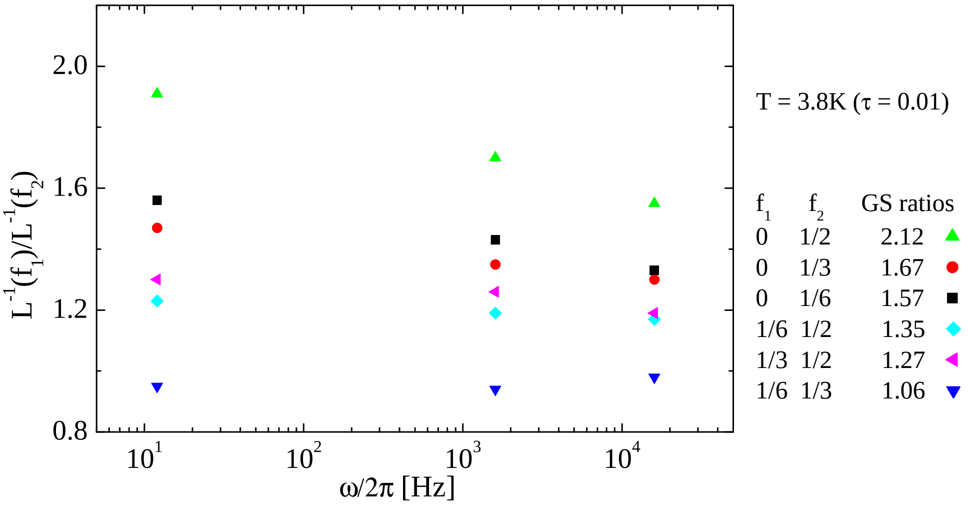

Figure 4.29: [sample2] Inverse sheet inductance ratios versus frequency at the lowest temperature.

The expression (3.6) in section 3.2.4 can be generalized to the case of an anisotropic film

$$\delta M(Z_1, Z_2) \approx \frac{M_{ss}}{\left(1+\dfrac{Z_1}{i\omega M_c}\right)^{1/2} \cdot \left(1+\dfrac{Z_2}{i\omega M_c}\right)^{1/2}} \tag{4.3}$$

At low temperature, $R_{Z_i} \ll \omega L_{Z_i}$ and $L_{Z_i}/M_c \ll 1$;

$$\delta M(Z_1, Z_2)_{T \ll T_c} \approx \frac{M_{ss}}{1 + L_a/M_c} \qquad L_a = \frac{1}{2}(L_1 + L_2) \qquad i = 1, 2$$

The arithmetic mean must be applied. This is valid at low temperature and for high frequencies, i.e. in a regime where the phase fluctuations can be neglected.

At high temperature, $Z_i/\omega M_c \gg 1$ and $L_{Z_i}/M_c \sim 1$;

$$\delta M(Z_1, Z_2)_{T \leq T_c} \approx \frac{i M_{ss} \omega M_c}{Z_g} \qquad Z_g = \sqrt{Z_1 \cdot Z_2}$$

The geometric mean must be applied.

We can anticipate that the arithmetic and the geometric means are almost the same, and due to our experimental resolution we are not sensitive to the small differences between them which, moreover, are irrelevant because of the suppression of the frustration dependence in $L(f)$ due to magnetic effects.

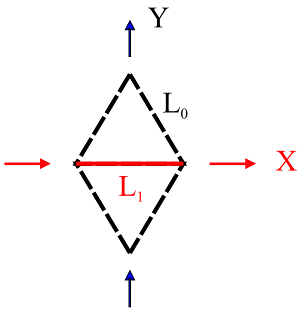

Figure 4.30: Star-triangle transformed fully frustrated ground state. The sheet inductance has two components related to the X and Y directions (L_x, L_y).

In the framework of the frustrated XY model the $f = 1/3$ GS was shown to be disordered (see section 4.3.1). In the case of the fully frustrated state, because of the inefficiency of the degeneracy removal mechanism and the size requirement the vortex-pattern can also be assumed as disordered. It was shown [110] that in a 2D disordered system with two phases ($\equiv L_x$ and L_y) equally distributed, the conductivity is given by the geometric mean of both phase conductivities. In our case this means that even at low temperature and high frequency the $f = 1/3$ and $f = 1/2$ states, which are two component random inductance networks, the geometric mean should be applied (instead of the arithmetic mean).

The state with no DWs (Fig.4.5b)) and the 1D network of 60° ZEDWs (Fig.4.7b)) are transformed into the same triangular lattice with $L_0 = (3\sqrt{3}/2)L_J$ and $L_1 = (3\sqrt{3})L_J$. In that case $X \perp 60°ZEDWs$ and $Y//60°ZEDWs$ with $L_x = (3/2)L_J, L_y = (9/4)L_J$ leading to the arithmetic mean $L_a = 1.875L_J$ and the geometric mean $L_g = [3\sqrt{3}/(2\sqrt{2})]L_J \cong 1.84L_J$.
The state with the 1D network of horizontal ZEDWs (Fig.4.6b)) and the 2D network of horizontal and 60° ZEDWs (Fig.4.8) are transformed into the same triangular lattice, but in that case $X//horizontal\ ZEDWs$ and $Y//60°ZEDWs$ with $L_x = 2L_J, L_y = (27/16)L_J$ leading to the arithmetic mean $L_a \cong 1.84L_J$ and the geometric mean $L_g = [3\sqrt{3}/(2\sqrt{2})]L_J \cong 1.84L_J$.

The four periodic states share the same geometric mean $L_g(1/2) = [3\sqrt{3}/(2\sqrt{2})]L_J \cong 1.84L_J$.

Frustrated state $f = 1/3$. The sheet inductance of the $f = 1/3$ state has also two components (L_x, L_y). The elementary cell of the striped state, which is selected by the screening current effects, looks like Fig.4.30 with $L_0 = 2L_J$ and $L_1 = 4L_J$. Then $L_x = \sqrt{3}L_J$ and $L_y = (2/\sqrt{3})L_J$. The arithmetic mean $L_a = [5/(2\sqrt{3})]L_J \cong 1.44L_J$ and the geometric mean which is the same for the zigzag state, is $L_g = \sqrt{2}L_J \cong 1.41L_J$. In addition we can give the geometric mean for the honeycomb sate $L_g = (4\sqrt{3}/5)L_J \cong 1.39L_J$.

Frustrated state $f = 1/6$. Once the star-triangle transformation is applied to the $f = 1/6$ state, the triangular lattice contains, as for the previous cases, bonds with three inductance values. The two considered directions of current in the striped state (Fig.4.24) are parallel (L_x) and perpendicular (L_y) to the stripes. One can certainly apply Kirchhoff's laws to find the sheet value: $L_0 = 2L_J, L_1 = 2[1/(2+\sqrt{3})]\left[1 + [1/(2+\sqrt{3})]\right] L_J \cong 0.68 L_J, L_2 = 2[1/(2-\sqrt{3})]\left[1 + [1/(2-\sqrt{3})]\right] L_J \cong 35.32 L_J$. But for the chosen current directions, one can introduce a unique parameter: the voltage deviation (per site) from the value in an uniform system (all identical inductances) [111]. Fig.4.31 shows how the voltage deviations (on each site) are distributed in the transformed triangular lattice. The sheet inductance is obtained by writing the current conservation on a single site.

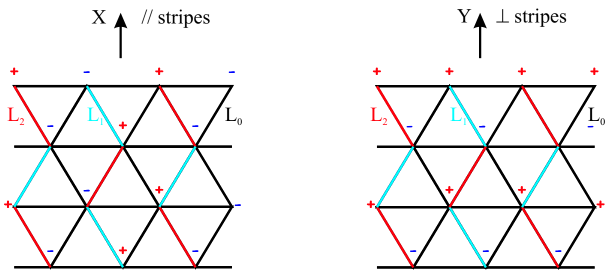

a) b)

Figure 4.31: Star-triangle transformed $f = 1/6$ striped ground state. The colored (black, blue and red) bonds show the inductance distribution. The signs (±) refer as the voltage deviations which have the same absolute value on all sites. a) current direction parallel to the stripes. b) current direction perpendicular to the stripes.

$$L_x = (1/\sqrt{3})\left[(L_0^{-1} + L_1^{-1})^{-1} + \left(L_0^{-1} + L_2^{-1}\right)^{-1}\right] L_J$$

$$L_y = \sqrt{3}\left[2L_0^{-1} + \left[L_0/2 + (L_1^{-1} + L_2^{-1})^{-1}\right]^{-1}\right]^{-1} L_J$$

The arithmetic mean is $L_a \cong 1.36$ and the geometric mean $L_g \cong 1.35$.

Sheet inductance $L(f)$ in the ground states - Summary

The magnetoinductances calculated in the ground states of the frustrated XY model are summarized in Table 4.1.

The inverse sheet inductance $L^{-1}(f)$, and hence the helicity modulus, grows up while the frustration is decreased until it reaches the unfrustrated value. Fig.4.32 shows that for the lowest temperature, for which the frustration structures are almost suppressed (Fig.4.27), there are still too many thermal fluctuations and thus we are far from the mean field calculated values. Indeed at high temperature the data are strongly affected by thermal fluctuations, and at low temperature by magnetic screening effects. For all

f	0	1/6	1/3	1/2
mean $< L >$ $[L_J]$	(isotropic) 0.87	$L_a = 1.36$	$L_g = 1.41$	$L_g = 1.84$

Table 4.1: Sheet inductance in the ground states $L(f)$. These calculated values are compared to the measured ones in Fig.4.32.

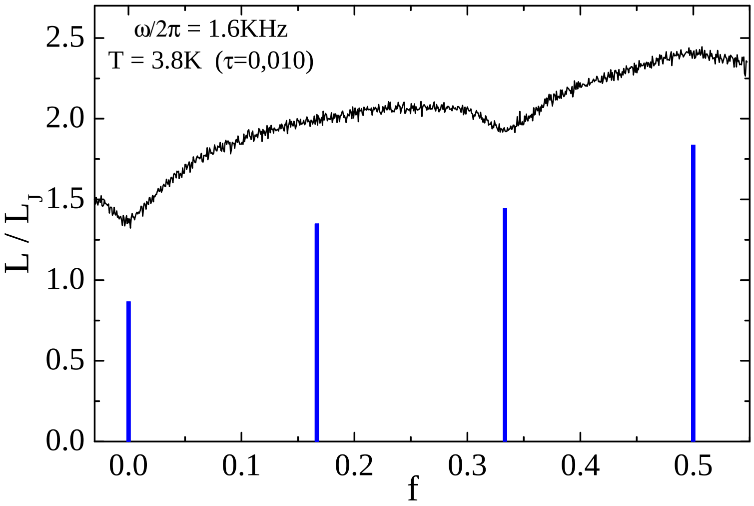

Figure 4.32: Measured sheet inductance $L(f)$ normalized with respect to the single junction inductance at zero field $L_J(T)$ as a function of the frustration. The mean field calculated values, at the selected frustrations, are indicated with blue bars.

selected ratios of Fig.4.28, except for $L(1/3)/L(1/6)$, the low temperature limit data are beyond the mean field calculated values. Surprisingly, the $L(1/3)/L(1/6)$ ratio values do not cross the mean field one, at least down to $\tau = 0.01$. The first measurements (Fig.4.1) show that at high temperature $L(1/6) < L(1/3)$, and while the temperature is lowered, the inequality is reversed, $L(1/6) > L(1/3)$, as confirmed by Fig.4.32 but in contradiction with the mean field calculation (Table 4.1). The ratio inversion happens in the temperature range $0.088 < \tau < 0.22$ (Fig.4.27). This might be due to the magnetic screening effects which would be more efficient at $f = 1/3$ than at $f = 1/6$. The reason for such behaviour may be the selection of a ground state vortex pattern by the magnetic energy which happens, at $f = 1/3$, at a higher temperature than at $f = 1/6$. But the associated transition temperature is predicted to be around $\tau = 0.01$ for the $f = 1/3$ state. Thus this behaviour remains controversial until the effects of the screening currents can be quantitatively predicted.

4.6 Vortex motion in the liquid state

In section 4.2, dedicated to the fully frustrated state, we introduced the idea of a crossover from a vortex liquid to a frozen vortex liquid regime. This was illustrated with Fig.4.11 which clearly shows the sharp (exponential) rise of the sheet resistance, from a high temperature phase dominated by thermally activated vortices to a lower temperature glass-like vortex phase (see section 4.2.4). Fig.4.33 illustrates this crossover at nominally zero field, i.e. the best "$f = 0$". The regime crossover in the dynamic response, possible at sufficiently short time scales, was already observed in ultrathin YBCO films [96].

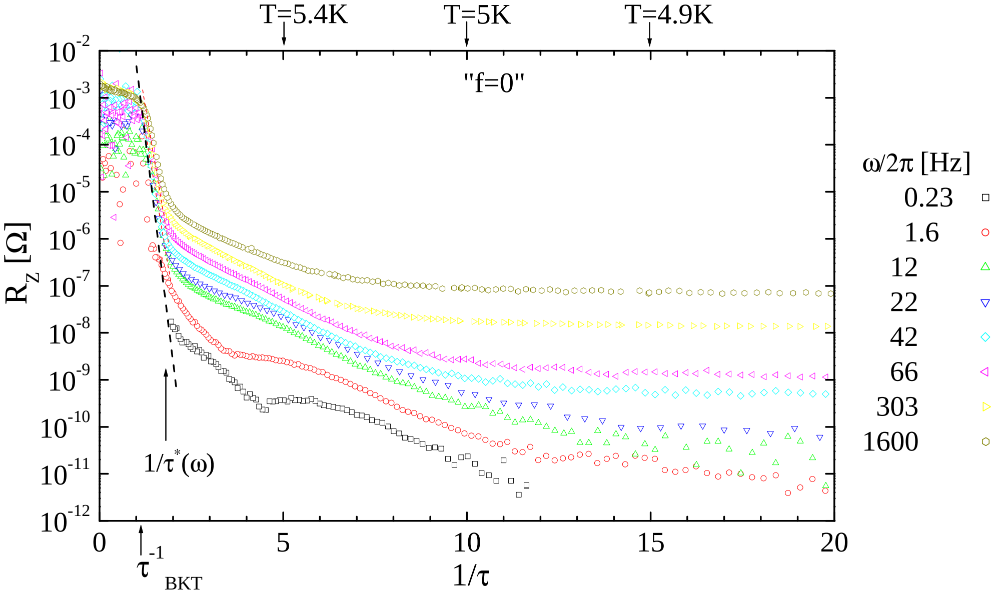

Figure 4.33: [sample2] Sheet resistance versus inverse reduced temperature at zero frustration, showing the thermally activated nature of the resistive transition below ($1/\tau^*(\omega)$). The bump above $1/\tau^*(\omega)$ observable for the lowest frequencies was discussed in section 3.7.

Above $\tau^*(\omega)$, in the thermal nucleation regime ($\tau^*(\omega) < \tau \leq \tau_{BKT}$), the single vortices experience a barrier-limited diffusion [112]. The contribution to the net sheet impedance Z due to the Brownian motion of non interacting (single) vortices in the potential energy lanscape created by the underlying lattice is [113]:

$$Z_v = R_v(T, f) + i\omega L_v(T, f) \approx R_v(T, f) = \phi_0^2\ n(T, f)\ \mu(T, f) \tag{4.4}$$

where n and μ are respectively the vortex density and mobility (in the temperature range of interest $0.5 \leq \tau \leq 0.8$, $R_Z \gg \omega L_Z$). The vortex mobility has a thermally activated form

$$\mu(T, f) = \mu_0 \exp[-E_b(f)/k_B T] \qquad \mu_0 = (\sqrt{3}/2)(a/\phi_0)^2 R_N \tag{4.5}$$

The frustration-dependent barrier energy $E_b(f)$ [56] is written in units of the coupling constant $J(T)$; $\Delta(f) = E_b(f)/J(T)$, thus:

$$\mu(\tau, f) = \mu_0 \exp[-\Delta(f)/\tau] \tag{4.6}$$

The total vortex density ($n(T, f)$) is given by the thermally nucleated vortices (n_T) and the field induced vortices (n_f).

4.6.1 Thermally nucleated vortices

At strictly zero field, the density of free vortices nucleated by thermal fluctuations, for $\tau < \tau_{BKT}$, is [114]:

$$n(T, 0) \equiv n_T = \frac{\beta}{(\sqrt{3}/2)a^2} \left(\frac{L}{a}\right)^{-\pi/\tau} \exp[-\pi/\tau] \tag{4.7}$$

The power law exponent comes from the Boltzmann factor with $E_{vortex} = -\pi J\ \ln(L/a)$; the exponential term is a cut-off due to the finite size of the sample; β is a constant of the order of one; $L/a \cong 1000$ is the sample size over lattice constant ratio.

4.6.2 Field-induced vortices

For a residual frustration $f \equiv \delta f \ll 1$, the density of free vortices induced by the applied magnetic field B is:

$$n(0, f) \equiv n_f = \frac{B}{\phi_0} = \frac{\delta f}{a^2}\frac{2}{\sqrt{3}} \tag{4.8}$$

The same result applies for a commensurate frustrated state $f^\star$ with $|f^\star - \delta f| \ll 1$. In that case, the induced vortices are free to move on the top of the commensurate state at $f^\star$.

4.6.3 Energy barriers

Putting together (4.8),(4.7), (4.6) and (4.5) in the vortex resistance expression (4.4), we get :

$$R_v(\tau, f) = \left[\beta \left(\frac{L}{a}\right)^{-\pi/\tau} \exp[-\pi/\tau] + \delta f\right] R_N\ \exp[-\Delta/\tau] \tag{4.9}$$

In the temperature range of interest, the thermal contribution to the vortex density is negligible when compared to the field contribution. The left term in the parenthesis is negligible when compared to the residual frustration $\delta f \approx 10^{-3}$ (see section 3.7.1). Then :

$$R_v(\tau, f) = \delta f R_N \exp[-\Delta/\tau] \tag{4.10}$$

This expression is valid for $\tau < \tau_{BKT}$. At the limit $\tau \to \tau_{BKT}$, $R_v = \delta f R_N$, where R_N is the normal state junction resistance. The thermal energy $k_B T \gg E_b$ and the dissipation

is due to vortex flux flow.
The magnitude of the energy barrier at zero frustration extracted from the slope of the fit in Fig.4.33 (dashed line) is $\Delta \cong 13J$. The barrier energy at zero field, calculated using [22], is slightly smaller than the one for square arrays: $\Delta(dice) \cong 0.19$, this value having been confirmed by four probe measurements of SIS JJAs [115]. The barrier energies measured at selected frustrated states (Figs.4.34 and 4.11) are summarized in Table 4.2.

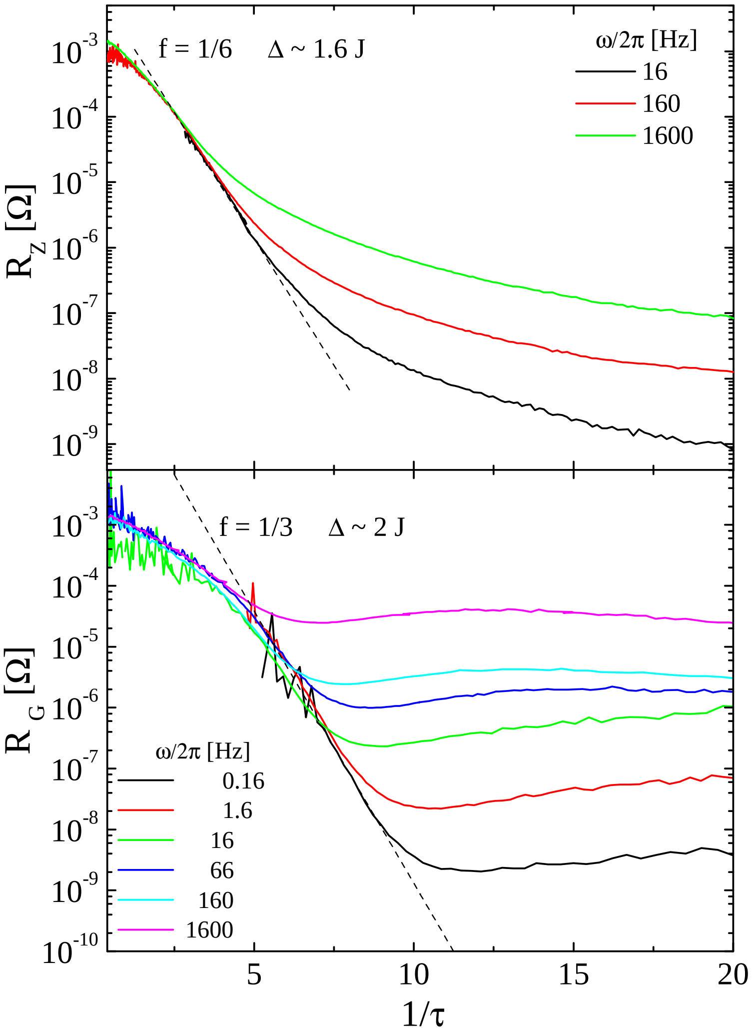

Figure 4.34: Sheet resistance versus inverse reduced temperature at $f = 1/6$ (top,[sample3]) and $f = 1/3$ (bottom,[sample2]). $\mathrm{Re}\{G\}^{-1}(1/\tau)$ exhibits more clearly the crossover temperature than $\mathrm{Re}\{Z\}(1/\tau)$.

According to the model of an isolated particle in a potential landscape, the magnetoresistance $R_Z(f)$ has a linear behaviour versus f (4.10). But $R_Z(f) \propto f^1$ only in a narrow

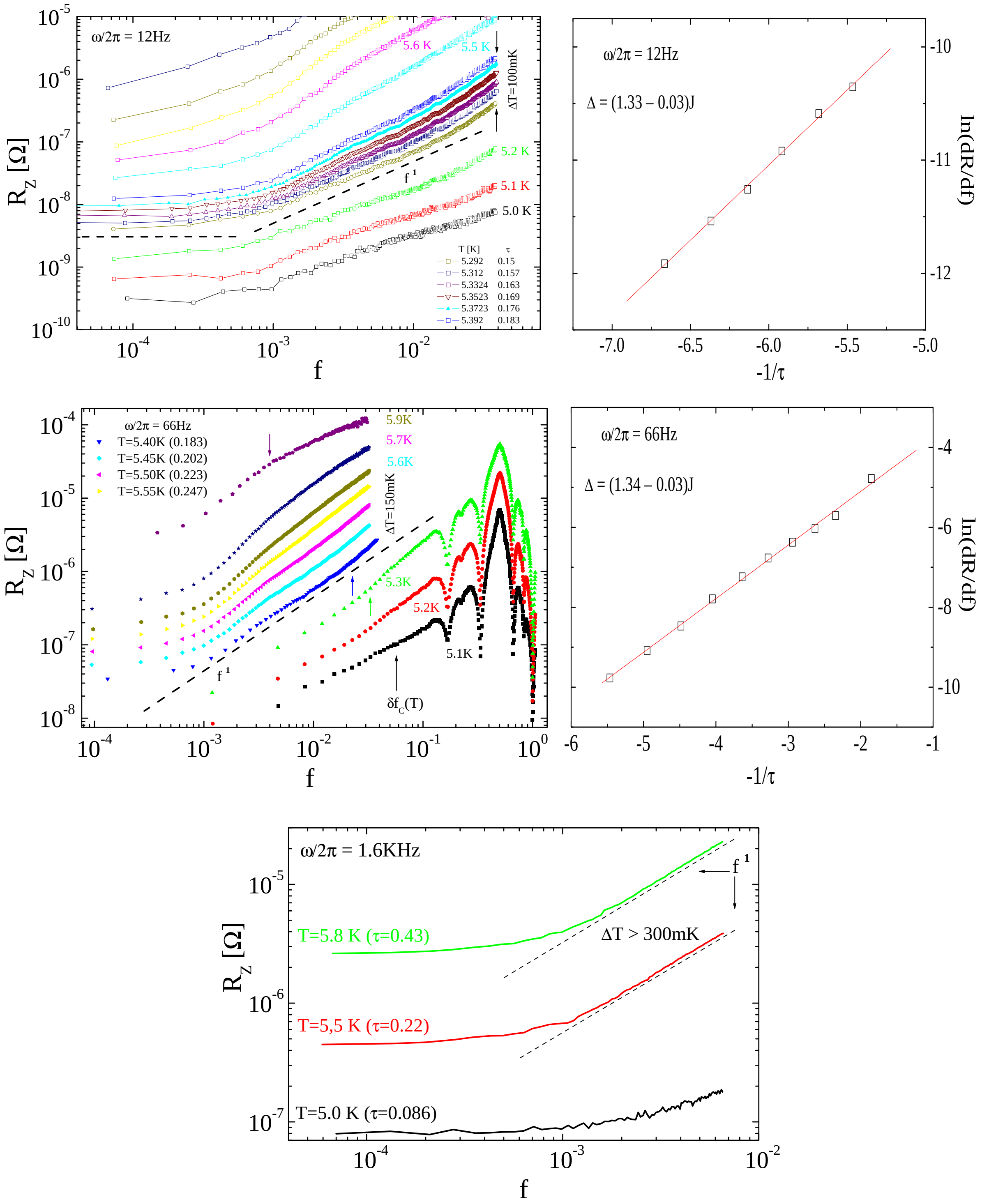

Figure 4.35: [sample2] Magnetoresistance near zero field at frequency $\omega/2\pi = 12$Hz, 66Hz and 1.6KHz. The colored arrows of the middle figure (for $\omega/2\pi = 66$Hz) indicate the upper limit $\delta f_c(T,\omega)$ below which the resistance is linear.

f	0	1/6	1/3	1/2
Barrier energy Δ $[J]$	13	1.6	2	0.9

Table 4.2: Barrier energies for selected frustrated states.

temperature range which is below $\tau^\star(\omega)$, as illustrated in Figs.4.35. These figures show that when the frequency is increased, the temperature range where $R_Z(f)$ is effectively proportional to f^1 (i.e. with a slope of one in log-log scales) is shifted to higher temperature and simultaneously becomes larger. Thus at zero field, above $\tau^\star(\omega)$ (Fig.4.33), the deviation from linearity for $f > \delta f_c$ illustrated in Figs.4.35, indicates an interaction between vortices which leads to a reduction of thermal activation and an increase of the single vortex energy barrier [56, 80]. The deviation from linearity near $f = 0$ results from residual field (see Fig.3.22); the upper limit δf_c below which the resistance is linear versus f, is observed to decrease with the temperature.
It is interesting to notice that the temperature range where $R \propto f^1$ (Figs.4.35) corresponds to the temperature range where the bump in $R(T)$ appears (see section 3.7), below $\tau^\star(\omega)$ (Fig.4.33). Indeed the dissipative process related to the bump was associated with single vortex motion. The barrier energy extracted from the derivative of expression (4.10), $\ln[dR/df]$ illustrated in Figs.4.35, is $\Delta \cong 1.3J$: this value is of the same order of the barrier energy measured in triangular JJAs [105], above $\tau^\star$. We have shown in section 3.7 that with only a few percent (or less) frustration, the dissipative process (the bump) may hide the BKT transition. This could explain the lower barrier energy measured in $R_Z(T)$ of [105]; indeed both types of samples (in this work and in [105]) were fabricated in the same way with the same material and in the same laboratory !

The barrier energy extracted from $R_Z(T)$ in the unfrustrated vortex liquid regime ($\tau > \tau^\star(\omega)$) is much higher than the predicted value for an infinite dice lattice; the same discrepancy was also observed for triangular arrays. Moreover, in this temperature range the nonlinearity of R versus f could be the signature of an interaction between vortices [80] which would lead to higher energy barriers. Another possible explanation could be related to a vortex diffusion controlled by surface barriers [116]: such barriers result from the competition between the attraction of vortices to the surface (force image effect) and their repulsion from the surface due to the interaction with the screening currents. In the 2D case, the effective barrier energy depends logarithmically on the frustration [117]. Such effects have been considered in layered high temperature superconductors (HTSC), but because of the small size of our samples they could be of significant importance.

Conclusions

This thesis was dedicated to the effects of the interplay between the applied magnetic field and the lattice geometry of Josephson junction arrays in the peculiar case of a dice lattice.

We started with a careful characterization of the samples. In particular, the values of the single junction critical current measured with a standard four probe method are in very good agreement with those obtained by the two-coil mutual inductance technique [94] we used to measure the transport properties of SNS JJAs. Magnetoimpedance curves $Z(f)$ show very pronounced structures at rational values of $f = 1/3, 1/6, 1/9, ...$ pointing to vortex states with a high degree of superconducting phase coherence, and are robust against thermal fluctuations, in particular for the vortex density $f = 1/3$. On the contrary, at full frustration ($f = 1/2$) the deep minimum in the inverse magnetoinductance $L^{-1}(f)$ indicates a strong suppression of the phase coherence associated with a huge dissipation shown by magnetoresitance curves $R(f)$. Comparisons between the fully frustrated state ($f = 1/2$), where the phase coherence is almost suppressed, and the strong coherent state $f = 1/3$ revealed a rich variety of phenomena. In order to understand these experimental facts, the features of the ground states at the selected vortex densities ($f = 1/3$ and $f = 1/2$) were considered.

The fully frustrated XY model on the dice lattice exhibits a ground state with well developed accidental degeneracy associated with the existence of zero energy domain walls [10]. At high temperature these domain walls form kinks and cross each other, leading to an entangled network of domain walls. Such kinks and intersections are points defects which weaken the phase coherence. Thus the nature of the observed depression in $L^{-1}(f)$ and the huge peak in $R(f)$ at $f = 1/2$ is quite different from the nature of the observations in fully frustrated superconducting wire networks [6]. In that case, the minimum in the transition line $T_c(f)$ and the pronounced depression of the critical current $I_c(f)$ at $f = 1/2$ are attributed to a localization phenomenon resulting from destructive quantum interferences of the Ginzburg-Landau wave functions (Aharonov-Bohm cages) [5]. Such localization effect is also observed in normal (non superconducting) wire networks [65, 66].
At low temperature there are two mechanism lifting the degeneracy of the fully frustrated ground state of JJAs.
In the framework of the FFXY model phase fluctuations of small amplitude in the vicinity of the ground state (spin waves) are shown to remove the accidental degeneracy only by tak-

ing into account the anharmonic contributions [10]. This *order-from-disorder* mechanism is then very weak. Moreover, the vortex ordering takes place, with an almost simultaneous onset of phase coherence, at a low temperature $\tau_c^{XY} \approx 0.01$ and in samples of macroscopic size. Because of these features, a true phase transition may be impossible to observe in JJAs.

Beyond the XY model the degeneracy is removed by the magnetic interaction between screening currents circulating in neighbouring cells. The associated magnetic energy increases when the temperature is lowered and the consequences manifest in various ways. The measured 2D penetration depth decreases until it becomes smaller than the lattice constant. Therefore the system is no more in a weak screening regime and the XY model is no more valid. To our knowledge this is the first time that such an effect is taken into account to understand the critical behaviour of frustrated JJAs and/or superconducting wire networks. Magnetic effects can be observed thanks to our measurement technique which probes the JJA superconducting phase. As a direct consequence the modulation of the magnetoimpedance $Z(f)$ by the applied magnetic field is suppressed and the frustration structures disappear. This is the main reason which explains why inverse magnetoinductance $L(f)$ measurements performed at low temperature cannot be understood on the basis of a mean field calculation combined with an analysis of the data which takes into account the anisotropic properties of the system.

In this low temperature regime the magnetic energy, which competes with the Josephson energy, allows selection of a vortex pattern whose ordering takes place at a higher temperature than τ_c^{XY} (helicity modulus vanishing) [10]. Therefore the XY phase transition is hidden by magnetic effects. Indeed the inverse magnetoinductance curves $L^{-1}(f)$ measured at temperatures below τ_c^{XY} show no peak at $f = 1/2$ which would be the signature of a phase transition.

The proposed scenario is a regime crossover, instead of a genuine phase transition, taking place at a frequency-dependent temperature τ_ω. Above τ_ω, in the XY regime, thermal fluctuations allow creation of an entangled network of zero energy domain walls carrying a large number of mobile point defects which weaken the phase coherence. When the temperature is lowered below τ_ω the domain wall network must disentangle in order to restore an equilibrium concentration of point defects and the regime crossover takes place from a high temperature phase characterized by a vortex liquid to a low temperature dynamically frozen vortex liquid [96]. The glass-like dynamics resulting from the slow disentanglement process is different from the one observed in numerical simulations [12].

Also the ground state of the uniformly frustrated XY model with $f = 1/3$ shows an accidental degeneracy associated with the existence of zero energy domain walls [13]. But in that case the degeneracy is so developed that it is not removed by the *order-from-disorder* mechanism. However, the helicity modulus is finite up to some critical temperature τ_c whereas the vortex pattern remains disordered down to T=0 [13].

Indeed the inverse magnetoinductance $L^{-1}(f)$ exhibits a pronounced peak at $f = 1/3$ although the vortex-pattern is disordered. The phase coherence is stabilized by pairs of half-vortices.

On the contrary of the fully frustrated state, the selection of a vortex pattern by the magnetic energy happens at a temperature well below τ_c, the critical temperature associated with the unbinding of fractional vortex pairs. This dynamics allows observation of a true phase transition at $\tau \approx 0.3$, which is a critical temperature value in good agreement with the one predicted by numerical [12] and analytical [13] calculations.

We also investigated the $f = 1/6$ state which shares with the $f = 1/3$ state the most pronounced structures in $Z(f)$.
As is the case for the $f = 1/3$ state the helicity modulus $\Gamma(\tau)$ at $f = 1/6$ indicates that the vortices which could enter into account in a possible BKT type phase transition are more probably fractional vortices than integer ones. The phase transition, when determined by the appearance of a phase coherent structure in $Z(f)$, happens at a temperature of the order of $\tau \approx 0.6$. Moreover, the ground state vortex patterns have configurations very similar to those of the $f = 1/3$ state.

The frequency behaviour we observe at low temperature is shared by many frustrated states, indicating some intrinsic features of SNS JJAs. Because of the nature of the coupling constant J in such arrays, experimentally unavoidable small variations of the geometrical parameters may lead to strong variations in J. Such disorder in the distribution of J induces a random potential in which single vortices created by residual frustration are free to be thermally activated, hopping between neighbouring cells. This scenario well explains the experimental observed dynamics.

The barrier energy value measured near zero field is still unexplained since it is two orders of magnitude higher than the calculated one. Such discrepancy is difficult to explain. A regime dominated by interacting vortices, instead of single (non interacting) vortices, could increase the effective energy barrier. One could also imagine a scenario involving a vortex diffusion controlled by surface barriers [117]. Near zero field, we observed an additional dissipative process in a temperature range where single vortices may play a leading role in the JJA dynamics. However, the reentrance of the sheet resistance measured at low frequency in this temperature range is still unexplained.

Appendix A

Calculation of the mutual inductance

The flux $\phi_{receive}$ induced through the receive coil is related to the drive current I_d by the mutual inductance function $M(Z_F)$ (Z_F being the sample sheet impedance). Actually, the quantity $M(Z_F)$ is is not an absolute value, but a variation of the mutual inductance $\delta M(Z_F)$. Anyway, to simplify the notation, we write $M(Z_F)$.

$$\phi_{receive} = M(Z_F)\ I_d(\vec{x}, t) \tag{A.1}$$

We consider the coils (drive and receive coils) as a set of regularly spaced identical (2D) circles (see illustration and parameters in Fig.3.1). The sample is excited with an AC magnetic field (vector potential $\vec{A}_d(\vec{x}, \omega_0)$) produced by the drive coil. Sheet currents $\vec{K}_F$ are induced in the sample. These currents produce AC magnetic fields with the same frequency $\omega_0/2\pi$ than the one of the AC drive current. The total vector potential is the sum of $\vec{A}_d$ and $\vec{A}_F$, where $\vec{A}_F$ is the vector potential due to the sheet normal $\vec{K}_N$ and superconducting $\vec{K}_S$ currents. Since the upper and lower parts of the receive coil form a gradiometer, $\vec{A}_d$ is compensated in both coils. This is the reason why the field through the receive coil is given only by $\vec{A}_F$.

The flux induced by the sample sheet currents is

$$\phi_{receive} = \int\limits_S \overrightarrow{B}_F(\vec{x}, t)\ d\overrightarrow{S} = \oint\limits_{\partial S} \overrightarrow{A}_F(\vec{x}, t)\ d\vec{\ell} \tag{A.2}$$

where S is the surface of the $N_r = 18$ loops of the receive coil.
and ∂S is the boarder path of the surface S, which means the circumference of the N_r loops.

We assume that the sample is a thin round (radius R) film located at $z = 0$.

The magnetic vector potential $\overrightarrow{A}(\vec{x}, t)$, for which we want to calculate the value at $r = R_r, z = h_r + \ell \cdot \delta h_r$ at time t, is determined by the Maxwell equations :

$$\overrightarrow{\nabla} \wedge \overrightarrow{B} = \mu_0 \vec{j} + \frac{1}{c^2}\dot{\overrightarrow{E}} \qquad \overrightarrow{\nabla} \wedge \overrightarrow{E} = -\dot{\overrightarrow{B}}$$

$$\overrightarrow{B} = \overrightarrow{\nabla} \wedge \overrightarrow{A} \qquad\qquad \overrightarrow{E} = -\overrightarrow{\nabla}\Phi - \dot{\overrightarrow{A}}$$

where the scalar electric potential Φ is zero since we do not consider any contribution from electric charges. In the Coulomb gauge, $\overrightarrow{\nabla}\overrightarrow{A} = 0$

$$\overrightarrow{E} = -\dot{\overrightarrow{A}} \tag{A.3}$$

$$\underbrace{\left(\frac{1}{c^2}\partial_t^2 - \Delta\right)}_{\text{D'Alembert operator } \Box} \overrightarrow{A}(\vec{x}, t) = \mu_0 \vec{j}(\vec{x}, t) \tag{A.4}$$

$$\overrightarrow{A} = \overrightarrow{A}_d + \overrightarrow{A}_s + \overrightarrow{A}_n \qquad \text{et} \qquad \vec{j} = \vec{j}_d + \vec{j}_s + \vec{j}_n$$

$\vec{j}_d(\vec{x}, t)$ is the drive current, $\vec{j}_n = \sigma_n \overrightarrow{E}$ is the normal current in the film, given by Ohm's law (σ_n is the conductivity) and the superconducting current $\vec{j}_s$ is given by the London equation

$$\vec{j}_s = \frac{-1}{\mu_0 \lambda_L^2} \left(\frac{\phi_0}{2\pi}\overrightarrow{\nabla}\varphi(\vec{x}, t) + \overrightarrow{A}\right) \tag{A.5}$$

where λ_L is the London penetration depth (for a film) and $\varphi(\vec{x}, t)$ is the phase of the superconducting order parameter. The term $\frac{\phi_0}{2\pi}\overrightarrow{\nabla}\varphi(\vec{x}, t)$ is associated with the dissipation due to vortices.

Sample sheet impedance

The film sheet impedance Z_F is defined by the relation

$$\overrightarrow{E} \overset{def}{=} Z_F \, \overrightarrow{K}_F = Z_F \, (\overrightarrow{K}_S + \overrightarrow{K}_N) \tag{A.6}$$

where the electric field $\overrightarrow{E}$ is given by (A.3) with a linear frequency response of the form

$$\overrightarrow{A}(\vec{x}, t) = \overrightarrow{A_0}(\vec{x}) \exp[i\omega_0 t]$$
$$\overrightarrow{E} = -i\omega_0 \overrightarrow{A}(\vec{x}, t) \tag{A.7}$$

We define an effective penetration depth for a thin film of thickness d

$$\Lambda \overset{def}{=} \frac{2\,\lambda^2}{d} \tag{A.8}$$

and

$$\overrightarrow{K}_S \overset{def}{=} \vec{j}_s \, d$$

is the sheet density of supercurrents. Using (A.5) and (A.8), it can be expressed as

$$\begin{aligned} \overrightarrow{K}_S &= \frac{-2}{\mu_0 \Lambda} \left(\frac{\phi_0}{2\pi}\overrightarrow{\nabla}\varphi + \overrightarrow{A}\right) \\ &\overset{def}{=} \frac{-1}{L_J} \left(\frac{\phi_0}{2\pi}\overrightarrow{\nabla}\varphi + \overrightarrow{A}\right) \end{aligned} \tag{A.9}$$

where $L_J = \frac{1}{2}\ \mu_0 \Lambda$ is the kinetic inductance.

$$\overrightarrow{K}_N \overset{def}{=} \vec{\jmath}_n\ d = \sigma_n\ d\ \vec{E} \ \overset{(A.7)}{=} -i\omega_0\ \sigma_n\ d\ \overrightarrow{A}(\vec{x},t) \tag{A.10}$$

The equation defining Z_F (A.6) becomes, using (A.7), (A.9) and (A.10),

$$i\omega_0\ \overrightarrow{A}(\vec{x},t) = Z_F\ \left[\frac{1}{L_J}\left(\frac{\phi_0}{2\pi}\overrightarrow{\nabla}\varphi + \overrightarrow{A}(\vec{x},t)\right) + i\omega_0\sigma_n d\overrightarrow{A}(\vec{x},t)\right] \tag{A.11}$$

where $\overrightarrow{A}(\vec{x},t) = \overrightarrow{A}_D + \overrightarrow{A}_F$ is found solving equation (A.4).

1. Low temperature limit
   $\sigma_n d << (\omega_0 L_J)^{-1}$ which is the case in our experimental conditions ($R_N >> \omega_0 L_J$). The equation (A.11) is simplified as follows

   $$\frac{\phi_0}{2\pi}\overrightarrow{\nabla}\varphi + \overrightarrow{A}(\vec{x},t) = \frac{i\omega_0\ L_J}{Z_F}\overrightarrow{A}(\vec{x},t) \tag{A.12}$$

   In absence of dissipation (no vortices) $Z_F \equiv Z_S = i\omega_0 L_J$ *the superfluid impedance.* To take into account the dissipation due to vortices ($\overrightarrow{\nabla}\varphi \neq 0$), the impedance is renormalized

   $$Z_S = i\omega_0 L_J\ \varepsilon(\omega,T) \tag{A.13}$$

   where $\varepsilon(\omega,T)$ [37] is a complex dielectric function which renormalizes the kinetic inductance L_J. Thus, from (A.11) we get

   $$Z_F = \left(\frac{1}{i\omega_0 L_J \varepsilon(\omega,T)} + \sigma_n d\right)^{-1}$$

   Using the relations (A.6), (A.7), (A.13) and the definition of L_J in (A.9), we write

   $$\overrightarrow{K}_S = \frac{-2}{\mu_0 \varepsilon \Lambda}\ \overrightarrow{A}(\vec{x},t) \tag{A.14}$$

2. High temperature limit
   The normal state sheet impedance is purely real

   $$Z_N = \frac{1}{\sigma_n d} = \frac{\rho_n}{d} \equiv R_N \tag{A.15}$$

   with R_N the normal state sheet resistance of the film.

Film induced sheet currents

We have to solve the equation (A.4) for $\overrightarrow{A}(\vec{x},t)$.
The origin of the vertical axe is located on the sample. The finite size of the sample is taken into account by cutting off the sheet currents at radius R using the Heaviside function

$$H(r-R)=\begin{cases} 1 & \text{si} \quad r\leq R \\ 0 & \text{sinon} \end{cases}$$

$$\vec{j}_s=\overrightarrow{K}_S\ \delta(z)\cdot\ H(r-R) \qquad\qquad \vec{j}_n=\overrightarrow{K}_N\ \delta(z)\cdot\ H(r-R)$$

We have to solve

$$\Box\overrightarrow{A}=\frac{-2}{\varepsilon\Lambda}\ \overrightarrow{A}\ \delta(z)\cdot H(r-R)-i\omega_0\mu_0\sigma_n d\ \overrightarrow{A}\ \delta(z)\cdot H(r-R)+\mu_0\ \vec{j}_D \tag{A.16}$$

to find $\overrightarrow{A}(z=0)$
Fig. A.1 shows the parameterization of the drive current in one loop of the coil.

$$\vec{j}_d(\vec{x},t)=I_d\ \delta(r-R_d)\left[\sum_{n=0}^{N_D-1}\delta(z-h_d-n\cdot\delta h_d)\right]\ \exp[i\omega_0 t]\cdot\hat{\varphi} \tag{A.17}$$

where $h_d+n\cdot\delta h_d$ is the position of the n^{th} loop of the coil versus the film at $z=0$.

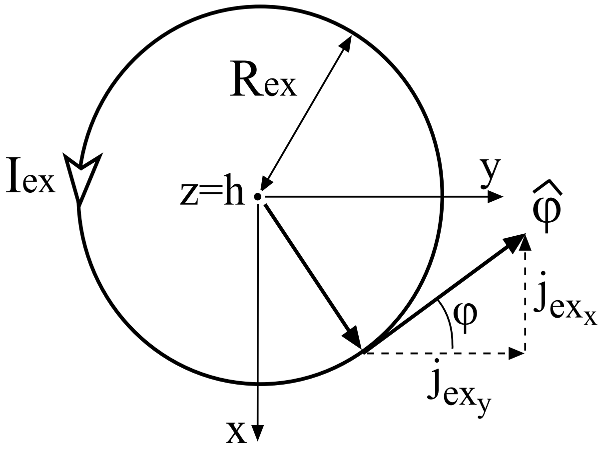

Figure A.1: Drive current distribution in the drive coil

Equation (A.16) is solved in the Fourier space.

Fourier space - definitions

Suppose $\vec{x}$ un vector of dimension d in the real space, $f(\vec{x})$ a scalar function. The Fourier transform (FT) of f, $\hat{f}(\vec{q})$, is defined by

$$FT\{f\}(\vec{q}) = \hat{f}(\vec{q}) = \int\limits_{-\infty}^{\infty} f(\vec{x})\ \exp[-i\ \vec{q}\cdot\vec{x}]\ d^d x$$

Inversely,

$$FT^{-}\{\hat{f}\}(\vec{x}) = f(\vec{x}) = \frac{1}{(2\pi)^d}\int\limits_{-\infty}^{\infty} \hat{f}(\vec{q})\ \exp[+i\ \vec{q}\cdot\vec{x}]\ d^d q$$

is the expression of f as a function of its Fourier transform in such a way that

$$FT^{-}\{FT\{f\}\} = f$$

This allows definition of the Dirac distribution

$$\delta(\vec{x}-\vec{x}') = \frac{1}{(2\pi)^d}\int\limits_{-\infty}^{\infty} \exp[i\ (\vec{x}-\vec{x}')\vec{q}\ ]\ d^d q$$

Properties

$$f(x,y,z=0) = \frac{1}{(2\pi)^3}\int \hat{f}(q_x,q_y)\ \exp[+i\ \vec{q}\cdot\vec{x}]\ d^3 q\Big|_{z=0} \tag{A.18}$$

$$\hat{f}(q_x,q_y,z=0) = \frac{1}{2\pi}\int \hat{f}(\vec{q})\ \exp[+iq_z\cdot z]\ dq_z\Big|_{z=0} = \frac{1}{2\pi}\int \hat{f}(\vec{q})\ dq_z \tag{A.19}$$

$$\begin{aligned} \nabla^n_{\vec{x}} f(\vec{x}) &\xrightarrow{FT} (i\ \vec{q})^n\cdot\hat{f}(\vec{q}) \\ \partial^n_t f(t) &\xrightarrow{FT} (i\ \omega)^n\cdot\hat{f}(\omega) \end{aligned} \tag{A.20}$$

Convolution product and properties

$$f(\vec{x})\otimes g(\vec{x}) = \int\limits_{-\infty}^{\infty} dq'_x dq'_y\cdot\ldots\ f(q_x-q'_x,q_y-q'_y,\ldots)\otimes g(q'_x,q'_y,\ldots) \tag{A.21}$$

$$f(\vec{q})\otimes g(\vec{q}) = g(\vec{q})\otimes f(\vec{q})$$

$$\begin{gathered} \hat{f}(\vec{q})\cdot\hat{g}(\vec{q}) = FT\{(f\otimes g)\}(\vec{q}) \\ \Updownarrow \\ FT\{(f\cdot g)\}(\vec{q}) = \hat{f}(\vec{q})\otimes\hat{g}(\vec{q}) \end{gathered} \tag{A.22}$$

Drive current The coordinate which corresponds to time t in the Fourier space is the frequency ω.

$$\begin{aligned} \hat{\jmath}_d(\vec{q},\omega) &= I_d \cdot \int dx\; dy\; \delta(x-x_d)\; \delta(y-y_d)\; \exp[-i(q_x x + q_y y)] \\ &\times \int dz\; \exp[-iq_z z] \sum_{n=0}^{N_D-1} \delta(z - h_d - n\cdot\delta h_d) \\ &\times \; 2\pi\; \delta(\omega-\omega_0)\; \cdot \hat{\varphi} \\ &= I_d \sum_{n=0}^{N_D-1} \exp[-i\; q_z(h_d + n\delta h_d)]\; 2\pi\; \delta(\omega-\omega_0)\; \cdot \mathcal{A} \end{aligned} \tag{A.23}$$

The term $\mathcal{A}$ represents the first integral (on $dx\; dy$ with the vector $\hat{\varphi}$). This integral is calculated by coordinate change

$$\begin{aligned} x &= r\;\cos\varphi & \qquad q_x &= q_t\;\cos\theta \\ y &= r\;\sin\varphi & q_y &= q_t\;\sin\theta \\ z &= z & q_z &= q_z \end{aligned} \tag{A.24}$$

$\hat{\varphi}$ and $\hat{\theta}$ are the vectors in the real and Fourier spaces.

$$r = \sqrt{x^2+y^2} \qquad q_t = \sqrt{q_x^2+q_y^2} \qquad \hat{\varphi} = \begin{pmatrix} -\sin\varphi \\ \cos\varphi \\ 0 \end{pmatrix} \qquad \hat{\theta} = \begin{pmatrix} -\sin\theta \\ \cos\theta \\ 0 \end{pmatrix}$$

The coordinate change Jacobian is equal to r, and $\mathcal{A}$ becomes

$$\begin{aligned} \mathcal{A} &= \int_0^{2\pi} d\varphi\; \hat{\varphi}\; \cdot \int_0^{\infty} dr\; r\; \exp[-i\; r\; q_t \cos\alpha]\; \delta(r - R_d) \\ &= R_d \int_0^{2\pi} d\varphi\; \hat{\varphi}\; \cdot \exp[-i\; R_d\; q_t \cos\alpha] \end{aligned} \tag{A.25}$$

$$\alpha = \varphi - \theta \Rightarrow \hat{\varphi} = \cos\alpha\; \hat{\theta} - \sin\alpha\; \hat{\theta}_\perp$$

$\hat{\theta}_\perp$ is the vector normal to $\hat{\theta}$.

$$\rightarrow\; \mathcal{A} = R_d \int_{-\theta}^{2\pi-\theta} d\alpha\; \cos\alpha\cdot\exp[-i\; R_d\; q_t\cos\alpha]\cdot\hat{\theta} + R_d \int_{-\theta}^{2\pi-\theta} d\alpha\; (-\sin\alpha)\cdot\exp[-i\; R_d\; q_t\cos\alpha]\cdot\hat{\theta}_\perp$$

The integration is 2π-periodic

$$\mathcal{A} = R_d\; \left[\int_0^{2\pi} d\alpha\; \cos\alpha\cdot\exp[-iR_d q_t\cos\alpha]\cdot\hat{\theta} + \int_0^{2\pi} d\alpha\; (-\sin\alpha)\cdot\exp[-iR_d q_t\cos\alpha]\cdot\hat{\theta}_\perp \right]$$

The second integral vanishes in the interval $\alpha \in [0, 2\pi]$ because de real and imaginary components are anti-symmetric versus $\alpha = \pi$.

$$\mathcal{A} = R_d \int_0^{2\pi} d\alpha \ \cos\alpha \ \exp[-iR_d q_t \cos\alpha] \cdot \hat{\theta} \tag{A.26}$$

'$\mathcal{A}$' can now be written as a Bessel function of the first kind at first order J_1,

$$J_1(u) = \frac{1}{\pi \ i} \cdot \int\limits_0^{\pi} d\alpha \ \cos\alpha \ \exp[i \cdot u \cdot \cos\alpha] \qquad [118]$$

which can be written (using $J_1(-u) = -J_1(u)$)

$$J_1(u) = -\frac{1}{2\pi \ i} \cdot \int\limits_0^{2\pi} d\alpha \ \cos\alpha \ \exp[-i \cdot u \cdot \cos\alpha] \tag{A.27}$$

In our case $u = q_t R_d$

$$\mathcal{A} = -2\pi \ i \ R_d \ J_1[q_t R_d] \ \cdot \hat{\theta} \tag{A.28}$$

This leads to a drive current in the Fourier space $\hat{j}_d(\vec{q}, \omega)$ (A.23)

$$\hat{j}_d(\vec{q}, \omega) = -(2\pi)^2 \ i \ I_d \ R_d \ J_1[q_t R_d] \sum_{n=0}^{N_D - 1} \exp[-i \ q_z(h_d + n\delta h_d)] \ \delta(\omega - \omega_0) \cdot \hat{\theta} \tag{A.29}$$

The normal- and super- currents are

$$\hat{j}_n(\vec{q}, \omega) = -i \ \omega_0 \ \sigma_n \ d \ \hat{A}(q_x, q_y, z = 0, \omega) \otimes \hat{H}(q_t)$$

$$\hat{j}_s(\vec{q}, \omega) = -\frac{2}{\mu_0 \varepsilon \Lambda} \ \hat{A}(q_x, q_y, z = 0, \omega) \otimes \hat{H}(q_t)$$

The equation for $\hat{A}(z = 0)$, (A.16) in the Fourier space is (using (A.20))

$$\left(\vec{q}^2 - K^2\right) \hat{A}(\vec{q}, \omega) = -\left(\frac{2}{\varepsilon\Lambda} + i\omega_0\mu_0\sigma_n d\right) \hat{A}_H + \ \mu_0 \hat{j}_d(\vec{q}, \omega) \tag{A.30}$$

$$K^2 = \omega^2/c^2 \qquad\qquad \hat{A}_H = \vec{A}(q_x, q_y, z = 0, \omega) \otimes \hat{H}(q_t)$$

We have to solve (A.30) for $\hat{A}(q_x, q_y, z = 0, \omega)$. Using the property (A.19), (A.30) becomes an implicit equation for $\hat{A}(q_x, q_y, z = 0, \omega)$

$$\begin{aligned}\hat{A}(z=0) &= \frac{1}{2\pi}\int \frac{dq_z}{\vec{q}^2 - K^2}\left[-\left(\frac{2}{\varepsilon\Lambda} + i\omega_0\mu_0\sigma_n d\right)\hat{A}_H + \mu_0\hat{j}_d(\vec{q},\omega)\right] \\ &= \underbrace{-\frac{1}{\pi}\left(\frac{1}{\varepsilon\Lambda} + \frac{i\omega_0\mu_0\sigma_n d}{2}\right)\hat{A}_H\int\frac{dq_z}{\vec{q}^2 - K^2}}_{\mathcal{C}} + \underbrace{\frac{\mu_0}{2\pi}\int dq_z\,\frac{\hat{j}_d(\vec{q},\omega)}{\vec{q}^2 - K^2}}_{\mathcal{D}} \qquad \text{(A.31)}\end{aligned}$$

Both integrals $\mathcal{C}$ and $\mathcal{D}$, are calculated at the end of this appendix.

$$\mathcal{C} = -\left(\frac{1}{\varepsilon\Lambda} + \frac{i\omega_0\mu_0\sigma_n d}{2}\right)\hat{A}_H \cdot \frac{1}{\tilde{q}_t} \qquad \text{(A.32)}$$

$$\mathcal{D} = \frac{\mu_0}{2\tilde{q}_t}\cdot\hat{j}_d(q_x, q_y, q_z = -i\tilde{q}_t, \omega) \qquad \text{(A.33)}$$

with

$$\tilde{q}^2 = \vec{q}^2 - K^2 \qquad\qquad \tilde{q}_t = \sqrt{q_t^2 - K^2}$$

Putting both integrals together, we get

$$\hat{A}(q_x, q_y, z = 0, \omega) = -(\hat{\Lambda}\tilde{q}_t)^{-1}\hat{A}_H + \frac{\mu_0}{2\tilde{q}_t}\hat{j}_d(q_x, q_y, q_z = -i\tilde{q}_t, \omega) \qquad \text{(A.34)}$$

$$\tilde{\Lambda} = \left((\varepsilon\Lambda)^{-1} + \frac{i\omega_0\mu_0\sigma_n d}{2}\right)^{-1}$$

where $\tilde{\Lambda}$ is an effective penetration depth renormalized by the normal currents.

We get an implicit equation for $\hat{A}_H$ defined in (A.30)

$$\begin{aligned}\hat{A}_H \overset{(A.30)}{=} \hat{A}(q_x, q_y, z = 0, \omega)\otimes\hat{H}(q_t) &= \left[-(\hat{\Lambda}\tilde{q}_t)^{-1}\hat{A}_H + \frac{\mu_0}{2\tilde{q}_t}\hat{j}_d\right]\otimes\hat{H} = \\ &= -(\hat{\Lambda}\tilde{q}_t)^{-1}\left[\hat{A}(z=0)\otimes\hat{H}\right]\otimes\hat{H} + \frac{\mu_0}{2\tilde{q}_t}\hat{j}_d\otimes\hat{H}\end{aligned}$$

Using the properties (A.22), it is possible to cancel the double convolution product (associative convolution product)

$$\hat{A}_H = -(\hat{\Lambda}\tilde{q}_t)^{-1}\underbrace{\left[\hat{A}(z=0)\otimes\hat{H}\right]}_{\hat{A}_H} + \frac{\mu_0}{2\tilde{q}_t}\hat{j}_d\otimes\hat{H}$$

$$\hat{A}_H = \frac{\mu_0}{2}\frac{\hat{j}_d\otimes\hat{H}}{\tilde{q}_t + \tilde{\Lambda}^{-1}} \qquad \text{(A.35)}$$

The total field $\hat{A}(\vec{q},\omega)$ is obtained putting (A.35) in (A.30). Nevertheless, we neglect $\hat{j}_d(q,\omega)$ in (A.30) since it is compensated by the gradiometer (this term has been used only to calculate $\hat{A}(z=0)$).

$$\hat{A}(q,\omega) = -\frac{1}{\tilde{q}^2}\,\frac{\mu_0 \hat{j}_d(q_x,q_y,-i\tilde{q}_t,\omega)\otimes \hat{H}(q_t)}{\tilde{q}_t\tilde{\Lambda}+1}$$

Transforming $\hat{A}(q,\omega)$ back to the real space (only for the $z-$component) ;

$$\begin{aligned}\hat{A}(q_x,q_y,z,\omega) &= \frac{1}{2\pi}\int dq_z\ \hat{A}(q,\omega)\exp[i\ q_z z] \\ &= -\frac{\mu_0}{\tilde{q}_t\tilde{\Lambda}+1}\hat{j}_d(q_x,q_y,-i\tilde{q}_t,\omega)\otimes\hat{H}(q_t)\frac{1}{2\pi}\cdot\underbrace{\int dq_z\frac{\exp[i\ q_z z]}{\tilde{q}_t^2+q_z^2}}_{\mathcal{F}} \qquad (A.36)\end{aligned}$$

$\mathcal{F}$ is calculated at the end of this appendix;

$$\mathcal{F} = \frac{\pi}{\tilde{q}_t}\ \exp[-\tilde{q}_t|z|]$$

Thus, (A.36) becomes

$$\hat{A}(q_x,q_y,z,\omega) = -\frac{\mu_0}{\tilde{q}_t\tilde{\Lambda}+1}\hat{j}_d(q_x,q_y,-i\tilde{q}_t,\omega)\otimes\hat{H}(q_t)\frac{1}{2\tilde{q}_t}\ \exp[-\tilde{q}_t|z|] \qquad (A.37)$$

We found the vector potential $\overrightarrow{A}(q_t,z,\omega)$ with the in-plane (q_t) and axial (z) components at frequency ω.
Remark : Since we did not take into account $\hat{j}_d(q,\omega)$ in (A.30), (A.37) is not the general solution of (A.34) for $z \neq 0$.

We can now calculate

1. the flux induced in the receive coil

$$\phi_{receive} = \oint \vec{A}(r=R_r, z=h_r+\ell\delta h_r)\vec{dl}$$

2. the sheet super currents distribution in the film

$$\vec{K}_S(q_t,z=0) = -\frac{2}{\mu_0\varepsilon\Lambda}\ \hat{A}(q_t,z=0)$$

3. the sheet normal currents distribution in the film

$$\vec{K}_N(q_t,z=0) = -i\omega_0\sigma d\ \hat{A}(q_t,z=0)$$

1. The mutual inductance

In the real space, (A.37) fir the ℓ^{th} loop of the receive coil

$$\overrightarrow{A}(r=R_r, z=h_r+\ell\cdot\delta h_r,\omega)=\frac{1}{(2\pi)^2}\int d^2q_t\ \exp[i(q_xx+q_yy)]\cdot\hat{A}(q_x,q_y,z=h_r+\ell\cdot\delta h_r,\omega) \tag{A.38}$$

Applying the same coordinate change (A.24) and the expression for $\hat{j}_d(q_x,q_y,-i\tilde{q}_t,\omega)$ (A.29), (A.38) becomes

$$\begin{aligned}\overrightarrow{A}(R_r,h_r+\ell\cdot\delta h_r,t) &= -I_d\ R_d\ \frac{i\mu_0}{2}\cdot\frac{1}{2\pi}\int d\omega\ \delta(\omega-\omega_0)\exp[i\omega t]\\ &\times\int_0^{2\pi} d\theta\int_0^{\infty} dq_t\ \frac{1}{\tilde{q}_t\tilde{\Lambda}+1}\ \exp[iq_tR_r\cos(\theta-\varphi)]\cdot q_t\ \exp[-\tilde{q}_t(h_r+\ell\delta h_r)]\\ &\times\sum_{n=0}^{N_D-1}\underbrace{\exp[-\tilde{q}_t(h_d+n\cdot\delta h_d)]/\tilde{q}_t\ J_1[q_tR_d]\ \cdot}_{\mathcal{J}}\hat{\theta}\otimes\hat{H}(q_t)\end{aligned} \tag{A.39}$$

from now on $K^2=\frac{\omega_0^2}{c^2}\equiv K_0^2$ because of $\delta(\omega-\omega_0)$.
The Fourier transform of the Heaviside function is [119]

$$\hat{H}(q_t)=\hat{H}(q_x,q_y)=2\pi R\ \frac{J_1(q_tR)}{q_t}$$

where R is the radius of the sample and J_1 the Bessel function of the first kind and first order (A.27).
Applying a coordinate change similar to the one of (A.24), the convolution product $\otimes$ defined in (A.21) can be written as

$$\begin{aligned}\mathcal{J}\otimes\hat{H} &= \int_0^{\infty} dq_t'q_t'\int_0^{2\pi} d\theta'\ \mathcal{J}(q_t',\theta')\ \hat{H}(q_t,q_t',\theta,\theta')\\ &= \int_0^{\infty} dq_t'q_t'\int_0^{2\pi} d\theta'\ \exp[-\tilde{q}_t'(h_d+n\cdot\delta h_d)]/\tilde{q}_t'\ J_1[q_t'R_d]\ 2\pi R\ \frac{J_1(q_t^\star R)}{q_t^\star}\cdot\hat{\theta}'\end{aligned}$$

where $\tilde{q}_t'=\sqrt{{q'}_t^2-K_0^2}$
et $q_t^\star=\sqrt{(q_x-q_x')^2+(q_y-q_y')^2}=\ldots=\sqrt{q_t^2+{q'}_t^2-2q_tq_t'\cdot\cos(\theta'-\theta)}$.

We call $\theta' - \theta = \theta^\star \Rightarrow d\theta' = d\theta^\star$. The vector $\hat{\theta}'$ is the superposition of

$$\hat{\theta}' = \cos\theta^\star \cdot \hat{\theta} - \sin\theta^\star \cdot \hat{\theta}_\perp$$

$$\mathcal{J} \otimes \hat{H} = \int_0^\infty dq_t' q_t' \int_0^{2\pi} d\theta^\star \; J_1[q_t' R_d] \; \frac{\exp[-\tilde{q}_t'(h_d + n\;\delta h_d)]}{\tilde{q}_t'} \; 2\pi R \; \frac{J_1(q_t^\star R)}{q_t^\star} \cdot (\cos\theta^\star \cdot \hat{\theta} - \sin\theta^\star \cdot \hat{\theta}_\perp)$$

As was the case for (A.26), the factor $\sin\theta^\star \cdot J_1(q_t^\star R)/q_t^\star$ is anti symmetric versus $\theta^\star = \pi$. The only contribution comes from the parallel vector $\hat{\theta}$

$$\begin{aligned}
\overrightarrow{A}(R_r, h_r + \ell \cdot \delta h_r, t) &= -I_d \; R_d \; \frac{i\mu_0}{2} \cdot \frac{\exp[i\omega_0 t]}{2\pi} \\
\times \; & \int_0^{2\pi} d\theta \int_0^\infty dq_t \; \frac{1}{\tilde{q}_t \tilde{\Lambda} + 1} \; \exp[i q_t R_r \cos(\theta - \varphi)] \cdot q_t \; \exp[-\tilde{q}_t(h_r + \ell \delta h_r)] \\
\times \; & \sum_{n=0}^{N_D - 1} \int_0^\infty dq_t' q_t' \int_0^{2\pi} d\theta^\star \; J_1[q_t' R_d] \; \frac{\exp[-\tilde{q}_t'(h_d + n\;\delta h_d)]}{\tilde{q}_t'} \; 2\pi R \; \frac{J_1(q_t^\star R)}{q_t^\star} \cdot \cos\theta^\star \cdot \hat{\theta}
\end{aligned} \tag{A.40}$$

We come back to the real space

$$\hat{\theta} = \cos\alpha \; \hat{\varphi} + \sin\alpha \; \hat{\varphi}_\perp \qquad \text{with } \alpha = \varphi - \theta \;\; \Rightarrow \;\; d\theta = -d\alpha$$

As previously, for the integral $\mathcal{A}$ (A.26), the term with $\hat{\varphi}_\perp$ vanishes and

$$\int_0^{2\pi} d\theta \exp[i q_t R_r \cos(\theta - \varphi)] \cdot \hat{\theta} = 2\pi i \; J_1(q_t R_r) \; \hat{\varphi}$$

Finally, the flux trough the receive coil is given by (A.2), and the mutual inductance function is identified according to (A.1) with $I = I_d \exp[i\omega_0 t]$

$$\phi_{receive} \equiv \sum_{l=0}^{(N_R/2)-1} \vec{A}(R_r, h_r + \ell \cdot \delta h_r) \; \vec{dl} = 2\pi R_r \sum_{l=0}^{(N_R/2)-1} A(R_r, h_r + \ell \cdot \delta h_r)$$

$$
\begin{aligned}
M(Z_F) = \; = \;& 2\pi^2 \mu_0 R R_r R_d \times \\
\times \;& \int_0^\infty \int_0^\infty dq_t dq_t' \frac{q_t q_t'}{\tilde{q}_t'} \cdot \frac{J_1(q_t R_r) J_1(q_t' R_d)}{\tilde{q}_t \tilde{\Lambda} + 1} \times \\
\times \;& \exp[-\tilde{q}_t h_r] \exp[-\tilde{q}_t' h_d] \; \frac{1 - \exp[-\tilde{q}_t (N_R/2)\; \delta h_r]}{1 - \exp[-\tilde{q}_t \delta h_r]} \; \frac{1 - \exp[-\tilde{q}_t' N_D \; \delta h_d]}{1 - \exp[-\tilde{q}_t' \delta h_d]} \times \\
\times \;& \int_0^{2\pi} d\theta^\star \; \frac{J_1(q_t^\star R)}{q_t^\star} \cos\theta^\star
\end{aligned}
\tag{A.41}
$$

The sums of $\exp[-q_t \delta h_\alpha]$ has been expressed as a geometrical progression.

$$
q_t^\star = \sqrt{q_t^2 + q'^2_t - 2 q_t q_t' \cdot \cos(\theta^\star)} \qquad \tilde{q}_t = \sqrt{q_t^2 - \frac{\omega_0^2}{c^2}}
$$

$$
\tilde{\Lambda} = \left((\varepsilon\Lambda)^{-1} + \frac{i\omega_0 \mu_0 \sigma_n d}{2} \right)^{-1} \overset{(A.13),(A.15)}{=} \frac{2}{i\omega_0\mu_0} \left[\frac{1}{Z_S} + \frac{1}{Z_N} \right]^{-1} = \frac{2}{i\omega_0\mu_0} \; \frac{1}{G_S + G_N}
$$

We clearly see the explicit dependence of M as a function of the film sheet impedance

$$
Z_F = \left[\frac{1}{Z_S} + \frac{1}{Z_N} \right]^{-1}
$$

or its equivalent sheet conductance $G_F = G_S + G_N$, expressed with both superconducting and normal components.

Since it has not yet been possible to numerically evaluate the expression for the finite sample (A.41), we consider the sample as an infinite film. This leads to a much more simple expression for $M(Z_F)$.

Infinite sample If we assume that the sample is an infinite film, the mutual inductance function $M(Z_F)$ can be calculated in the same way, but without the Heavyside function which cuts the sheet currents off at the sample size

$$
\vec{j}_s = \vec{K}_S \delta(z) \qquad \vec{j}_n = \vec{K}_N \delta(z)
$$

This simplifies the calculation and we obtain an analogous expression but with only one integration

$$
M(Z_F) = \pi \; \mu_0 \; \cdot \; \int_0^\infty dq_t \; \frac{F_d(\tilde{q}_t, q_t) \cdot F_r(\tilde{q}_t, q_t)}{\tilde{q}_t \tilde{\Lambda}(Z_S, Z_N) + 1} \cdot \frac{q_t}{\tilde{q}_t} \; \exp[-\tilde{q}_t (h_r + h_d)] \tag{A.42}
$$

$$
F_\alpha(\tilde{q}_t, q_t) = R_\alpha \; J_1(q_t R_\alpha) \; \frac{1 - \exp[-\tilde{q}_t N_\alpha \; \delta h_\alpha]}{1 - \exp[-\tilde{q}_t \delta h_\alpha]}
$$

Displacement current effect In our experimental situation the effects of the displacement currents are negligible. There is a significant effect only above a few GHz, near the micro wave and infra red regions of the light spectrum. To evaluate the effects of the displacement currents on the mutual inductance M we compare the total variation of the response with, and without, the contribution of $\tilde{q}_t$. The total variation of the response is difference between the normal state and the perfect diamagnetic state (i.e. when $\Lambda = 0$). This is called the saturation value, M_{ss}, since it corresponds to $M(Z_F = 0)$.

$$M(Z_F = 0, \omega_0 = 0)\Big|_{\overrightarrow{E}=0} = 145.2nH$$

$$M(Z_F = 0, \omega_0 = 10^{10})\Big|_{\overrightarrow{E}\neq 0} = 145.9nH$$

For such high frequencies, one could observe delay effects of the interaction propagation between the coils and the sample.
Since $\omega_0^2/c^2 << q_t^2$, $\tilde{q}_t = q_t$, we ignore this contribution and we get

$$M(Z_F) = \int_0^\infty dq_t \, \frac{\tilde{M}(q_t)}{1 + \dfrac{2q_t}{i\omega_0\mu_0} Z_F}$$

The function $\tilde{M}(q_t) = \pi\mu_0 \; F_d(q_t) \cdot F_r(q_t) \;\; \exp[-q_t(h_r + h_d)]$ contains all the geometrical parameters and defines the saturation value

$$M_{ss} \equiv M(Z_F = 0) = \int_0^\infty dq_t \; \tilde{M}(q_t)$$

The second coil of the receive coil, the highest one, provides a contribution to $M(Z)$ in a similar way than the lowest coil but with an opposite sign due to the astatic configuration (gradiometer). The signal is then decreased by the quantity

$$\pi\mu_0 \; F_d(q_t)F_r(q_t) \; (\exp[-q_t(h_r + h_d)] - \exp[-q_t(h_{r2} + h_d)])$$

We use $\delta = h_{r2} - h_r$ the distance between both coils to write

$$\tilde{M}(q_t) = \pi\mu_0 \; F_d(q_t)F_r(q_t) \; \exp[-q_t(h_r + h_d)] \cdot (1 - \exp[-q_t\delta])$$

Even if the effect of the second coil is not so important we take it into account

with the lowest coil only : $M_{ss} \cong 145nH$

with the second coil too : $M_{ss} \cong 130nH$

2. The sheet super current distribution in the film

$$\hat{K}_S(q_t, z=0) = -\frac{2}{\mu_0 \varepsilon \Lambda}\,\hat{A}(q_t, z=0) \overset{A.34}{=} -\frac{1}{\varepsilon\Lambda}\,\frac{\hat{j}_d(q_z=-iq_t)}{\tilde{\Lambda}^{-1}+q_t}$$

To obtain the distribution current $\vec{K}_S(\rho)$ in the film, we have to transform $\hat{K}_S(q_t)$ back to the real space in the same way as for $\hat{A}(q_x, q_y, z, \omega)$ (A.39).

$$\vec{K}_S(\rho) = I_d \int_0^\infty dq_t\; q_t \frac{\tilde{K}(\rho)}{Z_S\left[\dfrac{1}{Z_S}+\dfrac{1}{Z_N}\right]+\dfrac{2Z_S}{i\omega_0\mu_0}q_t}\;\hat{\varphi}$$

$$\tilde{K}(\rho) = \exp[-q_t h_d] J_1(q_t\rho) F_d(q_t R_d)$$

3. The sheet normal current distribution in the film

$$\hat{K}_N(q_t, z=0) = -i\omega_0\sigma_n d\hat{A}(q_t, z=0) = -\frac{i\omega_0\mu_0}{2}\sigma_n d\frac{\hat{j}_d(q_z=-iq_t)}{\tilde{\Lambda}^{-1}+q_t}$$

In the same way as for $\vec{K}_S(\rho)$ we obtain in the real space

$$\vec{K}_N(\rho) = I_d \int_0^\infty dq_t q_t \frac{\tilde{K}(\rho)}{Z_N\left[\dfrac{1}{Z_S}+\dfrac{1}{Z_N}\right]+\dfrac{2Z_N}{i\omega_0\mu_0}q_t}\;\hat{\varphi}$$

Calculation of the integrals $\mathcal{C}$, $\mathcal{D}$ and $\mathcal{F}$ by residue.

Calculation of $\mathcal{C}$ The integral to compute is

$$\begin{aligned}
\int_{-\infty}^{+\infty} \frac{dq_z}{\vec{q}^2 - K^2} &= \int_{-\infty}^{+\infty} dq_z \, \frac{1}{q_x^2 + q_y^2 - K^2 + q_z^2} \\
&\equiv \int_{-\infty}^{+\infty} dq_z \, \frac{1}{q_t^2 - K^2 + q_z^2} \\
&\equiv \int_{-\infty}^{+\infty} dq_z \, \frac{\text{polynomial}(q_z) \text{ of power } 0}{\text{polynomial}(q_z) \text{ of power } 2} \equiv \int_{-\infty}^{+\infty} dq_z \; \mathrm{f}(q_z)
\end{aligned}$$

We write

$$\begin{aligned}
\tilde{q}^2 &= \vec{q}^2 - K^2 \\
\tilde{q}_t &= \sqrt{q_t^2 - K^2}
\end{aligned}$$

To use the theory of residues, we have to deal with complex numbers, $q_z \in \mathbf{C}$.
In such a case where the function to integrate is a fraction of polynomials with a denominator power $\geq$ of 2 than the numerator, the residues give rise to a result without taking care about the integral path.

$$\int_{-\infty}^{+\infty} \frac{dq_z}{\tilde{q}^2} = 2\pi i \sum_j \text{Residue}[\mathrm{f}(q_z), q_{z_j}] \tag{A.43}$$

where q_{z_j} are the j poles of $\mathrm{f}(q_z)$. The function has two simple poles at

$$q_z^2 = -\tilde{q}_t^2 \;\Rightarrow\; q_{z_j} = \pm i\tilde{q}_t$$

but only one is in the upper complex semi-plane which contains the integral path. Since it is a simple pole,

$$\begin{aligned}
\text{Résidus}[\mathrm{f}(q_z), iq_t] &= \lim_{q_z \to i\tilde{q}_t} \left[(q_z - i\tilde{q}_t) \, \frac{1}{\tilde{q}_t^2 + q_z^2} \right] \\
&= \lim_{q_z \to i\tilde{q}_t} \left[\frac{1}{i\tilde{q}_t + q_z} \right] \\
&= \frac{1}{2i\tilde{q}_t} = \frac{1}{2i \, \sqrt{q_t^2 - K^2}}
\end{aligned}$$

So the integral (A.43) is $\dfrac{\pi}{\tilde{q}_t}$, and

$$\mathcal{C} = -\frac{1}{\varepsilon\Lambda} \, \hat{A}(q_x, q_y, z = 0, \omega) \cdot \frac{1}{\tilde{q}_t}$$

Calculation of $\mathcal{D}$ The integral to compute is

$$\int_{-\infty}^{+\infty} dq_z \, \frac{\exp[-i\ q_z h]}{\tilde{q}_t^2 + q_z^2} \equiv \int_{-\infty}^{+\infty} dq_z\ f(q_z) \qquad \text{où } q_z \in \mathbf{C}$$

The singularities which can not be eliminated are the same as for the integral $\mathcal{C}$, which means two simple poles at $\pm i q_t$. The chosen integral path is the following

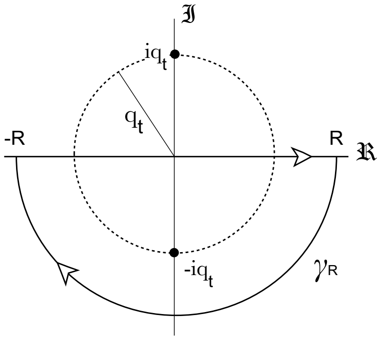

Figure A.2: Integral path in the complex plane.

$$\gamma = [\text{-R,R}] \cup \gamma_R \qquad \gamma_R = \text{R}\cdot \exp[i\pi(t+1)] \qquad \text{t} \in [0,1]$$

Théorème 1 (Residues)

$$\begin{aligned} \frac{1}{2\pi i} \oint_\gamma f(q_z)\ dq_z &= \sum_j Res[f, q_{z_j}] \cdot Indice_\gamma(q_{z_j}) \\ &= \int_{-R}^{R} f(q_z)\ dq_z + \int_{\gamma_R} f(q_z)\ dq_z \end{aligned}$$

The integral on γ_R goes to zero when R goes to infinity. Along γ_R, $q_z = R\exp[i\pi(t+1)]$

$$\begin{aligned} \int_{\gamma_R} f(q_z)\ dq_z &= \int_{\gamma_R} \frac{\exp[-i\ q_z h]}{\tilde{q}_t^2 + q_z^2} dq_z \\ &= \int_0^1 \frac{\exp[-ihR\exp^{i\pi(t+1)}]}{\tilde{q}_t^2 + R^2 \exp 2i\pi(t+1)}\ i\pi R \exp[i\pi(t+1)]\ dt \end{aligned}$$

The modulus is

$$\left| \int_{\gamma_R} f(q_z)\ dq_z \right| \le \int_0^1 \left| \frac{\exp[-ihR\exp^{i\pi(t+1)}]}{\tilde{q}_t^2 + R^2 \exp[2i\pi(t+1)]}\ i\pi R \exp[i\pi(t+1)] \right| dt$$

$$\leq \;\; \pi \int_{0}^{1} R \, \frac{\exp^{Rh\sin(\pi(t+1))}}{\tilde{q}_t^2 + R^2} \, dt = \pi \int_{0}^{1} g(t) \, dt$$

where we applied the Minkowsky inequality ($|a+b| \leq |a| + |b|$) and the propriety $|\, e^{z}| = e^{Re\{z\}}$.
Since $\sin(\pi(t+1)) \leq 0$ for t $\in$ [0,1], when $R \longrightarrow \infty$, g(t) $\longrightarrow 0$.

Notice that if we chose the semi-circle in the upper semi-plane as integral path containing the pole at $+iq_t$, it is not possible to annihilate the integral on the semi-circle. The parameterization would be $\gamma_R = R \cdot \exp[i\pi t]$. That would give rise to $\sin(\pi t) \geq 0 \; \forall t \in [0,1]$ in the exponential of g(t), instead of $\sin(\pi(t+1))$.

The non vanishing integral is

$$\int_{-\infty}^{+\infty} f(q_z) \, dq_z = -2\pi i \cdot \lim_{q_z \,\longrightarrow\, -i\tilde{q}_t} (q_z - (-i\tilde{q}_t)) \, \frac{\exp[-iq_z h]}{\tilde{q}_t^2 + q_z^2} = \frac{\pi}{\tilde{q}_t} \; \exp[-\tilde{q}_t h]$$

The term $\mathcal{D}$ can be written, using the expression of $\hat{j}_d$ (A.29),

$$\mathcal{D} = \frac{\mu_0}{2\tilde{q}_t} \cdot \hat{j}_d(q_x, q_y, q_z = -i\tilde{q}_t, \omega)$$

Calculation of $\mathcal{F}$

$$\mathcal{F} = \int_{-\infty}^{+\infty} dq_z \frac{\exp[i \; q_z z]}{\tilde{q}_t^2 + q_z^2} = \int_{-\infty}^{+\infty} f(q_z) \, dq_z$$

In that case, the singularities are the same as the previous ones, $\pm iq_t$. The difference is the sign (-) in the exponential. Since this sign and the previous note, the integral path is a semi-circle in the upper complex semi-plane $\gamma_R = R \cdot \exp[i\pi t]$. The pole selected by the index (cf. Theorem 1 (Residues)) is $+iq_t$. The calculation to cancel

$$\int_{\gamma_R} \frac{\exp[i \; q_z z]}{\tilde{q}_t^2 + q_z^2} \, dq_z$$

when $R \longrightarrow \infty$ is similar to that for integral $\mathcal{D}$. The result is the following

$$\left| \int_{\gamma_R} \frac{\exp[i \; q_z z]}{\tilde{q}_t^2 + q_z^2} \, dq_z \right| \;\; \leq \;\; \pi \int_{0}^{1} R \, \frac{\exp^{-R \cdot z \sin(\pi t)}}{\tilde{q}_t^2 + R^2} \, dt$$

The expression inside the integral goes to zero when $R \longrightarrow \infty$ as long as $z \geq 0$. We write $|z|$.

$$\mathcal{F} = 2\pi i \cdot \lim_{q_z \,\longrightarrow\, i\tilde{q}_t} (q_z - i\tilde{q}_t) \, \frac{\exp[iq_z|z|]}{\tilde{q}_t^2 + q_z^2} = \frac{\pi}{\tilde{q}_t} \; \exp[-\tilde{q}_t|z|] \tag{A.44}$$

Appendix B

Cryostat pictures

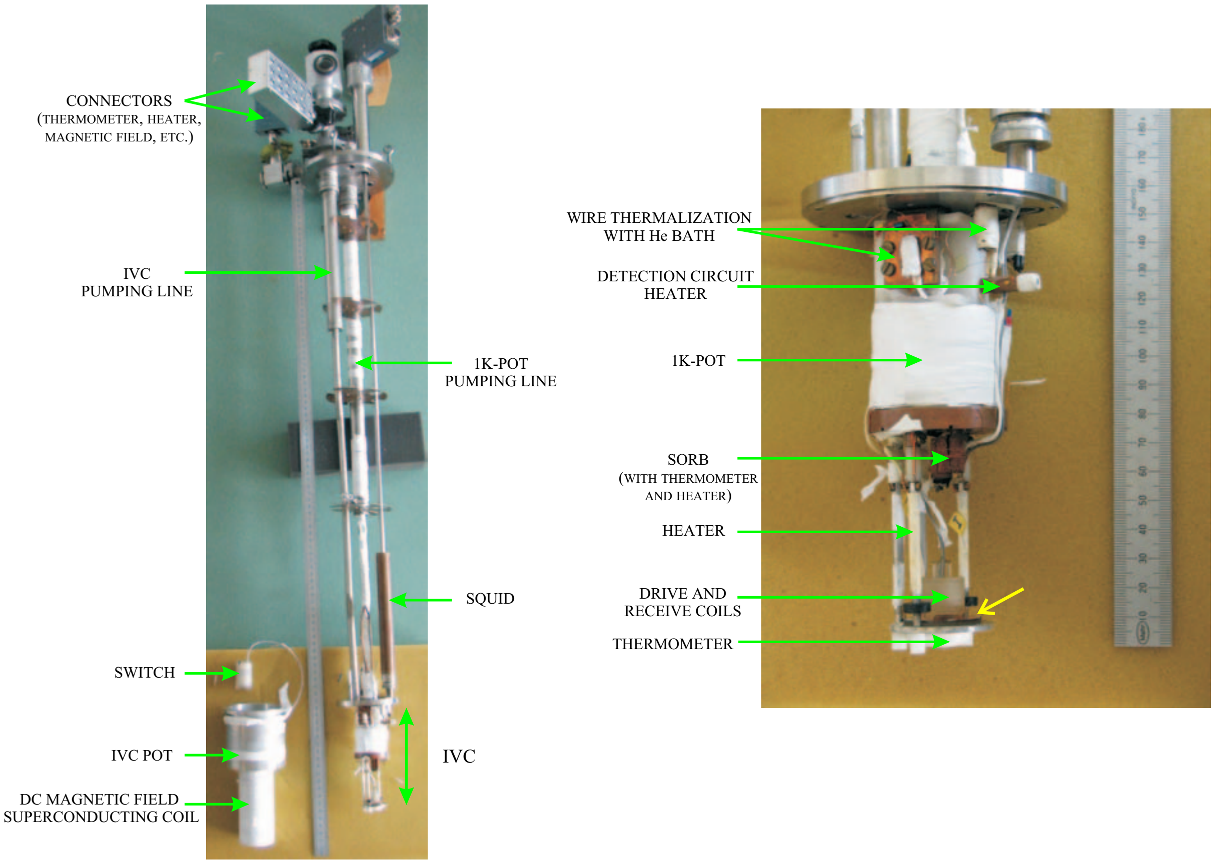

Figure B.1: Cryostat main elements. Left side: cryostat with magnetic field coil. Right side: Inner Vacuum Chamber (IVC). The yellow arrow indicates the sample. The main components are described in chapter 3

Appendix C

Electronic setup

Fig.C.1 is a diagram of the electronic configuration. The experiment is located inside a metallic cage which is connected to ground. Notice that this ground is especially dedicated to our experiments and is not shared with the building electric network. The cryostat is connected to the cage as well as all the electronic devices. To avoid ground loops, the shields of the cables which connect the electronic devices to the cryostat are connected only at one end.

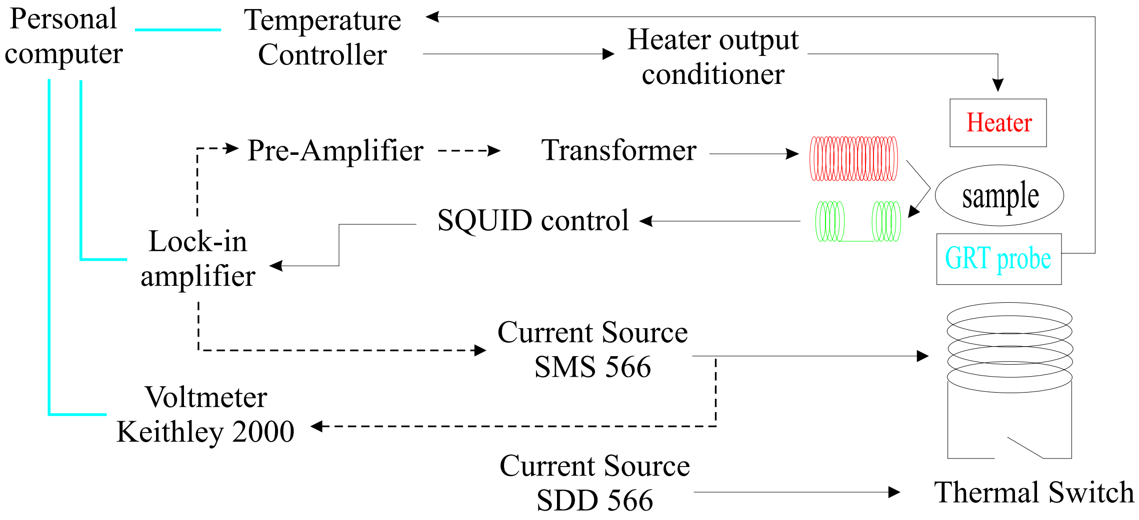

Figure C.1: Diagram of the electronic setup. The excitation is achieved by the EG&G7260 lock-in amplifier and the drive coil (Fig.3.1 and Table 3.1). The voltmeter Keithley 2000 is used to measure the effective current which flows in the frustration coil. The current source (SDD566) used to open the thermal switch is battery supplied to avoid ground loop problems.

Appendix D

Raw data treatment

D.1 Phase rotation and normalization

In section 3.2.4 we showed how to simplify the integral relation between the measured mutual inductance change and the sheet impedance using the δ function approximation. The aim of this appendix is to explain how we proceed to invert the integral relation in order to extract the components of Z. We first have to rotate the phase in such a way to get, in the normal state, the measured sheet resistance (section 2.2.1). Then, the modified raw data are normalized with respect to the full signal variation V_{ss}. The procedure is different for the three types of measurement, i.e. temperature, frustration and frequency measurements. The treatment of the temperature measurements is based on the critical current expression (2.7). Thus, at the end of this procedure, we get the parameter values of the critical current, and hence the reduced temperature (section 1.2.2, (1.6)). The single junction critical current is illustrated in section 2.2.3 where it is compared to the same quantity extracted from four probe measurements.

D.1.1 Temperature measurements

In addition to the signal measured with a lock-in (amplitude and phase components) the device has its own phase of reference which can be set between 0° and 360°. In order that the reel X and imaginary Y components give respectively the inductive and dissipative responses (as was the case in Fig.3.6), it is necessary to rotate the data in such a way that above the lead islands transition temperature (T_{CS}) the dissipative response is given by the eddy currents. This implies that the rotated real component at high temperature ($X_{ROT} < 0$) is given by the pick up and the eddy currents contribution as described in 3.2.4. Fig.D.1 shows an example of rotated data following the procedure described above (normal state criterium). In that case, for frequencies above about 20Hz, a frequency dependent dissipative signal appears at low temperature. If one try to set the dissipative component to zero at low temperature ($Y(T \ll T_{CS}) = 0$), then the final result (the sheet resistance R_Z) would exhibit a frequency dependence of the normal state plateau (at $T > T_{CS}$) !
Then we have to subtract the effect of the bad coil compensation (pick up) which manifests

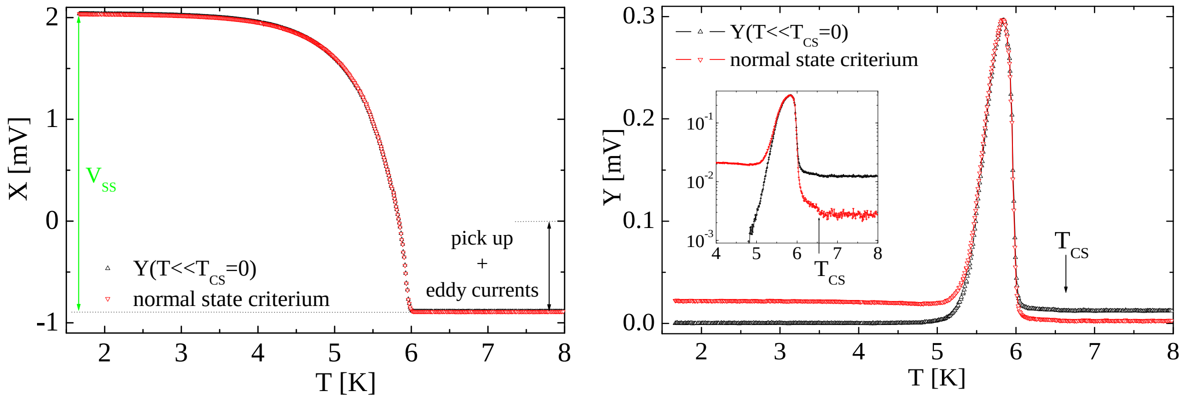

a) b)

Figure D.1: Raw data at $f = 0$ and frequency $\omega/2\pi = 303$Hz. Black curves: the phase is rotated such that the dissipative response $Y(T << T_{CS}) = 0$. Red curves: the phase is rotated such that $Y(T > T_{CS})$ given by the eddy currents. a) inductive X response and b) dissipative Y response. The inset shows the SC islands transition temperature T_{CS} and the small signal coming from eddy currents (red curve).

as an inductive signal only (see section 3.2.4).

$$\text{pick up} = X_{ROT}(T > T_{CS}) - Vss\left[1 + \left(\frac{R_N}{\omega_0 M_c}\right)^2\right]^{-1}$$

The second term in the right hand side of this equation is very small compared to X_{ROT} in the frequency range of our measurements. Nevertheless, we take it into account.
Finally we normalize both components with respect to V_{ss}.

$$X_{NORM} = \frac{X_{ROT} - \text{pick up}}{V_{ss}} \cdot \gamma \qquad\qquad Y_{NORM} = \frac{Y_{ROT}}{V_{ss}} \cdot \gamma$$

where $V_{ss} = X_{ROT}(T \ll T_{CS}) - X_{ROT}(T > T_{CS})$ is the total signal change. The saturation value at low temperature is never reached for a JJA as is the case for the superconducting film (see Fig.3.6). This is the reason why we introduce the γ factor. It is a correction of less than 1%, but it has a huge importance. The γ factor is determined with the help of a theoretical criterion based on the temperature dependence of the single junction critical current at low temperature (section 2.2.3, expression (2.7)).
If we suppose that all the junctions have the same geometrical properties then in the non frustrated state ($f = 0$), and for low temperatures, the single junction inductance $L_J(T)$ (section 1.2.2, (1.5)) is related to the sheet inductance through the geometrical factor (1.2.4)

$$L_{\square}^{-1} = 2/3\sqrt{3}L_J^{-1} = 2/3\sqrt{3}(2e/\hbar)I_{CJ}(T) \tag{D.1}$$

Using the single junction critical current expression (2.7)

$$L_\square^{-1}(T) = \frac{2\sqrt{3}}{3}\frac{64\pi}{(3+2\sqrt{2})}\frac{2k_BT_{CS}}{\hbar R_N}\frac{\ell_J}{\xi_N(T_{CS})}\left(\frac{T}{T_{CS}}\right)^{3/2}F[X(T)]\exp[-C\sqrt{T}] \tag{D.2}$$

with the same function $F[X(T)]$ and constant C as for (2.7).

If we plot $\ln[L_\square^{-1}/(T/T_{CS})^{3/2}F[X(T)]]$ versus $\sqrt{T}$ we get at low temperature a linear behaviour with a negative slope equal to the constant $-C$ and the intercept b given by

$$b = \ln[\frac{2\sqrt{3}}{3}\frac{64\pi}{(3+2\sqrt{2})}\frac{2k_BT_{CS}}{\hbar R_N}\frac{\ell_J}{\xi_N(T_{CS})}]$$

The sheet inverse inductance $L_\square^{-1}(T)$ is obtained from inductive measurements, the ratio $\ell_J/\xi_N(T_{CS})$ is given by the slope C and the normal state single junction resistance by the intercept b. The critical current is then completely known.

For frequencies higher than a few tens of hertz, at low temperature the dissipative component increases with the frequency (Fig.D.1), i.e. $R_Z(T \ll T_{CS})$ raises. This gives rise to a dramatic deviation from linearity of $L_G^{-1}(T \ll T_{CS})$, as illustrated in Fig.D.2. However, for low frequencies ($\omega/2\pi \leq 20$Hz) $L_G^{-1}(T \ll T_{CS}) = L_Z^{-1}(T \ll T_{CS})$.

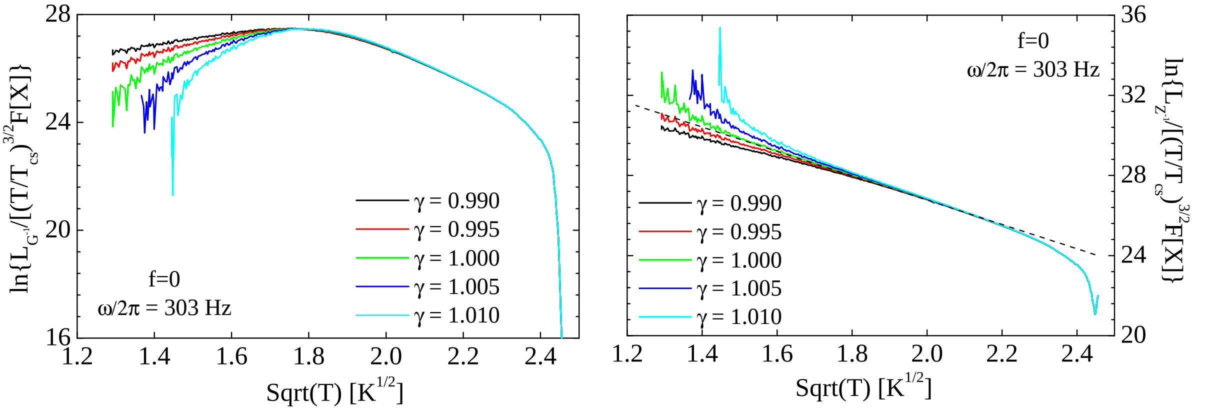

a) b)

Figure D.2: Unfrustrated state at high frequency. a) conductance imaginary component $L_\square^{-1} \equiv L_G^{-1}$. b) impedance imaginary component $L_\square^{-1} \equiv L_Z^{-1}$. The dashed line indicates the predicted linear low temperature behaviour.

The γ factor is determined in such a way to realize the best linear fit described above (ln-function), see Fig.D.3. The same γ factor is used for the treatment of frustration and frequency measurements. The fit parameters are *slope* $C = 5.73K^{-1/2}$ and *intercept* $b = 38.29$. With $T_{CS} = 6.61K$ these parameters lead to $\ell_J/\xi_N(T_{CS}) = 14.75$ and the single junction normal state resistance $R_{JN} = 23.9m\Omega$!

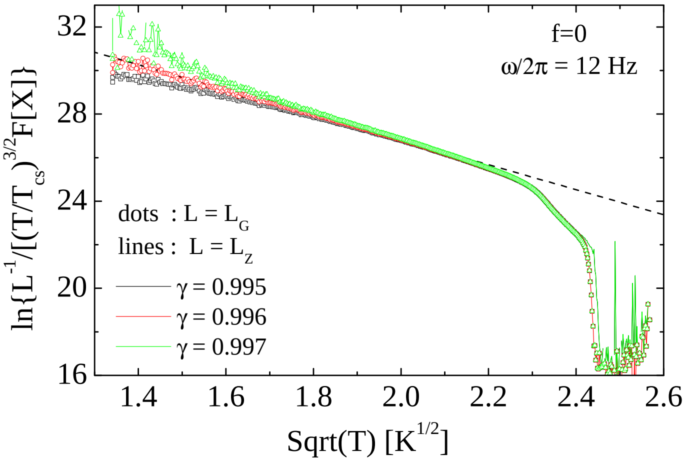

Figure D.3: Normalization γ factor; unfrustrated state at low frequency. $L_G \equiv L_Z$ except in the critical region. The γ value which realizes the best fit is $\gamma = 0.996$. The dashed line is the linear fit (parameters in text).

D.1.2 Frustration measurements

An important step of the treatment is the phase rotation. The measured phase must be rotated such that the dissipative component $Y(T > T_{CS})$ is set by the eddy currents (see section 3.2.4). Since this signal, as well as the low temperature response, are frequency dependent, it is necessary to perfome a temperature measurement at the same frequency and phase reference than the frustration measurements. The frustration data are then rotated according to the temperature data rotation which is needed to satisfy the previous conditions (eddy currents).

In addition to the normalization, the frustration scale must be shifted to compensate the offset (see section 3.7, Fig.3.14). Then, the frustration coil current scale I is normalized with respect to the most predominant f_n structure. Fig.D.4 shows an example where the chosen structures are those at $f_n = 1/3$. An approximative value for f is given by the field/current relation (see section 3.6).

$$I \rightarrow I' = I - offset$$

$$I' \rightarrow f = I' \cdot f_n / I'(f_n)$$

$$X_{NORM} = \frac{X_{ROT} - \text{pick up}}{V_{ss}} \cdot \gamma \qquad\qquad Y_{NORM} = \frac{Y_{ROT}}{V_{ss}} \cdot \gamma$$

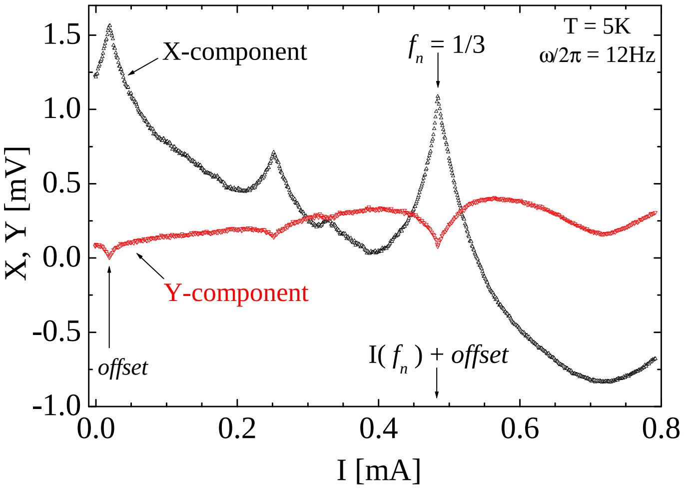

Figure D.4: Rotated X_{ROT} and Y_{ROT} components from a measurement at $T = 5K$ and a frequency $\omega/2\pi = 12$Hz. Most pronounced structures for $f_n = 1/3$.

D.1.3 Frequency measurements

This type of measurements does not allow rotation of the phase a posteriori because the phase continuously changes during the frequency measurement as illustrated in Fig.D.5, which shows the amplitude and the phase of the signal at different temperatures. The measurement is thus performed at an arbitrary fixed lock-in reference phase.

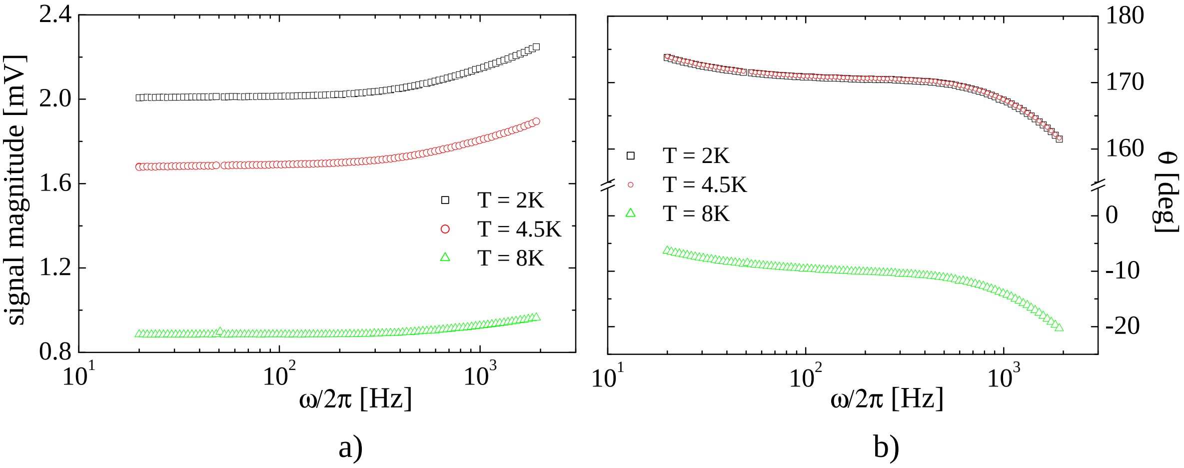

Figure D.5: Frequency dependence of the measured amplitude (a) and phase (b). Note that the phase does not change until the normal state is reached.

The same sequence of frequencies is measured at low temperature, at the temperatures of interest and in the normal state. The phase of the normal state ($\theta(T > T_{CS})$ in Fig.D.5) is the reference phase used to rotate the data in such a way that $Y(T > T_{CS}) = 0$. It is a way to simulate the auto-phase function of the lock-in. Then, in order to take the eddy currents effect into account, the phase is rotated again until the normal state values given in section 3.2.4 are reached. This implies a rotation of $\varphi = \tan^{-1}(Y/X) = \tan^{-1}(\frac{\omega M_c}{R_N \alpha})$ because $\frac{R_N}{\omega M_c} \gg 1$ for $\omega/2\pi \leq 10$KHz.

The frequency dependent V_{ss} and pick up are given by

$$V_{ss}(\omega) = X_{ROT}(T \ll T_{CS}, \omega) - X_{ROT}(T > T_{CS}, \omega)$$

$$\text{pick up}(\omega) = X_{ROT}(T > T_{CS}, \omega) - V_{ss}(\omega) \left[1 + \left(\frac{R_N}{\omega M_c} \right)^2 \right]^{-1}$$

Finally, the normalization expressions are identical to those for temperature measurements with the same γ factor which is almost frequency independent.

D.2 Numerical inversion

The numerical inversion procedure is based on the iterative Newton-Raphson algorithm [120]. The aim of this method is to simultaneously solve two coupled equations of two variables, in our case R_Z and L_Z

$$f_1(R_Z, L_Z) = X_{NORM} - I_d \; M' = 0$$

$$f_2(R_Z, L_Z) = Y_{NORM} - I_d \; M'' = 0$$

where X_{NORM} and Y_{NORM} are the normalized in phase and quadrature components of the voltage, M' and M'' are the real (3.4) and imaginary (3.5) components of the mutual inductance change (section 3.2.2) and I_d is the drive current. The iterations are based on an expansion in Taylor series of the first order of the 2D-vector $\mathbf{V}$ of values v_j ($v_1 \equiv R_Z$ and $v_2 \equiv L_Z$)

$$f_i(\mathbf{V} + \delta\mathbf{V}) = f_i(\mathbf{V}) + \sum \frac{\partial f_i}{\partial v_j} \delta v_j = 0$$

δv_j are corrections which simultaneously move the functions f_i to zero.

We first have to calculate the sum coefficients, $\frac{\partial f_i}{\partial v_j}$, and $f_i(\mathbf{V})$ to solve the above equation in order to find the corrections δv_j that are added to the old solutions v_j.

$$v_j^{n+1} = v_j^n + \delta v_j$$

Starting with the initial guess given by the rapid inversion procedure ((3.8) and (3.9) in section 3.2.4), we iterate the process until the corrections are smaller than some tolerance value.

Bibliography

[1] P. Martinoli and Ch. Leemann, J. Low Temp. Phys. **118**, 699 (2000), and references cited therein

[2] R. Fazio and H.S.J. van der Zant, Physics Reports **355**, 235 (2001), and references cited therein

[3] J. Villain, J. Phys. C **10**, 1717 (1977)

[4] R. Meyer, S.E. Korshunov, Ch. Leemann, and P. Martinoli, Phys Rev. B **66**, 104503 (2002)

[5] J. Vidal, R. Mosseri, and B. Douçot, Phys. Rev. Lett. **81**, 5888 (1998);
J. Vidal, *PhD thesis*, University Paris VI (1999), unpublished

[6] C.C. Abilio, P. Butaud, Th. Fournier, B. Pannetier, J. Vidal, S. Tedesco, and B. Dalzotto, Phys. Rev. Lett. **83**, 5102 (1999)

[7] B. Pannetier, C.C. Abilio, E. Serret, Th. Fournier, P. Butaud, and J. Vidal, Physica C **352**, 41 (2001)

[8] E. Serret, P. Butaud, and B. Pannetier, Europhys. Lett. **59**, 225 (2002)

[9] S.E. Korshunov, Phys. Rev. B **63**, 134503 (2001)

[10] S.E. Korshunov, Phys. Rev. B **71**, 174501 (2005)

[11] S.E. Korshunov and B. Douçot, Phys. Rev. Lett. **93**, 097003 (2004)

[12] V. Cataudella and R. Fazio, Europhys. Lett. **61**, 341 (2003)

[13] S.E. Korshunov, Phys. Rev. Lett. **94**, 087001 (2005)

[14] K.K. Likharev, Rev. Mod. Phys. **51**, 101 (1979)

[15] A.A. Golubov, Rev. Mod. Phys. **76**, 411 (2004)

[16] B.D. Josephson, Phys. Lett. **1**, 251 (1962)

[17] A. Barone and G. Paternò, *Physics and Applications of the Josephson Effect*, J. Wiley (1982)

[18] M. Tinkham, *Introduction to superconductivity*, Second edition, McGraw-Hill (1996)

[19] A.-L. Eichenberger, *PhD thesis*, University of Neuchâtel (1997), unpublished

[20] H.S.J. van der Zant, *PhD thesis*, Technische Universiteit Delft (1991), unpublished

[21] S. Teitel and C. Jayaprakash, Phys. Rev. Lett. **51**, 1999 (1983)

[22] C.J. Lobb, D.W. Abraham, and M. Tinkham, Phys. Rev. B **27**, 150 (1983)

[23] S. Teitel and C. Jayaprakash, Phys. Rev. B **27**, 598 (1983)

[24] W.Y. Shih and D. Stroud, Phys Rev. B **32**, 158 (1985)

[25] W.Y. Shih and D. Stroud, Phys Rev. B **28**, 6575 (1983)

[26] S.E. Korshunov, Phys Rev. Lett. **88**, 167007 (2002)

[27] S.E. Korshunov, A. Vallat, and H. Beck, Phys Rev. B **51**, 3071 (1995)

[28] J. Villain, R. Bidaux, J.P. Carton, and R. Conte, J. Phys. (Paris) **41**, 1263 (1980)

[29] R. Peierls, Ann. Inst. Henri Poincaré **5**, 177 (1935)

[30] N.D. Mermin and H. Wagner, Phys. Rev. Lett. **17**, 1133 (1966)

[31] J.M. Kosterlitz and D.J. Thouless, J. Phys. C**5**, L124 (1972); **6**, 1181 (1973)

[32] V.L. Berezinskii, Zh. Eksp. Teor. Fiz. **61**, 1144 (1971); V.L. Berezinskii, Sov. Phys. JETP **32**, 493 (1971); **34**, 610 (1972)

[33] J.M. Kosterlitz, J. Phys. C**7**, 1046 (1974)

[34] D.J. Resnick, J.C. Garland, J.T. Boyd, S. Shoemaker, and R.S. Newrock, Phys. Rev. Lett. **47**, 1542 (1981)

[35] D.J. Bishop and J.D. Reppy, Phys. Rev. Lett. **40**, 1727 (1978); Phys. Rev. B **22**, 5171 (1980)

[36] V. Ambegaokar, B.I. Halperin, D.R. Nelson, and E.D. Siggia, Phys. Rev. Lett. **40**, 783 (1978); Phys. Rev. B **21**, 1806 (1980)

[37] A.F. Hebard and A.T. Fiory, Physica 109&110B, 1637-1648 (1982)

[38] D.R. Nelson and J.M. Kosterlitz, Phys. Rev. Lett. **39**, 1201 (1977)

[39] S.R. Shenoy, J. Phys. C: Sol. Stat. Phys. **18**, 5143 (1985), erratum **20**, 2479 (1987)

[40] Ch. Leemann, Ph. Lerch, G.-A. Racine, and P. Martinoli, Phys. Rev. Lett. **56**, 1291 (1986)

[41] W.Y. Shih and D. Stroud, Phys Rev. B **30**, 6774 (1984)

[42] J. Lee, J.M. Kosterlitz, and E. Granato, Phys. Rev. B **43**, 11531 (1991)

[43] P. Olsson, Phys. Rev. Lett. **75**, 2758 (1995)

[44] V.I. Marconi and D. Dominguez, Phys. Rev. Lett. **87**, 017004 (2001)

[45] B. Berge, H.T. Diep, A. Ghazali, and P. Lallemand, Phys. Rev. B **34**, 3177 (1986)

[46] H. Eikmans, J.E. van Himbergen, H.J.F. Knops, and J.M. Thijssen, Phys. Rev. B **39**, 11759 (1989)

[47] D. Ariosa, A. Vallat, and H. Beck, J. Phys. France **51**, 1373 (1990)

[48] J. Affolter, M. Tesei, H. Pastoriza, Ch. Leemann, and P. Martinoli, Physica C **369**, 313 (2002)

[49] B.I. Halperin and D.R. Nelson, Phys. Rev. Lett. **41**, 121 (1978); erratum **41**, 519 (1978); D.R. Nelson and B.I. Halperin, Phys. Rev. B **19**, 2457 (1979); A.P. Young, Phys. Rev. B **19**, 1855 (1979)

[50] V.I. Marconi and D. Dominguez, Phys. Rev. Lett. **82**, 4922 (1999); V.I. Marconi and D. Dominguez, Phys. Rev. B **63**, 174509 (2001)

[51] M. Franz and S. Teitel, Phys. Rev. Lett. **73**, 480 (1994); M. Franz and S. Teitel, Phys. Rev. B **51**, 6551 (1995)

[52] S.A. Hattel and J.M. Wheatley, Phys. Rev. B **51**, 11951 (1995)

[53] B.J. Kim and P. Minnhagen, Phys. Rev. B **63**, 094514 (2001)

[54] J.P. Straley, A.Y. Morozov, and E.B. Kolomeisky, Phys. Rev. Lett. **79**, 2534 (1997)

[55] J.P. Straley and E.B. Kolomeisky, Phys. Rev. B **61**, 92 (2000)

[56] M.S. Rzchowski, S.P. Benz, M. Tinkham, and C.J. Lobb, Phys. Rev. B **42**, 2041 (1990)

[57] R. Meyer, J.L. Gavilano, B. Jeanneret, R. Théron, Ch. Leemann, H. Beck, and P. Martinoli, Phys. Rev. Lett. **67**, 3022 (1991); Physica A **191**, 458 (1992)

[58] R. Théron, *PhD thesis*, University of Neuchâtel (1992), unpublished

[59] C.J. Gorter and H.B.G Casimir, Physica **1**, 306 (1934)

[60] P. Martinoli, R. Théron, J.-B. Simond, R. Meyer, Y. Jaccard, and Ch. Leemann, Physica Scripta **T49**, 176 (1993)

[61] B. Sutherland, Phys. Rev. B **34**, 5208 (1986), and references cited therein.

[62] P.G. de Gennes, c. R. Acad. Sci. Ser. B, **292**, 9 and 279 (1981)

[63] S. Alexander, Phys. Rev. B **27**, 1541 (1983)

[64] F.H. Claro and G.H. Wannier, Phys. Rev. B **19**, 6068 (1979)

[65] C. Naud, G. Faini, and D. Mailly, Phys. Rev. Lett. **86**, 5104 (2001)

[66] J. Vidal, G. Montambaux, and B. Douçot, Phys. Rev. B **62**, 16294 (2000)

[67] S.E. Korshunov, R. Meyer, and P. Martinoli, Phys. Rev. B **51**, 5914 (1995)

[68] S.E. Korshunov, Phys. Rev. B **68**, 094512 (2003)

[69] Md. Ashrafuzzaman and H. Beck, Studies of High Temperature Superconductors, Vol. 43, Nova Science Pub, NY, 2002 (Chapter 5), and references cited therein.

[70] P. Minnhagen, Rev. Mod. Phys. **59**, 1001 (1987)

[71] B.A. Huberman, R.J. Myerson, and S. Doniach, Phys. Rev. Lett. **40**, 780 (1978)

[72] S.R. Shenoy, J. Phys. C: Sol. Stat. Phys. **18**, 5163 (1985), erratum **20**, 2480 (1987)

[73] R. Théron, J.-B. Simond, Ch. Leemann, H. Beck, P. Martinoli, and P. Minnhagen, Phys. Rev. Lett. **71**, 1246 (1993)

[74] A. Jonsson and P. Minnhagen, Phys. Rev. B **55**, 9035 (1997)

[75] H. Beck, Phys. Rev. B **49**, 6153 (1994)

[76] S.E. Korshunov, Phys. Rev. B **50**, 13616 (1994)

[77] B.J. Kim, P. Minnhagen, and P. Olsson, Phys. Rev. B **59**, 11506 (1999)

[78] M. Capezzali, H. Beck, and S.R. Shenoy, Phys. Rev. Lett. **78**, 523 (1997)

[79] Md. Ashrafuzzaman, M. Capezzali, and H. Beck, Phys. Rev. B **68**, 052502 (2003)

[80] B.J. Kim and P. Minnhagen, Phys. Rev. B **60**, 15043 (1999)

[81] M.J. Ferrari, F.C. Wellstood, J.J. Kingston, and J. Clarke, Phys. Rev. Lett. **67**, 1346 (1991)

[82] P.G. de Gennes, Rev. Mod. Phys. **36**, 225 (1964)

[83] P. Martinoli, Phys. kondens. Materie **16**, 53-93 (1973)

[84] L.J. van der Pauw, Philips Research Reports **13**, 1 (1958)

[85] N.W. Ashcroft and N.D. Mermin, *Solid State Physics*, Saunders College, CBS Publishing Asia LTD. (1976) page 8

[86] D.W. Abraham, C.J. Lobb, M. Tinkham, and T.M. Klapwijk, Phys. Rev. B **26**, 5268 (1982)

[87] G. Brändli and J.L. Olsen, *Mater. Sci. Eng.*, **4**, 61 (1969)

[88] S.P. Benz, M.S. Rzchowski, M. Tinkham, and C.J. Lobb, Phys. Rev. B **42**, 6165 (1990)

[89] C.M. Falco, W.H. Parker, S.E. Trullinger, and P.K. Hansma, Phys. Rev. B **10**, 1865 (1974)

[90] F.K. Wilhelm, A.D. Zaikin, and G. Schön, J. Low Temp. Phys. **106**, 305 (1997);
P. Dubos, H. Courtois, B. Pannetier, F.K. Wilhelm, A.D. Zaikin, and G. Schön, Pys. Rev. B **63**, 064502 (2001)

[91] Empirical temprature dependence fitted from the tables in B. Muhlschlegel, Z. Phys. **155**, 313 (1959)

[92] V. Ambegaokar and A. Baratoff. Phys. Rev. Lett. **10**, 486 (1963)
see also its Errata Phys. Rev. Lett. **11**, 104 (1963)

[93] F.W. Grover, *Inductance Calculations*, Dover Publications

[94] B. Jeanneret, J.L. Gavilano, G.-A. Racine, Ch. Leemann, and P. Martinoli, Appl. Phys. Lett. **55**, 2336 (1989)

[95] J.-P. Locquet, Y. Jaccard, A. Cretton, E.J. Williams, F. Arrouy, E. Mächler, T. Schneider, Ø. Fischer, and P. Martinoli, Phys. Rev. B **54**, 7481 (1996);
A. Rüfenacht, P. Chappatte, S. Gariglio, Ch. Leemann, J. Fompeyrine, J.-P. Locquet, and P. Martinoli, Sol. Stat. Elec. **47**, 2167 (2003)

[96] M. Calame, S.E. Korshunov, Ch. Leemann, and P. Martinoli, Phys. Rev. Lett. **86**, 3630 (2001)

[97] O. V. Lounasmaa, *Experimental Principals and Methods Below 1K*, Academic Press (1974)

[98] C.P. Poole Jr., H.A. Farach, and R.J. Creswick, *Superconductivity*, pages 326-327 and 342, Academic Press (1995)

[99] L. Landau and E. Lifchitz, *Physique théorique Tome V, Physique statistique* première partie, pages 412-420, Traduction française Edtitions MIR (1984)

[100] Morris Driels, *Linear Control Sys. Engin.*, McGraw-Hill

[101] L.E. DeLong, O.G. Symko, and J.C. Wheatley, Rev. Sci. Inst. **42**, 147 (1971)

[102] R.H. Dee, *Basic Solenoid construction*, Norton Company Supercon Division

[103] R. Théron, S.E. Korshunov, J.B. Simond, Ch. Leemann, and P. Martinoli, Phys. Rev. Lett. **72**, 562 (1994)

[104] S.E. Korshunov and B. Douçot, Phys. Rev. B **70**, 134507 (2004)

[105] S. Candia, Ch. Leemann, S. Mouaziz, and P. Martinoli, Physica C **369**, 309 (2002)

[106] G. Blatter, M.V. Feigel'man, V.B. Geshkenbein, A.I. Larkin, and V.M. Vinokur, Rev. Mod. Phys. **66**, 1125 (1994)

[107] T. Giamarchi and S. Bhattacharya, *High Magnetic Fields: Applications in Condensed Matter Physics and Spectroscopy*, p. 314, ed. C. Berthier *et al.* (2002);
T. Nattermann and S. Scheidl, Adv. Phys. 49, 607 (2000)

[108] N.F. Mott and E.A. Davis, *Electronic processes in non crystalline materials*, Clarendon Press, Oxford (1971)

[109] P. Martinoli, private communication

[110] A.M. Dykhne, Zh. Eksp. Teor. Fiz. **59**, 110 (1970); Sov. Phys. JETP **32**, 63 (1971)

[111] S.E. Korshunov, private communication

[112] P. Martinoli *et al.*, Physica (Amsterdam) **165**, 1163 (1990); M.W. Coffey and J.R. Clem, Phys. Rev. Lett. **67**, 386 (1991);

[113] R. Meyer, Ch. Nussbaum, J.L. Gavilano, B. Jeanneret, Ch. Leemann, and P. Martinoli, Physica A **191**, 458 (1992); B. Jeanneret, Ph. Flückiger, J.L. Gavilano, Ch. Leemann, and P. Martinoli, Phys. Rev. B **40**, 11374 (1989)

[114] S.T. Herbert, Y. Jun, R.S. Newrock, C.J. Lobb, K. Ravindran, H.-K. Shin, D.B. Mast, and S. Elhamri, Phys. Rev. B **57**, 1154 (1998)

[115] E. Serret, *PhD thesis*, Université Joseph Fourier (2002), unpublished

[116] C.P. Bean and J.D. Livingston, Phys. Rev. Lett. **12**, 14 (1964)

[117] L. Burlachkov, V.B. Geshkenbein, A.E. Koshelev, A.I. Larkin, and V.M. Vinokur, Phys. Rev. B **50**, 16770 (1994); L. Burlachkov, A.E. Koshelev, and V.M. Vinokur, Phys. Rev. B **54**, 6750 (1996)

[118] M. Abramowitz and I.A. Stegun, Handbook of Mathematical Functions, 5th ed. (1964), *National Bureau of Standards Applied Mathematics Series • 55*

[119] D.C. Champeney, *Fourier Transforms and their physical applications*, Academic Press (1973)

[120] W.H. Press, B.P. Flannery, S.A. Teukolsky, W.T. Vetterling, Numerical Recipes in Pascal, *Cambridge University Press* (1989)